

## Preface – The critical seventh year

T. Czigány\*

Department of Polymer Engineering, Faculty of Mechanical Engineering, Budapest University of Technology and Economics, Műegyetem rkp. 3., H-1111, Budapest, Hungary

### Dear Readers,

**eXPRESS Polymer Letters** has started its seventh volume. Even though seven is a lucky number, the seventh year in any relationship is often considered a critical one, as many things may appear usual, boring and worn-out by then. I strongly believe that **eXPRESS Polymer Letters** will maintain its good relationship with its readers, who will find new, interesting and useful articles in every issue of the seventh volume as well. I also hope that **eXPRESS Polymer Letters** will continue having a good relationship with its authors, too, and will receive plenty of ‘cutting-edge’ articles in 2013 just like in the previous years, even though the rejection rate has reached over 80% by now. Finally, I build upon our referees’ continuing professional reviewing work that has led to the ever growing impact factor and recognition of **eXPRESS Polymer Letters** so far. The journal has got its first impact factor of 1.452 by 2009, which was only its third year, and it was raised to 1.575 in 2010 and to 1.769 in 2011. Our short term goal is to raise and keep the impact factor above 2. We have very good chances to achieve this goal, as the 5-year impact factor of the journal is already 2.003. Our middle and long term goal is to increase the journal’s recognition to be on a level with the best journals in its field. Right now, **eXPRESS Polymer Letters** ranks at the end of the first third of all the journals of similar topics, but we would like it to rank in the top 10%. This would require a longer time, as we are one of the youngest journals in this field, so it is a really outstanding result to be in the top third only after six years. The credit for this goes to the article topics that are in the forefront of the researchers’ interest today. Tak-

ing a look back on the most popular and most cited articles of the past six years, we can conclude that the main topics are still the natural materials like biopolymers and biocomposites, (keywords include starch, wood, cellulose, chitosan, biodegradable, soybean oil), which is in accordance with the industry’s expectations toward researchers. However, articles about nano materials also maintain their popularity (keywords include nanofibres, nanoparticles, nanotubes, nanocomposites, graphene), even though as these materials have failed to meet the high industrial expectations, their significance and number have dropped markedly. Apart from this, articles about structure-property relationships, optimization of technological parameters, preparation of new structural materials, or development of polymers with special characteristics are popular, too. Based on all this, we look forward to the critical seventh year that we expect to bring continuous progress for the **eXPRESS Polymer Letters**. Finally, we are respectfully thankful for the professional work of our authors and referees, and in the name of the editor-in-chief, the international advisory board and the local editorial team, the editor wishes you a lot of success in year 2013. Sincerely yours,



Prof. Dr. Tibor Czigány, editor

\*Corresponding author, e-mail: [czigany@eik.bme.hu](mailto:czigany@eik.bme.hu)  
© BME-PT

# Nanospheres and nanocapsules of amphiphilic copolymers constituted by methoxypolyethylene glycol cyanoacrylate and hexadecyl cyanoacrylate units

I. Valente<sup>1</sup>, L. J. del Valle<sup>2</sup>, M. T. Casas<sup>2</sup>, L. Franco<sup>1</sup>, A. Rodríguez-Galán<sup>2</sup>, J. Puiggali<sup>2\*</sup>, D. Marchisio<sup>1</sup>

<sup>1</sup>Dipartimento di Scienza Applicata e Tecnologia, Politecnico di Torino, Corso Duca degli Abruzzi 24, 10129 Torino, Italy

<sup>2</sup>Departament d'Enginyeria Química, Universitat Politècnica de Catalunya, Av. Diagonal 647, E-08028 Barcelona, Spain

Received 11 June 2012; accepted in revised form 3 August 2012

**Abstract.** Nanospheres and nanocapsules of an amphiphilic copolymer having methylated polyethylene glycol and hexadecyl lateral groups were prepared by the solvent displacement method and using confined impinging jet mixers. Degradation, thermal properties and crystalline structure were investigated. Interestingly, pegylated chains hydrolyzed through ester bond cleavage, whereas the more hydrophobic hexadecyl ester groups were resistant to degradation in aqueous media. The copolymer crystallized from the melt, giving rise to spherulites with a negative birefringence and domains corresponding to crystallization of the different lateral groups. Size distribution and morphology of nanoparticles were mainly evaluated by electron microscopy. Nanocapsules were characterized by a stable membrane with a thickness close to 5 nm that allowed efficient encapsulation of a triglyceride oil. Triclosan was selected as an example of a hydrophobic drug to be loaded in both nanospheres and nanocapsules. The release behavior of these dosage forms was clearly different. Thus, the Burst effect was practically suppressed when using nanocapsules; in addition, these showed a sustained, controlled release over a greater time period. Antimicrobial activity of triclosan loaded nanospheres and nanocapsules was evaluated using Gram-negative and Gram-positive bacteria. The former were highly sensitive to the released triclosan whereas the latter strongly depended on the number of particles in the culture medium.

**Keywords:** biodegradable polymers, nanocapsules, drug release, antimicrobial activity, amphiphilic polymers

## 1. Introduction

Amphiphilic copolymers are interesting because of their ability to stabilize diverse interfaces in aqueous systems and, in particular, as drug delivery systems [1]. Amphiphilic compounds are characterized by the incorporation of polar and non-polar monomer units in a polymer chain. Their synthesis and preparation can be a difficult task, especially when controlling the ratio between both chemical units in the resulting polymer chain and the homogeneity of the final structure, is needed [2].

The utility of amphiphilic copolymers for delivery of therapeutic agents is due to their unique chemical composition, which allows micellization in aqueous solutions and formation of hydrophobic core regions. These serve as reservoirs for hydrophobic drugs that can be loaded with chemical, physical or electrostatic means, depending on the specific functionalities of the core-forming block and the solubilize. Furthermore, surface modification of particulate carriers with hydrophilic and flexible chains prevents their recognition by macrophages and rapid

\*Corresponding author, e-mail: [Jordi.Puiggali@upc.edu](mailto:Jordi.Puiggali@upc.edu)

elimination from the bloodstream [3, 4]. Pluronic<sup>®</sup>, which is constituted by poly(ethylene oxide) and poly(propylene oxide) blocks [5], is currently a common studied system, although copolymers containing poly(L-amino acid) and polyester hydrophobic blocks are gaining interest [2].

Amphiphilic molecules of cyanoacrylate have also been widely studied as drug delivery systems. These compounds are now prepared mainly by radical copolymerization reactions in monophasic organic solvents like dimethyl formamide or butanone [6, 7], or in two-phase solvents where the monomers dissolve each in one of the two phases [8–10]. Another method of preparation of cyanoacrylate amphiphilic copolymers is based on the condensation reaction of methoxy polyethylene glycol cyanoacetate and hexadecyl cyanoacetate with formaldehyde in the presence of an organic solvent like methylamine [11]. These methoxy polyethylene glycol cyanoacrylate-co-hexadecyl cyanoacrylate copolymers, abbreviated as poly(MePEGCA-co-HDCA), can be prepared with modulated hydrophobicity/hydrophilicity by adjusting the MePEGCA/HDCA monomer ratio. Some previous works focused on the preparation of nanoparticles from poly(MePEGCA-co-HDCA) with a hydrophilic/hydrophobic monomer ratio of 1:4 by nanoprecipitation and emulsion/solvent evaporation methods [11, 12]. Monomodal size distributions were obtained with characteristic mean particle sizes ranging between 98 and 199 nm and varying according to polymer concentration and the applied method. It was also demonstrated that nanoparticles have an adequate density of MePEG chains on their surface to provide enhanced stability in the blood compartment and ensure a long circulating characteristic [13, 14]. Nanoparticles of poly(alkyl cyanoacrylate) amphiphilic copolymers have recently been successfully used for other biomedical applications such as human brain endothelial cell imaging [15] and early Alzheimer's disease diagnosis and treatment [16].

Drug loaded nanoparticles of poly(MePEGCA-co-HDCA) have also recently been prepared using a new methodology based on solvent displacement in confined impinging jet mixers (CIJM) [17]. These devices allow continuous production, facilitate scaling-up and guarantee controllable operating parameters and conditions to improve final nanoparticle properties [18]. The solvent (e.g. acetone or tetrahydrofuran) and the anti-solvent streams (e.g. water)

are mixed under different flow conditions, defined by and labelled in terms of the anti-solvent/solvent flow rate ratio ( $R$ ) and the flow rate of the anti-solvent stream ( $F_w$ ). Besides their usefulness to get nanospheres constituted by the polymer alone, CIJM allow also the preparation of nanocapsules containing an oily core. Miglyol 812, a triglyceride of caprylic and capric fatty acids, seems appropriate to provide an oil core where water-insoluble drugs remain dissolved, resulting in high payload and a low release profile [19, 20].

The present work is devoted to the improvement of the physico-chemical characterization of poly(MePEGCA-co-HDCA), paying attention to its morphology and crystalline structure and also to its degradability. Furthermore, morphological features of poly(MePEGCA-co-HDCA) nanospheres and nanocapsules prepared using CIJM are described, and finally the drug loading and release from these nanoparticles are compared by using triclosan as an example of hydrophobic drug.

## 2. Experimental section

### 2.1. Materials

Methoxy poly(ethylene glycol) (MePEG) with a number average molecular weight of 2000 g/mol was purchased from Sigma-Aldrich (St. Louis, MO, USA). Poly(MePEGCA-co-HDCA) and poly(hexadecyl cyanoacrylate) (PHDCA) were synthesized as previously reported [11] being 3600 and 5100 g/mol, respectively, the number average molecular weights determined by gel permeation chromatography (GPC). Poly(MePEGCA-co-HDCA) was synthesized from a methoxypolyethylene glycol cyanoacetate to *n*-hexadecylcyanoacetate ratio of 1:4.

Triclosan for release experiments was purchased from Sigma Aldrich. A microbial culture was prepared with reagents and labware from Scharlab S.L. (Barcelona, Spain). The bacterial strains were *Escherichia coli* CECT 101 and *Micrococcus luteus* CECT 245 from the Spanish Collection of Type Culture (CECT, Valencia, Spain).

### 2.2. Measurements

Molecular weights were estimated by GPC using a liquid chromatograph (Shimadzu, model LC-8A, Shimadzu Corp., Tokyo, Japan) equipped with an Empower computer program (Waters Corporation, Massachusetts, USA). A PL HFIP gel column (Agilent Technologies Inc., CA, USA) and a refractive

index detector (Shimadzu RID-10A, Shimadzu Corp., Tokyo, Japan) were employed. The polymer was dissolved and eluted in tetrahydrofuran at a flow rate of 0.5 mL/min (injected volume 100  $\mu$ L, sample concentration 1.5 mg/mL). The average molecular weights were calculated using polystyrene standards.

$^1\text{H}$  nuclear magnetic resonance spectroscopy ( $^1\text{H}$  NMR) spectra were acquired with a Bruker AMX-300 spectrometer (Bruker Corp., Bremen, Germany) operating at 300.1 MHz. Chemical shifts were calibrated using tetramethylsilane as an internal standard. Dried deuterated chloroform was used as the solvent.

Calorimetric data were obtained by differential scanning calorimetry (DSC) with a TA Instruments Q100 (New Castle, DE, USA) series equipped with a refrigerated cooling system (RCS) operating from  $-90$  to  $550^\circ\text{C}$ . Experiments were conducted under a flow of dry nitrogen with a sample weight of approximately 10 mg while calibration was performed with indium. Heating and cooling runs were performed at rates of 20 and  $10^\circ\text{C}/\text{min}$ , respectively.

Wide angle X-ray diffraction patterns were obtained using a PANalytical X'Pert diffractometer (Panalytical B.V. Almelo, Netherlands),  $\text{Cu K}_\alpha$  radiation ( $\lambda = 0.1542$  nm) and a silicon monocrystal sample holder.

Spherulitic morphologies were studied using a Zeiss Axioskop 40 Pol light polarizing microscope (Carl Zeiss, Göttingen, Germany) equipped with a Linkam temperature control system configured by a THMS 600 heating and freezing stage connected to an LNP 94 liquid nitrogen cooling system. Micrographs were taken with a Zeiss AxiosCam MRC5 digital camera. A first-order red tint plate was employed to determine the sign of spherulite birefringence under crossed polarizers.

Spherulites for transmission electron microscopy (TEM) observations were grown from homogeneous melt-crystallized thin films placed between two cover glasses and prepared by evaporation of a dilute solution of the polymer in acetone. This experimental procedure made it possible to obtain films with an appropriate thickness for TEM observation.

The nanocapsule (NC) and nanospheres (NS) size distribution was determined by Dynamic Light Scattering (DLS, Zetasizer Nanoseries ZS90, Malvern Instrument Ltd., Malvern, UK), which measures accurately in the size range from 2 nm to 3  $\mu\text{m}$ .

Morphological observations of nanoparticles and nanocapsules were carried out with a Philips TECNAI 10 transmission electron microscope (Philips Electron Optics, Eindhoven, Holland) at an accelerating voltage of 80 kV and a Focus Ion Beam Zeiss Neon 40 instrument for scanning electron microscopy. Carbon coating was accomplished using a Mitec K950 Sputter Coater (Carl Zeiss, Göttingen, Germany) equipped with a film thickness monitor  $k150\times$  (Quorum Technologies Ltd., West Sussex, UK).

Negative staining and direct observation were employed to image the particles by TEM. In some cases, shadowing with Pt/C at an angle of  $15^\circ$  was performed to observe surface details and obtain information on the thickness of the specimen. The negative staining solution was prepared by diluting a 4% phosphotungstic acid solution with ethanol 100% in a proportion 1 to 4.

A UV-3600 spectrophotometer controlled by UVProbe v2.31 software (Shimadzu, Tokyo, Japan) was employed for triclosan load and release measurements.

### 2.3. Preparation of unloaded and triclosan loaded nanospheres and nanocapsules of poly(MePEGCA-co-HDCA)

Nanospheres and nanocapsules of poly(MePEGCA-co-HDCA) containing triclosan were prepared by the solvent displacement method (or nanoprecipitation) [21] using a CIJM with two inlet jets of 1 mm, one outlet jet of 2 mm and a mixing chamber of about 5 mm. More geometrical details on this device can be found in previous work [18]. For the preparation of nanoparticles, 150 mg of poly(MePEGCA-co-HDCA) was dissolved in 25 mL of warm acetone (i.e. polymer concentration of 6 mg/mL). To obtain triclosan loaded nanoparticles, 0.3% (w/v) of triclosan was added to the acetone solution. This solution was injected into the mixer by an infusion pump at a flow rate of 120 mL/min (KDS200, KD Scientific Inc., Holliston, MA, USA). Simultaneously, 25 mL of water was injected at the same rate through the second upstream inlet.  $R$  and  $F_W$  processing parameters were consequently 1 and 120 mL/min, respectively. Particles, spontaneously formed in the mixer chamber, were evacuated by the outlet jet, and then quenched in 25 mL of water under magnetic stirring. Finally, the acetone was evaporated in

a rotating device (30 minutes at room temperature) to obtain an aqueous suspension of nanospheres.

Nanocapsules were prepared by the same procedure after adding 200  $\mu\text{L}$  of Miglyol 812 (i.e. oil concentration of 8  $\mu\text{L}/\text{mL}$ ) to the initial organic solution of the copolymer in order to form the inner oily cavity. Nanocapsules had an oil to polymer mass ratio of 1.26.

Nanosphere and nanocapsule suspensions were extensively dialyzed (Spectra/Por<sup>®</sup> 3500 MWCO dialysis membrane, Spectrum, Huston, TX, USA) at 25°C for 4 hours against a Sørensen solution supplemented with 10% (v/v) of ethanol in order to remove all unloaded triclosan. Aliquots of 200  $\mu\text{L}$  of the sample suspension before and after dialysis underwent ultra-sound treatments and extracted with 1 mL of 70% ethanol to quantify triclosan by ultraviolet (UV) analysis (281 nm). Calibration curves were obtained by plotting the absorbance measured at 281 nm against triclosan concentration.

Entrapment efficiency (EE) and drug loading (DL) were determined by Equations (1) and (2), respectively. Occurrence of degradation during dialysis was not considered for DL evaluation (i.e. Equation (2) was referred to the initial polymer mass).

$$\text{EE} [\%] = 100 \cdot \frac{\text{Experimental drug loading}}{\text{Nominal drug loading}} \quad (1)$$

$$\text{DL} [\%] = 100 \cdot \frac{\text{Mass of drug in particles}}{\text{Mass of polymefr in particles}} \quad (2)$$

#### 2.4. Degradation experiments

Degradation was performed using small polymer disks with a diameter of 1 cm and a thickness of 1 mm prepared by press molding of approximately 150 mg of the material. The degradation medium consisted of 15 mL of milliQ water and two different degradation temperatures (4 and 18°C) were considered. Tablets were removed from the degradation medium at scheduled times, and were then well dried and weighed to calculate the weight loss. Some samples were also analyzed by <sup>1</sup>H NMR to evaluate the chemical degradation of the polymer.

#### 2.5. Release experiments

10 mL of the aqueous suspension containing triclosan loaded nanoparticles or nanocapsules (3 mg/mL) was confined in a dialysis bag which

was introduced in a vessel equipped with magnetic stirring and containing 20 mL of the selected release medium (i.e. a mixture (3/7 v/v) of Sørensen medium (pH 7.4) and ethanol). Aliquots (1 mL) were drawn at predetermined intervals to determine the amount of released triclosan by UV spectroscopy. The volume of the release medium was kept constant by addition of 1 mL of fresh medium after removal of each aliquot. All drug release tests were carried out using five replicates to control the homogeneity of the release and average the results. The triclosan remaining in the samples was determined again by UV analysis. In this case, aliquots (200  $\mu\text{L}$ ) of the dialysis bag sample were sonicated and extracted with 1 mL of 70% ethanol to ensure complete dissolution of triclosan.

The release kinetics can be calculated from experimental results by several theoretical models, typically first-order [22, 23], Higuchi [24, 25] and their combination [26]. Thus, the Higuchi-equation (Equation (3)) and first-order (Equation (4)) models were used to describe the first (0–60%) and second (40–100%) parts of the release, respectively:

$$\frac{M_t}{M_0} = k_h t^{1/2}, \quad \left( 0 \leq \frac{M_t}{M_0} \leq 0.6 \right) \quad (3)$$

$$\ln \left( 1 - \frac{M_t}{M_0} \right) = a - k_1 t, \quad \left( 0.4 \leq \frac{M_t}{M_0} \leq 1.0 \right) \quad (4)$$

where  $k_h$  is the Higuchi release constant,  $k_1$  is the first-order release constant,  $a$  takes into account the release in the first step,  $M_t$  is the percentage of drug released at time  $t$ , and  $M_0$  is the drug equilibrium percentage (considered as the maximum drug percentage).

#### 2.6. Antibacterial activity

The *in-vitro* antibacterial activity of triclosan loaded nanoparticles and nanocapsules was evaluated using the Gram-positive *Micrococcus luteus* (*M.luteus*) and Gram-negative *Escherichia coli* (*E.coli*) microorganisms.

Briefly, 7 mL of Luria-Bertani (LB) broth containing 10<sup>5</sup> CFU/mL was mixed with 1 mL of the nanosphere or nanocapsule aqueous suspension in sterile tubes. These were inverted 4–6 times to ensure mixing and incubated for 24 and 48 h in a shaking incubator at 100 rpm and a temperature of 37°C. Cultures of LB broth without and with bacteria were

performed as negative and maximum bacterial growth controls, respectively. Culture of pure LB broth was the negative control, and pure LB broth with nanoparticles or nanocapsules was also tested as turbidity blank.

Bacterial growth was determined by measuring turbidity at 600 nm by UV spectroscopy. The number of surviving bacteria was computed according to the relative growth rate (percentage), which was calculated from turbidity changes after 24 and 48 h of incubation. Activities were evaluated using six replicates for which the corresponding average value and standard deviation were determined. Two samples were considered statistically significantly different when ANOVA and  $\chi^2$ -test gave  $p \leq 0.05$ .

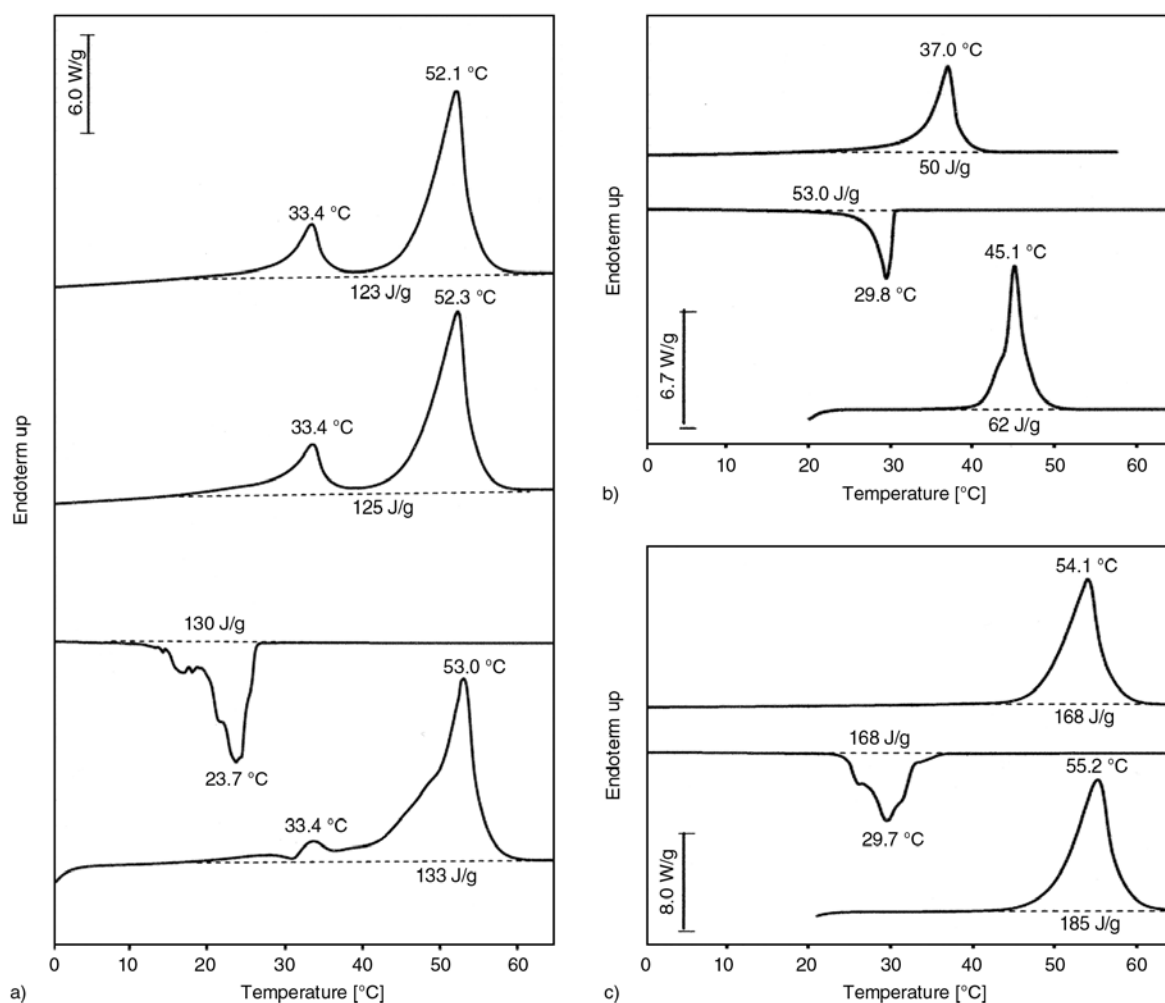
The antibacterial effect in a dose-response manner was also determined for triclosan-loaded nanocapsules by considering different dilutions of the sam-

ple and evaluating the relative growth, as noted above. The dose-response effect was analyzed by a logistic model using OriginPro v8 software (Origin Microcal Corp., Norhampton, MA, USA).

### 3. Results and discussion

#### 3.1. Thermal characterization of poly(MePEGCA-co-HDCA)

Poly(MePEGCA-co-HDCA) has a semicrystalline nature, as shown by the DSC scans in Figure 1a. Thus, the as-synthesized sample has a predominant peak at 53°C and a minor one close to 33–34°C, which should correspond to the melting of crystalline domains of PEG and hexadecyl (HD) alkyl groups, respectively. The sample easily crystallized from the melt, giving rise to a complex exothermic peak where the crystallization of the two indicated domains could not be well differentiated. It is inter-



**Figure 1.** DSC scans performed on poly(MePEGCA-co-HDCA) (a), PHDCA (b) and PEG (c) samples. Scans from bottom to top correspond to the heating run of the as-synthesized and the commercial samples, the cooling run from the melt state, the heating run of a hot crystallized sample and the heating run of a sample quenched from the melt state (a).

esting to note that the crystallinity of the as-synthesized sample, which came from evaporation of a dichloromethane solution, was slightly higher than that of the hot crystallized sample (i.e. the global melting enthalpy changed from 133 to 125 J/g). This increase was caused by the higher endothermic peak associated with the PEG domain (ca. 53°C) that could overcome the more deficient arrangement of the HD domain, which led to a very low melting peak at 33.4°C. This peak clearly increased after hot crystallization indicating an improved packing of HD chains. Some differences are also found in the melting peak associated with the PEG domain since a shoulder, which is indicative of a typical re-crystallization or lamellar thickening process, was observed for the as-synthesized sample whereas only a single peak was detected for the hot crystallized sample.

The DSC heating run of a quenched sample does not reveal significant changes and demonstrates that the sample crystallized easily even at the high cooling rates given by the equipment. Note that the glass transition temperature could not be well observed due to the high crystallinity of the sample but it should be close to  $-63^{\circ}\text{C}$ , as reported for PEG of low molecular weight [27]. Two points are worth highlighting from the thermal analysis: a) The sample undergoes a partial fusion at around  $34^{\circ}\text{C}$ , a temperature slightly lower than the human body temperature, at which the potential drug delivery systems should be applied; b) Despite the complexity of the sample, its crystallinity remains high at  $37^{\circ}\text{C}$ , which is the temperature at which samples are meant to be used.

For the sake of completeness, Figures 1b and 1c show representative DSC scans performed with PHDCA and PEG homopolymers, respectively. These traces clearly confirm the previous assignment given for the melting peaks of poly(MePEGCA-co-HDCA) and the similar crystallization temperature of both samples. Results also demonstrated that poly(MePEGCA-co-HDCA) has an intermediate melting enthalpy between those of the crystals constituted by the two types of lateral chains. The enthalpies associated with each peak (e.g. 21 and 104 J/g for the hot crystallized sample) fit reasonably well with the expected values (20 and 103 J/g) assuming a weight percentage of PEG close to 61%. Finally, the complexity of the crystallization exothermic peak of PEG, which extends over an interval of

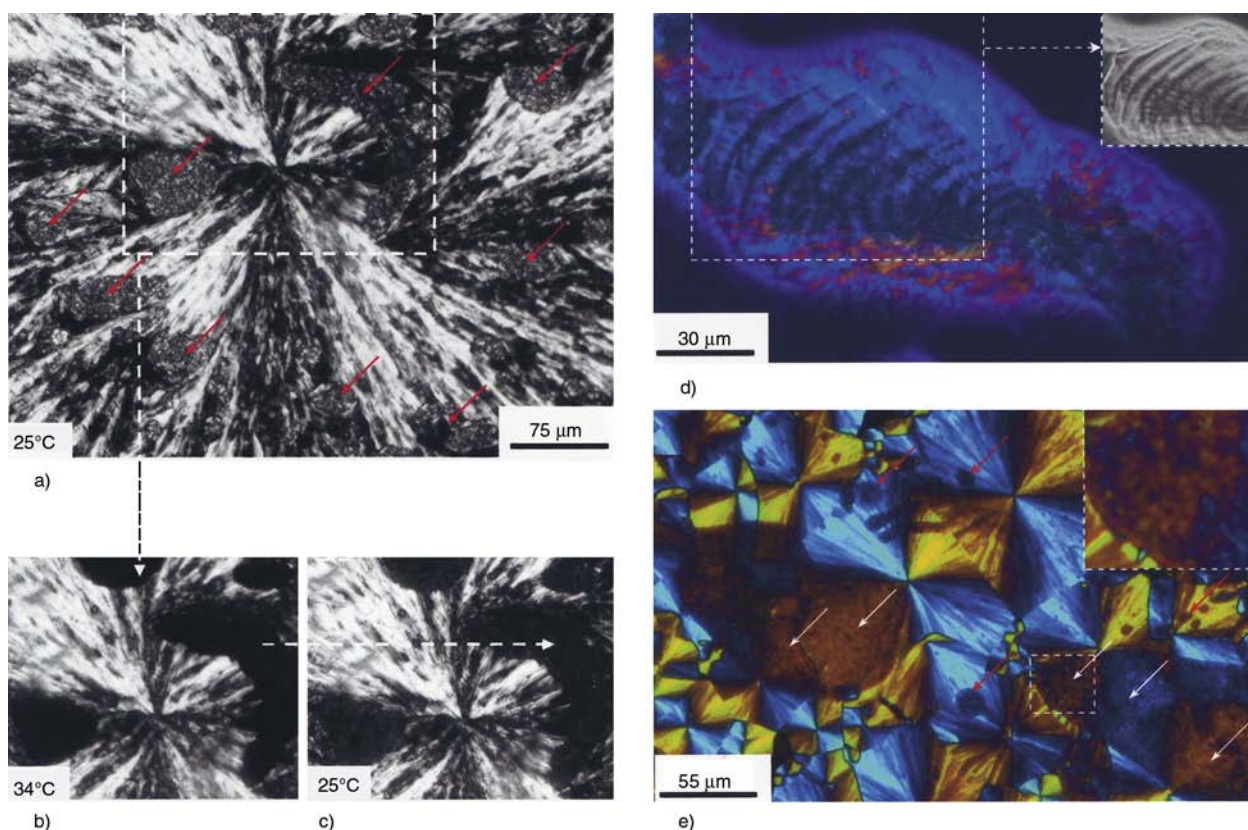
approximately  $15^{\circ}\text{C}$ , and the sharp appearance of the peak associated with the PHDCA homopolymer are worth noting. This also suggests a practically instantaneous primary crystallization that might result from a high nucleation density.

### 3.2. Spherulitic morphologies of poly(MePEGCA-co-HDCA)

Crystallization from the melt led to the formation of spherulites with a fibrillar/ringed texture corresponding to the crystallization of the PEG lateral chains, although domains constituted by HD units could also be envisaged. Figure 2a shows a typical crystallization performed at  $4^{\circ}\text{C}$  (i.e. at a low degree of supercooling) where well developed spherulites were observed, together with zones with a different texture (indicated by arrows in Figure 2a) that seem to be constituted by smaller microcrystals. These zones melted when the sample was heated to the melting temperature associated with the PHDCA domains (Figure 2b) and re-crystallized, giving textures similar to those initially observed when the temperature was decreased to room temperature (Figure 2c). Experiments clearly highlighted the complex crystallization process of samples constituted by blocks able to crystallize independently (i.e. those constituted by the PEG and HD lateral groups) and furthermore with a similar crystallization temperature. Phase separation and crystalline morphology studies of block copolymers are currently receiving much attention [28–32], and even microstructures that can be formed from the melt, from solution and for both thin and bulk samples have been extensively reviewed [33, 34]. Ringed spherulites with an interspacing close to  $9\ \mu\text{m}$  could also be detected in the specimens (Figure 2d) although at a lower ratio.

A fibrillar spherulitic texture was observed when crystallization was performed at lower temperatures (e.g.  $-24^{\circ}\text{C}$ ), as shown in Figure 2e. The nucleation density obviously increased with decreasing the crystallization temperature; consequently, smaller spherulites were found at the end of the crystallization process. In this way, an increase from 20 to 600 nuclei/ $\text{mm}^2$  was determined when the temperature decreased from 4 to  $-24^{\circ}\text{C}$ .

In all cases, a negative birefringence was characteristic of the PEG spherulites, whereas a more confusing sign was found for the domains constituted by the HD alkyl chains due to their smaller size. In

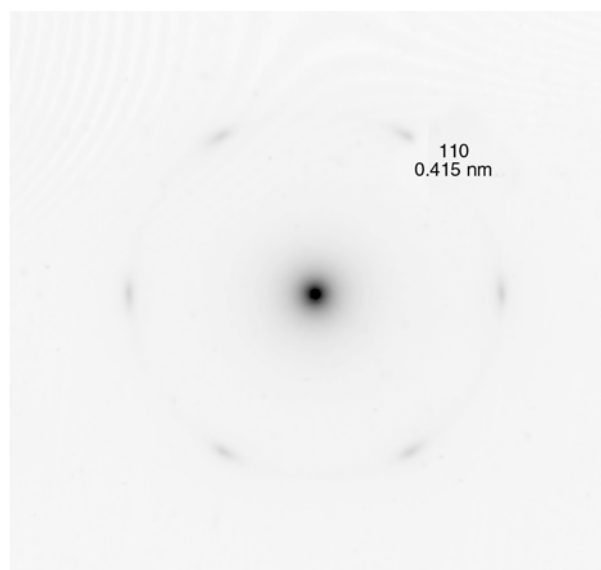


**Figure 2.** Polarizing optical micrographs of poly(MePEGCA-co-HDCA) isothermally crystallized at 4°C (a, b, c, d) and –24°C (e). Micrographs were taken at room temperature (a, d, e), at 34°C (b) and at room temperature after heating the crystallized sample to 34°C (c). A first-order red tint plate was used for micrographs (d) and (e). Inset of (d) shows a contrast phase image of a ringed spherulite. The inset of (e) shows a magnification of the dashed area where small and flat microcrystals can be envisaged. Arrows point to crystalline microdomains constituted by PHDCA.

fact, primary nucleation seemed to be much higher for these domains, giving rise to microcrystals. It should be pointed out that DSC data indicated that the hot crystallization of PHDCA proceeded rapidly, which was well justified by assuming a high primary nucleation. Optical micrographs revealed that the alkyl chain microcrystals had a flat appearance and usually appeared aggregated in such a way that the birefringence sign of the PEG spherulite was kept (see white and red arrows in Figure 2e). In some cases, these microcrystals led to the formation of spherulite arms with a speckled appearance (white arrows).

Phase separation was confirmed by electron diffraction since fibrillar textures and microcrystals gave rise to the typical  $hk0$  pattern of PEG and a well differentiated pattern with six reflections at 0.415 nm, respectively. This pattern (Figure 3) suggests a pseudo-hexagonal packing of alkyl chains, which is consistent with the well known first-order transition

undergone by long-chain paraffins at a few degrees below their melting point [35].



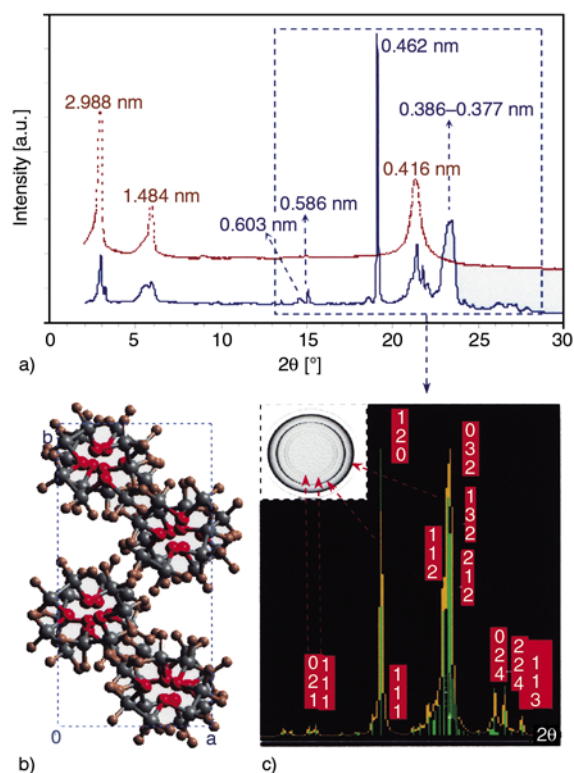
**Figure 3.** Electron diffraction patterns taken from fibrillar spherulites corresponding to HD domains



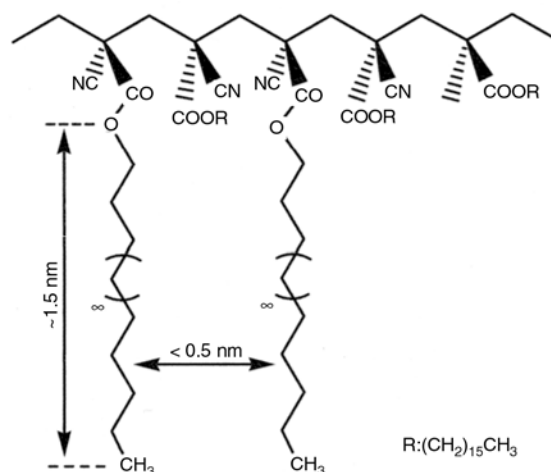
### 3.3. Crystalline structure of poly(MePEGCA-co-HDCA)

X-ray powder diffraction patterns (Figure 4a) of poly(MePEGCA-co-HDCA) revealed the presence of reflections characteristic of polyethylene glycol, as well as additional peaks which should be assigned to a crystalline structure associated with the packing of the hexadecyl lateral groups. The structure of polyethylene glycol is defined by a  $P2_1/a$  space group and a unit cell with parameters  $a = 0.805$  nm,  $b = 1.304$  nm,  $c$  (fiber axis) = 1.948 nm and  $\beta = 125.4^\circ$  that contains four  $7/2$  helices based on TTG sequences [36] (Figure 4b). The corresponding X-ray diffraction pattern (Figure 4c) was characterized by strong peaks at 0.462 nm (120 reflection) and 0.386–0.277 nm (112, 032, 132 and 212 reflections) and weak peaks at 0.603 and 0.586 nm, which are indexed as the 021 and 110 reflections.

All characteristic reflections of PEG, together with peaks at 2.988, 1.484 and 0.416 nm of remarkable intensity, can be well observed in the X-ray diffraction profile of poly(MePEGCA-co-HDCA). These



**Figure 4.** (a) Powder X-ray diffraction profiles of poly (MePEGCA-co-HDCA) (blue) and PHDCA (brown) samples. (b) Projection down the chain axis of the PEG structure showing the packing arrangement of the four  $7/2$  helices. (c) Simulated powder X-ray diffraction profile of PEG and corresponding diffraction pattern (inset).

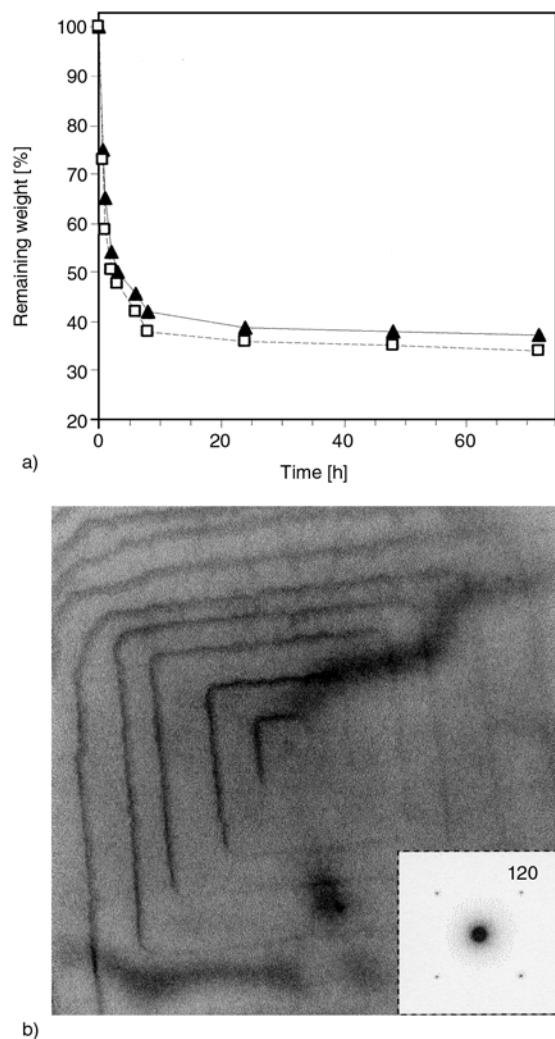


**Figure 5.** Schematic representation showing geometrical features concerning hexadecyl lateral groups of poly(MePEGCA-co-HDCA)

peaks, which are also detected in the diffractogram of PHDCA, suggest the presence of a hexagonal unit cell with parameters  $a = 0.479$  nm,  $b = 0.479$  nm,  $c$  (fiber axis) = 2.988 nm. Note that the strong peak at 0.416 nm corresponds to the 100, 010 and 110 reflections, which were also observed in the electron diffraction patterns of HDCA spherulitic domains, and that are typical of a hexagonal packing of polymethylene segments. The higher spacing peaks can be indexed as the 001 and 002 reflections of a cell which  $c$  axis parameter corresponds to two lateral groups since the dimension of the alkyl side group becomes close to 1.5 nm (i.e. the 002 spacing) if an extended zig-zag conformation is assumed (Figure 5). It must also be pointed out that a syndiotactic disposition of the hexadecyl lateral groups is preferred to avoid high steric hindrances between the polymethylene sequences of neighboring chain units (i.e. a value close to 0.25 nm should be expected for an isotactic configuration).

### 3.4. Hydrolytic degradation of poly(MePEGCA-co-HDCA)

Degradation of poly(MePEGCA-co-HDCA) in distilled water at temperatures of 18 and  $4^\circ\text{C}$  occurred over a maximum period of 8 h, followed by a slow process that extended over approximately 48 h. After that, the weight of the copolymer samples remained practically constant, at least over an exposure time of 300 h. The weight loss profiles at the two assayed temperatures were similar, although a slightly higher mass loss was detected at  $18^\circ\text{C}$  (Figure 6). Thus, weight losses of 63 and 67% were



**Figure 6.** (a) Plot of the remaining weight of a poly (MePEGCA-co-HDCA) disk sample versus exposure time in distilled water at 18 (□) and 5°C (▲). (b) Electron micrograph of PEG lamellar crystals recovered from the release medium. Inset shows the corresponding electron diffraction pattern.

determined at the end of the test performed at 4 and 18°C, respectively. Enhanced solubility at the higher temperature is the probable cause of the slight differences in the remaining weight.

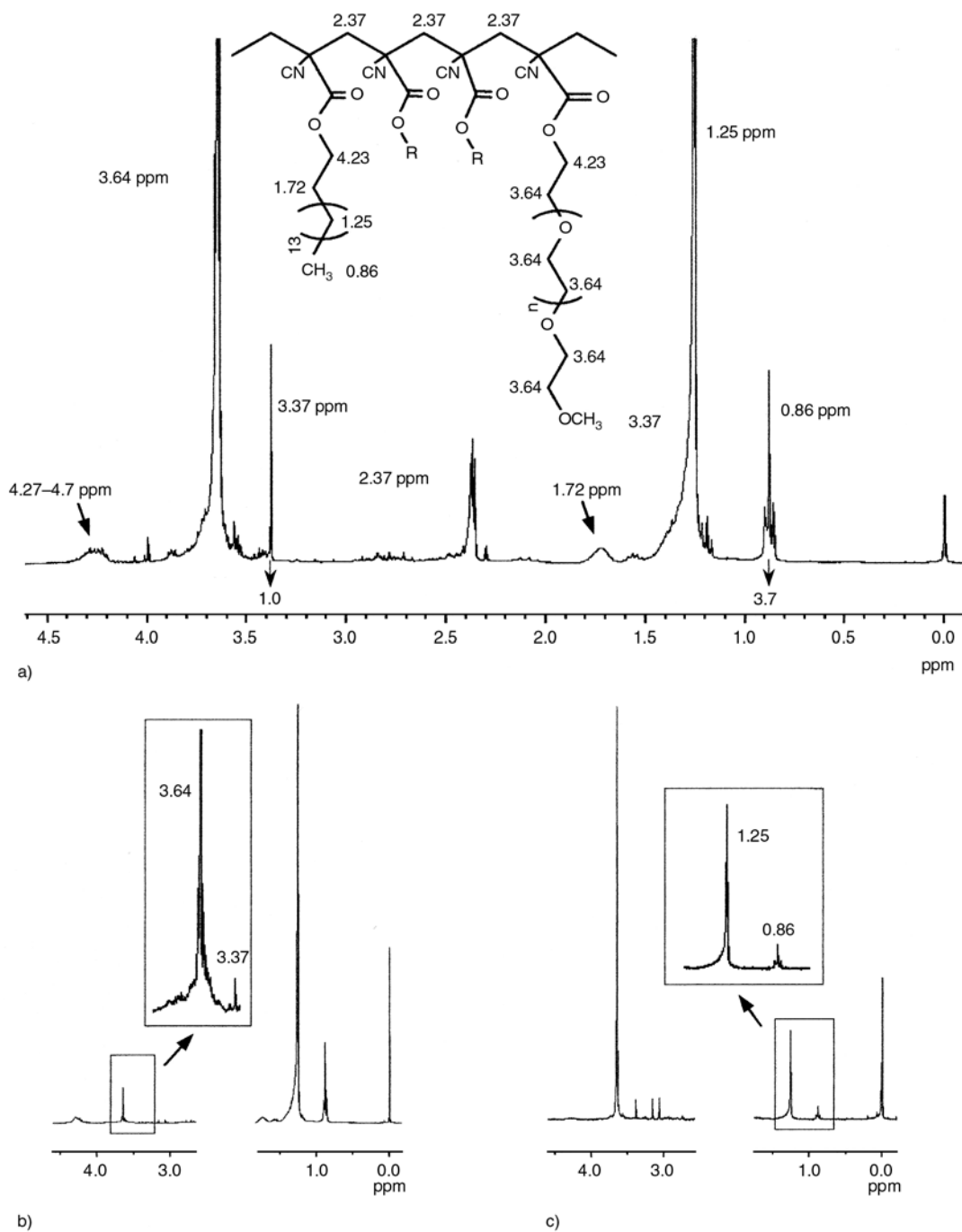
As already mentioned the copolymer was synthesized from a hydrophilic-to-hydrophobic monomer ratio of 1:4. However, this ratio should represent an ‘average’ value of the units incorporated to the polymer chain, and although the synthesis protocol is quite robust, it is likely that a distribution of hydrophilic-to-hydrophobic unit ratios exists in the final copolymer molecules. Thus, a significant weight loss should be expected from the presence of soluble fractions constituted by molecules with ratios of 1:2 or higher. The remaining part of the weight loss

should be attributed to the hydrolysis of the ester groups of the hydrophilic lateral pegylated chains. Figures 7a and 7b compare the  $^1\text{H}$  NMR spectra of the as-synthesized sample and that degraded up to a weight loss of 67%. The initial sample was characterized by an average molar ratio close to 1:4 between pegylated and hexadecyl (HD) lateral chains, as can be deduced from the areas of the signals at 3.37 and 0.86 ppm assigned to the methyl groups belonging to the two ester moieties [11]. Methylene groups of the main chain and the lateral hexadecyl and PEG groups also appeared well differentiated at 2.37, 1.25 and 3.64 ppm, respectively (Figure 7a).

Spectra of samples exposed to water clearly show how the PEG signals at 3.64 and 3.37 ppm practically disappeared while HD signals at 1.25 and 0.86 ppm remained with a remarkable intensity. In fact the hydrophilic-to-hydrophobic unit ratio decreases up to 1:110. Thus, the degradation process could be justified by an ester group cleavage involving mainly the pegylated chains.

According to the composition determined from NMR spectra, the MePEG lateral groups represented 55 wt% of the copolymer, which was slightly lower than the experimental weight loss. Thus, a percentage of the initial sample (i.e. chains with a high hydrophilic content) should be dissolved during exposure to the aqueous medium. In order to estimate this fraction, the as-synthesized sample was extracted with water in a time period during which degradation was practically negligible (i.e. less than 5% for 30 min of exposure). The extracted fraction corresponded to 10 wt% of the sample and its NMR spectrum (Figure 7c) indicated a 1:1.4 ratio between MePEG and HD lateral chains that was in agreement with the ratio expected for soluble molecules.

The preferential hydrolysis of pegylated chains was also corroborated by the  $^1\text{H}$  NMR spectra (not shown) of the residue extracted from the hydrolytic degradation medium after 72 h of exposure, which indicated a PEG/HD ratio higher than 15:1. Furthermore, lamellar crystals with the characteristic morphology of polyethylene glycol lamellae [37, 38] were recovered after evaporation of the degradation medium. Specifically, Figure 6b shows typical square lamellae of PEG and the corresponding electron diffraction pattern with intense 120 reflections at 0.462 nm.



**Figure 7.** (a)  $^1\text{H}$  NMR spectra of the as-synthesized poly(MePEGCA-*co*-HDCA) sample and chemical scheme of the assignment of signals (inset). (b)  $^1\text{H}$  NMR spectra of a poly(MePEGCA-*co*-HDCA) sample after 72 h of exposure to water at  $18^\circ\text{C}$ . (c)  $^1\text{H}$  NMR spectra of the extracted fraction of a poly(MePEGCA-*co*-HDCA) sample after 30 min of exposure to water at  $18^\circ\text{C}$ .

In conclusion,  $^1\text{H}$  NMR spectra pointed out that the sample weight loss occurred through ester bond cleavage of the hydrophilic pegylated chains and by solubilisation of a small fraction corresponding to the more hydrophilic copolymer fraction. It is interesting to note that the ester bond of the hydrophobic moiety was not highly susceptible to hydrolysis probably due to poor exposure to the degradation

medium. These results are in full agreement with preliminary studies on fetal calf serum which indicate that the hexadecyl homopolymer did not degrade during the first 3 h of incubation [12]. Finally, it is also interesting to note that degradation of pegylated chains can lead to the formation of anionic carboxylate groups, which still provide a hydrophilic character to the polymer.

### 3.5. Morphology of nanospheres and nanocapsules

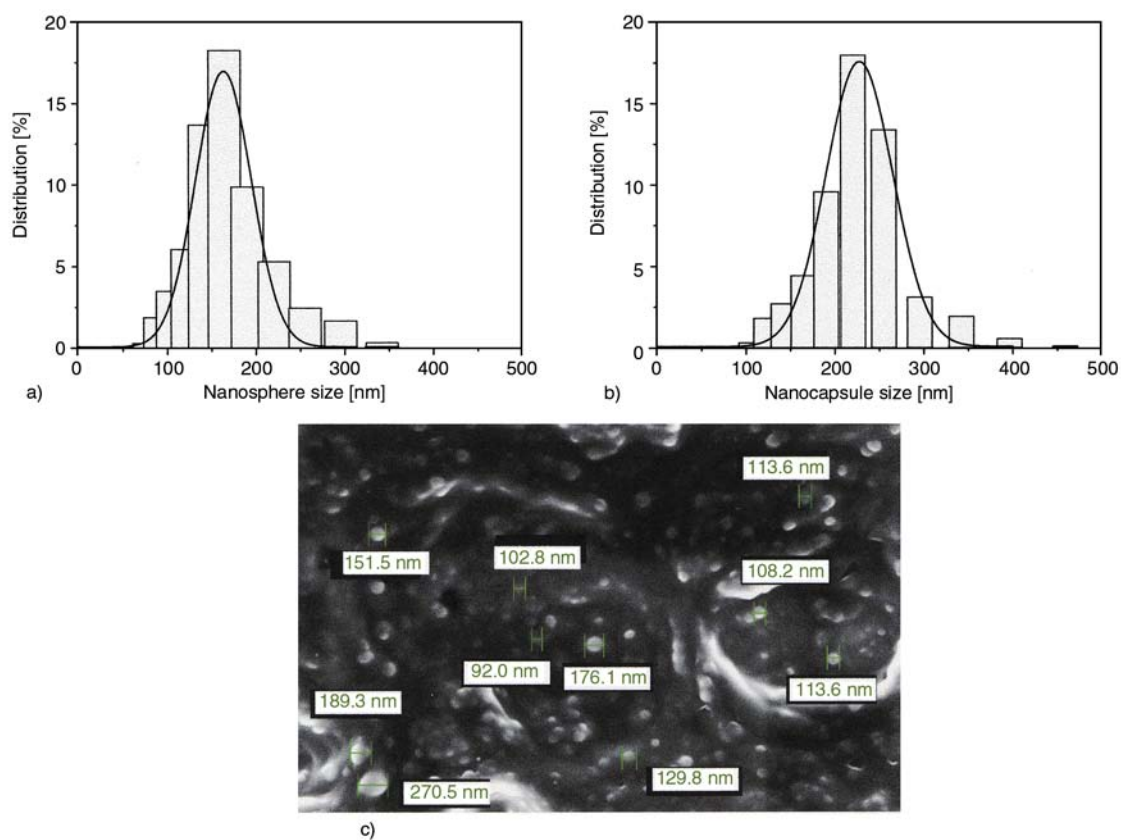
Particle size and size distribution are the most important characteristics of nanoparticle systems since they influence their biological fate, toxicity, targeting ability and even drug loading, drug release and stability. Many studies have demonstrated that nanoparticles of sub-micron size have a number of advantages over micro-particles, for example as a drug delivery system because of their small size and relative mobility. These properties can improve intracellular uptake and increase availability to a wider range of biological targets [39].

DLS analysis revealed a size difference between the triclosan loaded nanoparticles and nanocapsules. Thus, unimodal size distributions with mean diameters of  $160 \pm 60$  nm (Figure 8a) and  $230 \pm 60$  nm (Figure 8b), respectively, were found.

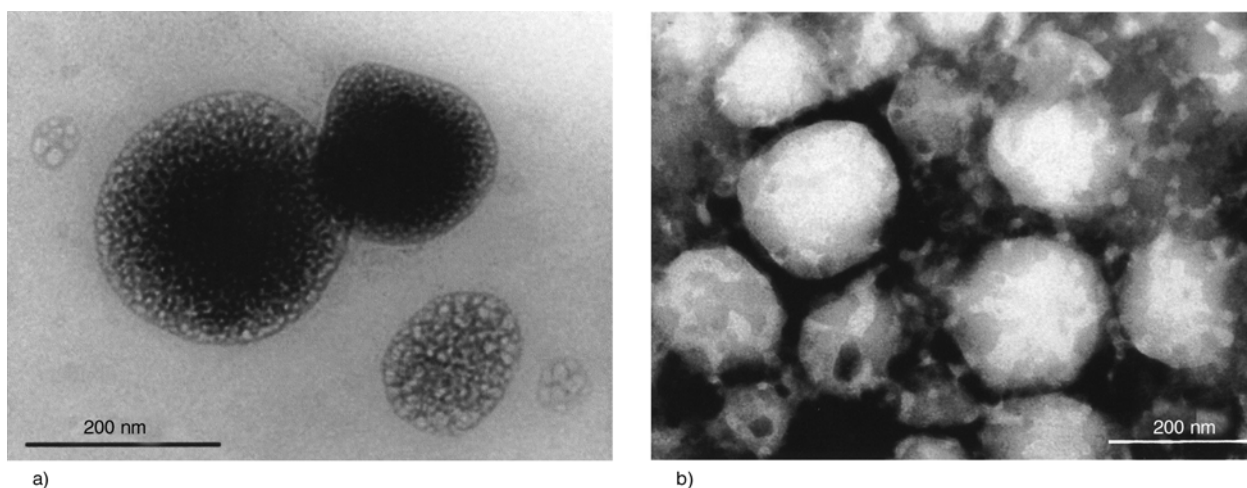
Scanning electron micrographs (Figure 8c) showed that nanoparticles were mostly spherical and had a rather variable diameter, in agreement with DLS results. Particles were generally found isolated although some aggregates could also be observed.

TEM micrographs taken at a higher magnification showed that particles, directly deposited on the carbon grid, were constituted by a porous dense polymer matrix (Figure 9a). Furthermore, these nanoparticles often appeared slightly deformed, their rounded appearance being lost, as clearly seen in the negative stained samples (Figure 9b). Nanoparticles were also shadowed with Pt/C to determine their thickness and confirm their spherical morphology. Thus, the maximum and minimum shadows in the micrograph in Figure 10 correspond to thicknesses of 230 and 115 nm, which are again in agreement with the particle size distribution determined by DLS measurements.

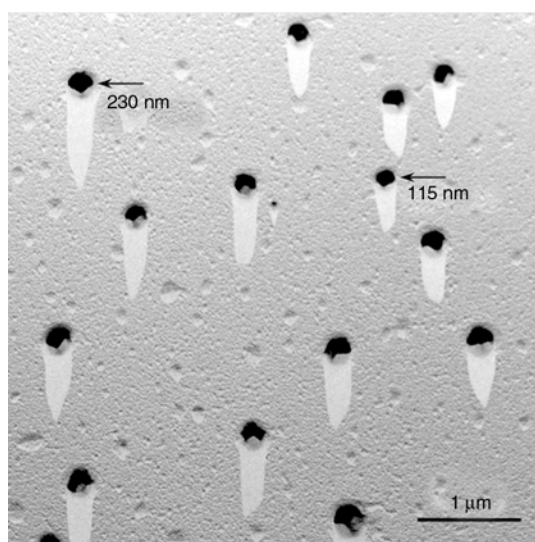
Medium magnification TEM images of nanocapsules (Figures 11a and 11c) showed their morphology and confirmed the underlying size distribution. This distribution extended over the 110–290 nm range, which covers smaller diameters than those deduced from DLS analysis. However, the predominant nanocapsule size (ca. 200 nm) was close to the average value previously determined. Direct and negative stained images showed that isolated



**Figure 8.** Size distribution of triclosan loaded nanospheres (a) and nanocapsules (b) of poly (MePEGCA-*co*-HDCA). Samples were prepared with an initial copolymer concentration of 6 mg/mL with  $R = 1$  and  $FR_W = 120$  mL/min. For nanocapsules an oil concentration of 8  $\mu$ L/mL was used. (c) Scanning electron micrograph of poly(MePEGCA-*co*-HDCA) nanospheres prepared as above indicated.



**Figure 9.** Positive (a) and negative (b) TEM micrographs taken at different magnifications of poly(MePEGCA-co-HDCA) nanospheres. Samples were prepared with  $R = 1$  and  $FR_W = 120$  mL/min and an initial copolymer concentration of 6 mg/mL, respectively.

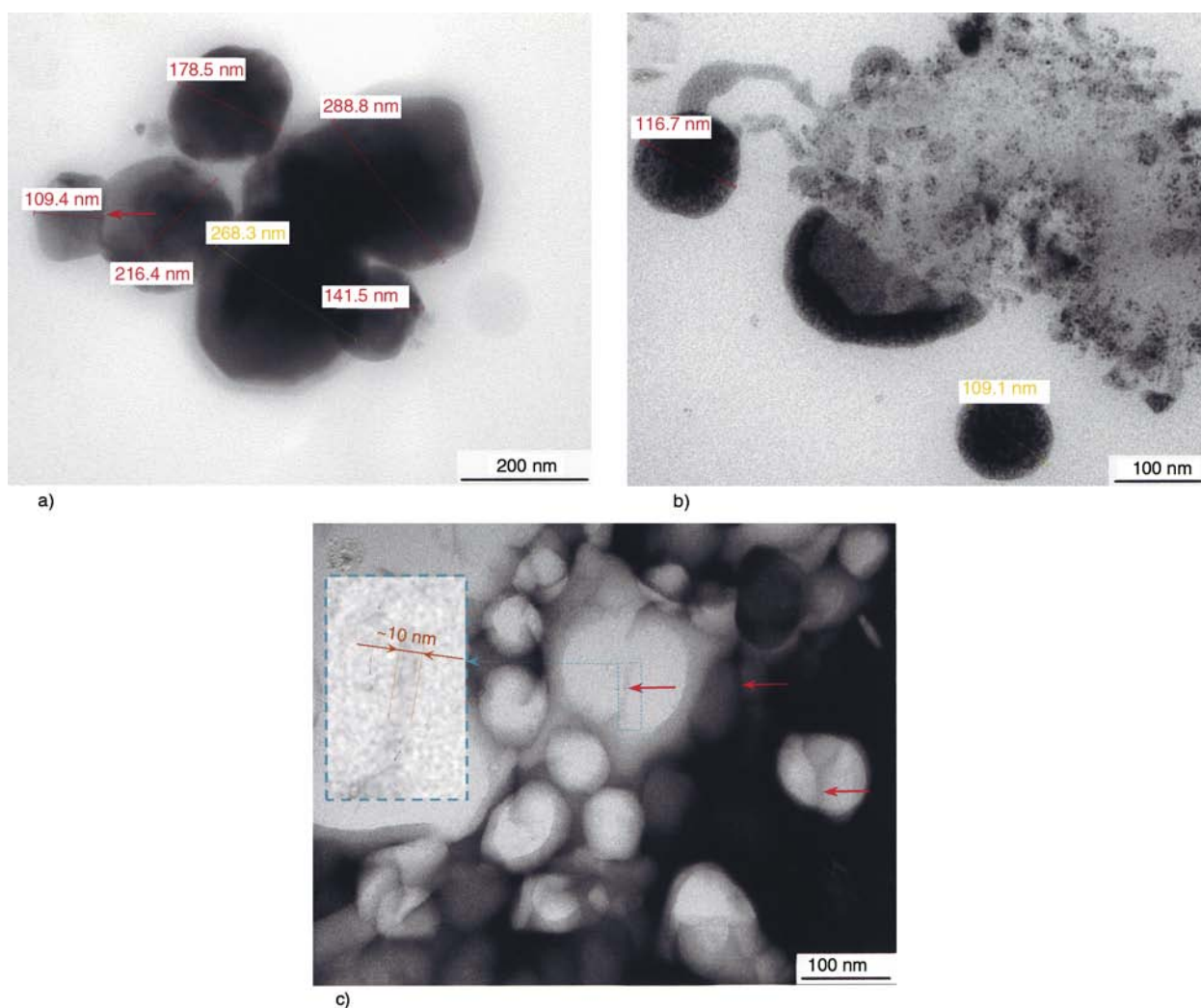


**Figure 10.** TEM micrograph of Pt/C shadowed poly (MePEGCA-co-HDCA) nanospheres

nanocapsules were practically spherical but easily deformed when they were aggregated. Thus, the adjacent nanocapsule membranes became parallel and planar (see arrows in the negative stained sample of Figure 11c), showing that the spherical shape is actually not rigid. Both the liquid content and the reduced stiffness of the polymer membrane should be taken into account. The inset of Figure 11c contains the two wall membranes with a probable thickness of approximately 5 nm, since it can be considered that the negativation salt had not penetrated in the nanocapsules or between adjacent membranes. Specimens obtained by direct deposition are sensitive to the large intensity of the electron beam. For

this reason, some nanocapsules broke down during observation and released their liquid content. Note in Figure 11b some dense particles corresponding to the polymer membrane on the edges of the oil released by the breaking down of the nanocapsule. Figures 12a and 12b reproduce bright field images of nanocapsules directly deposited onto the copper grid where the membranes can be clearly discerned in the projection contrast and a wall thickness close to 5 nm measured. Most nanocapsules were surrounded by a somewhat bright halo, which could be attributable to the oil released by the breaking down of the nanocapsule during observation.

The polymer matrix should be amorphous, but it is not discarded that side groups could crystallize. Moreover, some degraded pegylated chains and even some aggregated polymer molecules could be encapsulated, accounting for the dark zones found in nanocapsules (Figures 12a–12c). Pt/C shadowed samples (Figure 10d) revealed that nanocapsules usually collapse, giving rise to almost flat, rounded morphologies (note the shadow in Figure 12d, which suggests a small thickness). Flat morphologies were again a consequence of the oil release and the spongy structure of the polymer filled with liquid. It should be pointed out that shadowed samples allowed the detection of regular crystals inside the nanocapsule, as deduced from the surface details in Figure 12d. Specifically, aggregates of square crystals similar to those characteristic of PEG could be clearly envisaged.

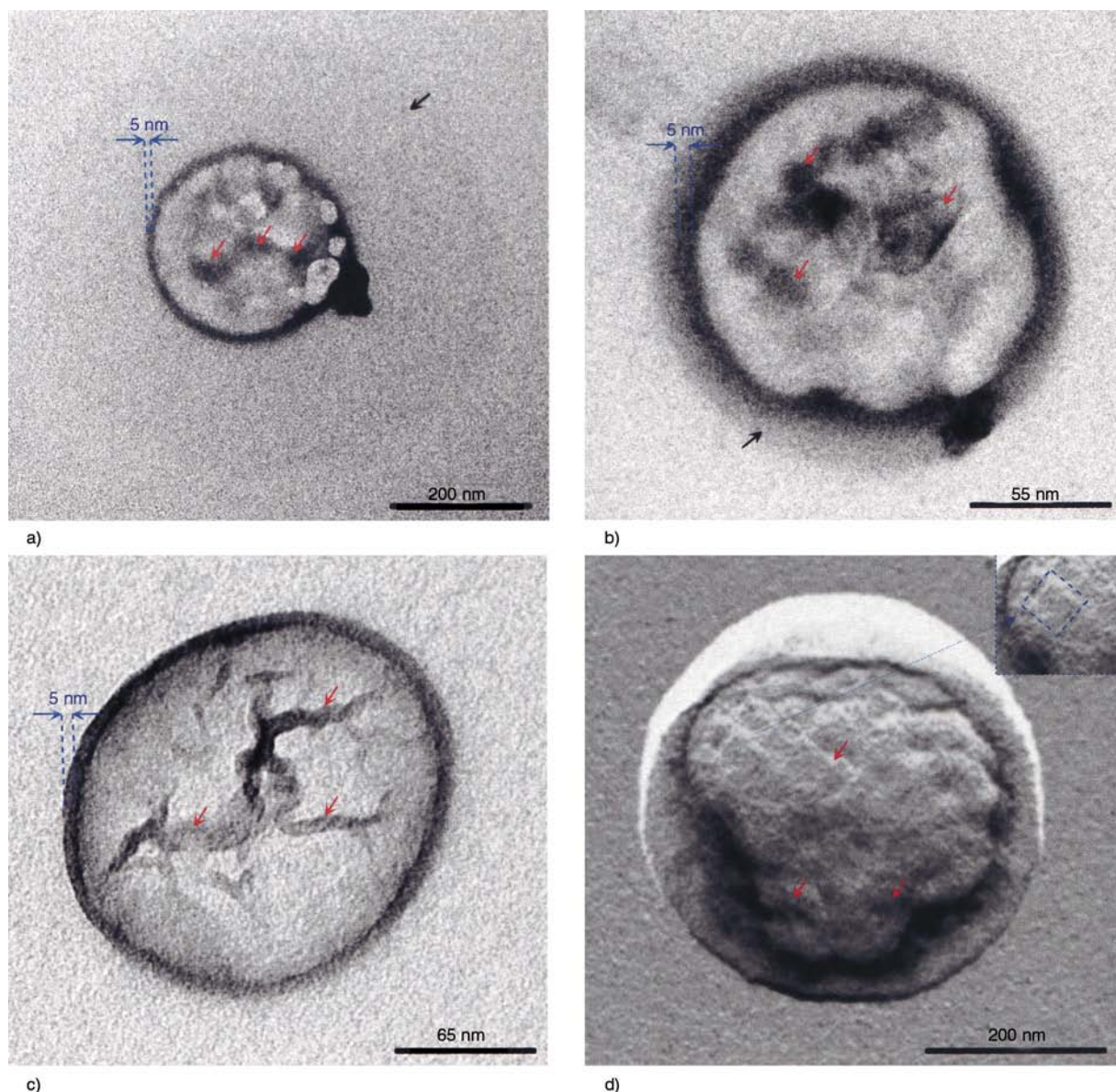


**Figure 11.** Positive (a, b) and negative (c) TEM micrographs taken at different magnifications of poly(MePEGCA-co-HDCA) nanocapsules containing Miglyol 812. Samples were prepared with  $R = 1$  and  $FR_W = 120$  mL/min and an initial copolymer and oil concentration of 6 and 8  $\mu\text{L}/\text{mL}$ , respectively. Red arrows indicate close contact between nanocapsules that led to deformation. Inset of (c) shows a high magnification of the area of contact between two nanocapsules.

### 3.6. Release of triclosan from nanospheres and nanocapsules

Encapsulation efficiency (EE) was high and similar for both nanospheres and nanocapsules since values of 92 and 91% were respectively determined. It is clear that the polymer and the preparation method were effective in encapsulating high doses of triclosan. Drug loading (DL) was consequently relatively high and again similar for both systems (43 and 44% for nanospheres and nanocapsules, respectively). The amount of drug entrapped determines the performance of the drug delivery system as it influences the rate and extent of drug release from the system. Both DL and EE depend on physicochemical properties and the interactions between the drug, the carrier matrix, the encapsulated oil and the surrounding medium.

Triclosan release has been studied in Sørensen medium containing 70 volume percentage of ethanol in order to increase the hydrophobicity of the medium and avoid reaching an equilibrium condition. The studied mixture had previously been found to give similar triclosan release results in more expensive serum-based media [40]. Release of triclosan from nanoparticles and nanocapsules is clearly different, as compared in Figure 13a. Thus, the profile of nanospheres showed an initial Burst effect up to a percentage close to 35% which was mainly caused by the drug deposited on or close to the particle surface, followed by a slower, gradual release indicative of an effective hydrophobic interaction between the drug and the hydrophobic hexadecyl groups. On the contrary, the Burst effect was not significant when using nano-

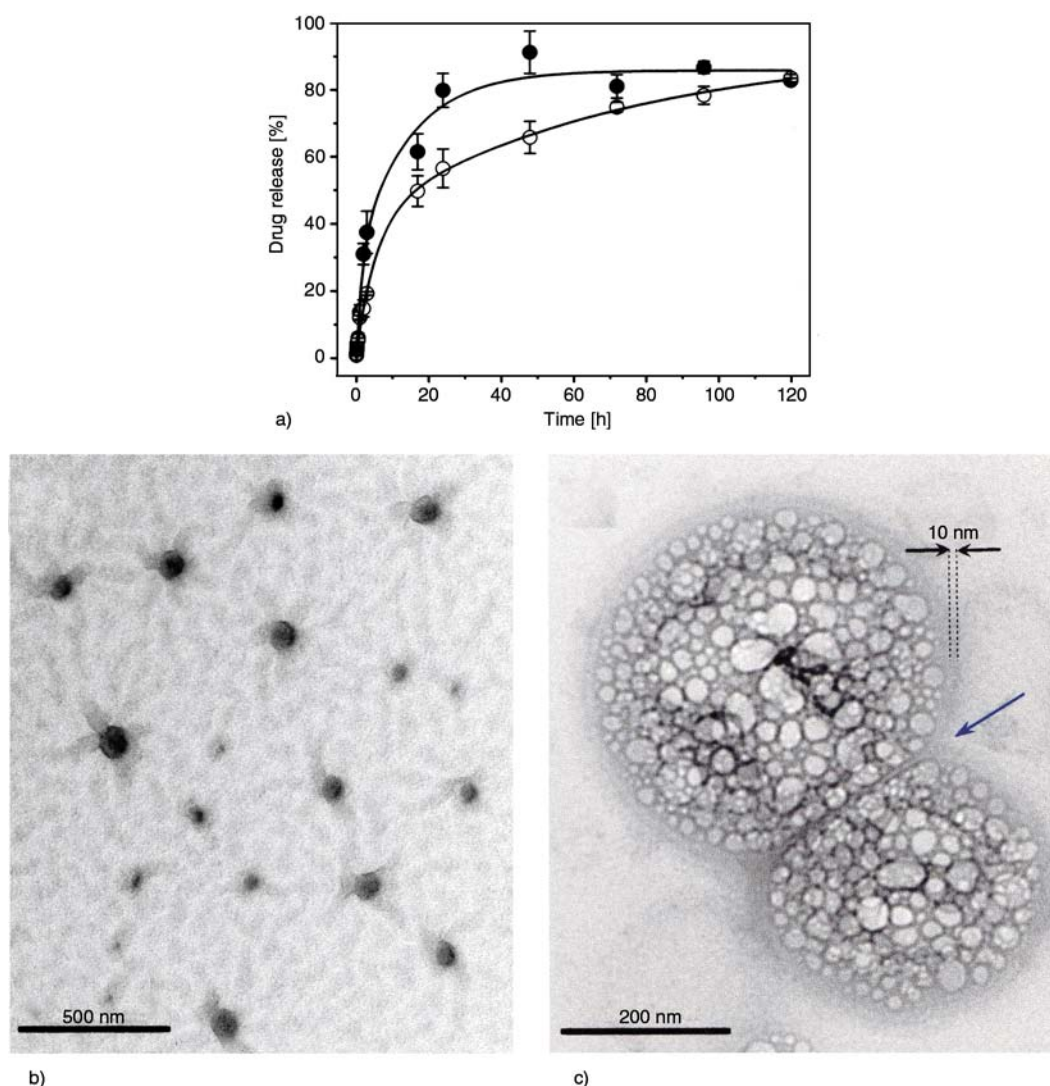


**Figure 12.** TEM micrographs (a, b, c) taken at different magnifications of poly(MePEGCA-co-HDCA) nanocapsules containing Miglyol 812. Sample (d) was shadowed with Pt/C. Red and black arrows point to pseudoregular geometries inside nanocapsules and spilled oil outside nanocapsules, respectively. Wall thickness of nanocapsules is indicated by the blue marks.

capsules and a sustained release over a period greater than 120 h was observed. The polymer was able to confine the oil effectively despite possible degradation of pegylated chains, and triclosan remained preferentially in the hydrophobic oil core, reducing the Burst effect and release rate.

Both nanospheres and nanocapsules showed a maximum drug release close to 80%. It seems that some triclosan was entrapped in the two cases and could not diffuse effectively through the polymer matrix or polymer membrane, respectively, at an appreciable rate.

Release of triclosan from nanospheres was interpreted with the first-order equation only, since the 40% initial release could be ascribed to a Burst effect, as above indicated. The kinetic constant for this step was  $0.073 \text{ h}^{-1}$ . In contrast, a combined model was required to interpret the release from nanocapsules. In this case, kinetic constants close to  $0.145 \text{ h}^{-0.5}$  and  $0.024 \text{ h}^{-1}$  were derived by fitting the first (Higuchi model) and second (first-order model) steps of the release. It is interesting to highlight the threefold decrease of the kinetic constant associated with the last release step, when using nanocapsules



**Figure 13.** (a) Comparison between cumulative triclosan release from poly(MePEGCA-*co*-HDCA) nanospheres (●) and nanocapsules (○) in a Sørensen/ethanol (3/7 v/v) medium. Vertical bars are the average values  $\pm$ SD. Theoretical simulated curves from calculated kinetic parameters and selected release models are drawn with solid lines. (b) TEM micrograph of poly(MePEGCA-*co*-HDCA) nanospheres after 120 hours of exposure to the degradation medium. (c) TEM micrograph of poly(MePEGCA-*co*-HDCA) nanocapsules after 120 hours of exposure to the degradation medium. The blue arrow points to the decrease of the membrane thickness caused by close contact of adjacent nanocapsules.

instead of nanospheres (i.e.  $0.024 \text{ h}^{-1}$  versus  $0.073 \text{ h}^{-1}$ ). Despite the expected low diffusion rate of triclosan in the polymer matrix, the result seems logical as there is a greater affinity between triclosan and glycerol than between the drug and the polymer matrix, resulting in an enhanced release from nanospheres. It must be pointed out that the assumption of the late-time Equation (4) for both NS and NC dosage forms implies that the amount of drug released at each time is proportional to the residual drug inside these forms.

TEM micrographs were taken at the end of the release experiments (120 h) to find evidence of degradation. Nanospheres appeared clearly isolated

and kept their rounded morphology and even their diameter size range (Figure 13b). Hence, no morphological changes were reported after exposure to the release medium. More interesting were the high magnification images of nanocapsules (e.g. Figure 13c) where two points merit attention: a) The membrane wall appeared well preserved and had even swelled slightly, as deduced from the increase of the wall thickness (a value close to 10 nm was measured). Note also that in this case the wall thickness clearly decreased upon close contact of nanocapsules. In addition, the detected degradation of pegylated chains did not affect the consistency of the nanocapsule membrane. As indicated before,



new anionic carboxylated groups should have formed by hydrolysis, providing again a hydrophilic outer surface that stabilized the membrane in the water containing release medium; b) Drops can be clearly envisaged in the nanocapsule cores. Molecules of the release media (ethanol and water) were likely to have crossed the membrane, causing a swelling effect and microphase separation.

### 3.7. Antibacterial effect of the nanospheres and nanocapsules loaded with triclosan

The antibacterial activity of triclosan loaded nanocapsules and nanospheres was tested by direct contact with microorganisms. Figure 14a shows the relative growth of *E.coli* (Gram-negative bacterium) and *M.luteus* (Gram-positive bacterium) after 24 and 48 hours of culture in the presence of these nanospheres and nanocapsules.

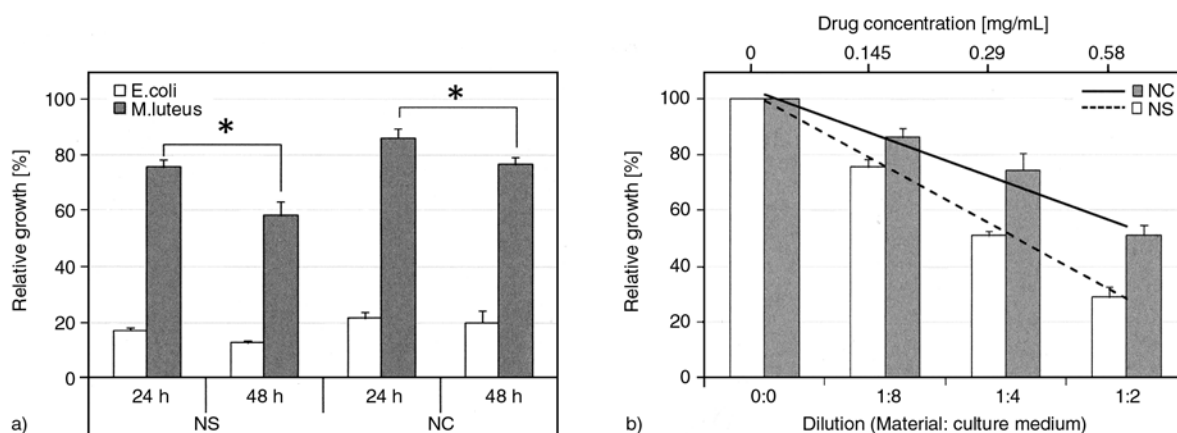
*E.coli* was especially sensitive to the antibacterial action of triclosan. Thus, the inhibition of bacterial growth after 24 h of culture was about 80% for both nanospheres and nanocapsules. It may be inferred from the above results that the antibacterial effect was due to the release of approximately 50 and 80% of loaded triclosan in the nanocapsules and nanospheres, respectively (Figure 13a). The triclosan release ensured that bacterial growth inhibition was maintained around 80% after 48 h of culture.

*M.luteus* showed greater resistance to triclosan as the inhibition of bacterial growth was only about 10 and 20% after 24 h of culture for nanocapsules and nanospheres, respectively (Figure 14a). Notice that,

as expected, inhibition was greater for the former because of their higher triclosan release rate. After 48 h of culture, a statistically significant increase in the inhibition of bacterial growth was reported, with values of 20 and 40% for nanocapsules and nanospheres, respectively. Note that the relative inhibition doubled with increasing the drug release period. Thus, results clearly indicate that progressive release of triclosan from both nanospheres and nanocapsules increased the antibacterial effect.

It is clear that *M.luteus* growth is sensitive to the amount of triclosan released, as is typical in the antimicrobial control of Gram-positive bacteria. Two approaches can be taken to solve this sensitivity problem: a) Preparation of nanospheres or nanocapsules with a higher drug load, which is not desirable since a change of the mass ratio between polymer and drug is required; b) Exposure of bacteria to a medium containing more nanospheres or nanocapsules.

Figure 14b shows the antimicrobial effect of triclosan loaded nanospheres and nanocapsules in relation to the number of dosage forms, which was easily managed by controlling the dilution of the NS/NC suspension with the broth medium. A direct linear relationship between the antibacterial effect and the number of triclosan loaded nanospheres and nanocapsules was logically found. Specifically, correlation coefficients,  $r$ , of 0.987 and 0.999 were obtained for the NS and NC relationships, respectively.



**Figure 14.** (a) Relative growth of *E.coli* and *M.luteus* in cultures constituted by 7 mL of the LC broth medium and 1 mL of the nanosphere (NS) or nanocapsule (NC) suspension. Asterisks indicate significantly different samples according to Tukey test,  $p < 0.05$ . (b) Relative growth of *M.luteus* in cultures constituted by different dilutions of the NS/NC suspension in the culture medium. Vertical bars are the average values  $\pm$ SD. Solid and dashed lines indicate the relationship between relative growth and dilution for NS and NC samples.

#### 4. Conclusions

The amphiphilic copolymer derived from methylated polyethylene glycol and hexadecyl cyanoacetate esters with a hydrophilic/hydrophobic monomer ratio close to 1:4 was semicrystalline and able to develop large spherulites by crystallization from the melt state. Morphological observations, calorimetric data and X-ray and electron diffraction patterns pointed out the existence of two crystalline domains. These could be associated with polyethylene glycol and a hexagonal phase corresponding to the packing of the long alkyl lateral groups.

The copolymer hydrolyzed in water by cleavage of ester bonds involving the hydrophilic polyethylene glycol groups, whereas ester bonds involving the hydrophobic hexadecyl groups appeared well preserved.

The solvent displacement method coupled with the use of CIJM was highly effective in preparing triclosan loaded nanospheres and nanocapsules. Encapsulation efficiency was always close to 90% and an approximate 40% drug load was easily obtained. Morphological observations and DLS measurements indicated that NS and NC samples had size distribution centered at around 160 and 230 nm, respectively. Nanocapsules were characterized by a polymer membrane with a thickness close to 5 nm, a spongy structure that was easily deformed and the presence of crystallizable PEG chains in the oil core. Nanocapsules kept their morphology during exposure to the release medium (minimum 72 h), although a slight swelling of the membrane wall was observed. Solvent molecules were able to cross the membrane, which was unaffected by the increase of the hydrodynamic pressure.

Nanospheres and nanocapsules exhibited a well differentiated triclosan release; specifically, the latter allowed a controlled, sustained release without Burst effect. The antimicrobial effect was also significantly different, especially when Gram-positive bacteria were assayed. A higher relative growth was always found for nanocapsules due to their lower triclosan release rate.

#### Acknowledgements

This research has been supported by grants from MCYT/FEDER and AGAUR (MAT2009-11503, 2009SGR-1208). We gratefully acknowledge the important contribution of Drs. Barbara Stella and Antonello Barresi of the Università and the Politecnico di Torino (Italy), respectively, during polymer synthesis and nanoparticles preparation.

#### References

- [1] Adams M. L., Lavasanifar A., Kwon G. S.: Amphiphilic block copolymers for drug delivery. *Journal of Pharmaceutical Sciences*, **92**, 1343–1355 (2003). DOI: [10.1002/jps.10397](https://doi.org/10.1002/jps.10397)
- [2] Willert M., Landfester K.: Amphiphilic copolymers from miniemulsified systems. *Macromolecular Chemistry and Physics*, **203**, 825–836 (2002). DOI: [10.1002/1521-3935\(20020401\)203:5/6<825::AID-MACP825>3.0.CO;2-R](https://doi.org/10.1002/1521-3935(20020401)203:5/6<825::AID-MACP825>3.0.CO;2-R)
- [3] Storm G., Belliot S. O., Daemen T., Lasic D. D.: Surface modification of nanoparticles to oppose uptake by the mononuclear phagocyte system. *Advanced Drug Delivery Reviews*, **17**, 31–48 (1995). DOI: [10.1016/0169-409X\(95\)00039-A](https://doi.org/10.1016/0169-409X(95)00039-A)
- [4] Gref R., Minamitake Y., Peracchia M. T., Langer R.: PEG-coated biodegradable nanospheres for intravenous administration. in 'Microparticulate systems for delivery of proteins and vaccines' (eds.: Cohen S., Bernstein H.) Marcel Dekker, New York, 279–306 (1996).
- [5] Lundsted L. G., Schmolka I. R.: The synthesis and properties of block copolymer polyol surfactants. in 'Block and graft polymerization' (ed.: Ceresa R. J.) John Wiley, London 1–103 (1972).
- [6] Srinivasulu B., Rao P. R., Sundaram E. V.: Synthesis and characterization of ethyl methacrylate-acrylamide copolymers. *Journal of Applied Polymer Science*, **43**, 1521–1525 (1991). DOI: [10.1002/app.1991.070430814](https://doi.org/10.1002/app.1991.070430814)
- [7] Sanayei R. A., O'Driscoll K. F., Klumperman B.: Pulsed laser copolymerization of styrene and maleic anhydride. *Macromolecules*, **27**, 5577–5582 (1994). DOI: [10.1021/ma00098a010](https://doi.org/10.1021/ma00098a010)
- [8] Puig J. E., Corona-Galvan S., Maldonado A., Schultz P. C., Rodriguez B. E., Kaler E. W.: Microemulsion copolymerization of styrene and acrylic acid. *Journal of Colloid and Interface Science*, **137**, 308–310 (1990). DOI: [10.1016/0021-9797\(90\)90068-Y](https://doi.org/10.1016/0021-9797(90)90068-Y)
- [9] Zhang L., Zeng Z., Chen Y., Wu C., Gao J.: Photoinitiated copolymerization of acrylamide and styrene in oil-in-water microemulsion. *Journal of Applied Polymer Science*, **66**, 2543–2549 (1997). DOI: [10.1002/\(SICI\)1097-4628\(19971226\)66:13<2543::AID-APP17>3.0.CO;2-Y](https://doi.org/10.1002/(SICI)1097-4628(19971226)66:13<2543::AID-APP17>3.0.CO;2-Y)

- [10] Vašková V., Juraničová V., Bartoň J.: Polymerization in inverse microemulsions, 3. Copolymerization of water- and oil-soluble monomers initiated by radical initiators. *Die Makromolekulare Chemie*, **192**, 1339–1347 (1991).  
DOI: [10.1002/macp.1991.021920611](https://doi.org/10.1002/macp.1991.021920611)
- [11] Peracchia M. T., Desmaële D., Couvreur P., d'Angelo J.: Synthesis of a novel poly(MePEG cyanoacrylate-co-alkyl cyanoacrylate) amphiphilic copolymer for nanoparticle technology. *Macromolecules*, **30**, 846–851 (1997).  
DOI: [10.1021/ma961453k](https://doi.org/10.1021/ma961453k)
- [12] Peracchia M. T., Vauthier C., Desmaële D., Gulk A., Dedieu J.-C., Demoy M., d'Angelo J., Couvreur P.: Pegylated nanoparticles from a novel methoxypolyethylene glycol cyanoacrylate-hexadecyl cyanoacrylate amphiphilic copolymer. *Pharmaceutical Research*, **15**, 550–556 (1998).  
DOI: [10.1023/A:1011973625803](https://doi.org/10.1023/A:1011973625803)
- [13] Peracchia M. T., Fattal E., Desmaële D., Besnard M., Noël J. P., Gomis J. M., Appel M., d'Angelo J., Couvreur P.: Stealth® PEGylated polycyanoacrylate nanoparticles for intravenous administration and splenic targeting. *Journal of Controlled Release*, **60**, 121–128 (1999).  
DOI: [10.1016/S0168-3659\(99\)00063-2](https://doi.org/10.1016/S0168-3659(99)00063-2)
- [14] Brigger I., Chaminade P., Desmaële D., Peracchia M. T., d'Angelo P., Gurny R., Renoir M., Couvreur P.: Near infrared with principal component analysis as a novel analytical approach for nanoparticle technology. *Pharmaceutical Research*, **17**, 1124–1132 (2000).  
DOI: [10.1023/A:1026465931525](https://doi.org/10.1023/A:1026465931525)
- [15] Brambilla D., Nicolas J., Le Droumaguet B., Andrieux K., Marsaud V., Couraud P.-O., Couvreur P.: Design of fluorescently tagged poly(alkyl cyanoacrylate) nanoparticles for human brain endothelial cell imaging. *Chemical Communications*, **46**, 2602–2604 (2010).  
DOI: [10.1039/b924028d](https://doi.org/10.1039/b924028d)
- [16] Le Droumaguet B., Nicolas J., Brambilla D., Mura M., Maksimenko A., de Kimpe L., Salvati E., Zona C., Airoidi C., Canovi M., Gobbi M., Magalit N., La Ferla B., Nicotra F., Scheper W., Flores O., Masserini M., Andrieux K., Couvreur P.: Versatile and efficient targeting using a single nanoparticulate platform: Application to cancer and alzheimer's disease. *ACS Nano*, **6**, 5866–5879 (2012).  
DOI: [10.1021/nn3004372](https://doi.org/10.1021/nn3004372)
- [17] Lince F., Bolognesi S., Stella B., Marchiso D. L., Dosio F.: Preparation of polymer nanoparticles loaded with doxorubicin for controlled drug delivery. *Chemical Engineering Research and Design*, **89**, 2410–2419 (2011).  
DOI: [10.1016/j.cherd.2011.03.010](https://doi.org/10.1016/j.cherd.2011.03.010)
- [18] Lince F., Marchiso D. L., Barresi A. A.: Smart mixers and reactors for the production of pharmaceutical nanoparticles: Proof of concept. *Chemical Engineering Research and Design*, **87**, 543–549 (2009).  
DOI: [10.1016/j.cherd.2008.11.009](https://doi.org/10.1016/j.cherd.2008.11.009)
- [19] Fresta M., Cavallaro G., Giammona G., Wehrli E., Puglisi G.: Preparation and characterization of polyethyl-2-cyanoacrylate nanocapsules containing anti-epileptic drugs. *Biomaterials*, **17**, 751–758 (1996).  
DOI: [10.1016/0142-9612\(96\)81411-6](https://doi.org/10.1016/0142-9612(96)81411-6)
- [20] Mosqueira V. C. F., Legrand P., Pinto-Alphandary H., Puisieux F., Barratt G.: Poly(D,L-lactide) nanocapsules prepared by a solvent displacement process: Influence of the composition on physicochemical and structural properties. *Journal of Pharmaceutical Sciences*, **89**, 614–626 (2000).  
DOI: [10.1002/\(SICI\)1520-6017\(200005\)89:5<614::AID-JPS7>3.3.CO;2-Z](https://doi.org/10.1002/(SICI)1520-6017(200005)89:5<614::AID-JPS7>3.3.CO;2-Z)
- [21] Fessi H., Puisieux F., Devissaguet J. Ph., Ammoury N., Benita S.: Nanocapsule formation by interfacial polymer deposition following solvent displacement. *International Journal of Pharmaceutics*, **55**, R1–R4 (1989).  
DOI: [10.1016/0378-5173\(89\)90281-0](https://doi.org/10.1016/0378-5173(89)90281-0)
- [22] Gibaldi M., Feldman S.: Establishment of sink conditions in dissolution rate determinations. Theoretical considerations and application to nondisintegrating dosage forms. *Journal of Pharmaceutical Sciences*, **56**, 1238–1242 (1967).  
DOI: [10.1002/jps.2600561005](https://doi.org/10.1002/jps.2600561005)
- [23] Wagner J. G.: Interpretation of percent dissolved-time plots derived from *in vitro* testing of conventional tablets and capsules. *Journal of Pharmaceutical Sciences*, **58**, 1253–1257 (1969).  
DOI: [10.1002/jps.2600581021](https://doi.org/10.1002/jps.2600581021)
- [24] Higuchi T.: Rate of release of medicaments from ointment bases containing drugs in suspension. *Journal of Pharmaceutical Sciences*, **50**, 874–879 (1961).  
DOI: [10.1002/jps.2600501018](https://doi.org/10.1002/jps.2600501018)
- [25] Higuchi T.: Mechanism of sustained-action medication. Theoretical analysis of rate of release of solid drugs dispersed in solid matrices. *Journal of Pharmaceutical Sciences*, **52**, 1145–1149 (1963).  
DOI: [10.1002/jps.2600521210](https://doi.org/10.1002/jps.2600521210)
- [26] Baker R. W.: *Controlled release of biologically active agents*. Wiley, New York (1987).
- [27] Lestel L., Guegan P., Boileau S., Cheradame H., Laupretre F.: Influence of the chemical nature of cross-links on the local dynamics of bulk poly(ethylene oxide) networks as studied by carbon-13 NMR at temperatures well above the glass-transition temperature. *Macromolecules*, **25**, 6024–6028 (1992).  
DOI: [10.1021/ma00048a025](https://doi.org/10.1021/ma00048a025)

- [28] Muthukumar M., Ober C. K., Thomas E. L.: Competing interactions and levels of ordering in self-organizing polymeric materials. *Science*, **277**, 1225–1232 (1998).  
DOI: [10.1126/science.277.5330.1225](https://doi.org/10.1126/science.277.5330.1225)
- [29] Zhu L., Chen Y., Zhang A., Calhoun B. H., Chun M., Quirk R. P., Cheng S. Z. D., Hsiao B. S., Yeh F., Hashimoto T.: Phase structures and morphologies determined by competitions among self-organization, crystallization, and vitrification in a disordered poly(ethylene oxide)-*b*-polystyrene diblock copolymer. *Physical Reviews B*, **60**, 10022–10031 (1999).  
DOI: [10.1103/PhysRevB.60.10022](https://doi.org/10.1103/PhysRevB.60.10022)
- [30] Ryan A. J., Hamley I. W., Bras W., Bates F. S.: Structure development in semicrystalline diblock copolymers crystallizing from the ordered melt. *Macromolecules*, **28**, 3860–3868 (1995).  
DOI: [10.1021/ma00115a016](https://doi.org/10.1021/ma00115a016)
- [31] Schäffer E., Thurn-Albrecht T. P., Russell T. P., Steiner U.: Electrically induced structure formation and pattern transfer. *Nature*, **403**, 874–877 (2000).  
DOI: [10.1038/35002540](https://doi.org/10.1038/35002540)
- [32] Kawai T., Rahman N., Matsuba G., Nishida K., Kanaya T., Nakano M., Okamoto H., Kawada J., Usuki A., Honma N., Nakajima K., Matsuda M.: Crystallization and melting behavior of poly(L-lactic acid). *Macromolecules*, **40**, 9463–9469 (2007).  
DOI: [10.1021/ma070082c](https://doi.org/10.1021/ma070082c)
- [33] Müller A. J., Arnal M. L., Balsamo V.: Crystallization in block copolymers with more than one crystallizable block. in ‘Lecture notes in physics: Progress in understanding of polymer crystallization’ (eds.: Reiter G., Strobl G.) Springer, Berlin, Vol 714, 229–259 (2007).  
DOI: [10.1007/3-540-47307-6\\_13](https://doi.org/10.1007/3-540-47307-6_13)
- [34] Nandan B., Hsu J.-Y., Chen H.-L.: Crystallization behavior of crystalline-amorphous diblock copolymers consisting of a rubbery amorphous block. *Polymer Reviews*, **46**, 143–172 (2006).  
DOI: [10.1080/15321790600646802](https://doi.org/10.1080/15321790600646802)
- [35] Nielsen J. R., Hathaway C. E.: Infrared spectra of normal paraffins in the hexagonal crystal form. *Journal Molecular Spectroscopy*, **10**, 366–377 (1963).  
DOI: [10.1016/0022-2852\(63\)90182-6](https://doi.org/10.1016/0022-2852(63)90182-6)
- [36] Takahashi Y., Tadokoro H.: Structural studies of polyethers,  $(-(\text{CH}_2)_m-\text{O}-)_n$ . X. Crystal structure of poly(ethylene oxide). *Macromolecules*, **6**, 672–675 (1973).  
DOI: [10.1021/ma60035a005](https://doi.org/10.1021/ma60035a005)
- [37] Lotz B., Kovacs A. J.: Properties of copolymers composed of one poly-ethylene-oxide and one polystyrene block. I. Preparation, composition and microscopy study of single crystal (in French). *Colloid and Polymer Science*, **209**, 97–114 (1966).  
DOI: [10.1007/BF01500628](https://doi.org/10.1007/BF01500628)
- [38] Lotz B., Kovacs A. J., Bassett G. A., Keller A.: Properties of copolymers composed of one poly-ethylene-oxide and one polystyrene block II. Morphology of single crystals. *Colloid and Polymer Science*, **209**, 115–124 (1966).  
DOI: [10.1007/BF01500629](https://doi.org/10.1007/BF01500629)
- [39] Panyam J., Labhasetwar V.: Biodegradable nanoparticles for drug and gene delivery to cells and tissue. *Advanced Drug Delivery Reviews*, **55**, 329–347 (2003).  
DOI: [10.1016/S0169-409X\(02\)00228-4](https://doi.org/10.1016/S0169-409X(02)00228-4)
- [40] Zurita R., Puiggali J., Rodríguez-Galán A.: Triclosan release from coated polyglycolide threads. *Macromolecular Bioscience*, **6**, 58–69 (2006).  
DOI: [10.1002/mabi.200500147](https://doi.org/10.1002/mabi.200500147)

# Tuning the processability, morphology and biodegradability of clay incorporated PLA/LLDPE blends via selective localization of nanoclay induced by melt mixing sequence

L. As'habi<sup>1</sup>, S. H. Jafari<sup>1\*</sup>, H. A. Khonakdar<sup>2</sup>, R. Boldt<sup>3</sup>, U. Wagenknecht<sup>3</sup>, G. Heinrich<sup>3</sup>

<sup>1</sup>School of Chemical Engineering, College of Engineering, University of Tehran, 11155-4563, Tehran, Iran

<sup>2</sup>Iran Polymer and Petrochemical Institute, 14965-115, Tehran, Iran

<sup>3</sup>Leibniz Institute of Polymer Research Dresden, Hohe Str. 6, D-01069, Dresden, Germany

Received 14 May 2012; accepted in revised form 8 August 2012

**Abstract.** Polylactic acid (PLA)/linear low density polyethylene (LLDPE) blend nanocomposites based on two different commercial-grade nanoclays, Cloisite<sup>®</sup> 30B and Cloisite<sup>®</sup> 15A, were produced via different melt mixing procedures in a counter-rotating twin screw extruder. The effects of mixing sequence and clay type on morphological and rheological behaviors as well as degradation properties of the blends were investigated. The X-ray diffraction (XRD) results showed that generally the level of exfoliation in 30B based nanocomposites was better than 15A based nanocomposites. In addition, due to difference in hydrophilicity and kind of modifiers in these two clays, the effect of 30B on refinement of dispersed phase and enhancement of biodegradability of PLA/LLDPE blend was much more remarkable than that of 15A nanoclay. Unlike the one step mixing process, preparation of nanocomposites via a two steps mixing process improved the morphology. Based on the XRD and TEM (transmission electron microscopic) results, it is found that the mixing sequence has a remarkable influence on dispersion and localization of the major part of 30B nanoclay in the PLA matrix. Owing to the induced selective localization of nanoclays in PLA phase, the nanocomposites prepared through a two steps mixing sequence exhibited extraordinary biodegradability, refined morphology and better melt elasticity.

**Keywords:** biodegradable polymers, mixing methods, polylactic acid, nanocomposites

## 1. Introduction

In recent years, environmental pollution has become a great concern due to the high impact of plastic wastes in daily use. To cope with this problem, the commodity synthetic polymers can be replaced with the biodegradable polymers which are susceptible to microbial action. The most popular and biodegradable polymers are aliphatic polyesters, such as polylactic acid (PLA), polycaprolactone (PCL), poly (butylene adipate-co-terephthalate) (PBAT) and polyhydroxybutyrate (PHB). Amongst the biodegradable polymers, PLA has a number of interesting properties including biodegradability,

good mechanical properties, and processability. For these reasons PLA is an interesting candidate for producing commercial biodegradable materials. However, high brittleness and cost of PLA are two major obstacles for commercialization and many applications [1–3].

Oyama showed that reactive blending of PLA with EGMA poly (ethylene-glycidyl methacrylate) improves the elongation at break of PLA. These improvements in mechanical properties were achieved without sacrificing the heat resistance of PLA. It was deduced that crystallization of the PLA matrix plays a significant role in toughening [4].

\*Corresponding author, e-mail: [shjafari@ut.ac.ir](mailto:shjafari@ut.ac.ir)

Preparation of blends, conventional composites and nanocomposites using inorganic fillers or nanofillers are among the routes to improve some of the properties of PLA and reducing the production cost. Thermal stability, gas barrier properties, strength, low melt viscosity, are among the properties that can be improved by these multiphase systems [5]. The nanocomposite technology is a beneficial route for improving biodegradability and processability of these blends.

Amongst the petrochemical-based polymers, polyethylene (PE) is one of the most consumed polymers especially in the packaging industry. This polymer can degrade under oxygen and ultra violet radiation however, the degradation rate of PE after disposal is very slow. Therefore a blend nanocomposite of PLA and linear low-density polyethylene (LLDPE) may be a suitable choice for excellent biodegradable material.

According to the American Society for Testing and Materials (ASTM), a biodegradable plastic is a plastic that degrades because of the action of naturally occurring microorganisms such as bacteria, fungi, and algae. There is a difference between a biodegradable and a compostable plastic. A compostable plastic is a plastic that undergoes degradation by biological processes during composting to yield carbon dioxide, water, inorganic compounds, and biomass at a rate consistent with other known compostable materials and leaves no visually distinguishable or toxic residues. Therefore, all compostable plastics are biodegradable, but the reverse is not true. A major problem with PLA matrix is the slow rate of degradation as compared to the rate of waste accumulation. Often, an unfavorable hydrolytic degradation rate will limit the PLA applications compared to the other biodegradable polymers. Considerable efforts have been made to control and accelerate the hydrolytic degradation rate. Despite the considerable number of reports concerning the enzymatic degradation of PLA [6–8] and various PLA blends [9], the compost degradability of PLA and its blend with conventional petrochemical-based polymers are still very little known. Very limited researches on degradation behavior of PLA/PE exist in the literatures [10–12] till date. Singh and coworkers studied the degradation behavior of LLDPE/PLA blend [10]. They pointed out that the blend of LLDPE/PLA (80wt% LLDPE and 20% PLA) degrades faster than pure LLDPE. They also found

that the mechanical properties of this system depend on the blending ratios and the compatibilizer content [11].

PLA/PE blends have also attracted a huge interest because it complements brittleness of the PLA. Studies have shown that blending of PLA with LLDPE resulted in a significant increase in PLA ductility and toughness on expense of strength and modulus [13–17]. Anderson and coworkers [13] showed that for the amorphous PLA the toughening was achieved only when a poly (L-lactide) (PLLA)-PE block copolymer was used as compatibilizer. On the other hand Kim and coworkers investigated blends of PLLA and low-density polyethylene (LDPE) and found that the domain size of dispersed phase decreased and the tensile properties enhanced significantly by using a reactive compatibilizer having glycidyl methacrylate (GMA) functional group [14]. Because of the immiscibility of this system, several researchers employed different compatibilizers to further tailoring the properties [16–17]. Rezgui *et al.* [16] studied the plastic deformation and modeled the creep behavior of LDPE reinforced with PLA. They pointed out that the deformation damage of LDPE/PLA blends increased with increasing PLA content. They also found that with increasing concentrations of PLA, the blend showed higher Young's modulus, stiffer viscoelastic response and earlier fracture [17].

PLA/clay nanocomposites have already been extensively studied in terms of mechanical, thermal, fire retardancy and crystallization behavior. However, to date there have been very limited reports on the tuning of PLA/LLDPE properties especially biodegradability by addition of nanoparticles and developing the PLA/LLDPE blend nanocomposites. Recently Nuñez and coworkers studied the PLA/LLDPE nanocomposites based on sepiolite [18]. They showed that the compatibilized blends prepared without clay have higher thermal degradation susceptibility and tensile toughness than those prepared with sepiolite and significant changes in complex viscosity and melt elasticity values were observed. This blend nanocomposites exhibited similar thermal degradation, lower tensile strength, and Young's modulus and increased elongation at break and tensile toughness, complex viscosity, and storage modulus compared with the nanocomposite of PLA.

However, the most crucial factor in enhancement of properties in nanocomposites is the extent of interaction between nanoclay and polymer matrix which leads to the selective localization of nanoclay in multiphase systems. In this context addition of compatibilizer to a clay-containing multiphase system can have its own contribution towards clay positioning and its state of dispersion due to induced changes in the system thermodynamic. This topic has been discussed intensively in the literature [19–29]. Undoubtedly, the mixing procedure has also a strong effect on the localization of nanoclay. The simplest and most widely reported mixing procedure is the simultaneous feeding of all components in to the mixer. A second alternative is first to incorporate the nanoclay into a polymer having the higher affinity and then adding the rest of components. Depending on these mixing sequences, the nanoclay may migrate from one phase to the other to reach its equilibrium distribution which involves particle displacement inside the blend [19]. This phenomenon has been discussed in the case of different nanocomposites hybrid [20–24]. Elias *et al.* [21] studied polypropylene (PP)/polystyrene (PS)/silica blend and the effect of the sequence of addition where the silica was first mixed with PP and the obtained composite was then mixed with PS. They observed that all the hydrophilic silica moves from the PP with which it has lower affinity towards the PS preferred phase. In a series of reports Gubbels *et al.* [21–23] introduced carbon black in polystyrene/polyethylene system to obtain electrical conductivity. They clearly illustrated some of the influential factors on the distribution of nanofillers and their effects on the material properties. Zaikin *et al.* [24] have varied the sequence of mixing for carbon black filled polymer blends and found enhanced conductivity when the filler had to cross the interface. In this study the compatibilized blend nanocomposites of PLA and LLDPE were prepared. LLDPE was chosen as a counterpart of PLA due to its superior mechanical properties, low price and major use for packaging. A terpolymer (EBAGMA) of ethylene, butylacrylate (BA) and glycidylmethacrylate (GMA) was selected as a compatibilizer for the PLA/LLDPE system. The chemical groups of this compatibilizer are similar to poly (ethylene-glycidyl methacrylate) which was used by Oyama [4] as a reactive component for improving the brittleness of PLA. The aim of our work is to improve the brittle-

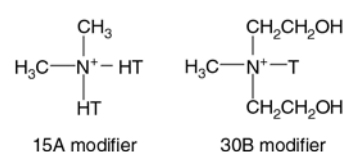
ness of PLA with a suitable composition of the most consumed polymer (LLDPE) with keeping its high modulus, and its biodegradability. For this reason the blend composition of 75/25 was selected.

Considering the importance of PLA/LLDPE system from the environmental viewpoints and the influential role of nanoclay on biodegradability, morphology and processability of the system and also in view of the very limited research on this particular system the current work is aimed to explore the influence of mixing procedure as one of the most influential kinetic parameters on localization of nanoclay and its effects on processability, biodegradability and morphology of compatibilized PLA/LLDPE/clay system.

## 2. Experimental

### 2.1. Materials and samples preparation

Poly lactide (4042D) used in this study was a commercial product of NatureWorks (USA). The ratio of L and D isomeric forms in this grade of PLA is about 96/4. The linear low density polyethylene (LLDPE) used was also a commercial grade (LL 4004EL) supplied by ExxonMobile Chemical (USA), having a melt flow index of 3.6 g/10 min (190°C, 2.16 kg). The Elvaloy® PTW (EBAGMA) which is a terpolymer of ethylene, butylacrylate (BA) and glycidylmethacrylate (GMA) with MFI of 12 g/10 min (190°C, 2.16 kg) supplied by DuPont (USA) was used as a reactive compatibilizer. Two different commercial nanoclays (Southern Clay Products, Inc.), Cloisite® 30B (30B), MMT-Na<sup>+</sup> modified with bis-(2-hydroxyethyl) methyl tallow alkyl ammonium cations and Cloisite® 15A (15A), MMT-Na<sup>+</sup> modified with dimethyl, dehydrogenated tallow, quaternary ammonium cations were used. The chemical structures of modifiers are showed in Figure 1. Before mixing, all the polymers and the nanoclays were dried in a vacuum oven at 50°C for 24 h. A counter-rotating twin-extruder (ZSK 30) equipped with gravimetric feeders and a strand pelletizer, were employed to compound the hybrids. In order to investigate the effect of mixing methods, the nano-



**Figure 1.** Structure of Cloisite 30B and Cloisite 15A modifiers

composites were prepared in two ways. In one step mixing procedure, all the components were added to the extruder all together. In the other method all the nanocomposites were prepared in a two steps mixing procedure in which the nanoclay was pre-compounded with the polymer having the higher affinity followed by the addition of the obtained material to the second polymer during a second extrusion step. In other words, in the 30B based nanocomposites due to the better affinity of the 30B modifier with PLA, 30B nanoclay was first mixed with PLA and the resulting composite was then mixed with LLDPE and compatibilizer. In the 15A based nanocomposites, 15A nanoclay was first mixed with LLDPE and this composite was then mixed with PLA and compatibilizer. A screw speed of 150 rpm and a feed rate of 10 kg/h were used for all runs. The extrusion temperature profile was set from 160 to 190°C from hopper to die. The blend and nanocomposite pellets were then dried in a vacuum oven at 50°C for 24 h prior for characterization. The PLA/LLDPE blend compositions were 75/25. The compatibilized blend and nanocomposites had about 5 wt% compatibilizer. The nanoclay loading in each nanocomposite samples was about 3, 4.5 and 6 wt% of the total mixture. The nanoclay content and its type are indicated by a number and a letter in the sample name (e.g., 3% 30B it means 3 wt% Cloisite 30B).

## 2.2. Characterization

Wide Angle X-Ray Scattering (WAXS) analyses were performed on injection molded specimens with XRD 3003 (Seifert-FPM Freiberg/Sa, Germany) using Cu-K $\alpha$  X-ray source. Since WAXS is sensitive to any orientation in the sample, therefore the injection molded samples with lower orientation than that of the extruded samples were used for the WAXS measurements. The continuous scanning angle range used in this study was from 1 to 10° at 40 kV and 30 mA. The scanning rate was 1°/min with a step size of 0.05°. Standard tensile test samples (ISO 527-1) were prepared by injection molding operated at 175 to 205°C from hopper to die with the back pressure of 2 bars.

The dispersion of the nanoclay platelets in the blend was studied by means of a transmission electron microscopy (TEM). The samples were cryo-ultramicrotomed from extruded strands in thin section (approximately 40 nm thick) at -180°C with a dia-

mond knife. The sections were observed by means of a Carl Zeiss LIBRA<sup>®</sup> 200 MC, Germany, using an accelerated voltage of 200 kV.

Scanning electron microscopy (SEM) was used to characterize the morphology of the blends and nanocomposites. An extruded polymer strand was immersed in liquid nitrogen for some time and a brittle fracture was performed. All specimens after proper drying were sputter coated with 3 nm Pt prior to examination and observed under a NEON 40 EsB (Carl Zeiss, Oberkochen, Germany).

Biodegradability was studied on a homemade compost instrument at (58±2)°C. The organic compost, with a C/N ratio of 8.7/1, was supplied by Dandy's Top soil Co. (UK). Biodegradation was monitored in every 7 days for a period of approximately 5 months by measuring the residual mass and carbon dioxide (CO<sub>2</sub>) evolution according to the ASTM 5338, 2003. The buried samples were recovered, washed with distilled water, and dried at room temperature before being weighed. Test specimens were prepared by compression molding with a thickness of 1 mm. The shape of the original test samples was 3 × 3 × 0.1 cm<sup>3</sup>. The average values of two measurements were reported. The samples were prepared by compression molding (Paul-otto Weber, Germany) at 205°C for 6 minutes preheating and one minute holding at 100 kN. The samples were then cooled to 70°C using circulating water, after which they were directly cooled to room temperature.

The basic rheological measurements in the melt state were carried out by means of an ARES rotational rheometer, Rheometric Scientific, Inc., USA, using small amplitude oscillatory frequency sweeps and temperature sweeps. The selected geometry for frequency sweeps and heating/cooling sweeps in the molten state was the parallel plate geometry (gap of about 2 mm, and diameter of 25 mm). The rheological measurements were performed on compression molded disks obtained under the same compression molding conditions described before.

## 3. Results and discussion

### 3.1. WAXS

The type of filler dispersion in the polymer matrix was determined by WAXS. This technique allows the determination of the spaces between structural layers of the silicate utilizing Bragg's law:  $\sin \Theta = n\lambda/2d$ , where  $\lambda$  corresponds to the wave length of the X-ray radiation used in the diffraction experi-



ment,  $d$  the spacing between diffracting lattice planes and  $\Theta$  is the measured diffraction angle.

Figure 2 shows the X-ray diffraction (XRD) patterns of the organoclays and the nanocomposites of compatibilized PLA/LLDPE systems. As it is seen from Figure 2, all the hybrids, namely PLA/LLDPE/30B and PLA/LLDPE/15A, show the X-ray diffraction peaks characteristic of unexfoliated structures at different clay contents. The XRD patterns were analyzed and the data corresponding to the gallery spacings ( $d_{001}$ ) are presented in Table 1.

As indicated in Figure 2a, the neat Cloisite 30B shows the (001) diffraction at  $2\Theta = 4.75^\circ$ . This peak corresponds to an interlayer spacing of 18.6 Å. The characteristic ( $d_{001}$ ) of 30B for PLA/LLDPE/30B nanocomposites shifted to the  $2\Theta = 2.6^\circ$  corresponding to a d-spacing of 34 Å, which indicates that some PLA molecular chains were intercalated between the organoclay galleries, forming an inter-

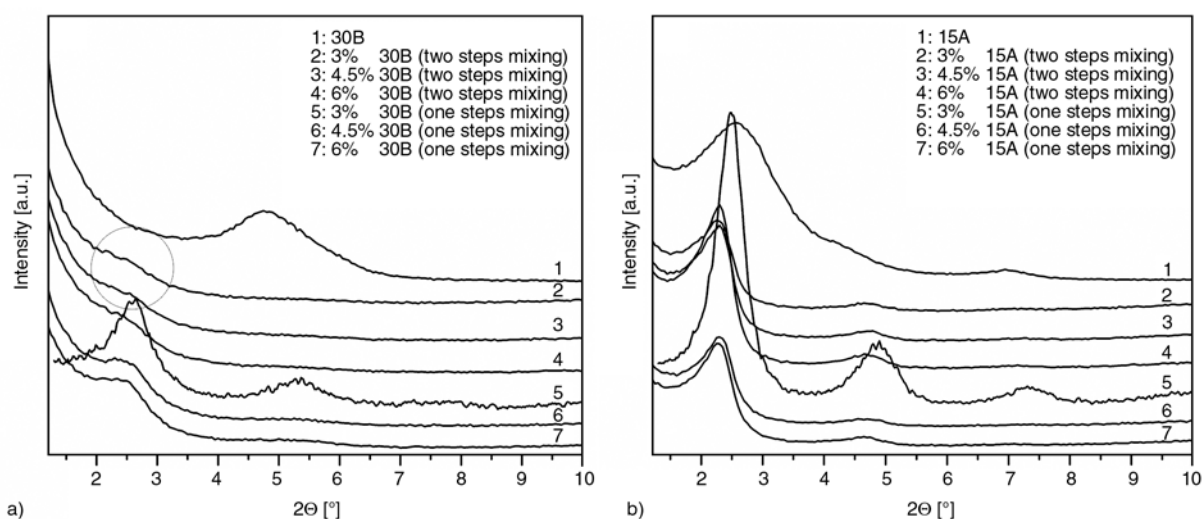
calated structure. All PLA/LLDPE/30B nanocomposites prepared in one step mixing show the same d-spacing.

From Figure 2, the effect of mixing methods on dispersion of nanoclays can be analyzed. To study the dispersibility of clay layers in two phases, the components were mixed in two steps. It can be seen from Figure 2a that the melt mixing of PLA/30B nanocomposites at different clay contents with pure LLDPE and compatibilizer led to the increase of the gallery spacing which indicates a higher level of silicate layers exfoliation throughout the PLA/LLDPE matrix. It is noticeable that the intensity of diffraction peaks of 30B based nanocomposites which were prepared in the two-step mixing procedure is much smaller and wider as compared to other mixing procedure. So practically, it can be concluded that these peaks ( $2\Theta = 2-2.25^\circ$ ) disappeared in the 30B based nanocomposites prepared by the two-step mixing procedure. It signifies an improved distribution, level of exfoliation and considerable decrease in the ordered clay structure. Although, XRD is very useful tool for the measurement of d-spacing in intercalated systems, combination of XRD and TEM should be utilized for a precise result. In the 15A based blend nanocomposites (PLA/LLDPE/15A) unlike the 30B based nanocomposites, the d-spacing of silicate layers differs only slightly from that of neat 15A. It can be due to different cationic modifiers present on the clay surfaces. Comparing to the cationic modifier of the 30B surface, the modifier of Cloisite 15A has less affinity with PLA matrix due to the non-polar nature

**Table 1.** XRD data for pristine organoclays and PLA/LLDPE blend nanocomposites

Samples	$d_{001}$ [Å]		$2\Theta$ [°]	
	$d_{001}$ [Å]	$2\Theta$ [°]	$d_{001}$ [Å]	$2\Theta$ [°]
Cloisite 30B (30B)	18.6	4.75		
Cloisite 15A (15A)	34.6	2.55		
	<b>One step mixing</b>		<b>Two steps mixing</b>	
	$d_{001}$ [Å]	$2\Theta$ [°]	$d_{001}$ [Å]	$2\Theta$ [°]
PLA/LLDPE/3% 30B	34	2.6	—*	—*
PLA/LLDPE/4.5% 30B	34	2.6	—*	—*
PLA/LLDPE/6% 30B	34	2.6	—*	—*
PLA/LLDPE/3% 15A	35.3	2.5	39.3	2.25
PLA/LLDPE/4.5% 15A	38.4	2.3	38.4	2.3
PLA/LLDPE/6% 15A	39.2	2.25	38.4	2.3

\*Due to wideness of the peaks, determination of the exact position of the peaks is very difficult.



**Figure 2.** WAXS patterns of pristine organoclays and compatibilized PLA/LLDPE nanocomposites (a) 30B based nanocomposites, (b) 15A based nanocomposites

of 15A and polar nature of PLA. This result confirms that the structure of clay modifier is one of the most important factors that can influence the level of dispersion of nanoclays. The nanocomposites with 3, 4.5 and 6 wt% 15A content exhibited X-ray peaks similar to the neat Cloisite 15A but with different intensities. The extraordinary intensity of the diffraction peak for the nanocomposite with 3 wt% 15A content may have also been an effect of the sample preparation or local clay order or crystallites.

In PLA/LLDPE/15A based nanocomposites, the characteristic (001) peak of the 15A at  $2\theta = 2.55^\circ$  appears at 2.5, 2.3 and  $2.25^\circ$  for hybrids containing 3, 4.5 and 6 wt%, respectively.

In order to study the effect of mixing procedure on selective localization of 15A, the LLDPE was pre-compounded with the 15A and then the obtained material was added to the PLA and compatibilizer during a second extrusion step. Unlike the 30B based nanocomposites, the effect of mixing procedure on intercalation of silicate layers was not significant. However, slight increase in  $d_{001}$  at lower content of 15A (3 wt%) can be noticed. In other words, the differences between the d-spacing values for all the equivalent loadings of 15A at different mixing procedures are relatively small and therefore they all should have similar intercalated structures. It seems that the polar nature of PLA and compatibilizer is responsible for this good level of interaction between 30B and PLA leading to better intercalation/exfoliation of the nanoclay layers. However, it is difficult for XRD to reveal definitive conclusions about the definite structure and particularly localization of the silicate layers in the phases. Thus, TEM technique is necessary to characterize the morphology of the composites.

## 3.2. Microscopic analysis

### 3.2.1. TEM analysis

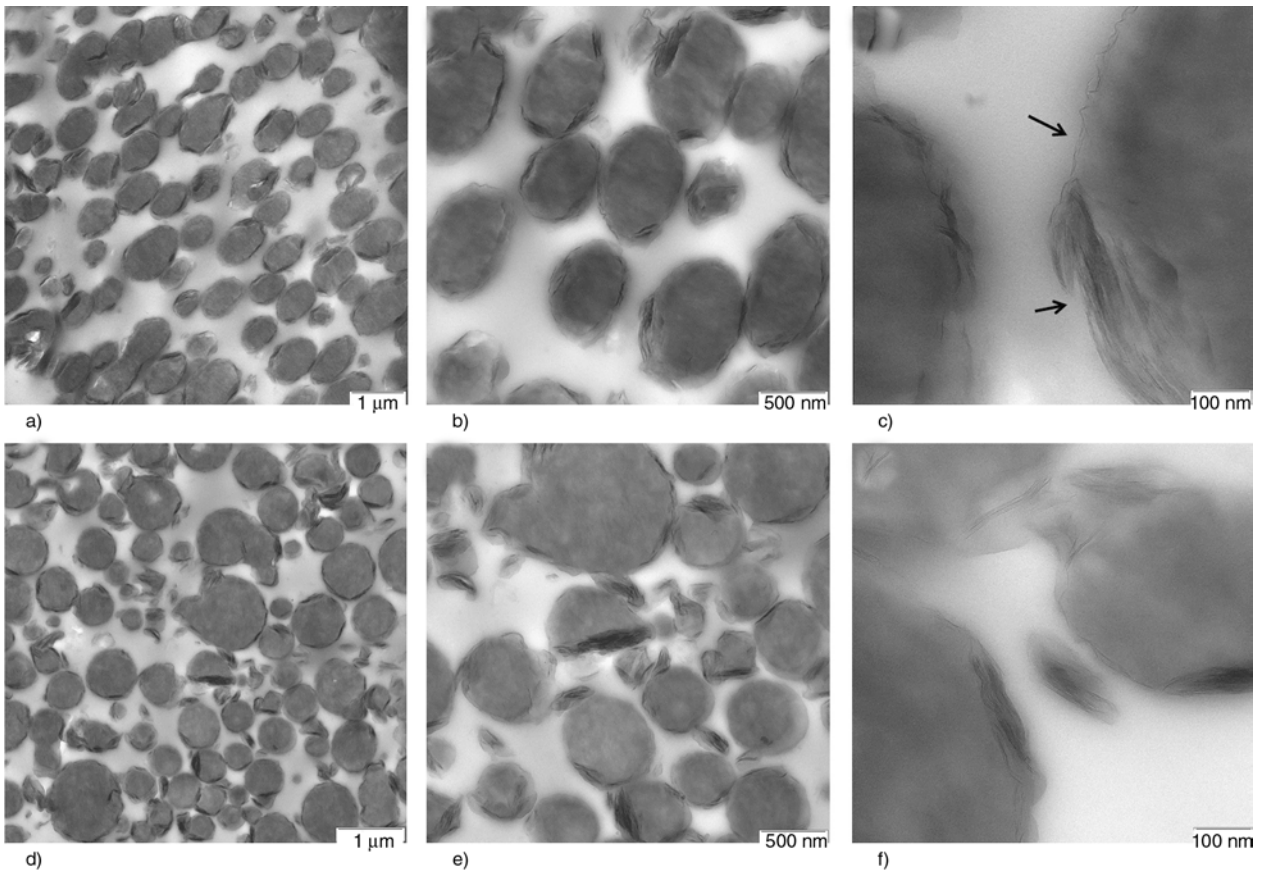
Combination of XRD and TEM is useful to obtain a precise result. TEM micrographs of PLA/LLDPE nanocomposites with different magnifications are illustrated in Figures 3 and 4. The typical two-phase structure can be seen in these TEM micrographs, in which the dark grey and white parts correspond to LLDPE and PLA phases, respectively. The dark lines are the cross section of the clay layers that have been delaminated and dispersed in the polymer matrix. For the sake of brevity only TEM analy-

sis of PLA/LLDPE nanocomposites containing 4.5 wt% nanoclays are shown here because all the LLDPE/PLA based nanocomposites at different clay contents show almost similar behavior.

The TEM images for PLA/LLDPE/30B based nanocomposites presented in Figure 3a–3c are indicative of an intercalated/exfoliated structure. Some partly exfoliated clay platelets are located at the interface between PLA and LLDPE. But, besides the exfoliated organoclay layers, some organoclay stacks are also visible, mostly in the PLA phase (Figure 3a and 3c). These stacks are responsible for the XRD pattern corresponding to the non-exfoliated organoclay seen from the XRD results of this sample.

The sequence of the addition of components is of importance and can have a strong effect on the localization of nanoclay. In one step mixing method as all the components were added simultaneously to the extruder, the process is complex involving mixtures of solids and viscous fluids and the simultaneous evolution of the morphology of the polymer blend together with the dispersion and migration of the particles inside the molten material [19]. Since the compatibilizer melts at temperature significantly lower (approximately at  $75^\circ\text{C}$ ) than the other two polymers, it encompasses the 30B nanoparticles preferentially. It can be seen from Figure 3a–3c that the main part of nanoclay is localized at the interface between PLA and LLDPE. However, some of the 30B particles are observed to have crossed the interface and distributed in PLA matrix. This implies that the adsorbed compatibilizer macromolecules on clay surface are desorbed by PLA macromolecules. It seems that due to high barrier energy for desorption and short mixing time, some 30B particles reside at the interface [24].

In the two steps mixing method (Figure 3d–3f), first the 30B particles were incorporated in to the PLA having higher affinity and then the mixture was compounded with LLDPE and compatibilizer in a separate mixing run. Figure 3d–3f shows that unlike the one step mixing, 30B are distributed mainly within PLA phase in the two steps mixing method. Some partly exfoliated clay platelets within PLA phase are also visible (Figure 3f). As it can be seen from Figure 3 the level of exfoliation is better in two step mixing and this is consistent with the wider and lower diffraction peak appearing in the XRD pattern of the equivalent samples which were



**Figure 3.** TEM micrographs of compatibilized PLA/LLDPE nanocomposites (a–c) prepared through one step mixing at different magnifications, (d–f) prepared through two steps mixing at different magnifications (all samples contain 4.5 wt% 30B)

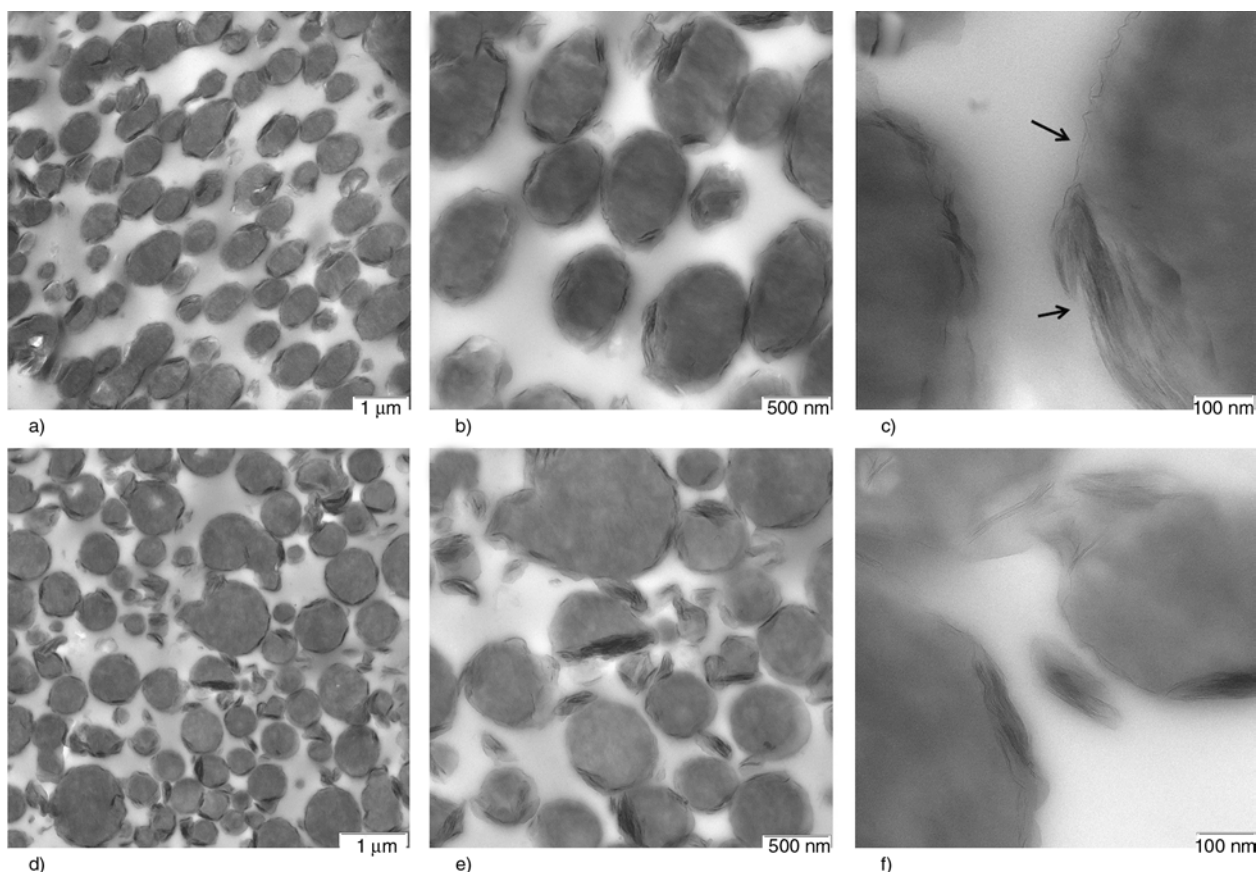
prepared through one step mixing, as shown in Figure 2a curve 3. It is noticeable that some partly exfoliated clay platelets are also localized at the interface between PLA and LLDPE.

The TEM micrographs of PLA/LLDPE/15A based nanocomposites prepared through different methods are shown in Figure 4a–4f. In 15A based nanocomposites unlike the 30B based nanocomposites, the organoclay is localized mainly at the interface while only small tactoids are observable in the PLA phase. The main reason behind this might be the lesser affinity of 15A with PLA phase. Significant difference is not observed between the samples which were prepared through different methods. In both the mixing methods, the nanoclays are localized mainly at the interface. The clay is well distributed at the interface and a few larger tactoids are observable plus some exfoliated single sheets.

Through two steps mixing, one can discern larger amount of tactoids in PLA phase. Since in two step mixing, the 15A particles are added first to LLDPE followed by compounding with the PLA and compatibilizer, these particles are embedded in LLDPE

phase. The migration of nanoclays from the matrix to the dispersed phase takes place more easily than from dispersed droplet to the matrix. However it is quite evident that migration of nanoclays from the matrix to the dispersed phase is not the only possible migration type [25]. It is interesting to underline that in spite of higher affinity between LLDPE and 15A, no localization of this organoclay within LLDPE phase is observed in any sample obtained by different mixing methods. One possible reason for this behavior is the higher viscosity of LLDPE than that of the PLA (as it will be seen later), due to which the diffusion of the PLA chain around and into the nanoclay aggregates can be more easily compared with that of the LLDPE at the initial stage of melt mixing.

On the other hand, most of the nanoclays have a tendency to be further dispersed on the phase interface driven by the mixing flow because the carboxylic group of modifier on surface of the nanoclays has good affinity to both the PLA and the compatibilizer phases. As it can be seen from Figure 4b the nanoclays are distributed in the phase



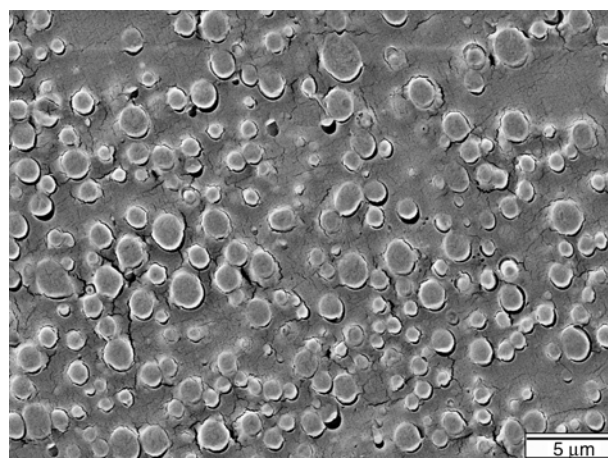
**Figure 4.** TEM Micrographs of PLA/LLDPE/15A based nanocomposites (a–c) prepared through one step mixing at different magnifications, (d–f) prepared through two steps mixing at different magnifications (all samples contain 4.5 wt% 15A)

interface layer and arranged more or less ordered along the surface of the LLDPE droplets, acting as the emulsifier [26] to enwrap the discrete domains. This interfacial localization of the nanoclays could prevent the coalescence of the LLDPE domains effectively which helps compatibilization during melt mixing. Therefore, both the thermodynamically and kinetically driven compatibility is possible to occur [27, 28]. Such interface localization of the nanoclays, as a result, improves the interfacial adhesion of the PLA/LLDPE blend matrix evidently as confirmed by the SEM micrographs presented Figures 6 and 7.

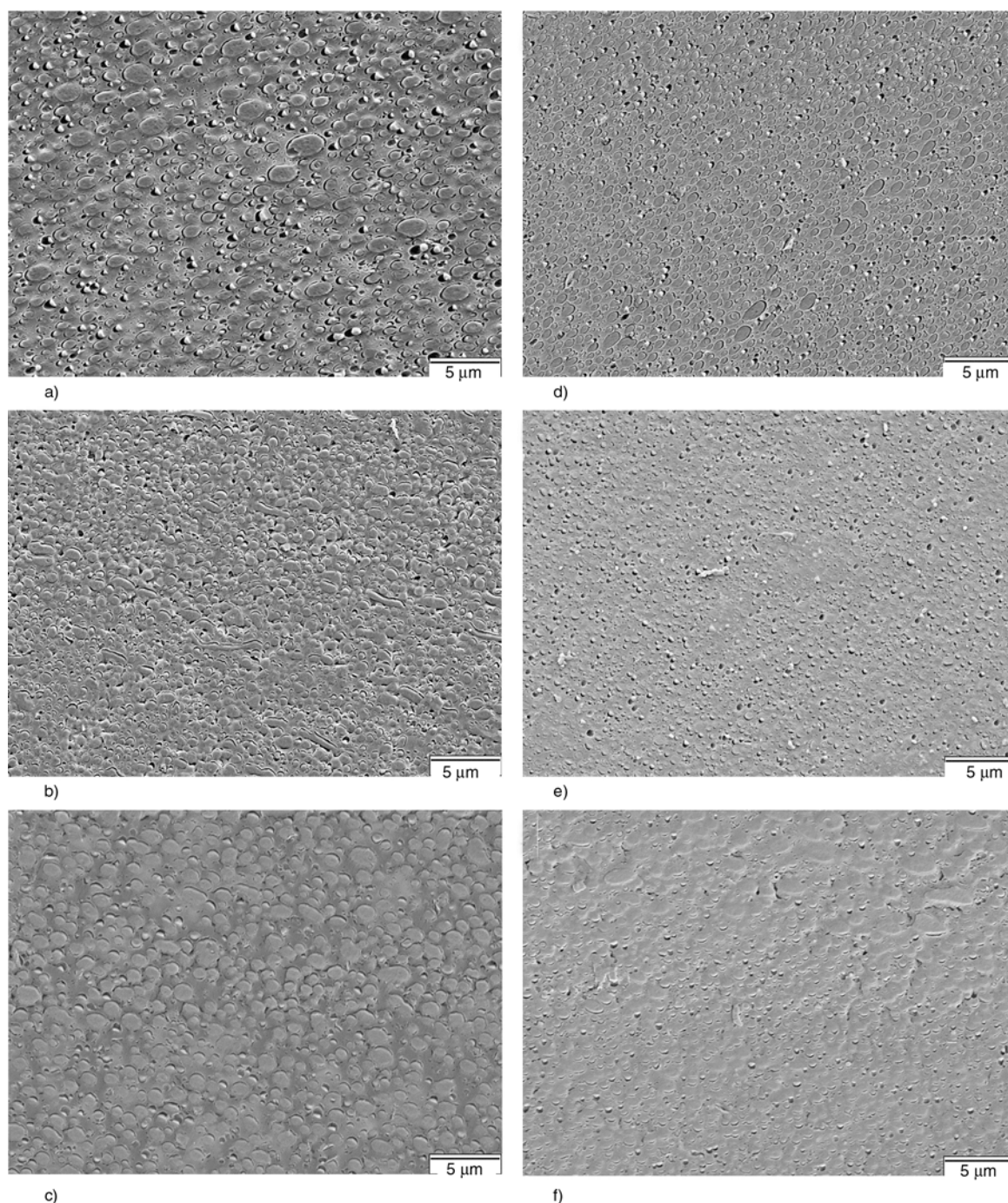
Comparing the dispersion of these nanocomposites through different mixing methods one can conclude that mixing of the components in two steps has no influence or literally has only a very marginal effect on the state of dispersion of the nanoclays in all these materials. However the localization of the main part of the nanoclay was different significantly in 30B based nanocomposites prepared through different mixing methods.

### 3.2.2. SEM analysis

SEM micrographs of the cryo-fractured surfaces provide morphological information complementary to the TEM results. The corresponding SEM micrographs of the cryo-fractured surface for the neat PLA/LLDPE, 30B and 15A based nanocomposites through different mixing methods are presented in Figures 5, 6 and 7, respectively. It can be seen from



**Figure 5.** SEM micrographs of compatibilized PLA/LLDPE blend

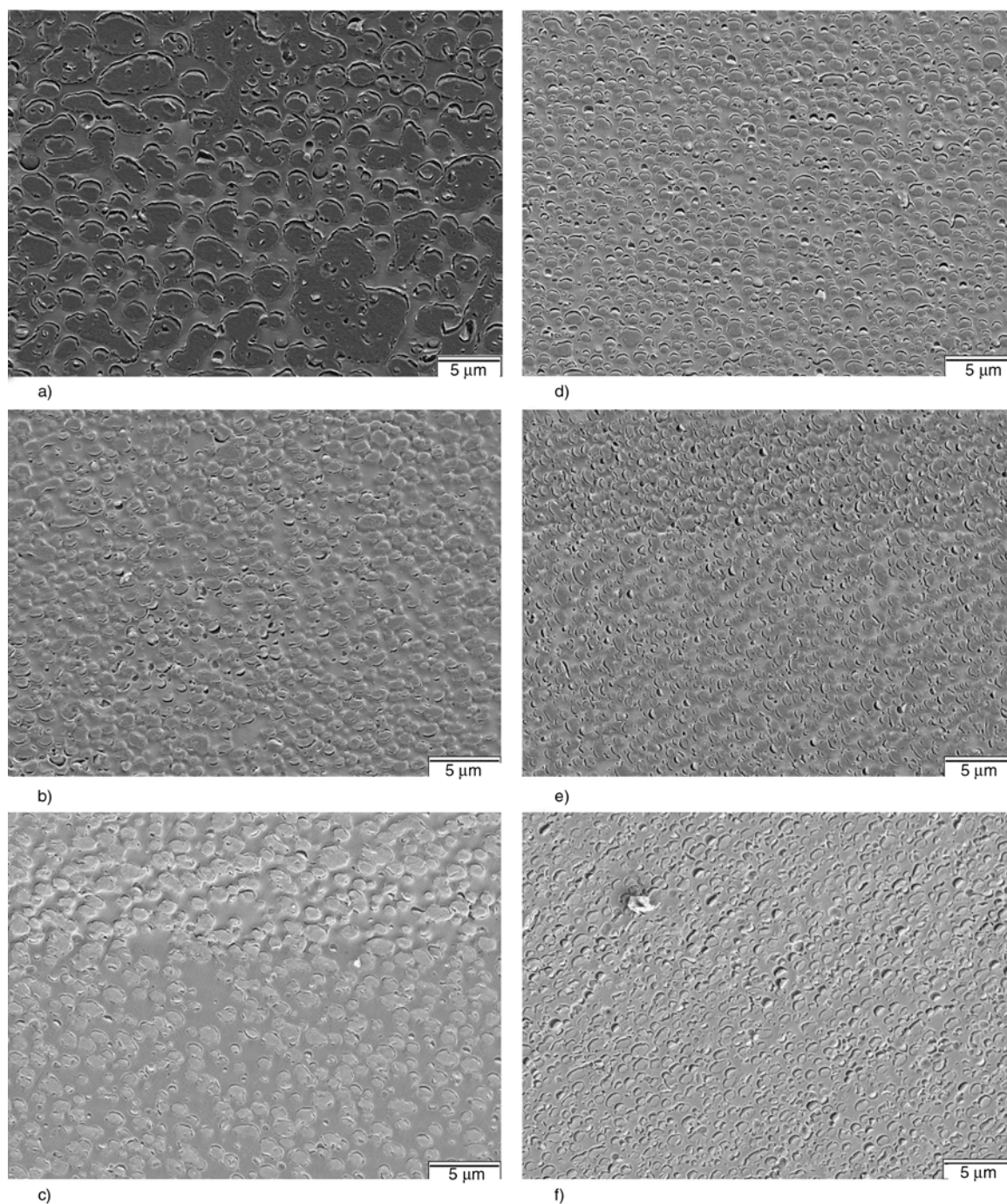


**Figure 6.** SEM micrographs of compatibilized PLA/LLDPE/30B based nanocomposites, through one step mixing: (a) 3 wt% 30B, (b) 4.5 wt% 30B, (c) 6 wt% 30B; through two steps mixing: (d) 3 wt% 30B, (e) 4.5 wt% 30B, (f) 6 wt% 30B

the SEM micrographs that all the samples have typical droplet-in matrix morphologies. The size of dispersed particles in all the samples which prepared for SEM was measured by Scandium software (Olympus Soft Imaging Solutions GmbH). The number of measurements for each series was 60 particles. The number of the particles per  $\text{cm}^2$  was approximately 8 000 000 particles. The data corre-

sponding to the average particle size (D) are presented in Table 2.

A size reduction of the dispersed phases can be seen with addition of 30B nanoclays compared with neat PLA/LLDPE. The lower droplet sizes of the dispersed phase for nanocomposites could be due to reduction of the interfacial energy and inhibition of coalescence by the presence of a solid barrier around



**Figure 7.** SEM micrographs of compatibilized PLA/LLDPE/15A based nanocomposites, through one step mixing: (a) 3 wt% 15A, (b) 4.5 wt% 15A, (c) 6 wt% 15A; through two steps mixing: (d) 3 wt% 15A, (e) 4.5 wt% 15A, (f) 6 wt% 15A.

the dispersed phase or some partly localization of nanoclays at the interface as evidenced by TEM results (Figure 3). On the other hand, localization of organoclay at the interface of the blend is one of the equisetive mechanisms of size reduction of the dispersed phase. Unlike the 30B, the incorporation of 15A to PLA/LLDPE system leads to increase of the dispersed phase from 0.87 to 2.3  $\mu\text{m}$ . As it can be seen from Table 2 no reduction of dispersed phase

are observable in 15A based nanocomposites at different mixing methods. This could be explained by the localization of the main part of the 30B in the PLA phase which enhance the PLA viscosity (the addition of 30B increases the viscosity of the blend which will be seen later and also better exfoliation of this type of nanoclay in the matrix comparing to the 15A as evidenced by the XRD and TEM results.

**Table 2.** Average particle size of compatibilized PLA/LLDPE blend and its nanocomposites

Samples	Average particle size [ $\mu\text{m}$ ]			
	One step mixing	Standard deviation	Two steps mixing	Standard deviation
PLA/LLDPE	0.87	0.13	–	–
3% 30B	0.73	0.32	0.59	0.18
4.5% 30B	0.65	0.28	0.56	0.13
6% 30B	0.95	0.26	0.67	0.26
3% 15A	2.30	0.74	0.94	0.33
4.5% 15A	1.15	0.37	0.92	0.30
6% 15A	1.06	0.35	0.76	0.26

Furthermore the difference in the dispersed phase particle size for the 30B and 15A based nanocomposites is presumably due to the superior ability of the nanoclay modifiers with the PLA to suppress the coalescence. Due to the better affinity of 30B modifier with PLA, one should note that at higher content of nanoclays (6 wt%), the reduction of dispersed particle size is not significant (Figures 6c, 6d and 7c, 7f). It can be attributed to the agglomeration of nanoclays at higher loading of nanoclays. In the case of the samples prepared through two steps mixing, a uniform dispersion of the LLDPE droplets with finer sizes can be observed. This could be the result of the longer mixing time during two steps extrusion or localization of the main part of the nanoclays in the PLA phase which can affect the viscosity of the matrix.

### 3.3. Rheological behavior

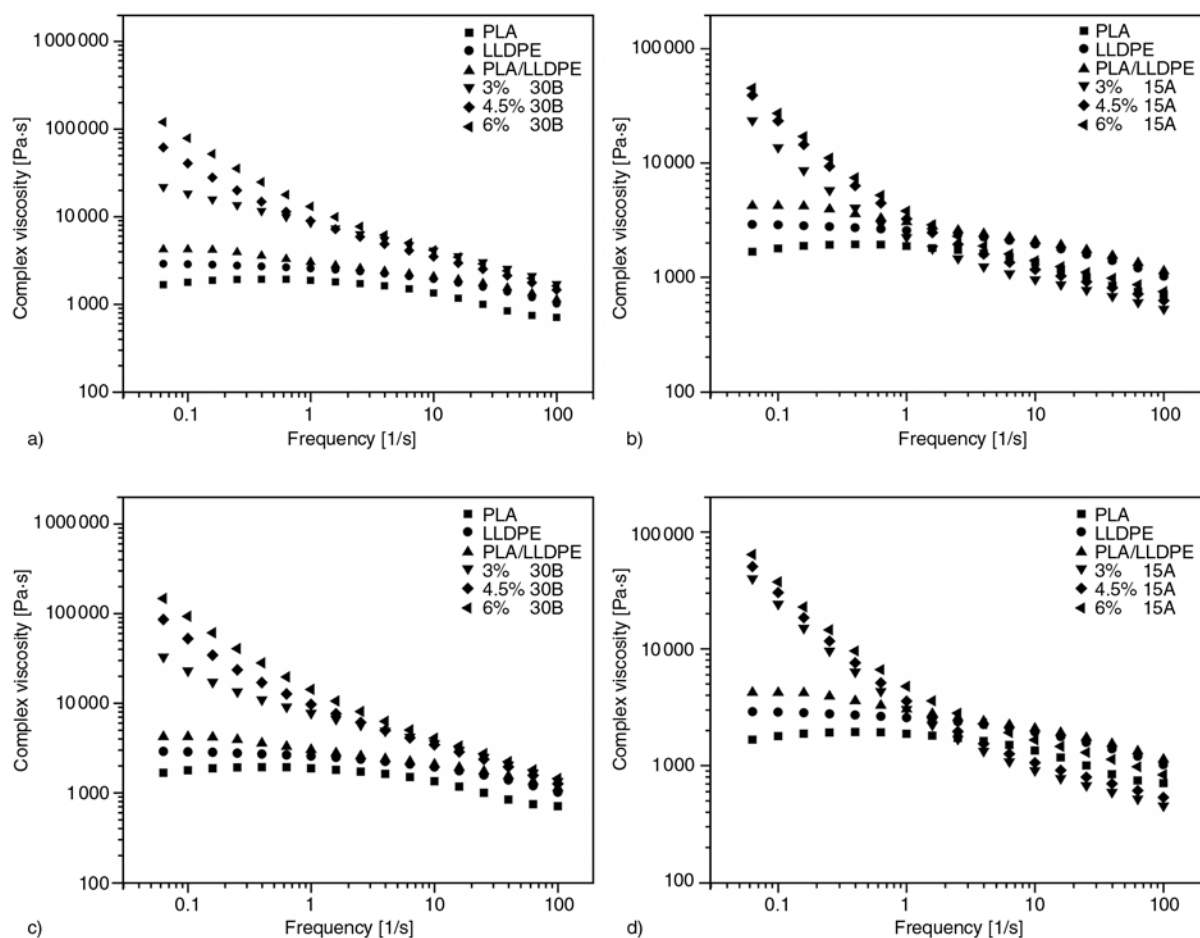
For optimization of the polymer processing conditions the knowledge of melt rheological behavior is necessary. As the rheological behavior of multi phase system is intimately related to its morphology, in this section we investigate how these morphological differences influence the rheological behavior of this multiphase system. The complex viscosity ( $\eta^*$ ), storage modulus ( $G'$ ) and loss modulus ( $G''$ ) as a function of frequency of blend components and compatibilized PLA/LLDPE nanocomposites at 180°C are presented in Figures 8, 9 and 10. Regarding the rheological behavior, the complex viscosity of the neat blend without clay is higher than those of the individual components. Considering the viscosities of blend components it is seen that the reactive PLA/LLDPE/Elvaloy PTW blend has higher viscosity than the values predicted by a linear mixing rule. This can be due to the effect of reactive compatibilization.

As it can be seen from Figure 8 the neat blend as well as the blend components shows shears thinning behavior at higher frequency. However, a short Newtonian plateau can be identified in viscosity curves of PLA/LLDPE and blend components at low frequency. The rheological behavior of the blends with nanoclay is quite different. On comparing the melt viscosity of compatibilized PLA/LLDPE blend and its nanocomposites it is found that the span of the Newtonian plateau region shrinks (especially at low frequencies) with the addition of nanoclays. The melt behaviors of the PLA/LLDPE nanocomposite indicate their typical non-Newtonian viscosity behavior. The PLA/LLDPE nanocomposites exhibits shear thinning behavior in the complex viscosity curve.

It is well known that the presence of fillers in polymer melts not only increases their shear viscosity but also affects their shear rate dependency [30]. By fitting power law model (which is mostly used for many kinds of nanocomposites) to the viscosity curve of PLA/LLDPE nanocomposites, the values of  $n$  for PLA/LLDPE nanocomposites were calculated and listed in Table 3.

Figures 8a and 8b show that by increasing the nanoclay contents the complex viscosity of PLA/LLDPE blend increases monotonically. However, this increase at higher content of nanoclays (at least 4.5 wt%) is less pronounced. This change in behavior towards a solid like behavior can be attributed to the morphological changes i.e. refinement of the dispersed phase by addition of nanoclays to this system [29]. Referring to the SEM micrographs due to agglomeration of nanoclay particles at higher loading, the significant refinement of the dispersed phase is not observable (Figures 6c and 7c).

Contrary to 30B, different loadings of 15A do not show significant effect on viscosity behavior. In other words the viscosity behavior of PLA/LLDPE/15A based nanocomposite is almost the same especially at higher frequency. It seems that for this system at least 3 wt% 15A is the optimum clay loading for solid like behavior. However, from Figures 8 and Table 3 one can notice that the extent of shear thinning behavior of PLA/LLDPE/15A based nanocomposites appears to be slightly higher than that for 30B based nanocomposites. Moreover, the complex viscosity of the PLA/LLDPE/15A based nanocomposites is lower than 30B based nanocomposites.



**Figure 8.** Complex viscosity as a function of frequency for PLA/LLDPE blend nanocomposites prepared via: (a) and (b) one step mixing, (c) and (d) two steps mixing

posites and also less than that of neat PLA/LLDPE blend when a shear rate of 1 [1/s] was reached.

The observed lower viscosity of 15A nanocomposites as compared to 15B based samples in the first look might seem to be related to the matrix degradation, however it has been reported that both 15A and 30B have limited neutralizing capacity of the acids produced during hydrolytic degradation and hence, no huge differences were observed between the two fillers on matrix hydrolytic degradation [38]. Therefore the observed lower viscosity of 15A based nanocomposites as compared to 30B based

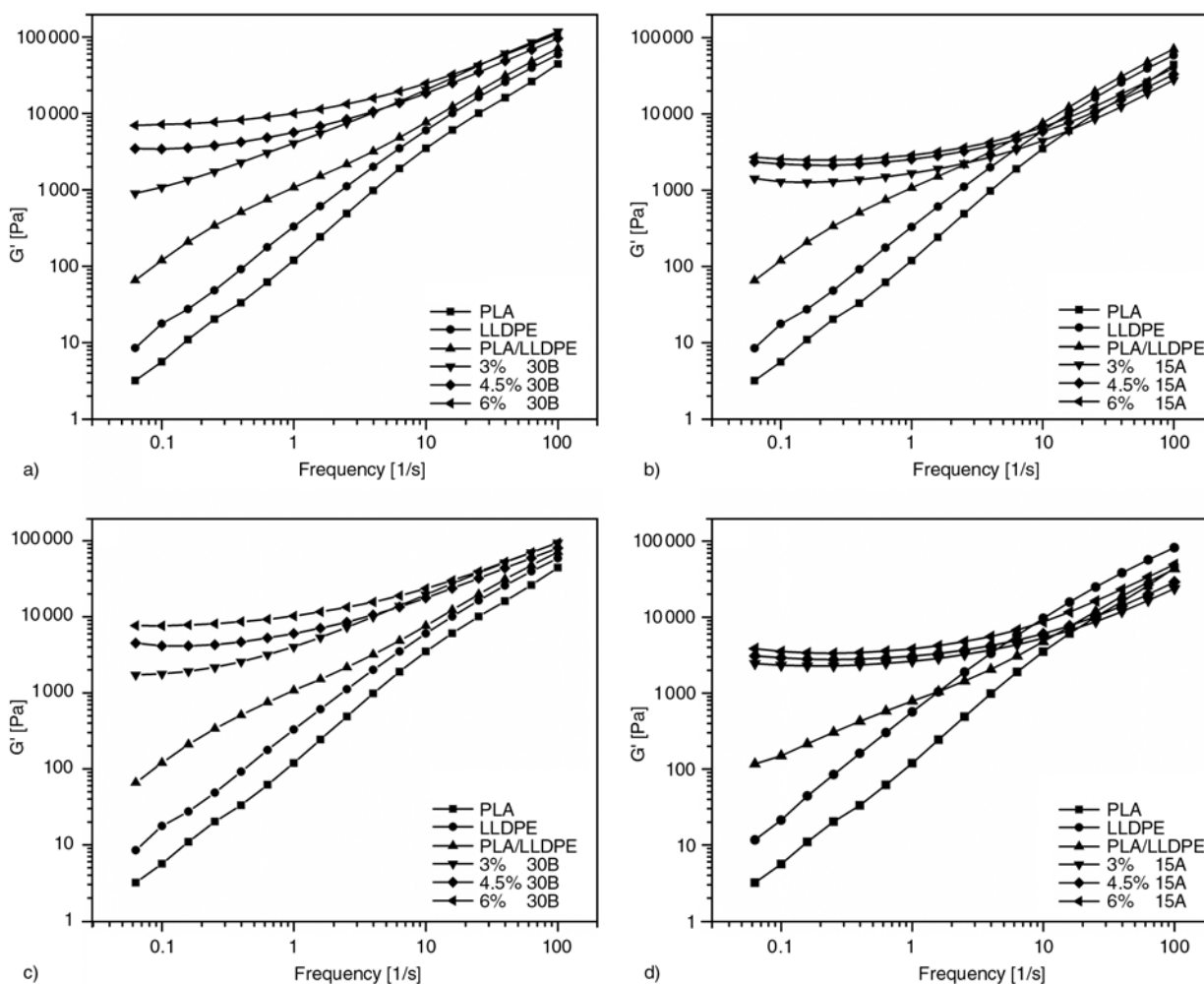
samples may be due to the higher level of filler-polymer interaction in the 30B based system.

Figures 8c and 8d show the viscosity behavior of nanocomposites which were prepared through two steps mixing. As it is seen nanocomposites prepared through two steps mixing show similar trend in viscosity behavior comparing to the nanocomposites with the equivalent loadings of nanoclays prepared via one step mixing method. However, the nanocomposites prepared via two steps mixing show higher viscosity. This can be due to the main localization of 30B and some partly localization of 15A in the PLA matrix depicted in TEM images (Figures 3 and 4). Figure 9a depicts an increase of storage modulus with increase in frequency for neat PLA/LLDPE blend comparing with blend components. Furthermore the storage modulus of nanocomposites is even much higher than the neat blend and the development of a plateau in storage modulus is observable in case of nanocomposites. As it can be seen from Figure 9a, with increasing the 30B content, the storage modulus of nanocomposites enhances.

**Table 3.** Power law exponent of PLA/LLDPE nanocomposites

Samples	Power low exponent (n)	
	One step mixing	Two steps mixing
PLA/LLDPE/3% 30B	0.67	0.61
PLA/LLDPE/ 4.5% 30B	0.53	0.47
PLA/LLDPE/ 6% 30B	0.44	0.40
PLA/LLDPE/ 3% 15A	0.53	0.41
PLA/LLDPE/ 4.5% 15A	0.47	0.40
PLA/LLDPE/ 6% 15A	0.48	0.45





**Figure 9.** Storage modulus ( $G'$ ) as a function of frequency for PLA/LLDPE blend nanocomposites prepared via: (a) and (b) one step mixing, (c) and (d) two steps mixing

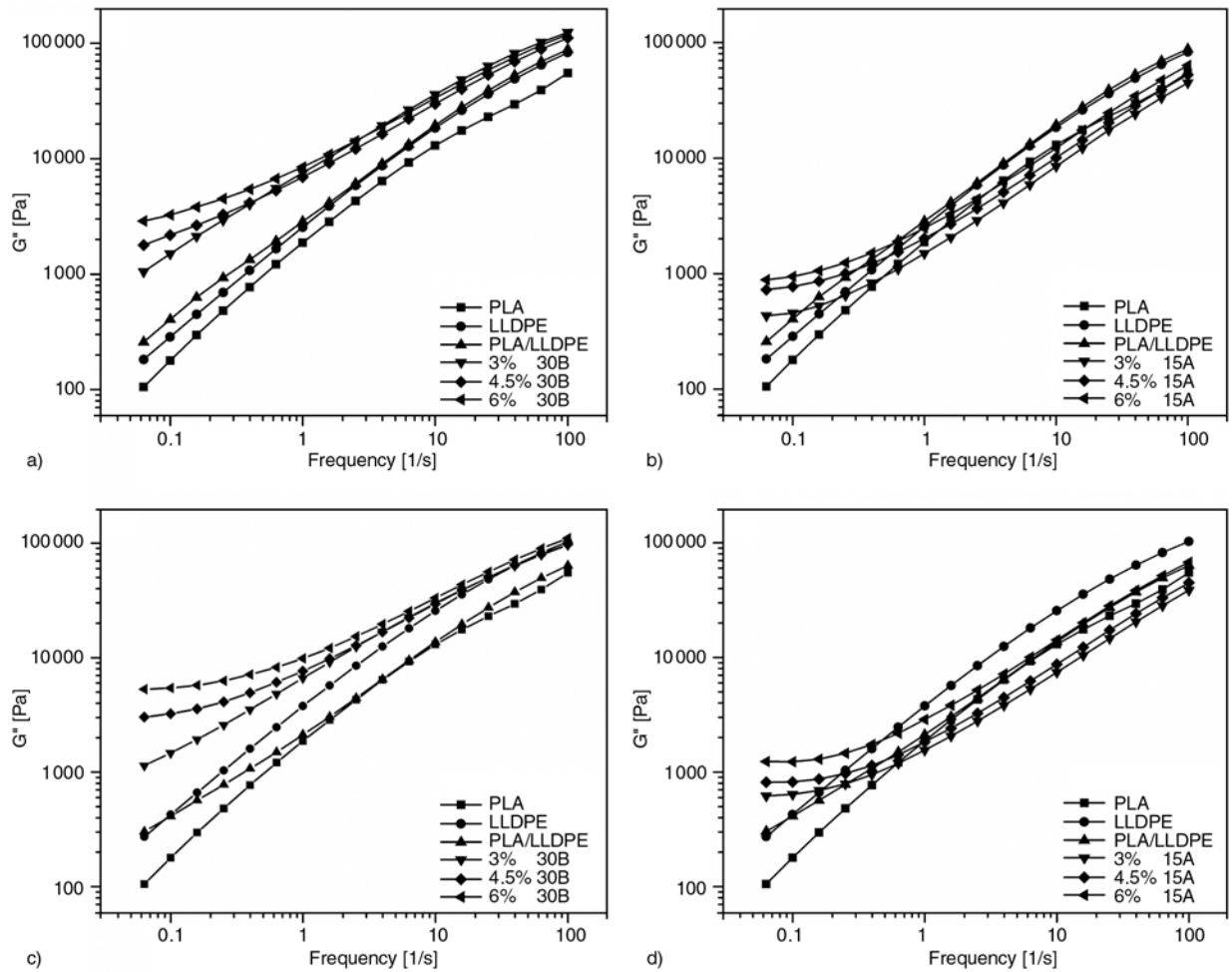
At 4.5 wt% 30B loadings the frequency dependence nearly disappears at lower frequency. This non-terminal behavior is due to formation of gel structure which highly restrains the long-range relaxation of the matrix PLA chains. However, the enhancement of elasticity of 6 wt% 30B comparing to 4.5 wt% 30B is not remarkable. This can be attributed to agglomeration of 30B nanoclays at higher loadings of nanoclay. At higher content of 30B, although the clay is aggregated, the elastic properties enhance slightly.

Unlike the 30B based nanocomposites, in 15A based nanocomposites the remarkably enhanced elasticity is not found by increasing the clay content. This may be due to the less interaction of the PLA/15A and internal structure of the PLA/LLDPE/ 15A based nanocomposites. As evidenced by the SEM results the particle size of dispersed phase in 15A based nanocomposites is higher than that of 30B based nanocomposites. Additionally, the smaller the

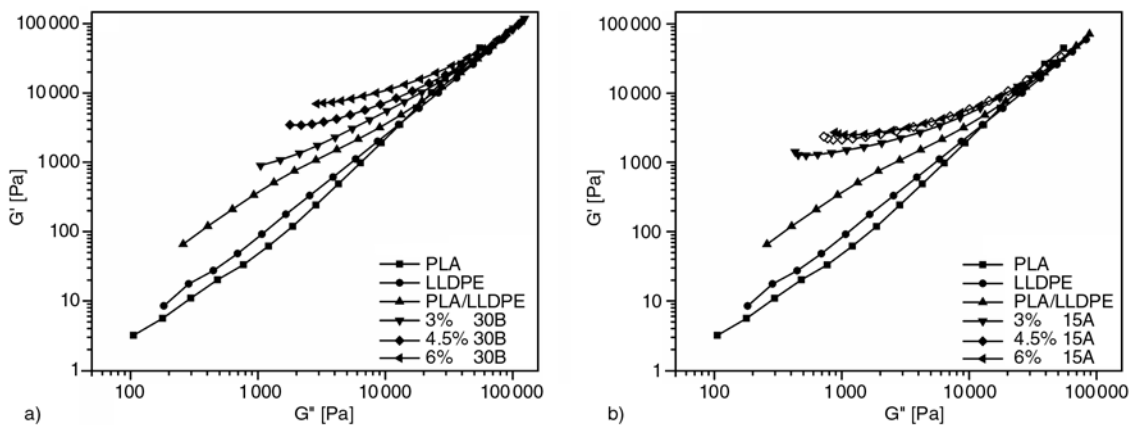
size of particles (thus the larger surface area of particles) in a nanocomposite, the lower the concentration of the filler will be that may give rise to elasticity and shear thinning behavior [31].

The loss modulus of blend nanocomposites show similar trend at different nanoclays content (Figure 10). However, due to elasticity the differences in storage modulus are more remarkable. From Figure 9 and 10, one can notice that the storage modulus ( $G'$ ) is higher than loss modulus ( $G''$ ) at high frequency region for both the blend and nanocomposites. In the case of samples prepared via the two steps mixing (Figures 9c and 9d and 10c and 10d), all the nanocomposites (30B and 15A based nanocomposites) show higher storage and loss modulus compared to the samples prepared via the one step process.

Furthermore the Cole-Cole plots were used in order to examine the structural changes in the nanocomposites at constant temperature. Figure 11 shows



**Figure 10.** Loss modulus ( $G''$ ) as a function of frequency for PLA/LLDPE blend nanocomposites prepared via: (a) and (b) one step mixing, (c) and (d) two steps mixing



**Figure 11.** Cole-Cole plots for PLA/LLDPE nanocomposites: (a) 30B based nanocomposites, (b) 15A based nanocomposites prepared via one step mixing

the Cole-Cole plots of PLA/LLDPE blend and nanocomposites prepared by one step mixing process. Neat PLA and LLDPE show characteristic homopolymer-like terminal flow behavior, (terminal zone slope is about 2). The deviation between PLA/LLDPE blend and its nanocomposites shows

structural changes from liquid-like to solid-like with increasing the clay content. This can be attributed to the formation of network structures. The 30B based nanocomposites show such structure at 4.5 wt% of nanoclay. Additionally, as the clay content is increased, a distinctively larger devi-

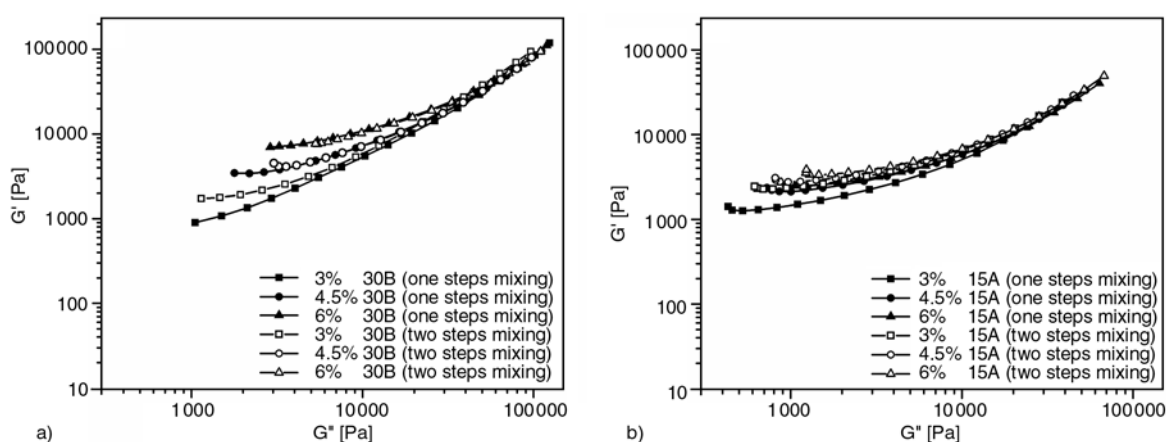
ation is observed as compared to the PLA/LLDPE blend.

Unlike the 15A based nanocomposites, this deviation is much more pronounced at higher content of 30B and also at different contents of 30B. In other words, the 15A based nanocomposites show similar structures at different contents of clay. Furthermore in 15A based nanocomposites the solid like behavior (i.e. the plateau region at low frequency) takes place at 3 wt% 15A loading. Figure 12 shows the Cole-Cole plots for all PLA/LLDPE nanocomposites prepared by different mixing methods. As it can be seen from Figure 12a in 30B based nanocomposites (especially at higher content of 30B) at the equivalent clay content both samples which were prepared via different mixing methods show similar structure. However, through two steps mixing, the development of a plateau in storage modulus at lower loss modulus is observable at lower clay content (3 wt% 30B) as compared to the one step mixing. This indicates the significant effect of two steps mixing on formation of a network structure and solid like behavior at lower nanoclay loading. Unlike the 30B based nanocomposites, the effect of mixing methods on the structure is not significant for 15A based nanocomposites. As it can be seen the deviation between the structures is not remarkable. All the 15A based nanocomposites prepared via different mixing methods with equal clay content show similar structures. These findings further confirm the morphological finding concerning the stronger effect of mixing procedure on properties in the 30B based nanocomposites than in 15A.

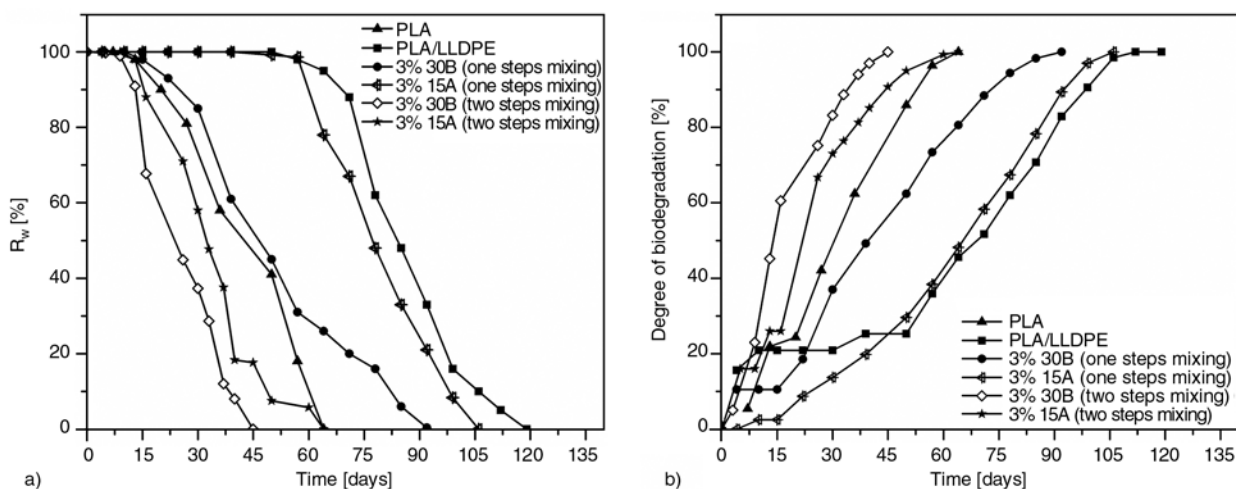
### 3.4. Biodegradability

The degradation of polymeric blends especially under environmental conditions is a very important issue from commercialization point of view. More exciting aspect of this research is the biodegradability of PLA in presence of LLDPE and also enhancement of biodegradability of PLA/LLDPE after nanoclay incorporation. In this work, the biodegradation process of all the samples was studied in a compost environment at temperature well above ambient i.e.  $58 \pm 2^\circ\text{C}$ . This is because the rate of degradation of pure PLA is very slow at the ambient temperature [32, 33]. To study the degradation of the PLA/LLDPE blend and its nanocomposites in compost, a respirometric test was done [34, 35].

The residual weight percentages of the initial test samples with time (weight loss), which reflect the structural changes in the test samples, and the rate of biodegradation with time are presented in Figure 13a and 13b, respectively. As it can be seen from Figure 13a within two weeks, the extent of weight loss is almost the same for both pure PLA and PLA/LLDPE blend. However, after two weeks, a change occurs in the weight loss of PLA. The rate of the weight loss increase after one month, and within two months, it is completely degraded in the compost. This confirms the two steps degradation process of PLA. During the initial phases of degradation, the high molecular PLA chains hydrolyze to lower molecular weight oligomers. In the second step, the microorganisms in the environment continue the degradation process by converting these lower molecular weight components to carbon diox-



**Figure 12.** Cole-Cole plots for PLA/LLDPE nanocomposites: (a) 30B based nanocomposites, (b) 15A based nanocomposites prepared via different mixing methods



**Figure 13.** Time-dependence of: (a) weight residual percentage ( $R_w$ ); (b) degree of biodegradation ( $\text{CO}_2$  evolution) of pure PLA, PLA/LLDPE and its nanocomposites

ide, water, and humus. Unlike weight loss or fragmentation which reflects the structural changes in the test sample,  $\text{CO}_2$  evolution provides an indicator of the ultimate biodegradability (Figure 13b). Figure 13b shows the rate of carbon dioxide releasing which is the result of the degradation of lower molecular weight components to carbon dioxide and water. As it can be seen from Figure 13b, after two weeks the rate of biodegradability (as a released  $\text{CO}_2$ ) of PLA has increased. A compost pile is a great source of microbial activity, because it has a high moisture content and temperature. This in turn provides a tremendous amount and variety of organisms able to attack and digest compostable materials. The compost microorganisms continue the degradation process by converting these lower molecular weight components to carbon dioxide and water. The amount of released  $\text{CO}_2$  and the rate of  $\text{CO}_2$  evolution are in agreement with the weight loss results. The difference between the starting point of the weight loss and the beginning point of the  $\text{CO}_2$  evolution can be due to experimental error. Similar result has been reported by other researchers [36]. Furthermore, the PLA/LLDPE blend shows a longer induction time and a lower rate of degradation in comparison with the neat PLA. This can be attributed to the too slow rate of degradation and non-degradability of LLDPE phase dispersed throughout the PLA matrix under compost condition. The results showed that in spite of addition of 25 wt% LLDPE to the PLA, this blend system can degrade completely under compost condition after 4 months. Interestingly, the biodegradability of the neat PLA/LLDPE blend is significantly enhanced after

nanoclay incorporation. This indicates the catalytic role of the clay interfaces in the hydrolytic degradation of PLA chains.

In other words, the presence of terminal hydroxylated edge groups of the silicate layers may be one of the factors responsible for this behavior. In PLA/LLDPE nanocomposites, the hydroxyl groups of stacked and intercalated silicate layers which are dispersed in the PLA matrix can initiate heterogeneous hydrolysis of the PLA matrix after absorbing water from the compost. This process takes some time to start. For this reason, according to Figure 13a, the weight loss and degree of hydrolysis of PLA/LLDPE and its nanocomposites is almost similar up to 15 days. However, after 15 days there is a sharp weight loss in the case of PLA/LLDPE/30B nanocomposites prepared through the one step mixing process. This means that those 15 days are critical time to start heterogeneous hydrolysis, and due to this type of hydrolysis the matrix degrades into very small fragments and is eliminated with the compost. Several authors [37–39] supported this conclusion of the catalytic effect of nanoclays on the biodegradation or hydrolytic degradation of PLA. As it is seen from Figure 13, this critical time increases to 60 days in the case of 15A based nanocomposites which were prepared through the one step mixing. Comparison of the effects of 30B and 15A on the rate of biodegradation having somewhat different hydrophilicity, different kinds of modifier and slight filler dispersion differences based on WAXS data (Figure 2) and TEM micrographs (Figures 3a–3c and 4a–4c), can explain the slightly lower rate constants observed for the 15A based nanocomposites.

One can notice that at the same time the degree of biodegradation of 30B based nanocomposites is nearly two times higher than that of 15A based nanocomposites.

Another possible factor that controls the biodegradability of PLA/LLDPE blend is the degree of crystallinity. The degradation of amorphous phase is easier than the crystalline phase. The effect of nanoclays on crystallization behavior of PLA/LLDPE blend has been studied systematically in our previous work and the results showed that 15A nanoclay is more effective than 30B nanoclay in improving the crystallinity of PLA/LLDPE blend. For this reason the effect of 30B nanoclay in enhancement of biodegradability of PLA/LLDPE blend is much more remarkable than 15A nanoclay.

In the case of nanocomposites prepared through two steps mixing, due to localization of the main part of the nanoclays in PLA matrix, the enhancement of biodegradability is significant. As it can be seen from Figure 13 the 30B based PLA/LLDPE nanocomposites degrade completely after 45 days. Interestingly the rate of biodegradability of PLA/LLDPE nanocomposites prepared through two steps mixing is higher than pure PLA. It is to be noted that the higher rate of biodegradability through the two-step mixing process may also be due to reduction of PLA molecular weight as a result of the two-step extrusion process in which PLA is subjected to more intensive shearing at longer times. However, since the main mechanism of PLA degradation is hydrolysis, which is highly under influence of clay presence, the enhanced rate of biodegradation can be mainly attributed to the clay positioning influenced by the two-step mixing process. Unlike the one step mixing, the difference between degradability rate of 15A and 30 B is not too significant. This can be attributed to the different localization of nanoclays induced by the different mixing methods. These data clearly indicate that mixing methods and localization of nanoclays have a significant effect on the rate of biodegradation.

#### 4. Conclusions

Two different PLA/LLDPE nanocomposite systems based on two different kinds of nanoclays were prepared through different mixing methods. Comparison of the effects of 30B and 15A on the morphology of PLA/LLDPE, based on different kinds of modifier and affinity, can explain the lower level of

exfoliation and dispersion observed for the 15A based nanocomposites as compared to 30B based nanocomposites. In all the nanocomposites some partly exfoliated clay plates are located at the interface between PLA and LLDPE. Such interfacial localization of the nanoclays, as a result, improves the interfacial adhesion of the PLA/LLDPE blend matrix distinctly and refines the dispersed phase. Unlike 30B, the influence of 15A on the reduction of the dispersed phase is not remarkable. This could be explained by the mainly localization of 30B in the PLA phase which enhances the viscosity of PLA and also better exfoliation of this nanoclay in the matrix as compared to the 15A. Through two steps mixing in 30B based nanocomposites, nanoclays localized mainly in PLA phase. In spite of having higher affinity between LLDPE and 15A, no localization of this organoclay within LLDPE phase is observable in 15A based nanocomposites prepared via different mixing methods. Only some portions of 15A migrate to the PLA phase. From the rheological measurement, it is found that the complex viscosity and storage and loss modulus were related to the dispersion state and localization of nanoclays at the nanocomposites. Our results suggest that for 30B based nanocomposites 4.5 wt% 30B is the optimum loading of nanoclay. However, this amount shifts to lower content (3 wt%) nanoclay in 15A based nanocomposites. Furthermore the improvement of the rheological properties with increasing the clay contents in 30B based nanocomposites was remarkable compared to the 15A based nanocomposites. In the case of samples which were prepared via two steps mixing, all nanocomposites (30B and 15A based nanocomposites) show higher rheological properties compared to the samples prepared through one step mixing. This can be due to the localization of nanoclays in the PLA matrix. Biodegradability results showed that the hydroxyl groups of stacked and intercalated silicate layers which are dispersed in the PLA matrix can initiate heterogeneous hydrolysis of the PLA matrix after absorbing water from the compost. Comparison of the effects of 30B and 15A on the rate of biodegradation, based on somewhat different hydrophilicity, different kinds of modifier and slight filler dispersion differences, can explain the slightly lower rate constants observed for the 15A based nanocomposites. This investigation revealed that the mixing methods and localization of nanoclays has a signifi-

cant effect on the morphology and rate of biodegradation. The main target of this study is to achieve a good morphology which leads to a good properties, processability and PLA degradability at moderate cost.

## References

- [1] Okamoto K., Toshima K., Matsumura S.: Degradation of poly(lactic acid) into repolymerizable oligomer using montmorillonite K10 for chemical recycling. *Macromolecular Bioscience*, **5**, 813–820 (2005). DOI: [10.1002/mabi.200500086](https://doi.org/10.1002/mabi.200500086)
- [2] Chang J-H., An Y. U., Sur G. S.: Poly(lactic acid) nanocomposites with various organoclays. I. Thermo-mechanical properties, morphology, and gas permeability. *Journal of Polymer Science Part B: Polymer Physics*, **41**, 94–103 (2003). DOI: [10.1002/polb.10349](https://doi.org/10.1002/polb.10349)
- [3] Ray S. S., Okamoto M.: Polymer/layered silicate nanocomposites: A review from preparation to processing. *Progress in Polymer Science*, **28**, 1539–1641 (2003). DOI: [10.1016/j.progpolymsci.2003.08.002](https://doi.org/10.1016/j.progpolymsci.2003.08.002)
- [4] Oyama H. T.: Super-tough poly(lactic acid) materials: Reactive blending with ethylene copolymer. *Polymer*, **50**, 747–751 (2009). DOI: [10.1016/j.polymer.2008.12.025](https://doi.org/10.1016/j.polymer.2008.12.025)
- [5] Pavlidou S., Papaspyrides C. D.: A review on polymer-layered silicate nanocomposites. *Progress in Polymer Science*, **33**, 1119–1198 (2008). DOI: [10.1016/j.progpolymsci.2008.07.008](https://doi.org/10.1016/j.progpolymsci.2008.07.008)
- [6] Ray S. S., Okamoto M.: Biodegradable polylactide and its nanocomposites: Opening a new dimension for plastics and composites. *Macromolecular Rapid Communications*, **24**, 815–840 (2003). DOI: [10.1002/marc.200300008](https://doi.org/10.1002/marc.200300008)
- [7] Reeve M. S., MaCarthy S. P., Downey M. J., Gross R. A.: Polylactide stereochemistry: Effect on enzymatic degradability. *Macromolecules*, **27**, 825–831 (1994). DOI: [10.1021/ma00081a030](https://doi.org/10.1021/ma00081a030)
- [8] Iwata T., Doi Y.: Morphology and enzymatic degradation of poly(L-lactic acid) single crystals. *Macromolecules*, **31**, 2461–2467 (1998). DOI: [10.1021/ma980008h](https://doi.org/10.1021/ma980008h)
- [9] Hakkarainen M., Karlsson S., Albertsson A. C.: Rapid (bio)degradation of polylactide by mixed culture of compost microorganisms – Low molecular weight products and matrix changes. *Polymer*, **41**, 2331–2338 (2000). DOI: [10.1016/S0032-3861\(99\)00393-6](https://doi.org/10.1016/S0032-3861(99)00393-6)
- [10] Singh G., Kaur N., Bhuida H., Bajpai P. K., Mandal U. K.: Degradation behaviors of linear low-density polyethylene and poly(L-lactic acid) blends. *Journal of Applied Polymer Science*, **124**, 1993–1998 (2012). DOI: [10.1002/app.35216](https://doi.org/10.1002/app.35216)
- [11] Singh G., Bhunia H., Rajor A., Choudhary V.: Thermal properties and degradation characteristics of polylactide, linear low density polyethylene, and their blends. *Polymer Bulletin*, **66**, 939–953 (2011). DOI: [10.1007/s00289-010-0367-x](https://doi.org/10.1007/s00289-010-0367-x)
- [12] Raghavan D., Emekalam A.: Characterization of starch/polyethylene and starch/polyethylene/poly(lactic acid) composites. *Polymer Degradation and Stability*, **72**, 509–517 (2001). DOI: [10.1016/S0141-3910\(01\)00054-4](https://doi.org/10.1016/S0141-3910(01)00054-4)
- [13] Anderson K. S., Lim S. H., Hillmyer M. A.: Toughening of polylactide by melt blending with linear low-density polyethylene. *Journal of Applied Polymer Science*, **89**, 3757–3768 (2003). DOI: [10.1002/app.12462](https://doi.org/10.1002/app.12462)
- [14] Kim Y. F., Choi C. N., Kim Y. D., Lee K. Y., Lee M. S.: Compatibilization of immiscible poly(L-lactide) and low density polyethylene blends. *Fibers and Polymers*, **5**, 270–274 (2004). DOI: [10.1007/BF02875524](https://doi.org/10.1007/BF02875524)
- [15] Wang Y., Hillmyer M. A.: Polyethylene-poly(L-lactide) diblock copolymers: Synthesis and compatibilization of poly(L-lactide)/polyethylene blends. *Journal of Polymer Science Part A: Polymer Chemistry*, **39**, 2755–2766 (2001). DOI: [10.1002/pola.1254](https://doi.org/10.1002/pola.1254)
- [16] Rezgui F., G'Sell C., Dahoun A., Hiver J. M., Sadoun T.: Plastic deformation of low-density polyethylene reinforced with biodegradable polylactide, Part 1: Microstructural analysis and tensile behavior at constant true strain-rate. *Polymer Engineering and Science*, **5**, 117–125 (2011). DOI: [10.1002/pen.21797](https://doi.org/10.1002/pen.21797)
- [17] Rezgui F., G'Sell C., Dahoun A., Hiver J. M., Sadoun T.: Plastic deformation of low-density polyethylene reinforced with biodegradable polylactide, Part 2: Creep characterization and modeling. *Polymer Engineering and Science*, **5**, 126–132 (2011). DOI: [10.1002/pen.21796](https://doi.org/10.1002/pen.21796)
- [18] Nuñez K., Rosales C., Perera R., Villarreal N., Pastor J. M.: Poly(lactic acid)/low-density polyethylene blends and its nanocomposites based on sepiolite. *Polymer Engineering Science*, **52**, 988–1004 (2012). DOI: [10.1002/pen.22168](https://doi.org/10.1002/pen.22168)
- [19] Fenouillot F., Cassagnau P., Majesté J-C.: Uneven distribution of nanoparticles in immiscible fluids: Morphology development in polymer blends. *Polymer*, **50**, 1333–1350 (2009). DOI: [10.1016/j.polymer.2008.12.029](https://doi.org/10.1016/j.polymer.2008.12.029)
- [20] Elias L., Fenouillot F., Majesté J. C., Cassagnau P.: Morphology and rheology of immiscible polymer blends filled with silica nanoparticles. *Polymer*, **48**, 6029–6040 (2007). DOI: [10.1016/j.polymer.2007.07.061](https://doi.org/10.1016/j.polymer.2007.07.061)

- [21] Gubbels F., Blacher S., Vanlathem E., Jerome R., Deltour R., Brouers F., Teyssie Ph.: Design of electrical composites: Determining the role of the morphology on the electrical properties of carbon black filled polymer blends. *Macromolecules*, **28**, 1559–1566 (1995). DOI: [10.1021/ma00109a030](https://doi.org/10.1021/ma00109a030)
- [22] Gubbels F., Jerome R., Vanlathem E., Deltour R., Blacher S., Brouers F.: Kinetic and thermodynamic control of the selective localization of carbon black at the interface of immiscible polymer blends. *Chemistry of Materials*, **10**, 1227–1235 (1998). DOI: [10.1021/cm970594d](https://doi.org/10.1021/cm970594d)
- [23] Gubbels F., Jerome R., Teyssie P., Vanlathem E., Deltour R., Calderone A., Parente V., Bredas J. L.: Selective localization of carbon black in immiscible polymer blends: A useful tool to design electrical conductive composites. *Macromolecules*, **27**, 1972–1974 (1994). DOI: [10.1021/ma00085a049](https://doi.org/10.1021/ma00085a049)
- [24] Zaikin A. E., Zharinova E. A., Bikmullin R. S.: Specifics of localization of carbon black at the interface between polymeric phases. *Polymer Science Series A*, **49**, 328–336 (2007). DOI: [10.1134/S0965545X07030145](https://doi.org/10.1134/S0965545X07030145)
- [25] Elias L., Fenouillot F., Majesté J-C., Martin G., Casagnau P.: Migration of nanosilica particles in polymer blends. *Journal of Polymer Science Part B: Polymer Physics*, **46**, 1976–1983 (2008). DOI: [10.1002/polb.21534](https://doi.org/10.1002/polb.21534)
- [26] Wu D., Zhang Y., Zhang M., Yu W.: Selective localization of multiwalled carbon nanotubes in poly( $\epsilon$ -caprolactone)/polylactide blend. *Biomacromolecules*, **10**, 417–424 (2009). DOI: [10.1021/bm801183f](https://doi.org/10.1021/bm801183f)
- [27] Li Y., Shimizu H.: Novel morphologies of poly(phenylene oxide) (PPO)/polyamide 6 (PA6) blend nanocomposites. *Polymer*, **45**, 7381–7388 (2004). DOI: [10.1016/j.polymer.2004.09.018](https://doi.org/10.1016/j.polymer.2004.09.018)
- [28] Ray S. S., Bousmina M.: Effect of organic modification on the compatibilization efficiency of clay in an immiscible polymer blend. *Macromolecular Rapid Communications*, **26**, 1639–1646 (2005). DOI: [10.1002/marc.200500447](https://doi.org/10.1002/marc.200500447)
- [29] A'shabi L., Jafari S. H., Khonakdar H. A., Baghaei B.: Morphological, rheological and thermal studies in melt processed compatibilized PA6/ABS/clay nanocomposites. *Journal of Polymer Research*, **18**, 197–205 (2011). DOI: [10.1007/s10965-010-9407-3](https://doi.org/10.1007/s10965-010-9407-3)
- [30] Kim H. B., Choi J. S., Lee C. H., Lim S. T., Jhon M. S., Choi H. J.: Polymer blend/organoclay nanocomposite with poly(ethylene oxide) and poly(methyl methacrylate). *European Polymer Journal*, **41**, 679–685 (2005). DOI: [10.1016/j.eurpolymj.2004.10.042](https://doi.org/10.1016/j.eurpolymj.2004.10.042)
- [31] Durmus A., Kasgoz A., Macosko C. W.: Linear low density polyethylene (LLDPE)/clay nanocomposites. Part I: Structural characterization and quantifying clay dispersion by melt rheology. *Polymer*, **48**, 4492–4502 (2007). DOI: [10.1016/j.polymer.2007.05.074](https://doi.org/10.1016/j.polymer.2007.05.074)
- [32] Kale G., Kijchavengkul T., Auras R., Rubino M., Selke S. E., Singh S. P.: Compostability of bioplastic packaging materials: An overview. *Macromolecular Bioscience*, **7**, 255–257 (2007). DOI: [10.1002/mabi.200600168](https://doi.org/10.1002/mabi.200600168)
- [33] Lunt J.: Large-scale production, properties and commercial applications of polylactic acid polymers. *Polymer Degradation and Stability*, **59**, 145–152 (1998). DOI: [10.1016/S0141-3910\(97\)00148-1](https://doi.org/10.1016/S0141-3910(97)00148-1)
- [34] Weir N. A., Buchanan F. J., Orr J. F., Farrar D. F., Dickson G. R.: Degradation of poly-L-lactide. Part 2: Increased temperature accelerated degradation. *Journal of Engineering Medicine*, **218**, 321–330 (2004). DOI: [10.1243/0954411041932809](https://doi.org/10.1243/0954411041932809)
- [35] Ray S. S., Yamada K., Ogami A., Okamoto M., Ueda K.: New polylactide/layered silicate nanocomposite: Nanoscale control over multiple properties. *Macromolecular Rapid Communication*, **23**, 943–947 (2002). DOI: [10.1002/1521-3927\(200211\)23:16<943::AID-MARC943>3.0.CO;2-F](https://doi.org/10.1002/1521-3927(200211)23:16<943::AID-MARC943>3.0.CO;2-F)
- [36] Ray S. S., Yamada K., Okamoto M., Ogami A., Ueda K.: New polylactide/layered silicate nanocomposites. 3. High-performance biodegradable materials. *Chemistry Materials*, **15**, 1456–1465 (2003). DOI: [10.1021/cm020953r](https://doi.org/10.1021/cm020953r)
- [37] Maiti P., Batt C. A., Giannelis E.: Renewable plastics: Synthesis and properties of PHB nanocomposites. *Polymeric Materials Science and Engineering*, **88**, 58–59 (2003).
- [38] He H., Lee L. J.: Poly(lactic-co-glycolic acid) and functional hydrogels for drug delivery applications. *ANTEC Conference Proceedings*, **3**, 3356–3360 (2004).
- [39] Zhou Q., Xanthos M.: Nanoclay and crystallinity effects on the hydrolytic degradation of polylactides. *Polymer Degradation and Stability*, **93**, 1450–1459 (2008). DOI: [10.1016/j.polymdegradstab.2008.05.014](https://doi.org/10.1016/j.polymdegradstab.2008.05.014)

# Sensing strain and damage in polyurethane-MWCNT nano-composite foams using electrical measurements

A. Baltopoulos, N. Athanasopoulos, I. Fotiou, A. Vavouliotis, V. Kostopoulos\*

Applied Mechanics Laboratory, Department of Mechanical Engineering and Aeronautics, University of Patras, GR 265 04, Rio – Patras, Greece

Received 30 May 2012; accepted in revised form 19 August 2012

**Abstract.** This work deals with the damage identification in polymeric foams through the monitoring of the electrical resistance of the system. To assess this idea electrically conductive rigid Poly-Urethane (PUR) foams at various densities were prepared. Multi-Wall Carbon Nanotubes (MWCNT) were dispersed in the host polymer at various concentrations through high shear mixing to provide electrical conductivity to the system. The PUR/MWCNT foams exhibited varying electrical conductivity on a wide range of densities and nano-filler contents. The prepared foams were subject to compression tests. Electrical resistance was recorded online during the tests to monitor the change of the bulk property of the materials. A structural-electrical cross-property relation was exhibited. The distinctive phases of foam compression were successfully identified from the electrical resistance profile recorded during the tests. A characteristic master curve of the change of electrical resistivity with respect to load and damage is proposed and analyzed. It was shown that the found electrical resistance profile is a characteristic of all the MWCNT contents and depends on density and conductivity. MWCNT content contributes mainly to the sensitivity of electrical sensing in the initial stage of compression. Later compression stages are dominated by foam microstructural damage which mask any effect of CNT dispersion. Micro-structural observations were employed to verify the experimental findings and curves.

**Keywords:** smart polymers, nano-composite foams, electrical conductivity, damage mechanism sensing

## 1. Introduction

The addition of carbon nano-fillers (nanofibers (CNF), nanotubes (CNT) etc.) into plastics has been shown to affect the various properties of the resulting material and effectively increase the electrical conductivity of the system by several orders of magnitude [1]. This is attributed to the formation of a conductive network of the conductive nano-fillers, which can be described as a percolated network. The increased electrical conductivity of the nano-reinforced materials has given rise to their use in various applications [2].

Polymeric foams (e.g. Rigid PolyUrethane (PUR)) represent a very interesting and useful sub-group,

finding vast range of applications due to their versatility. In structural applications, they are commonly used due to the weight saving capabilities they can offer in the design (e.g. as sandwich cores).

Combining nano-fillers with foam materials, nano-reinforcement of foams has been developed and studied the past decade, but mainly focused on the mechanical and thermal properties. Electrical conductivity of nano-composite foams is much less studied. Works on the electrical properties of nano-reinforced polymeric foams are rather sporadic [3–10]. The relationship between the resulting electrical conductivity and the density of the rigid foams for given CNT concentrations was reported in [6] but only recently described further [10].

\*Corresponding author, e-mail: [kostopoulos@mech.upatras.gr](mailto:kostopoulos@mech.upatras.gr)



The advantage electrical properties can offer is the capability to utilize self-sensing concepts for monitoring strain and/or damage [11]. Electrical resistance change method has been successfully employed as a health monitoring technique to follow strain and internal damages evolution in composite materials. It has successfully been applied on nano-composite polymers [12–15], on carbon fibre reinforced plastics (CFRP) [16–20] and in glass fibre reinforced plastics (GFRP) with conductive additives to increase matrix electrical conductivity (e.g. carbon nanotubes [21–23]). Attempts to model the electrical sensing and piezo-resistive response of the materials have also been reported [12, 13, 15, 24]. Even for Silicone-Carbide based ceramic matrix composites online monitoring of damage accumulation was achieved by measuring electrical properties [25]. Furthermore, cross-property relations between electric and elastic properties for metal foams have been developed in [26] for direct definition of elastic properties from electrical measurements.

The use of the electric field has been proposed and demonstrated to perform very well in defining various other properties. For example, electrical measurements have been used to monitor the foaming process and polymerization of polymeric foams [27] while dielectric measurements have been used for measuring the density of polymer foams [28]. Brady *et al.* [29] developed electrically conductive poly-pyrrole coated PUR foam. The conductance of the foam was found to change linearly with the compressive load applied; single and repeated. For aluminium foams, Kim *et al.* [30] developed a set of mathematical relationships based on experimental data to obtain mechanical properties (elastic modulus, compressive strength, densification strain) using electrical conductivity as a Non-Destructive Inspection method.

Xiang *et al.* [9] developed electrically conductive PUR foams (1 wt% CNT content and density between 200–550 kg/m<sup>3</sup>) and studied the temperature dependence of the electrical resistivity of the foam, ultimately utilizing this dependence for sensing. They showed that the foams exhibited a consistent and repeatable negative temperature coefficient of resistivity. The reduction of the cell walls' thickness causes the decrease in the distance between adjacent CNTs. The authors noted that the nearer and straighter CNTs, accordingly, create more

effective conductive paths within the matrix, which readily permit charge to transport, resulting in the decrease in the volume resistivity.

Based on the available literature, it is made obvious that potential synergies between electrical properties and nano-composite foams remain rather unexplored. In this work, we investigate the use of electrical measurements for strain sensing and eventually damage monitoring in nano-composite foams. For this purpose, PUR foams having different Multi-Wall CNT (MWCNT) concentrations and different densities were developed. The developed three-phase material (polymer, MWCNT and CO<sub>2</sub>) exhibited varying electrical properties with respect to the microstructure variables. The DC electrical conductivity of the various foams was studied under quasi-static compression loading. Continuous electrical recordings during the compression tests were investigated and compared against the stress state of the material. The deformation and damage evolution in foamed polymers from a micro-structural point of view was studied in comparison to the recorded electrical measurements. Identifying the loading and damage state of the foam with the proposed method could provide a novel tool for strain and damage monitoring of foams in composite structures.

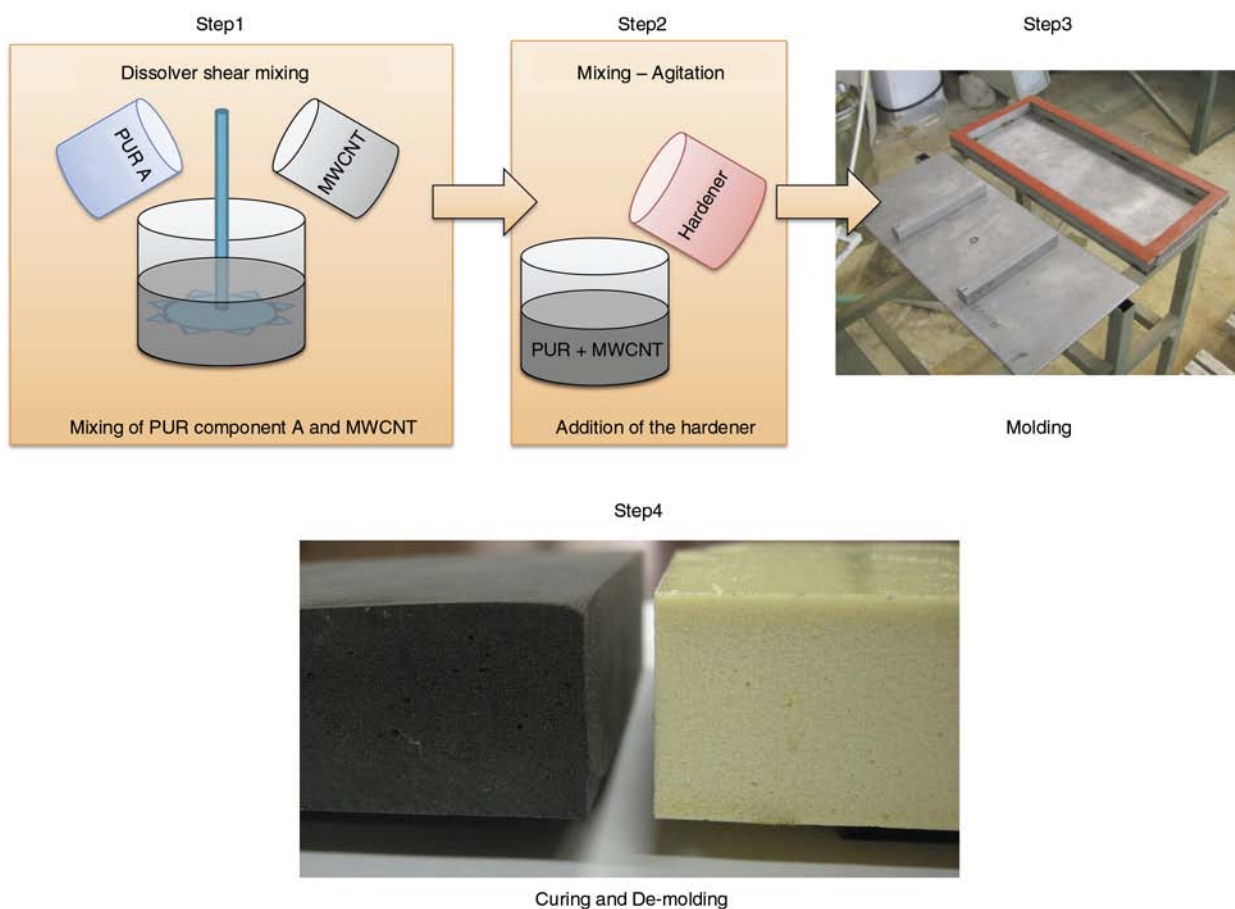
## 2. Materials and experimental setup

### 2.1. Materials and manufacturing

A two-component PUR system from R&G Faser-verbundwerkstoffe GmbH (Waldenbuch, Germany) was used in this study as the polymer host matrix. The A component of the system is the polyol mixture (under the commercial name of Rigid PUR foam, Product code: 170090). The B component is a 4,4'-diphenylmethane diisocyanate mixture (under the commercial name PUR Hardener 1000, Product code: 170105-2011) suitable for the production of polyurethane foam. Foaming of the material is achieved by the CO<sub>2</sub> gas product of the chemical reaction. The bulk polymer density is ~1200 kg/m<sup>3</sup>. MWCNT produced by catalyzed CVD were supplied by Arkema (France). According to the manufacturer, their diameters were 10–15 nm and they were more than 500 nm long, resulting in an aspect ratio (AR) in the range of 35–50. Previous studies [19, 31, 32] utilizing the same batch of CNTs showed good mechanical and electrical results for polymer composites. Therefore the same procedure was fol-

lowed and the nanotubes were used as received, i.e. no treatment or functionalization took place. To eliminate any humidity present, prior to use the nanotubes were placed in an oven at 60°C overnight. High-shear mixing approach successfully exhibited and investigated in other studies [10, 31, 32] was used to incorporate the nano-fillers. The processing steps are illustrated in Figure 1. MWCNT were dispersed in the A component of the PUR system using high-shear mixing dissolver device (under the commercial name DISPERMAT®) by VMA Getzmann GmbH (Reichshof, Germany). A rotating disk introduces shear forces to the mixture creating a vortex flow (doughnut effect). The vortex flow leads to a continuous mixing of the compound. The shear forces disentangle the CNT and reduce their agglomerates. Indications have been that dissolver shear mixing has minor effect on the characteristics of the MWCNT (e.g. CNT length) [31, 33]. The duration of mixing was 6 hrs at 2500 rpm and was chosen based on previous experience [31, 32] and initial trials [10]. The temperature of the mixture was monitored

throughout the process. Mixing was performed under controlled temperature between 45–60°C using the double wall container of the dissolver. Water of controlled temperature ran through the mantle. Once the dispersion was prepared, the hardener was added to the mixture at a ratio of 100:144 (A:B) according to the supplier (Figure 1 – Step2). The whole mixture was then mechanically stirred for 30 sec, until the foaming reaction was noticeable. The mixture was poured in a stainless steel mould which was hermetically sealed (Figure 1 – Step3). The mould was placed in a press and was kept there to cure at room temperature for 24 hrs followed by a post-curing phase for 4 hrs at 50°C. After complete curing cycle had finished, the foamed material was de-moulded. The result of the moulding process was a rectangular foam plate 200×100×30 mm<sup>3</sup> (Figure 1 – Step4). From each plate the required specimens were cut using a microtome. To avoid any surface anomalies which would affect the electrical measurement, each specimen was then grinded sequentially using 4 different levels of sand-



**Figure 1.** Nano-composite foam preparation process: Step1 – Shear mixing of MWCNT in polyol component, Step2 – Addition of the hardener to the mixture, Step3 – Molding, Step4 – Curing and de-molding: Neat (right) and MWCNT (left) foam

**Table 1.** Materials prepared for the study

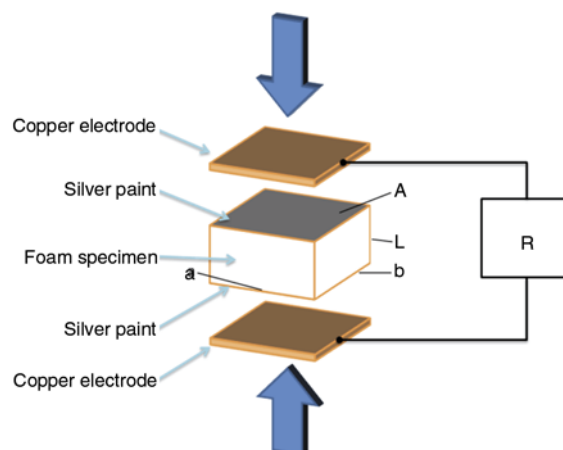
	Density group 1	Density group 2
Group name	Light foams	Dense foams
Density	250–300 kg/m <sup>3</sup>	350–400 kg/m <sup>3</sup>
MWCNT content (weight per cent)	3% 5%	2% 3% 5%

paper (500, 1000, 2000 and 4000) on all sides. After this, the density of each specimen was calculated by measuring the dimensions and the weight of each specimen. In principle, two foam density ranges were targeted; 250–300 kg/m<sup>3</sup> (20–25% relative density) and 350–400 kg/m<sup>3</sup> (30–35% relative density). Nevertheless, foams having various different densities were produced. For convenience, the first group of densities will be referred to as Light Foam, while the second one as Dense Foam.

Two MWCNT concentrations per weight were chosen to be studied; 3% and 5%. For the higher density, 2 wt% MWCNT was also investigated. These values correspond to the weight percentage of the CNT to the polymer and CNT mixture. The materials developed and studied in this work are summarized in Table 1.

## 2.2. Experimental testing

Compression tests were carried out according to ASTM-C365. Square specimens were cut from each plate having 25 mm sides and 10 mm thickness. The thickness direction coincided with the thickness direction of the initial rectangular foam plate. Compression was performed using an INSTRON 8872 (Norwood, USA) servo-hydraulic universal testing machine with a crosshead displacement set at 0.4 mm/min. Compression was terminated when the load reached ~15k N. For each material developed (shown in Table 1) 3 specimens were tested. Prior to any electrical measurement, following commonly reported procedures, commercially available conductive silver paint (under the commercial name RS 186-3593) supplied by RS Components Ltd (Northants, UK) was applied on the sides in contact with the electrodes (Figure 2) to minimize any contact resistance for the electrical measurements. Prior to mechanical testing, to account for any contact resistance influence to the measurements, different levels of small loads were applied to the samples at increments of 5 N up to 50 N corresponding to a maximum of ~80 kPa of pressure. For all the samples the resistance was nearly constant irrespec-



**Figure 2.** Exploded view of the experimental measurement configuration: electrical resistance recording during compression

tive of the applied load, indicating a good electrical contact between the electrodes and the sample.

For measuring the DC electrical resistance of the materials during the compression test (Figure 2), the silver-painted sides of the sample were placed in contact with two copper plates which served as the electrodes. A high-performance KEITHLEY 2002 digital multimeter by Keithley Instruments, Inc. (Ohio, USA) was used in a 2-probe configuration for measuring the electrical resistance. The electrical resistance of the complete system (electrode-specimen-electrode) was recorded throughout the compression test. Given the geometry of each specimen (Figure 2), the bulk volume conductivity at each instance of the test was calculated based on Equation (1):

$$\sigma = \frac{L}{RA} = \frac{t}{Rab}, \quad \rho = \frac{1}{\sigma} \quad (1)$$

where  $\sigma$  is the electrical conductivity,  $L$  is the length of the specimen,  $A$  is the cross-sectional area of the specimen,  $t$  is the thickness of the specimen,  $a$  and  $b$  are the cross-sectional dimensions of the specimen,  $R$  is the electrical resistance measurement, and  $\rho$  is the electrical resistivity. Furthermore, combining the applied compressive load on the sample and the geometric characteristics of the specimen, the pressure can be derived. For each material, five specimens were tested. All measurements were performed at room temperature.

Scanning Electron Microscopy (SEM) for microstructural and fracture characterization was performed with a LEO SUPRA 35VP by Carl Zeiss Microscopy GmbH (Jena, Germany). Different mag-

nification levels were employed to evaluate different aspects of the materials. Low magnification was used to assess the microstructure of the foam as well as to verify the damaged microstructure after the test. Higher magnification of fractured surfaces was used to evaluate the dispersion of the CNT as well as to capture indications on the wall thickness of the microstructure.

### 3. Results and discussion

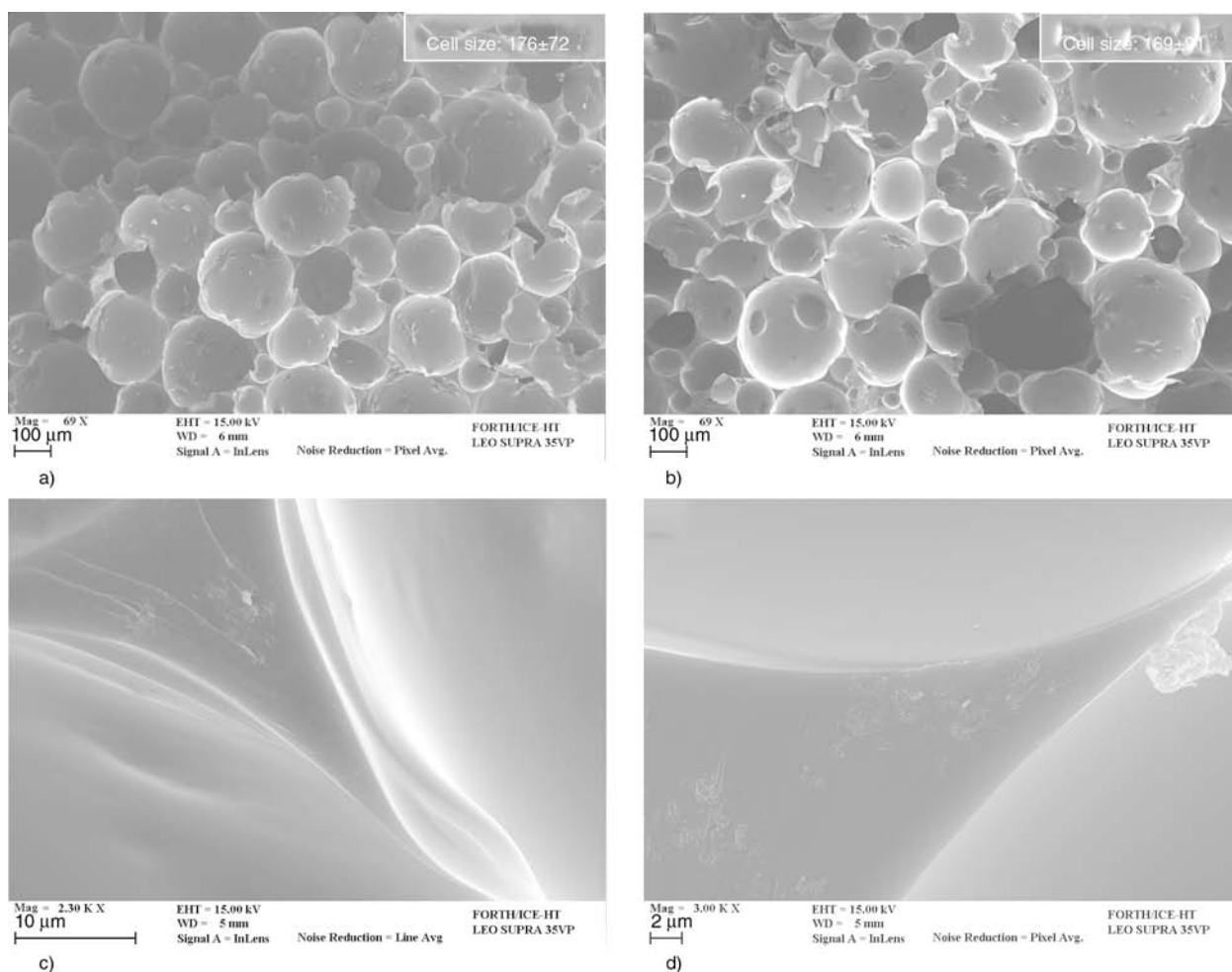
#### 3.1. Preparation and cellular structure

The effective dispersion of CNT in polymers, as a research field, has attracted considerable attention due to the challenge to disentangle the agglomerates of CNT and create a homogeneous distribution throughout the host matrix. For the development of electrically conductive foams this process is also a very important step. The high shear mixing process used in this work has been shown to produce good results in dispersing the nano-fillers and developing electrically conductive polymers. At the levels of

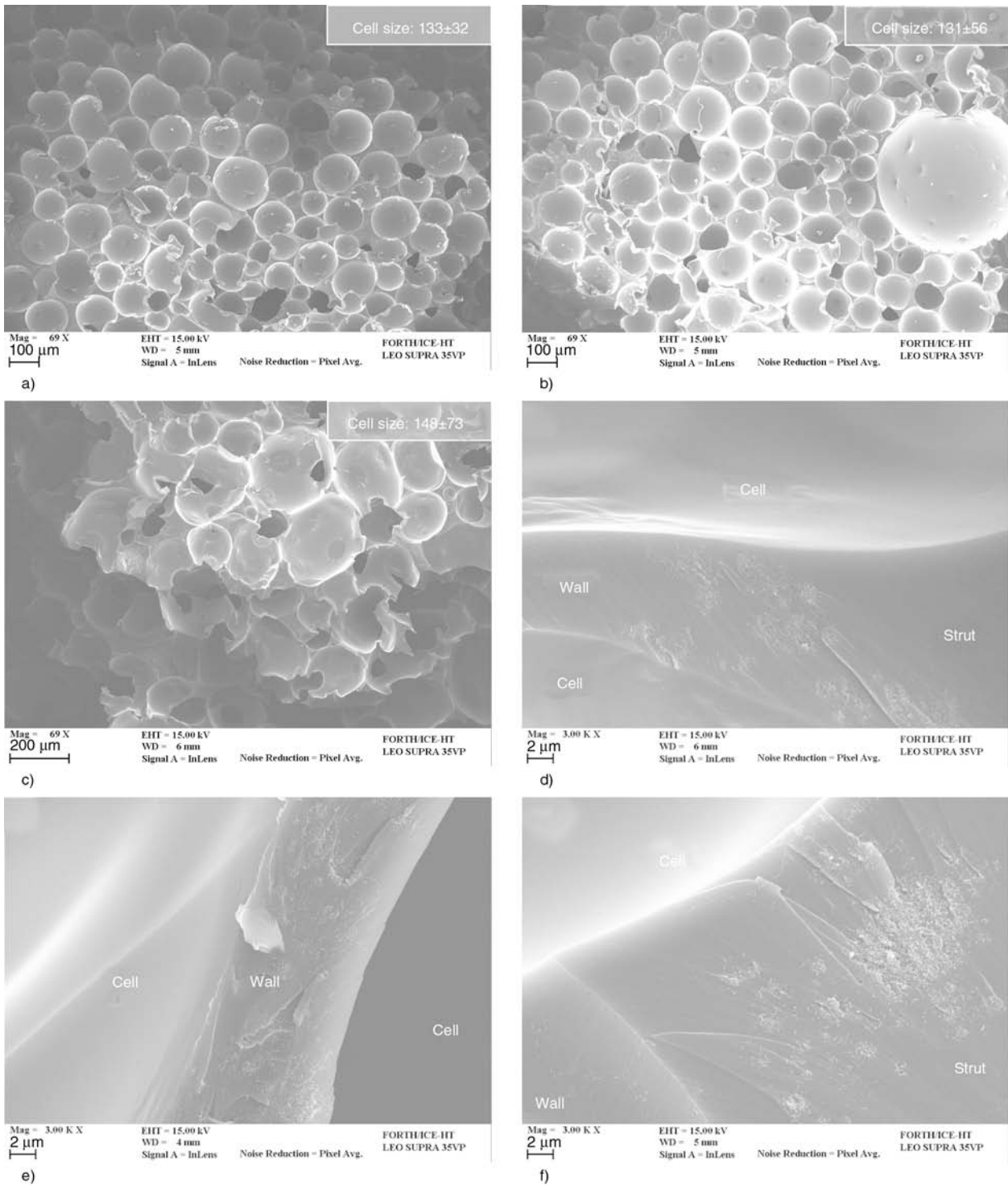
content investigated in this study (>2 wt%) it is very difficult to avoid nano-filler agglomerations in the final polymer. Nevertheless, an initial target is to achieve relatively high electrically conductive foams.

The addition of CNT, as is commonly observed in various similar studies, has effectively increased the viscosity of the mixture (A component and CNTs), due to the extended surface interaction between the fillers and the matrix. At 5 wt% CNT content the mixture resembled a paste, making it difficult both to handle the mixture and effectively utilizing the method to disperse the CNTs. To decrease the viscosity to a level where processing would be more effective, the temperature of the mixture was increased to 60°C.

The developed foams are complex three-phase materials consisting of the polymer, the MWCNT and CO<sub>2</sub> bubbles. SEM micrographs (Figure 3 and 4) provide visual evidence of the foam microstructure where the three phases are distinguishable.



**Figure 3.** SEM micrographs of the light nano-composite foam: (a, b) foam microstructure for 3 and 5 wt% MWCNT, (c, d) dispersion in foam for 3 and 5 wt% MWCNT



**Figure 4.** SEM micrographs of the dense nano-composite foam microstructure: (a–c) foam microstructure for 2, 3 and 5 wt% MWCNT, (d–f) dispersion in foam for 2, 3 and 5 wt% MWCNT

The effect of CNT on PUR foams in terms of processing and final microstructure has been investigated in a number of studies [8, 10, 34, 35]. The indications are that the effect of CNT on the final microstructure is moderate and CNT do not contribute a heterogeneous nucleation factor that can change the microstructure. In this study, SEM characterization performed on the developed materials

confirms these reports. The microstructure of the foams can be seen in Figure 3a, 3b and Figure 4a–4c together with the elaborated values for the average cell size. The observation reveals that the addition of CNT in the mixture has practically a minor effect on the cell size for foams with similar density. The deviation of the cell size seems to increase with the addition of CNT.

Figure 3c, 3d and Figure 4d–4f present a series of SEM micrographs focused on the strut-to-wall transition area for the different developed materials. These images provide a means to assess the achieved dispersion of CNT within the polymer. It is evident that agglomerations are present in all the cases, which is expected considering the high level of MWCNT in the polymer. In between the agglomerations individually dispersed CNT are also seen. Groups of bundled CNT form spherical structures which have a diameter in the range of 2  $\mu\text{m}$ . For the dense foams of 5 wt% CNT, concentrated agglomerations are witnessed (Figure 4f). In the case of the light foams the thinning of the cell walls is obvious as well as the arrangement of CNT in the transition zone. CNT, either in small agglomerations or individual, are seen at the tip of the cell wall which has a thickness less than 2  $\mu\text{m}$  (Figure 3d). Similar indications are available for the dense foams, where a network of CNT is seen in the cell wall region (Figure 4d).

Despite the agglomerated state of CNT which decreases the effectiveness of nano-reinforcement, a conductive distribution of the CNT is achieved and has been verified by the measured electrical conductivity. The dependence of the electrical conductivity on the foaming process, the achieved micro-structure, the MWCNT content and the relative foam density has been described in [10] and is not discussed further here.

### 3.2. Evolution of apparent electrical properties during mechanical compression

As a first indication of the electrical response of the foams to mechanical load, the recorded bulk electrical resistance values during quasi-static compressive loading are presented in Figures 5 and 6 for the

light and dense foam groups respectively. The measurements were performed in the through thickness direction as shown in Figure 2. The change of electrical resistance during loading is evident for all material groups. A general agreement between the specimens with the same physical characteristics is noted. Consistent patterns are exhibited by specimens within the same group. Furthermore the patterns present similarities among the same density groups. Repeatability of the measurements was verified for each sample prior to the test for the elastic region of the compression curve (strain <5%), by repeated loading-unloading.

For the light foams (Figure 5), the electrical resistance ( $R$ ) pattern during loading exhibits a consistent behaviour for both nano-filler contents. The response gives repeatable results for all the specimens within the same group. Minor differences within the same group are noticed in the initial part of the curve, but do not change the whole pattern. All electrical resistance curves start with an abrupt linear drop, reaching local minimum around 400–500 N of load. Further increase of the load, leads to an increase in  $R$  until a local maximum is reached between 2–3 kN of applied load. Increasing the applied load further, the resistance  $R$  decreases monotonically until 15 kN, where the experiment was stopped. At this final phase the decreasing trend was almost linear. The initial values of the curves are all at the same range for both sets of nano-filler contents; 60–90 k $\Omega$  for 3 wt% MWCNT and 0.6–1.6 k $\Omega$  for the 5 wt% MWCNT. This difference between the two groups was expected due to the increase in the nano-filler content as verified in [10].

Figure 6 presents the recorded values for the dense foam group. The pattern for the dense foams is similar for the two lower nano-filler contents. For the

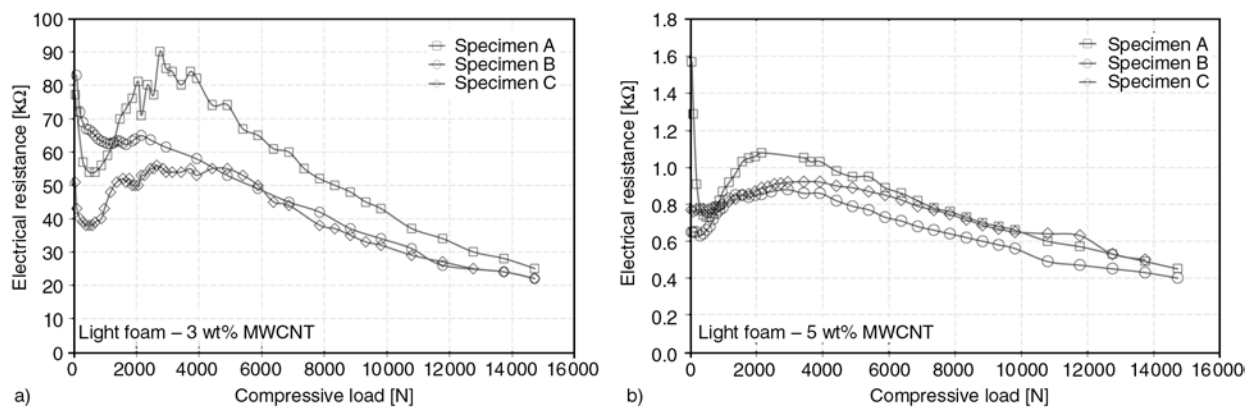


Figure 5. Electrical resistance Vs. compressive load: light foams (a) 3 wt%, (b) 5 wt% MWCNT

highest content a different response is observed. All MWCNT contents exhibit an initial drop in the

measured resistance, up to between 200–400 N of applied load. For the low MWCNT contents, an increase in the applied load further from 500 N results in a short plateau for the resistance  $R$ ; up till 3 kN for 2% and 4 kN for 3%. Continuing further to increase the load, an asymptotic decrease up to a final resistance value is exhibited until the load reaches 15 kN. For the 5 wt% MWCNT concentration, a clear intermediate plateau is not revealed. Rather a local minimum is shown, followed by an asymptotic increase in the final part of the curve. Again, the recorded response curves exhibit high repeatability among the specimens, with only minor differences in the response.

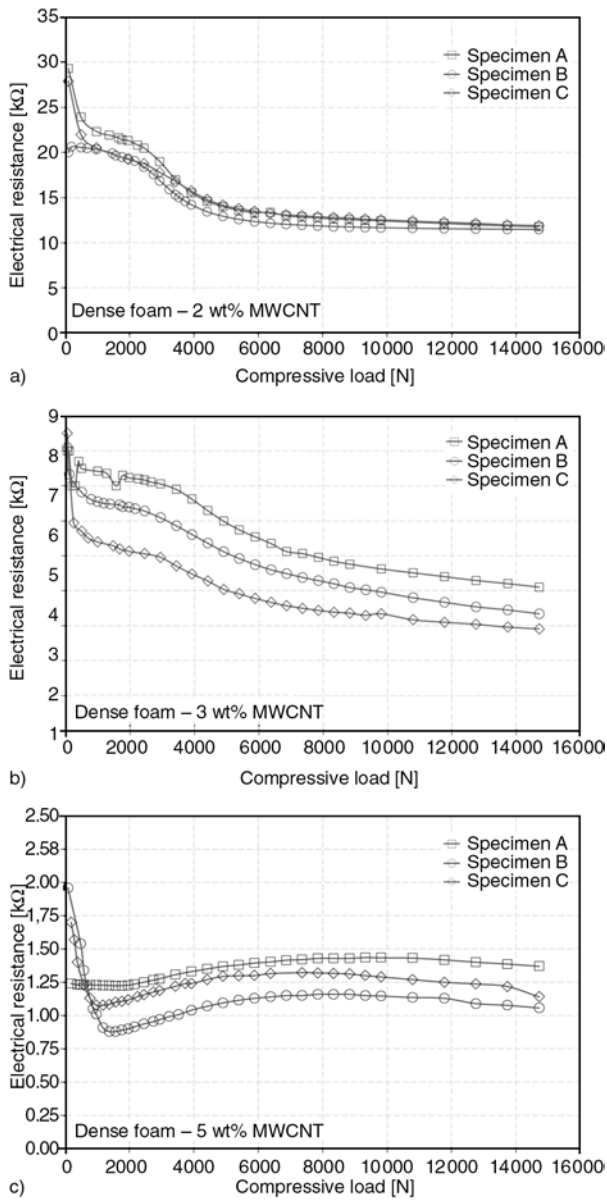


Figure 6. Electrical resistance Vs. compressive load: dense foams (a) 2 wt%, (b) 3 wt%, (c) 5 wt% MWCNT

To better reveal the information within the electrical response it is useful and commonly employed to express the normalized relative values of resistance. These are presented in Figure 7 together with the stress values against derived strain, for the two density groups. The values to prepare these figures were calculated based on the recordings of the experiment, as opposed to Figure 5 and 6 where the raw data are reported.

From the mechanical point of view, the elaborated stress-strain curves follow the extensively documented behaviour of cellular solids; an initial linear increase in stress followed by an elasto-plastic yielding (called plateau region) and reaching the densification region where stress increases rapidly. It can be noted that the stress-strain curves of the nano-composite foams deviate slightly from the ‘nominal’ description in that the linear and plateau regions are not clearly distinct. Instead, in this region the materials show an increasing linear behaviour, which is a common observation among polymer foams [36] and indicates plastic yielding earlier than usual. Nevertheless, the difference in the slope of the two phases is noticeable.

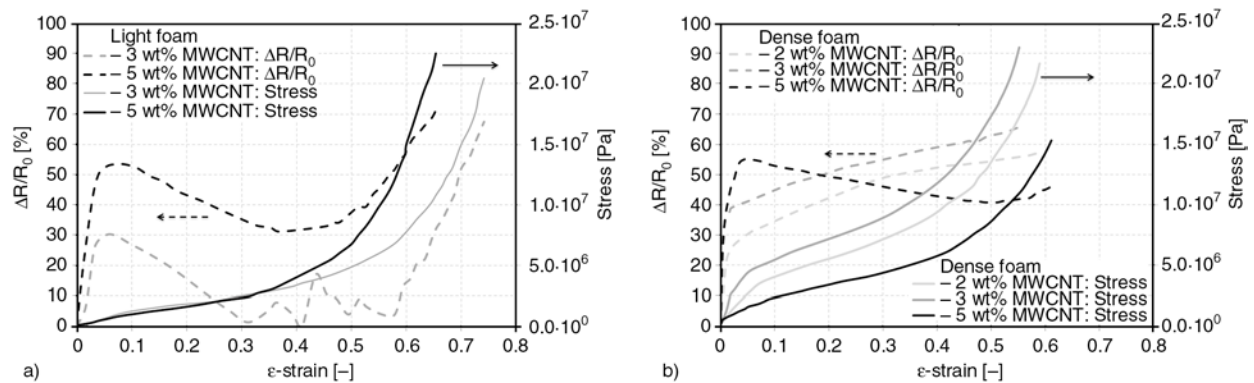


Figure 7. Stress and relative electrical resistance change ( $\Delta R/R_0$ ) Vs. strain (a) light foams, (b) dense foams

From the perspective Figure 7 offers, the electrical response is more informative and the relation between the mechanical and electrical behaviour is becoming more evident. The effect of CNT on the mechanical behaviour of the foams is also visible in the same diagram, which can directly be taken into account in the electrical response evaluation.

For the light foams, starting from non-strained foams,  $\Delta R/R_0$  increases linearly up to nearly 5% strain and forms a peak extending between 6–8% of strain. As strain increases corresponding to a linearly increasing load,  $\Delta R/R_0$  decreases linearly until 30–40% strain. At this point an extended local minimum is reached and any further increase in strain is followed by an increase in  $\Delta R/R_0$ . The unstable response for the 3% CNT content is directly related to the mechanical response. The material exhibits a prolonged yielding region, which is reflected by the electrical measurements.

The dense foams exhibit a similar mechanical but a different electrical behaviour. For low mechanical load levels and strains below 4%, the  $\Delta R/R_0$  value increases linearly. From that point on, by increasing the strain,  $\Delta R/R_0$  continues to increase by a different rate until almost 30%. In the meantime stress continues to increase following a narrower slope. After that point the rate of increase of  $\Delta R/R_0$  decreases further, but still attains an increasing trend. This holds true for the lower CNT contents studied. For the dense foam having 5 wt% CNT (black lines), the mechanical performance seems to be poorer than the other CNT concentrations. This is evident by the low elastic modulus exhibited in the linear region and the overall lower stresses. Additionally, it is very interesting to note that this is also exhibited by the behaviour of  $\Delta R/R_0$ . The  $\Delta R/R_0$  curves for the dense 5% foam samples resemble those of the light foam.

It is interesting to point out that for the cases where the transition of the mechanical response from the linear to the yielding plateau is not clearly expressed; the electrical response exhibits a peak. The transition can be identified by the change of the slope of the electrical curve from positive to negative. For the case where the mechanical transition from Stage I to Stage II is much clearer, the respective electrical curve exhibits a transition point where the positive slope decreases slightly.

Based on experimental indications, it can be said that the nano-filler content affects the sensitivity of the

electrical response to mechanical stimulus. This can be observed by comparing the amount of change in electrical properties versus the amount of change in the mechanical response, which is expressed by the initial slope of the curves in Figure 7. The trend implies that the higher the CNT content the more sensitive the system is. This CNT loading-performance sensitivity has been reported in other sensing studies utilizing CNTs in polymer [2, 37] and in fibrous composites [18, 22, 32]. Furthermore, the contribution of the CNTs in sensing is expected to be expressed more in the elastic region rather than the yielding plateau. The reason for this is that crushing of the cells occurs at a higher scale level. Any influence at nano-scale would be shadowed. Nevertheless, the conductivity they offer to the nano-polymer system still remains. Therefore, it is believed that the influence of the CNT dispersion in the later stages of damage is much lower. As a matter of fact, their use is primarily for early sensing of damage.

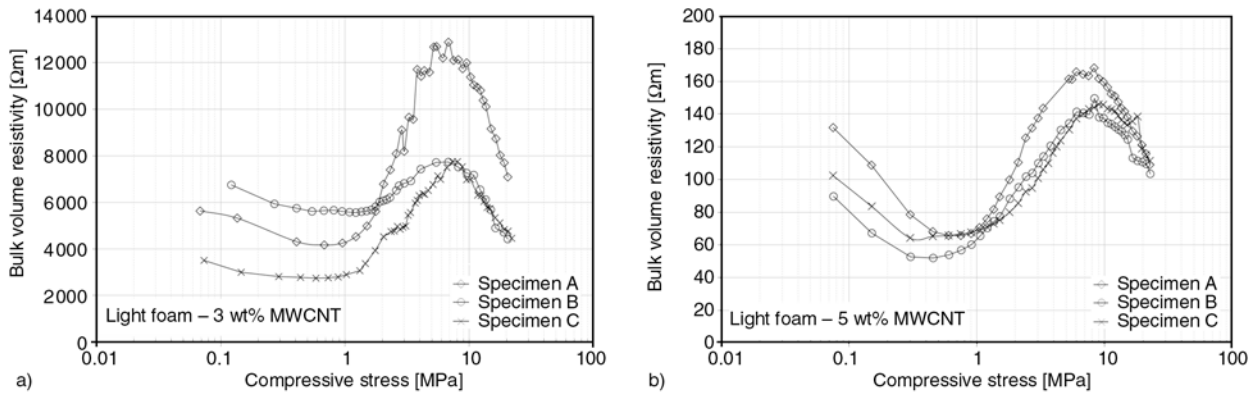
The difference in the electrical response of dense foam with 5 wt% MWCNT and the other two nano-filler concentrations is attributed to the dispersion of the nano-fillers. The mechanical performance resembles that of light weight foam. At this high level of weight fraction, effective dispersion to achieve optimal distribution for mechanical performance is very challenging. Agglomerations are observed percolating to reach a conductive network through individually dispersed CNT. These agglomerations can act as stress raisers/concentration points. Considering the thinner cross-section (cell walls) available to transfer the compressive loads, the presence of agglomerations magnifies their effect.

### 3.3. Non-dimensional electrical measurements as a function of stress state

Having the aforementioned observations and diagrams as a basis, we attempt here to identify pattern behaviours, introduce the failure/damage mechanisms into perspective for sensing using electrical measurements and define key parameter for detecting the damage evolution in polymer foams.

Firstly, the recorded values are expressed in a non-dimensional basis. The bulk volume resistivity of the foams is elaborated solving Equation (1) for the resistivity term. The stress values have already been calculated previously. To verify that the stress and electrical behaviour correlate, we plot the elaborated bulk volume resistivity against stress. Bulk





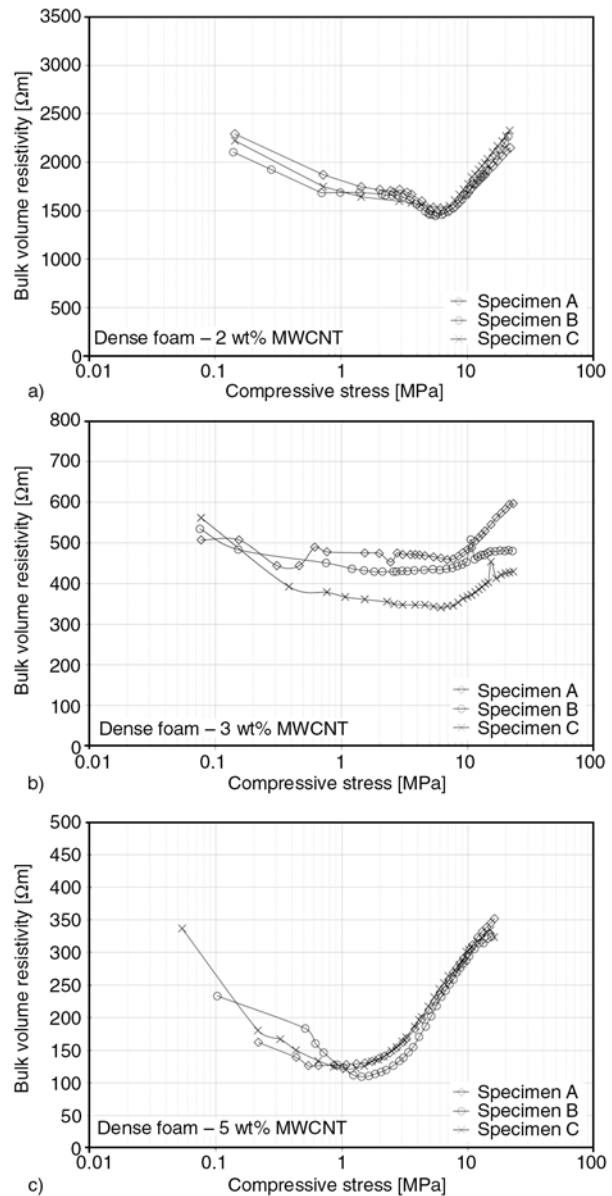
**Figure 8.** Bulk electrical property change Vs. stress for light foams: (a) 3 wt% and (b) 5 wt% MWCNT

volume resistivity takes into account the dimensional change of the specimens and thus is believed to convey clearer information on the state of the materials. A logarithmic scale is used for stress values to enhance the exhibited transitions between the variables. The resulting curves are shown in Figure 8 and 9 for the light and dense foam groups respectively.

To analyze and explain the observations of the electrical resistivity, the mechanisms involved in the deformation are revisited here, focusing on the failure of cellular solids under compression. Along the way, we assess the effect of these mechanisms on the electrical properties.

The mechanical response curve of foam under compression is characterized by three stages. Each reflects different micro-structural compliance and failure mechanisms. [36, 38–40]

As already mentioned, the first stage is the linear-elastic response of the foam. During this stage, a number of deformation mechanisms occurs with the more dominant ones being the cell wall bending in combination with the compression of the gas contained within the closed foam cells. In this stage, stress increases linearly with deformation. The modulus exhibited depends on the density of the foam. In principle at this level of stress, strain is recoverable, hence is characterized as elastic. Nevertheless, experimental observations here and in other studies have a reported non-recoverable deformation already from this stage, attributed to statistical fracture of cells and localized stress concentrations. This is expected to be reflected by the electrical properties too. Damage in the microstructure is expected to interrupt the conductive paths and increase resistivity. Recoverable deformation is generally expected to recoverably decrease the electrical resistivity.



**Figure 9.** Bulk electrical property change Vs. stress for dense foams: (a) 2 wt%, (b) 3 wt% and (c) 5 wt% MWCNT

This is attributed to the local re-arrangement of the CNT [2, 9] due to the compressive stresses. The CNT

contacts increase and more conductive paths are available, decreasing the exhibited resistivity.

The second stage of ideally elastic-plastic foams is characterized by continued deformation at nearly constant stress, usually forming a plateau. During this stage, plastic yielding occurs and thus strain increases more rapidly than stress. The mechanisms associated with the yielding/collapse plateau, vary depending on the properties of the cell-walls. For rigid foams, macroscopic plastic yielding in the micro-structure is related to fracture of the walls due to buckling failure [39]. In compression, the failure behaviour of low-density foams is dominated by the early collapse of large porous cells which triggers macroscopic fracture of the specimen, whereas high-density foams exhibit more uniform deformation, which results in ductile-like fracture mode under quasi-static loading [41]. This results in the fracture of the material microstructure on the mechanical level. The fracture interrupts the continuity of the material and breaks the available conductive paths. Fractured cell walls are still in contact thus contributing to electrical conduction. However, resistivity now is higher because contact resistance is higher than conduction within the network. This is reflected by the increase of the bulk volume resistivity.

The final stage of stress-strain curve is the densification. At this stage, the stress rises steeply and the foam begins to respond as an increasingly compact solid. The cellular structure within the material has collapsed compacting in a lamellar microstructure. For further deformation compression of the solid material is required. Essentially, the resulting lamellae from the collapsed cells are compacted tightly. This mechanism increases the contact surface between the material formerly comprising the cell walls, providing larger paths for electrical conduction and thus decreased resistivity.

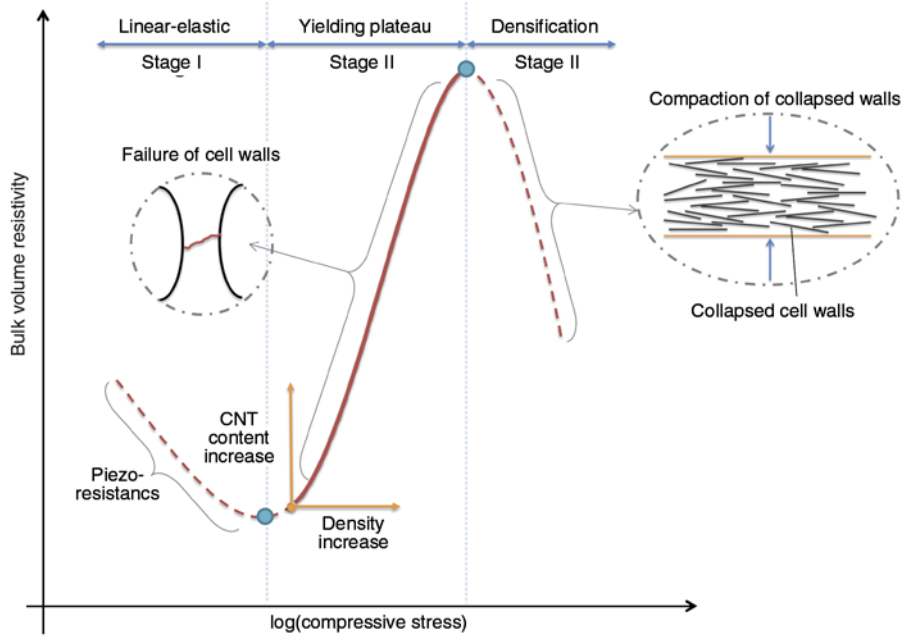
In the view of the above-said, for the light foams, the distinct stages are identified for both CNT concentrations. In Stage I, the bulk electrical resistivity is decreasing with the increase of the applied stress. The mechanical response of the foam is nearly linear in semi-log axis (Figure 8a). A minimum around 1 MPa for the 3 wt% MWCNT and 0.8–0.9 MPa for the 5 wt% MWCNT is consistently observed for all the specimens. This point corresponds to nearly 10% compressive strain. In Stage II, resistivity increases (nearly 3–4 times) and it reaches a peak at

a stress around 8–9 MPa. The stress is high enough to start causing larger scale cell fracture. This continues, as the stress increases further, more and more cells fracture up to a point where many cells have been destroyed. At this point the resistivity shows a maximum at around 9 MPa, which is the same for both nano-filler contents. This point corresponds to 55–65% strain. After this point the last stage starts where the resistivity decreases again until the end of the experiment. The broken sides of each cell start to touch and with the increased load they are pressed against each other. This leads to a better contact between the conductive cell walls and thus the decrease in resistivity.

For the dense foam, the behaviour is similar to the one described above (Figure 9). The two first stages are clearly identified. The transition from Stage I to Stage II corresponding to the minimum in resistivity is observed at the range of 7–8 MPa. For the high CNT content this point is around 1.1 MPa (very close to the transition for light foams). The third characteristic stage is not observed as the experiment was stopped early in terms of stress (all loading curves reached a maximum of 20 MPa). As it is seen the applied load did not suffice to lead to the compression of the fractured walls. The trend of the curves however indicates a maximum to be expected close to 11–13 MPa, as previously described. It is believed that the bell-shaped exhibited by the light foams would be expressed if the compressive load extended further higher.

### 3.4. Damage evolution sensed through electrical properties

In this section, we attempt to illustrate the described information in a characteristic diagram for damage sensing through electrical properties. We introduce a sigmoid curve that incorporates the aforementioned observations and is based on the damage mechanisms involved (Figure 10). The X-axis is the logarithmic compressive stress while the Y-axis is the elaborated bulk volume resistivity. The curve consists of three parts corresponding to the different stages of the mechanical response of the foams. The first stage giving a decrease in resistivity represents the elastic response in compression. The second stage corresponds to yielding with an increase of resistivity. The third stage showing a decrease in resistivity corresponds to the densification of the foam. The

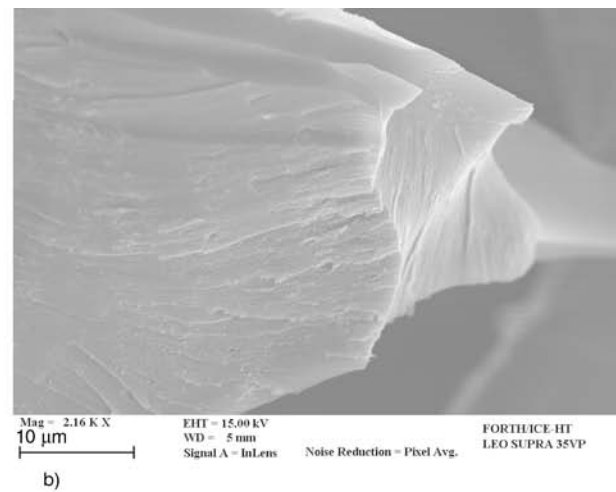
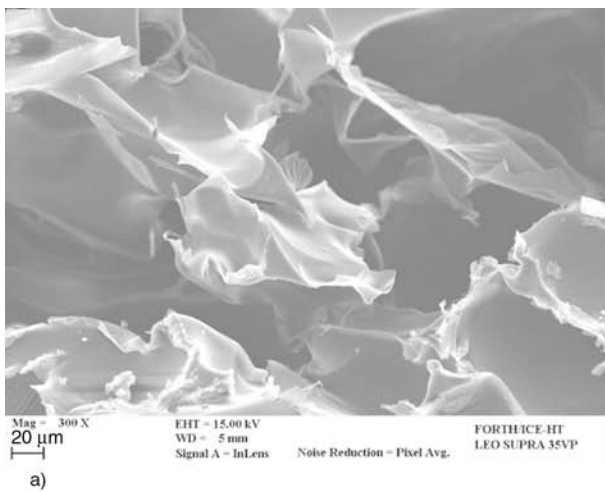


**Figure 10.** Damage evolution in foams sensed through electrical properties: qualitative electrical property change and involved damage mechanisms

proposed curve can be used for identifying the different damage stages of a foam.

Different conduction mechanisms are associated to each stage of the curve. Stage I is claimed to express the piezo-resistive part, as it exhibits the highest dependence on the MWCNT content. Stage II is dominated by the cell wall fracture, which effectively interrupts the conductive network by excluding large parts of it. Thus resistivity increase is expected. Stage III is believed to essentially express the compaction of the failed cell walls, which are conductive due to the CNT within the polymer. The proposed mechanism for Stage III (Figure 10 – right inset) is justified by SEM micrographs (Figure 11),

where the cell walls are visible in the form of flakes. Here the cell walls are shown in their form after compression and previous figures showed the CNT within the cell walls. Considering the situation reversely, it is expected that the compaction of these flakes leads to the electrical response (Figure 10). The effectiveness of CNT dispersion in the system is pre-dominantly affecting Stage I of the curve. In the later damage stages, micro- and macro-scale fracture shadows any effect of CNT dispersion. Fracture of the foam micro-structure breaks large parts of the conductive network and the only issue still contributing is the conductivity of the polymer struts and cell walls. Thus CNT dispersion seems to



**Figure 11.** SEM micrographs of the failed microstructure: (a) collapsed cell walls in the form of flakes, (b) close-up of MWCNT dispersion in the failed cross-section of the cell walls

matter less at the later stages, as long as the CNT-polymer remains conductive.

Furthermore, it is believed that the exact location of the master-curve on the X-Y plane is defined by several parameters characterizing the material system. Two main parameters can already been identified; density and nano-filler content. Firstly, based on density the curve is shifted to the left for light foams, to the right for denser ones. This is based on the observation that for the dense foams the peak and Stage III decrease is not expressed up to the stress reached. It is believed that because cell walls are thicker in dense foams, they can withstand higher stresses. To this end, the peak value expressing ‘saturation’ of damaged cells and indicating the transition to Stage III may also shift to higher stresses. Secondly, from the experimental results it was seen that the nano-filler content controls the conductivity level of the foam and both the amount of the resistivity drop and the drop rate expressed in Stage I. Essentially, the level of conductivity shifts the curve on the vertical axis.

This diagram can serve as an initial attempt to formulate a cross-property relation for polymer foams [26, 30], but further experimental evidences are needed to quantify and standardize the findings to form a cross-property relation.

#### 4. Conclusions

Electrically conductive PUR foams with varying levels of electrical conductivity were successfully prepared at various densities and using different MWCNT concentrations. MWCNT were dispersed in the polyol component of PUR using high shear mixing. From this base material, conductive foams having different densities were produced. The foams exhibited varying levels of DC electrical conductivity which have been related to nano-filler concentration and density in [10], laying the ground for this work.

Here, for the first time, the evolution of electrical properties of the foams during compressive loading until failure was investigated. Initial results are analysed and damage mechanisms are proposed to explain the observed performance. The recordings were consistent within the same material groups and the overall behaviour of electrical properties was repeatable and characteristic. Three different regions are observed in the diagram of the volume resistivity versus compressive load. The aforemen-

tioned regions are correlated with the three discrete regions of the stress – strain curve of the foam. In the first region (linear elastic) the resistivity decreases as the compressive load increases while the second region (yielding plateau) due to breakage of the cells the volume resistivity increases. In the third region (densification) the volume resistivity decreases again because the collapsed cells are compacted tightly. Each stage is associated to a different mechanisms respectively; piezo-resistivity, micro-structure failure, compaction of failed microstructure.

The nano-phase dispersion controls the overall conductivity of the system and the sensitivity of the initial loading stage. The later stages are more related to macroscale damage of the structure thus masking any influence from the CNT dispersion; electrical conductivity of the polymer is only required. For denser foams, the technique may seem less efficient but it is believed that it is due to the bearing capability of the microstructure that this occurs.

In the range of CNTs content that we studied the electrical resistivity – stress curves a range of similarities exists. The above laid the grounds for establishing a damage evolution diagram for sensing through electrical properties illustrating the information collected. This diagram proved to be characteristic for the foams studied offering novel potential for the developed systems.

The information, mechanisms and formulations presented in this work may enable the development of dedicated advanced Non-Destructive Inspection techniques for foams and sandwich composite struc, as well as modelling attempts to express the aforementioned observations, especially in Stage II which represents the largest fraction of the materials life. Such techniques could enable on-line damage identification as well as production qualification and become part of novel more advanced monitoring systems [42]. As a matter of fact, similar techniques have demonstrated their suitability to offer prompt information particularly on the production progress of the ‘packing’ and ‘gelation’ stages of polymeric foams, otherwise not so easily possible [27].

#### Acknowledgements

This work was supported by the ‘Innovative Action for Plastics and Composites’ of the Regional Innovation Pole of Western Greece. The authors would like to thank Mrs. Myrto Matzakou for her contribution in the preparation of the materials as well as her support in the experimental work.

## References

- [1] Du J-H., Bai J., Cheng H-M.: The present status and key problems of carbon nanotube based polymer composites. *Express Polymer Letters*, **1**, 253–273 (2007). DOI: [10.3144/expresspolymlett.2007.39](https://doi.org/10.3144/expresspolymlett.2007.39)
- [2] Karapappas P., Tsotra P., Scobbie K.: Effect of nanofillers on the properties of a state of the art epoxy gel-coat. *Express Polymer Letters*, **5**, 218–227 (2011). DOI: [10.3144/expresspolymlett.2011.21](https://doi.org/10.3144/expresspolymlett.2011.21)
- [3] Rizvi R., Kim J-K., Naguib H.: Synthesis and characterization of novel low density polyethylene–multi-wall carbon nanotube porous composites. *Smart Materials and Structures*, **18**, 104002/1–104002/10 (2009). DOI: [10.1088/0964-1726/18/10/104002](https://doi.org/10.1088/0964-1726/18/10/104002)
- [4] Yang Y., Gupta M. C., Dudley K. L., Lawrence R. W.: Conductive carbon nanofiber–polymer foam structures. *Advanced Materials*, **17**, 1999–2003 (2005). DOI: [10.1002/adma.200500615](https://doi.org/10.1002/adma.200500615)
- [5] Xu X-B., Li Z-M., Shi L., Bian X-C., Xiang Z-D.: Ultralight conductive carbon-nanotube–polymer composite. *Small*, **3**, 408–411 (2007). DOI: [10.1002/smll.200600348](https://doi.org/10.1002/smll.200600348)
- [6] Harikrishnan G., Singh S. N., Kiesel E., Macosko C. W.: Nanodispersions of carbon nanofiber for polyurethane foaming. *Polymer*, **51**, 3349–3353 (2010). DOI: [10.1016/j.polymer.2010.05.017](https://doi.org/10.1016/j.polymer.2010.05.017)
- [7] Antunes M., Mudarra M., Velasco J. I.: Broad-band electrical conductivity of carbon nanofibre-reinforced polypropylene foams. *Carbon*, **49**, 708–711 (2011). DOI: [10.1016/j.carbon.2010.10.032](https://doi.org/10.1016/j.carbon.2010.10.032)
- [8] Yan D-X., Dai K., Xiang Z-D., Li Z-M., Ji X., Zhang W-Q.: Electrical conductivity and major mechanical and thermal properties of carbon nanotube-filled polyurethane foams. *Journal of Applied Polymer Science*, **120**, 3014–3019 (2011). DOI: [10.1002/app.33437](https://doi.org/10.1002/app.33437)
- [9] Xiang Z-D., Chen T., Li Z-M., Bian X-C.: Negative temperature coefficient of resistivity in lightweight conductive carbon nanotube/polymer composites. *Macromolecular Materials and Engineering*, **294**, 91–95 (2009). DOI: [10.1002/mame.200800273](https://doi.org/10.1002/mame.200800273)
- [10] Athanasopoulos N., Baltopoulos A., Matzakou M., Vavouliotis A., Kostopoulos V.: Electrical conductivity of polyurethane/MWCNT nanocomposite foams. *Polymer Composites*, **33**, 1302–1312 (2012). DOI: [10.1002/pc.22256](https://doi.org/10.1002/pc.22256)
- [11] Chung D. D. L.: Self-monitoring structural materials. *Materials Science and Engineering R: Reports*, **22**, 57–78 (1998). DOI: [10.1016/S0927-796X\(97\)00021-1](https://doi.org/10.1016/S0927-796X(97)00021-1)
- [12] Rizvi R., Cochrane B., Biddiss E., Naguib H.: Piezoresistance characterization of poly(dimethyl-siloxane) and poly(ethylene) carbon nanotube composites. *Smart Materials and Structures*, **20**, 094003/1–094003/9 (2011). DOI: [10.1088/0964-1726/20/9/094003](https://doi.org/10.1088/0964-1726/20/9/094003)
- [13] Wichmann M. H. G., Buschhorn S. T., Gehrman J., Schulte K.: Piezoresistive response of epoxy composites with carbon nanoparticles under tensile load. *Physical Review B*, **80**, 245437/1–245437/8 (2009). DOI: [10.1103/PhysRevB.80.245437](https://doi.org/10.1103/PhysRevB.80.245437)
- [14] Wichmann M. H. G., Buschhorn S. T., Böger L., Adelung R., Schulte K.: Direction sensitive bending sensors based on multi-wall carbon nanotube/epoxy nanocomposites. *Nanotechnology*, **19**, 475503/1–475503/5 (2008). DOI: [10.1088/0957-4484/19/47/475503](https://doi.org/10.1088/0957-4484/19/47/475503)
- [15] Wang L., Wang X., Li Y.: Relation between repeated uniaxial compressive pressure and electrical resistance of carbon nanotube filled silicone rubber composite. *Composites Part A: Applied Science and Manufacturing*, **43**, 268–274 (2012). DOI: [10.1016/j.compositesa.2011.10.017](https://doi.org/10.1016/j.compositesa.2011.10.017)
- [16] Park J-M., Kim P-G., Jang J-H., Wang Z., Kim J-W., Lee W-I., Park J-G., DeVries L. K.: Self-sensing and dispersive evaluation of single carbon fiber/carbon nanotube (CNT)-epoxy composites using electromechanical technique and nondestructive acoustic emission. *Composites Part B: Engineering*, **39**, 1170–1182 (2008). DOI: [10.1016/j.compositesb.2008.03.004](https://doi.org/10.1016/j.compositesb.2008.03.004)
- [17] Abry J. C., Choi Y. K., Chateauminos A., Dalloz B., Giraud G., Salvia M.: In-situ monitoring of damage in CFRP laminates by means of AC and DC measurements. *Composites Science and Technology*, **61**, 855–864 (2001). DOI: [10.1016/S0266-3538\(00\)00181-0](https://doi.org/10.1016/S0266-3538(00)00181-0)
- [18] Kostopoulos V., Vavouliotis A., Karapappas P., Tsotra P., Paipetis A.: Damage monitoring of carbon fiber reinforced laminates using resistance measurements. Improving sensitivity using carbon nanotube doped epoxy matrix system. *Journal of Intelligent Material Systems and Structures*, **20**, 1025–1034 (2009). DOI: [10.1177/1045389X08099993](https://doi.org/10.1177/1045389X08099993)
- [19] Nofar M., Hoa S. V., Pugh M. D.: Failure detection and monitoring in polymer matrix composites subjected to static and dynamic loads using carbon nanotube networks. *Composites Science and Technology*, **69**, 1599–1606 (2009). DOI: [10.1016/j.compscitech.2009.03.010](https://doi.org/10.1016/j.compscitech.2009.03.010)
- [20] Vavouliotis A., Paipetis A., Kostopoulos V.: On the fatigue life prediction of CFRP laminates using the electrical resistance change method. *Composites Science and Technology*, **71**, 630–642 (2011). DOI: [10.1016/j.compscitech.2011.01.003](https://doi.org/10.1016/j.compscitech.2011.01.003)
- [21] Sotiriadis G., Tsotra P., Paipetis A., Kostopoulos V.: Stiffness degradation monitoring of carbon nanotube doped glass/vinylester composites via resistance measurements. *Journal of Nanostructured Polymers and Nanocomposites*, **3**, 90–95 (2007).

- [22] Böger L., Wichmann M. H. G., Meyer L. O., Schulte K.: Load and health monitoring in glass fibre reinforced composites with an electrically conductive nanocomposite epoxy matrix. *Composites Science and Technology*, **68**, 1886–1894 (2008).  
DOI: [10.1016/j.compscitech.2008.01.001](https://doi.org/10.1016/j.compscitech.2008.01.001)
- [23] Gao L., Thostenson E. T., Zhang Z., Chou T-W.: Coupled carbon nanotube network and acoustic emission monitoring for sensing of damage development in composites. *Carbon*, **47**, 1381–1388 (2009).  
DOI: [10.1016/j.carbon.2009.01.030](https://doi.org/10.1016/j.carbon.2009.01.030)
- [24] Baltopoulos A., Kostopoulos V., Pambaguian L.: Sensing capabilities of multifunctional composite materials using carbon nanotubes. in '61<sup>st</sup> International Astronautical Congress 2010 (IAC 2010), Prague, Czech Republic' Vol 13, 11004–11012 (2010).
- [25] Ortona A., D'Angelo C., Bianchi G.: Monitoring sandwich structured SiC ceramics integrity with electrical resistance. *NDT&E International*, **46**, 77–82 (2012).  
DOI: [10.1016/j.ndteint.2011.11.007](https://doi.org/10.1016/j.ndteint.2011.11.007)
- [26] Sevostianov I., Kováik J., Simanik F.: Correlation between elastic and electric properties for metal foams: Theory and experiment. *International Journal of Fracture*, **114**, 23–28 (2002).  
DOI: [10.1023/A:1022674130262](https://doi.org/10.1023/A:1022674130262)
- [27] Torres-Sánchez C., Corney J.: Identification of formation stages in a polymeric foam customised by sonication via electrical resistivity measurements. *Journal of Polymer Research*, **16**, 461–470 (2009).  
DOI: [10.1007/s10965-008-9249-4](https://doi.org/10.1007/s10965-008-9249-4)
- [28] Hutzler S., Verbist G., Weaire D., van der Steen J. A.: Measurement of foam density profiles using AC capacitance. *Europhysics Letters*, **31**, 497–502 (1995).  
DOI: [10.1209/0295-5075/31/8/013](https://doi.org/10.1209/0295-5075/31/8/013)
- [29] Brady S., Diamond D., Lau K-T.: Inherently conducting polymer modified polyurethane smart foam for pressure sensing. *Sensors and Actuators A: Physical*, **119**, 398–404 (2005).  
DOI: [10.1016/j.sna.2004.10.020](https://doi.org/10.1016/j.sna.2004.10.020)
- [30] Kim A., Hasan M. A., Nahm S. H., Cho S. S.: Evaluation of compressive mechanical properties of Al-foams using electrical conductivity. *Composite Structures*, **71**, 191–198 (2005).  
DOI: [10.1016/j.compstruct.2004.10.016](https://doi.org/10.1016/j.compstruct.2004.10.016)
- [31] Vavouliotis A., Fiamegou E., Karapappas P., Psarras G. C., Kostopoulos V.: DC and AC conductivity in epoxy resin/multiwall carbon nanotubes percolative system. *Polymer Composites*, **31**, 1874–1880 (2010).  
DOI: [10.1002/pc.20981](https://doi.org/10.1002/pc.20981)
- [32] Vavouliotis A., Karapappas P., Loutas T., Voyatzi T., Paipetis A., Kostopoulos V.: Multistage fatigue life monitoring on carbon fibre reinforced polymers enhanced with multiwall carbon nanotubes. *Plastics, Rubber and Composites*, **38**, 124–130 (2009).  
DOI: [10.1179/174328909X387928](https://doi.org/10.1179/174328909X387928)
- [33] Huang Y. Y., Terentjev E. M.: Dispersion of carbon nanotubes: Mixing, sonication, stabilization, and composite properties. *Polymers*, **4**, 275–295 (2012).  
DOI: [10.3390/polym4010275](https://doi.org/10.3390/polym4010275)
- [34] Yan D., Xu L., Chen C., Tang J., Ji X., Li Z.: Enhanced mechanical and thermal properties of rigid polyurethane foam composites containing graphene nanosheets and carbon nanotubes. *Polymer International*, **61**, 1107–1114 (2012).  
DOI: [10.1002/pi.4188](https://doi.org/10.1002/pi.4188)
- [35] Saha M. C., Kabir Md. E., Jeelani S.: Enhancement in thermal and mechanical properties of polyurethane foam infused with nanoparticles. *Materials Science and Engineering A*, **479**, 213–222 (2008).  
DOI: [10.1016/j.msea.2007.06.060](https://doi.org/10.1016/j.msea.2007.06.060)
- [36] Rusch K. C.: Load-compression behavior of brittle foams. *Journal of Applied Polymer Science*, **14**, 1263–1273 (1970).  
DOI: [10.1002/app.1970.070140514](https://doi.org/10.1002/app.1970.070140514)
- [37] Ku-Herrera J. J., Avilés F.: Cyclic tension and compression piezoresistivity of carbon nanotube/vinyl ester composites in the elastic and plastic regimes. *Carbon*, **50**, 2592–2598 (2012).  
DOI: [10.1016/j.carbon.2012.02.018](https://doi.org/10.1016/j.carbon.2012.02.018)
- [38] Gibson L. J., Ashby M. F.: *Cellular solids: Structure and properties* (second edition). Cambridge University Press, Cambridge (1997).
- [39] Deschanel S., Vanel L., Godin N., Maire E., Vigier G., Ciliberto S.: Mechanical response and fracture dynamics of polymeric foams. *Journal of Physics D: Applied Physics*, **42**, 214001/1–214001/14 (2009).  
DOI: [10.1088/0022-3727/42/21/214001](https://doi.org/10.1088/0022-3727/42/21/214001)
- [40] Rusch K. C.: Energy-absorbing characteristics of foamed polymers. *Journal of Applied Polymer Science*, **14**, 1433–1447 (1970).  
DOI: [10.1002/app.1970.070140603](https://doi.org/10.1002/app.1970.070140603)
- [41] Zhang J., Lin Z., Wong A., Kikuchi N., Li V. C., Yee A. F., Nusholtz G. S.: Constitutive modeling and material characterization of polymeric foams. *Journal of Engineering Materials and Technology*, **119**, 284–291 (1997).  
DOI: [10.1115/1.2812258](https://doi.org/10.1115/1.2812258)
- [42] Baltopoulos A., Vavouliotis A., Kostopoulos V., Polydorides N., Pambaguian L.: Electrical tomography as a tool for non-destructive assessment of composite structures. in 'Emerging technologies in non-destructive testing V' (eds.: Paipetis A. S., Matikas T. E., Aggelis D. G., Van Hemelrijck D.) CRC Press, Boca Raton, 389–394 (2012).  
DOI: [10.1201/b11837-70](https://doi.org/10.1201/b11837-70)

# Fabrication and formation mechanism of poly(L-lactic acid) ultrafine multi-porous hollow fiber by electrospinning

Q. Z. Yu\*, Y. M. Qin

College of Materials and Textile Engineering, Zhejiang Materials and Light Chemical and Textile Engineering Experiment Center, Jiaxing University, 314001 Jiaxing Zhejiang, P. R. China

Received 16 June 2012; accepted in revised form 22 August 2012

**Abstract.** Poly(L-lactic acid) (PLLA) ultrafine multi-porous hollow fibers are fabricated by electrospinning with methylene dichloride as solvent. The Kirkendall effect has been widely applied for the fabrication of hollow structure in metals and inorganic materials. In this study, a conceptual extension is proposed for the formation mechanism: the development of porous hollow fiber undergoes three stages. The initial stage is the generation of small voids or pits on the surface of the fiber via surface diffusion and phase separation; the second stage is the formation of multi-pores penetrating the core of the fiber through the interaction of Kirkendall effect, surface diffusion and phase separation; the third stage is dominated by surface diffusion of the core material along the pore surface. To explore the formation conditions, the factors including ambient temperature, relative humidity (R. H.), molecular weight and fiber diameter are studied. The longitudinal and cross sectional morphologies of these fibers are examined by scanning electron micrograph (SEM). The results show that the prerequisite for the formation of uniform porous hollow PLLA fibers include moderate ambient temperature (10~20°C) and appropriate molecular weight for the PLLA, as well as the diameter of the fiber in the range of several micrometers to about 100 nanometers.

**Keywords:** biodegradable polymers, electrospinning, multi-porous hollow fiber, microstructure, mechanism

## 1. Introduction

Many of the applications of electrospun fibers could be greatly enhanced by increasing the surface area and porosity of the fibers. To this purpose, reliable production of porous nanofibers in a simple and inexpensive way has been attempted by a number of groups. Previous methods of producing porous polymer fibers relied on either the electrospinning of blends followed by selective removal of one of the phases or phase separation based on the evaporation of solvent or in the presence of vapor.

PLLA nonwoven fibrous matrices have been widely used in various tissue regenerative therapies because of their excellent mechanical properties and biocompatibility [1–3]. Many researchers have engaged

in fabricating multi-porous PLLA fiber membrane with various methods. Lee and his coworker [4] fabricated dual-porosity structure PLLA/MMT fibers by combining electrospinning with salt leaching method. Qi *et al.* [5] fabricated PLLA fibers with micro- and nano-porous structure by electrospinning a ternary system of nonsolvent/solvent/PLLA. It is reported by Zhang *et al.* [6] when PLLA was dissolved in dimethylformamide (DMF) and methylene chloride (CH<sub>2</sub>Cl<sub>2</sub>) mixed solvent with different ratios, semi-hollow fiber with porous inner structure and compact shell wall was formed by controlling the content of DMF in the mixed solvents. But there is little report that the micro- and nano-porous outer structures of PLLA ultrafine hollow fibers were

\*Corresponding author, e-mail: [w2003yqz@126.com](mailto:w2003yqz@126.com)

fabricated only by electrospinning with only one solvent. Although Bognitzki *et al.* [7] reported the use of dichloromethane yielded PLLA fibers with a regular pore structure by electrospinning and considered the regular phase morphology is generated by rapid phase separation during the electrospinning process. There has been no report about the fabrication of PLLA ultrafine hollow fibers with multi-porous outer structure by electrospinning and detailed analysis about the formation mechanism of this structure.

The Kirkendall effect is a classical phenomenon in metallurgy [8–9]. It basically refers to a non-equilibrium mutual diffusion process through an interface of two metals so that vacancy diffusion occurs to compensate for the unequal material flow. Atomic diffusion occurs through vacancy exchange and not by the direct interchange of atoms. The net directional flow of matter is balanced by an opposite flow of vacancies, which can condense into pores or annihilate at dislocations. In a spherical material system where the fast-diffusion phase is enclosed by the slower one, the Kirkendall effect can also apply and manifest itself by forming hollow crystals composed of a compound shell. Coming to the nanoscale, due to the structural perfection and wide availability of single crystal metal nanoparticles, the Kirkendall effect can result in smooth and uniform-sized hollow compound nanocrystals [10–12]. An extension to cylindrical nanotubes has recently been reported via either a solid – solution, solid – gas, or solid – solid reaction [13–16].

In this paper, PLLA ultrafine hollow fibers with multi-porous outer structure were prepared only by electrospinning with only one solvent. The exact growth mechanism for the formation of this structure is still under investigation, but on the basis of experimental observations, a mechanism based on the ‘Kirkendall effect + surface diffusion’ model [8] was proposed.

## 2. Experimental section

### 2.1. Materials

PLLA ( $M_w$ : 100 000~70 000,  $M_w/M_n$ : 1.40) chips were purchased from Jiaying Haobang Science and Technology Development Co., Jiaying, China. Methylene dichloride, A. R., was supplied from Guoyao Chemical Company, Shanghai, China. Hexafluoroisopropanol (HFIP), A. R., was purchased from

Huaweiruike Chemical Limited Company, Beijing, China. Pyrrole monomer was distilled under reduced pressure and stored below 0°C. All the other reagents were analytical grade, and were used without further purification.

## 2.2. Preparation

### 2.2.1. Preparation of PLLA fibers

10 or 12 wt% PLLA in methylene dichloride or HFIP was prepared by dissolving PLLA chips in methylene dichloride or HFIP under magnetic stirring for at least 5 hrs, the solution was held in a syringe for electrospinning. A voltage of 12 kV was applied to the solution and the fibers were collected on the flat aluminum plate. The distance from the tip of the nozzle to the collector was 15 cm.

### 2.2.2. Preparation of PLLA/polypyrrole(PPy) composite fibers

PPy was introduced by the *in situ* polymerization on the surface of the obtained PLLA fibers mentioned above section. Typically, 0.25 g of pyrrole was dissolved in 20 mL of 1 M H<sub>2</sub>SO<sub>4</sub> solution with stirring. Some PLLA fibers with a length of 200 mm immersed into the above solution followed by ultrasonication for 30 min to allow the fibers to be saturated with the pyrrole solution. 0.61 g of ammonium persulfate (APS) in 20 mL of 1 M H<sub>2</sub>SO<sub>4</sub> solution was added dropwise to the above mixture with the ultrasonic aided dispersing. Then the polymerization proceeded for 5 h without any dispersing. The fibers were then washed 3 times with 40 mL of deionized water and acetone in sequence. Finally, the fibers were dried under vacuum and stored for usage.

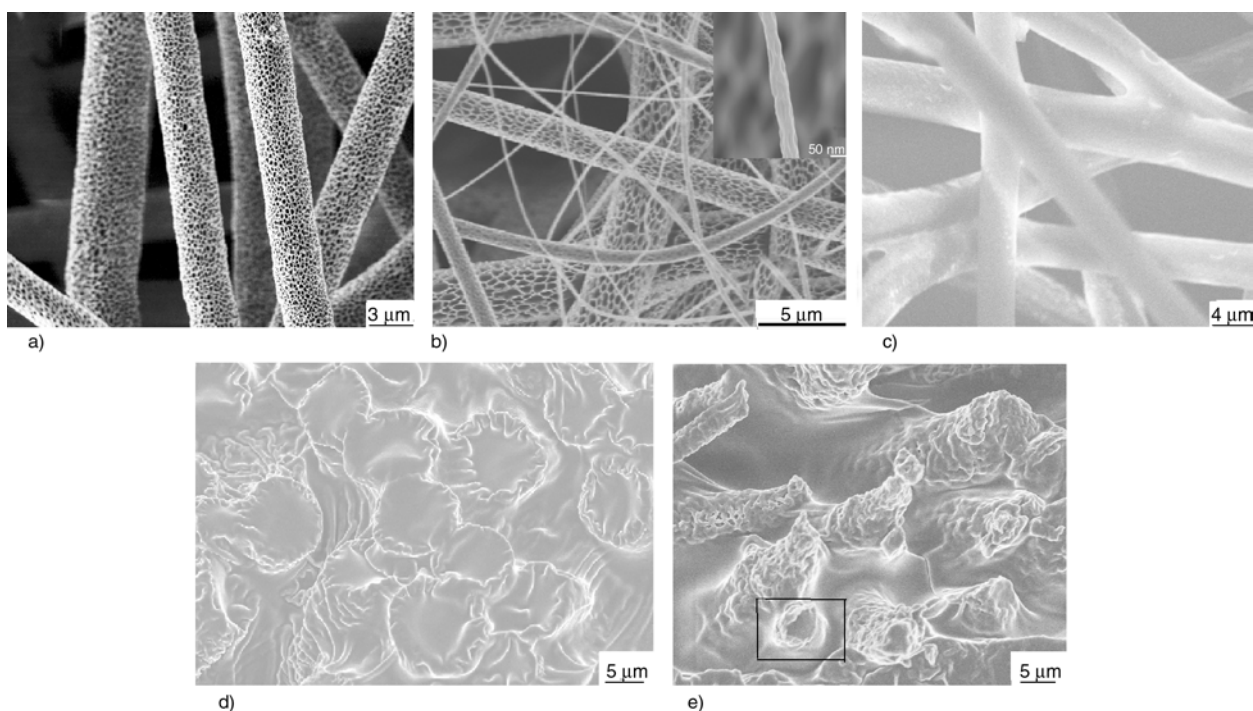
## 2.3. Characterization

The morphologies of electrospun PLLA fibers fabricated under different conditions were observed using Hitachi JSM–5510 SEM. The specimen used for imaging the cross-section of the electrospun fiber was prepared by dropping a drop of collodion on the sample, followed by cutting with a sharp knife.

## 3. Results and discussion

Fixing the PLLA weight percent [wt%] in methylene dichloride at 12 wt%, the SEM images of fibers fabricated at 15°C and different R. H. are shown in

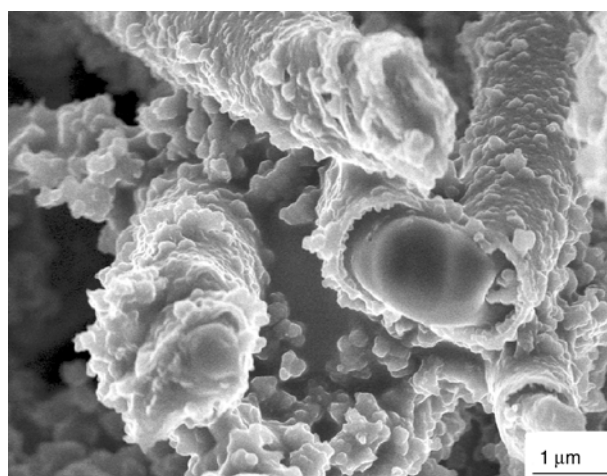




**Figure 1.** SEM images of the fibers fabricated at 15°C and different R. H. (a) 28%, with higher molecular weight ( $M_W$ : 100 000,  $M_W/M_n$ : 1.40) PLLA; (b) 49%, the inset is the corresponding higher-magnification image of a nanofiber, with higher molecular weight ( $M_W$ : 100 000,  $M_W/M_n$ : 1.40) PLLA; (c) 49%, with lower molecular weight ( $M_W$ : 70 000,  $M_W/M_n$ : 1.40) PLLA; (d) cross section of (a); (e) cross section of (b).

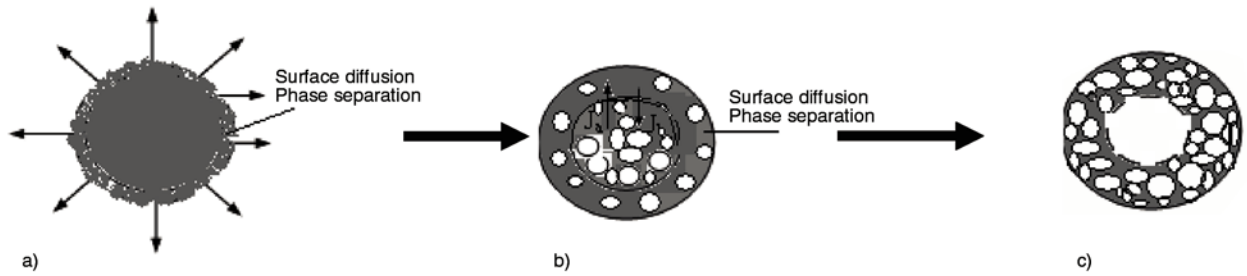
Figure 1. Figure 1a–1c is the longitudinal morphologies of these fibers and Figure 1d–1e is the corresponding cross-sectional one. From Figure 1, it can be found that most fibers are multi-porous fibers with diameters ranging from 3 to 7.2  $\mu\text{m}$ , but the fibers fabricated at 15°C, 28% R. H. are more uniform in diameter and pore size than those fabricated at 15°C, 49% R. H. The most interesting thing is that, from Figure 1d–1e, we noticed that some fibers with diameters range from 3 to 7.2  $\mu\text{m}$  not only have multi-porous outer structure, but also have visible holes in the inner region of the fibers. That is, these fibers are hollow fibers with multi-porous outer structure; although the holes of some fibers are closed because of becoming too soft to maintain the shape when they were cut and at the action of the solidification of collodion.

To further confirm the hollow structure, these PLLA fibers were used as matrix to fabricate PLLA/PPy composite fibers by *in situ* polymerization. The obtained PLLA/PPy composite fibers have obvious core-shell structure and smooth fractured surface of the core, as shown in Figure 2 [17]. This fact demonstrates these PLLA fibers are really hollow fibers.



**Figure 2.** SEM image of the cross section of PLLA/PPy micro fibers [17]

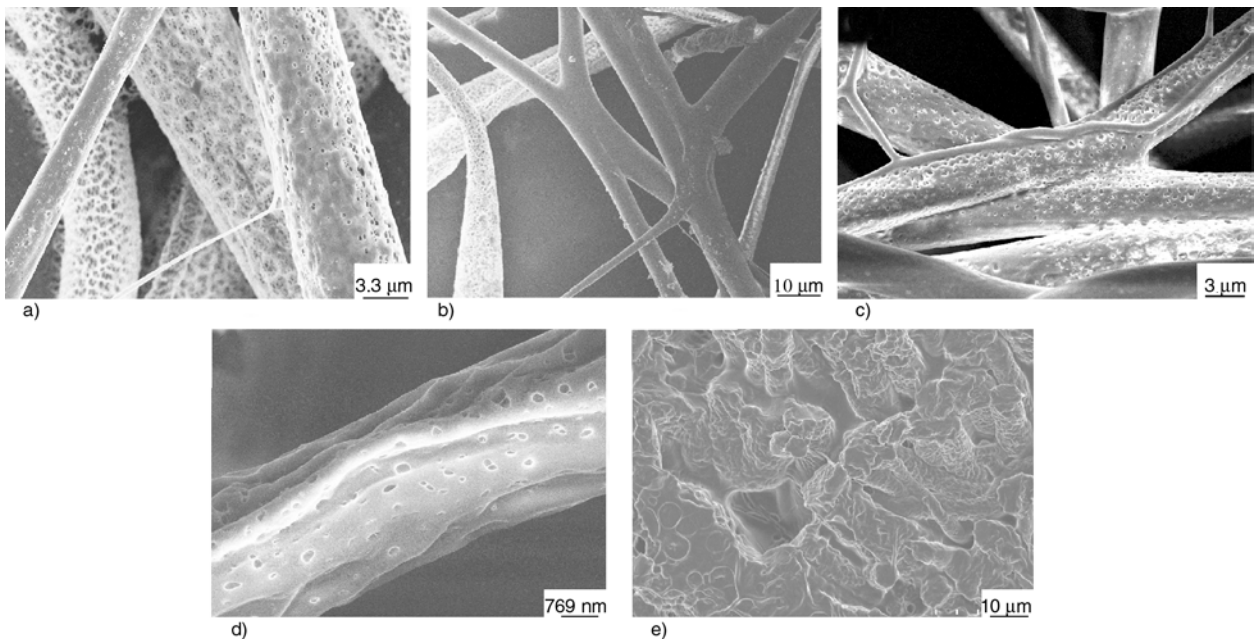
Some reports [7] considered the formation of pores or pits in the electrospinning fibers controlled by a rapid phase separation induced by the evaporation of the solvent and a subsequent rapid solidification. The exact mechanism of porous hollow fiber fabricated by electrospinning with only one solvent is not fully understood. Here, we propose a formation mechanism based on the void formation in ‘Kirk-



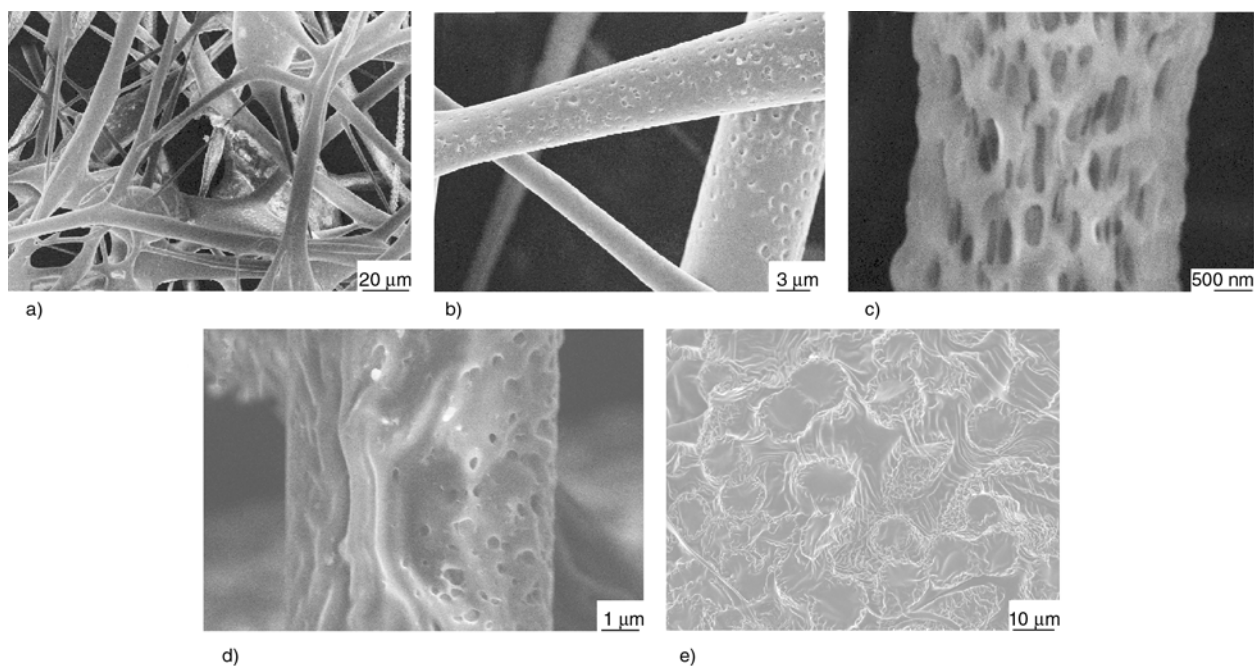
**Figure 3.** Simplified schematic representation of the formation of porous hollow structure (cross section) (a) the initial stage, (b) the second stage, (c) the third stage

endall effect + surface diffusion' model [16]. Figure 3 shows schematically this generalized model. In the initial stage (Figure 3a), due to the rapid volatilization of the methylene dichloride through surface diffusion result in the dropping of the surface temperature, the phase separation occur and form the voids or pits on the surface of the fiber [16]. In the second stage (Figure 3b), driven by concentration gradient, the methylene dichloride molecules diffuse outward continuously and the PLLA molecular chains condense inward. The mutual diffusion rates of the methylene dichloride and PLLA molecular differ by a considerable amount. For the diffusion flux,  $J_a > J_b$  ( $a$  index methylene dichloride and  $b$  index PLLA). A large quantity of vacancies diffusion occur to compensate for the unequal material flow between methylene dichloride molecules and PLLA molecular chains, the voids are enclosed by the slower PLLA molecular chains. In a sub-micro

system, due to the finite volume and spatial confinement, a high vacancy supersaturation can readily be reached [10]. Thus, the voids have a high chance to touch the outer layer of the fiber, resulting in the multi-pores penetrating the core of the fiber. The voids coalesce into bigger ones and touch the compound layer ab, on one hand breaking the connection between PLLA molecular chains and on the other hand establishing new bridges as fast transport paths for the methylene dichloride molecules. At this stage (Figure 3c), diffusion of molecules of the remaining methylene dichloride along the bridges, i.e. the pore surface, to the reaction front becomes the dominant material transport process. The methylene dichloride can redistribute itself at the open surface of the methylene dichloride and PLLA mixture via fast surface diffusion. While within the methylene dichloride and PLLA mixture, the material exchange mechanism remains the



**Figure 4.** SEM images of the fibers fabricated at (a) and (b) 26°C, 50% R. H.; (c) and (d) 26°C, 80% R. H.; (e) cross section of (a). PLLA weight percent in methylene dichloride was 12 wt%.



**Figure 5.** (a) SEM images of the fibers fabricated at 34°C, 60% R. H. (b), (c) and (d) the corresponding high magnification of (a) in different sections; (e) cross section of (a). PLLA weight percent in methylene dichloride at 12 wt%.

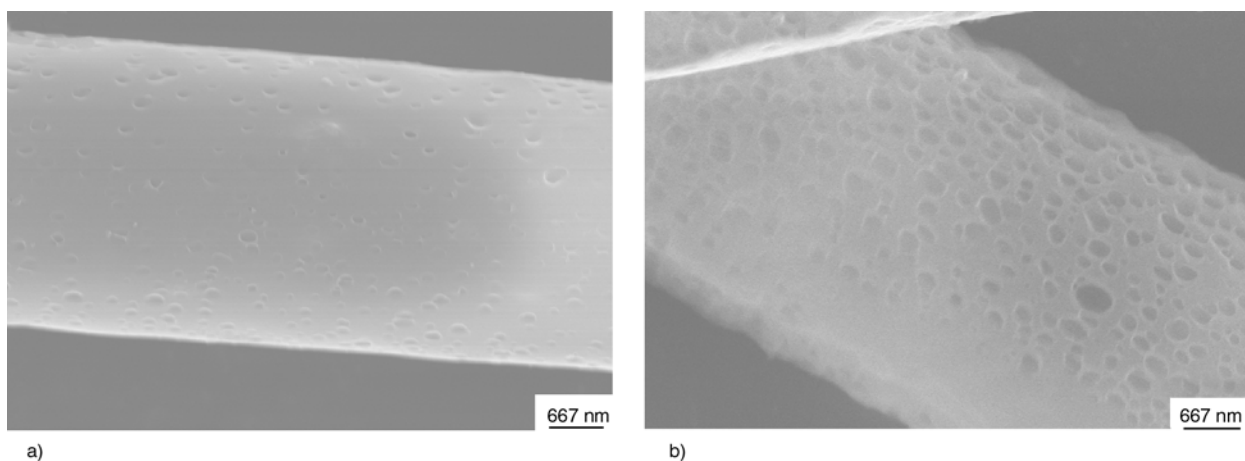
same, viz. bulk interdiffusion associated with Kirkendall effect. Therefore vacancies are continuously generated and flow inward. The hollow multi-porous fiber is formed.

To further explore the formation conditions, we fabricated some fibers above 20°C. When the ambient temperature was above 20°C, the obtained fibers with diameters of several micrometers are not uniform in both the morphologies and diameters, as shown in Figures 4–5. Some sections of the fibers only have some pits on the surface; while some sections have no visible pores. Moreover, the pore size and distribution of the pores in the sections with multi-pores are also not uniform; while some sections also have multi-pores penetrating the core of the fiber (Figures 4a, 4e and Figures 4c–4e).

These indicate that under too high ambient temperature (above 20°C), the electrospinning jet is unstable due to the rapid volatilization of the solvent through surface diffusion. It can be confirmed by observing the shapes of the jets.

Appropriate ambient temperature is the prerequisite to fabricate uniform porous hollow PLLA fibers by electrospinning. As we know, the boiling temperature of methylene dichloride is 39.8°C. The closer the ambient temperature to the methylene dichloride boiling temperature is, the higher its volatilization rate is.

In addition, the collapsed wrinkled skins are also found on some sections of the fibers (Figure 4d and Figure 5d). One of the explanations is that at high ambient temperature, especially when it is near its boiling temperature, the solvent evaporation rate is very high through fast surface diffusion, and this might induce the formation of fibers with sheath-core structure due to the different solidification speed between the outer layer and the inner layer. The further solidification and shrinkage of the core would result in local collapse of outer layer [18, 19]. The surface diffusion and phase separation resulted in pits on the surface of nanofibers with a diameter smaller than about 50 nm, as shown in the inset of Figure 1b. Surface diffusion becomes the dominant solvent transport process due to the very higher surface area in the nanofibers. The rapid evaporation of methylene dichloride on the surface of the fibers and fast solidification induce the formation of fibers with sheath-core structure. The further solidification and shrinkage of the core result in pits occurred on the surface of the fibers. If the fibers with a diameter larger than several micrometers, due to the large space, a high vacancy supersaturation will be difficult to be reached. Thus, the voids have a low chance to touch the outer layer of the fiber, resulting in some pits not penetrating the core of the fiber.



**Figure 6.** SEM images of the fibers fabricated at 8°C, 45% R. H. with different PLLA concentrations (a) 10 wt%; (b) 8 wt%, PLLA  $M_w$  was 100 000 and  $M_w/M_n$  was 1.40

As weight percent of PLLA is fixed at 12 wt%, using the lower molecular weight PLLA ( $M_w$ : 70 000,  $M_w/M_n$ : 1.40) to electrospin the PLLA fibers, the obtained fibers only have pits on their surface, as shown in Figure 1c. The low molecular weight PLLA has high molar percent of polymer molecular, which upon methylene dichloride evaporation contributes to retain less methylene dichloride to form porous surface [20]. In addition, the low molecular weight PLLA has more molecules with relatively lower molecular weight and shorter molecular chains, the diffuse rate of these PLLA molecules are higher than those PLLA molecules with higher molecular weight, and result in less quantity of vacancies diffusion resulting from Kirkendall effect occur to compensate for the unequal material flow between methylene dichloride molecules and PLLA molecular chain. Thus, it will become difficult to reach a high vacancy supersaturation and reduce the chance of voids to touch the outer layer of the fiber, resulting in some pits not penetrating the core of the fiber.

We also observed the PLLA fibers fabricated by electrospinning at 8°C have only pits on the surface, as shown in Figure 6. Moreover, the pits enlarged with the PLLA concentration decreased. This is because of the low temperature result in slow evaporation rate and diffusion rate of methylene dichloride, forming fewer vacancies and low gas pressure within the fibers. Thus it is difficult to form enough large pores.

This can be confirmed by using HFIP, which has lower volatilization rate than that of  $\text{CH}_2\text{Cl}_2$  at the

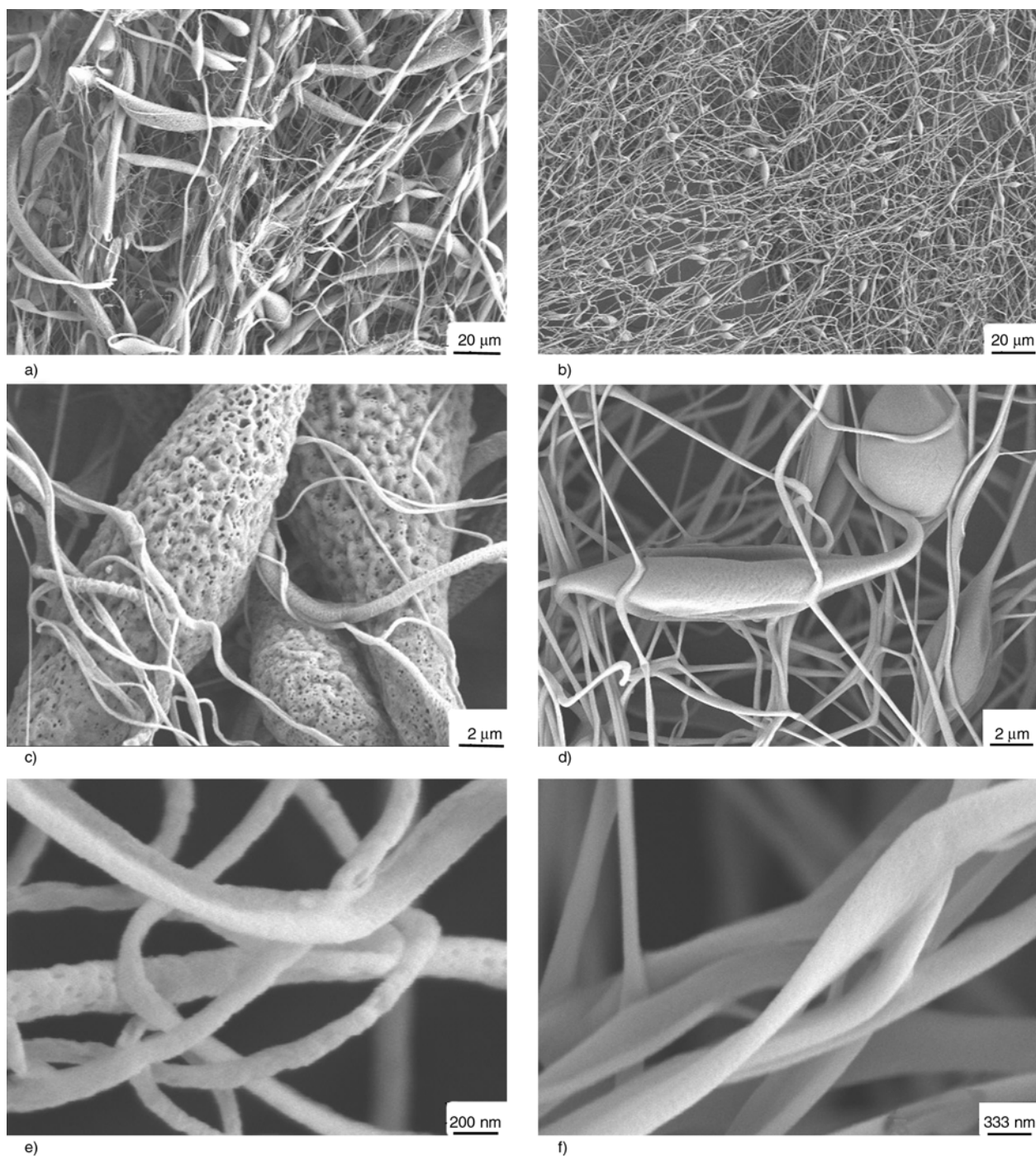
same ambient temperature, as the solvent for PLLA solution. Figures 7a, 7c, 7e and Figures 7b, 7d, 7f are the SEM images of the samples fabricated by using  $\text{CH}_2\text{Cl}_2$  or HFIP as solvent, respectively. It can be seen that the obtained fibers all have beads due to the low viscosity, but it can be obviously seen that the fibers fabricated by using  $\text{CH}_2\text{Cl}_2$  as solvent are multi-porous fibers while the fibers fabricated by using HFIP as solvent are not (Figure 7f), only some pits can be found even in the bigger beads (Figure 7d).

#### 4. Conclusions

PLLA hollow fiber with multi-porous outer structure can be fabricated by electrospinning with only one solvent. But it must be fabricated at moderate ambient temperature (10~20°C), using appropriate molecular weight ( $M_w$ : about 100 000,  $M_w/M_n$ : about 1.40) PLLA to electrospin and has a diameter in the range of several micrometers to 100 nanometers.

The formation of multi-porous hollow fiber is a complex process. We propose a formation mechanism of the result of mutual action of ‘Kirkendall effect, surface diffusion and phase separation’.

We believe the technique described here can be extended to many other materials for the fabrication of such kind of fibrous scaffolds with potential applications not only in tissue engineering, but also in catalysis, sensing, encapsulation, drug delivery and filtration.



**Figure 7.** SEM images of the fibers fabricated by different solvent (a)  $\text{CH}_2\text{Cl}_2$ , (c) and (e) the corresponding high magnification of (a) in different sections; (b) HFIP, (d) and (f) the corresponding high magnification of (b) in different sections. The ambient temperature was  $28^\circ\text{C}$ , and R. H. was 25%. PLLA weight percent in solvent was 10 wt%. PLLA  $M_w$  was 100 000 and  $M_w/M_n$  was 1.40.

### Acknowledgements

This work was supported by the National Natural Science Foundation of China (No. 51073072), the Zhejiang Provincial Natural Science Foundation of China (No. Y4100745), the Key Laboratory Open Foundation of Advanced Textile Materials & Manufacturing Technology of Zhejiang Sci-Tech University from Ministry of Education of China (No. 2009007)

### References

- [1] Scaffaro R., Morreale M., Mirabella F., La Mantia F. P.: Preparation and recycling of plasticized PLA. *Macromolecular Materials and Engineering*, **296**, 141–150 (2011).  
DOI: [10.1002/mame.201000221](https://doi.org/10.1002/mame.201000221)

- [2] Rajeswari R., Sundarrajan S., Venugopal J. R., Mukherjee S., Ramakrishna S.: Advances in polymeric systems for tissue engineering and biomedical applications. *Macromolecular Bioscience*, **12**, 286–311 (2012). DOI: [10.1002/mabi.201100325](https://doi.org/10.1002/mabi.201100325)
- [3] Naveena N., Venugopal J., Rajeswari R., Sundarrajan S., Sridhar R., Shayanti M., Narayanan S., Ramakrishna S.: Biomimetic composites and stem cells interaction for bone and cartilage tissue regeneration. *Journal of Materials Chemistry*, **22**, 5239–5253 (2012). DOI: [10.1039/C1JM14401D](https://doi.org/10.1039/C1JM14401D)
- [4] Lee Y. H., Lee J. H., An I-G., Kim C., Lee D. S., Lee Y. K., Nam J-D.: Electrospun dual-porosity structure and biodegradation morphology of Montmorillonite reinforced PLLA nanocomposite scaffolds. *Biomaterials*, **26**, 3165–3172 (2005). DOI: [10.1016/j.biomaterials.2004.08.018](https://doi.org/10.1016/j.biomaterials.2004.08.018)
- [5] Qi Z., Yu H., Chen Y., Zhu M.: Highly porous fibers prepared by electrospinning a ternary system of non-solvent/solvent/poly(L-lactic acid). *Materials Letters*, **63**, 415–418 (2009). DOI: [10.1016/j.matlet.2008.10.059](https://doi.org/10.1016/j.matlet.2008.10.059)
- [6] Zhang K., Wang X., Jing D., Yang Y., Zhu M.: Bionic electrospun ultrafine fibrous poly(L-lactic acid) scaffolds with a multi-scale structure. *Biomedical Materials*, **4**, 035004/1–035004/7 (2009). DOI: [10.1088/1748-6041/4/3/035004](https://doi.org/10.1088/1748-6041/4/3/035004)
- [7] Bognitzki M., Czado W., Frese T., Schaper A., Hellwig M., Steinhart M., Greiner A., Wendorff J. H.: Nanostructured fibers via electrospinning. *Advanced Materials*, **13**, 70–79 (2001). DOI: [10.1002/1521-4095\(200101\)13:1<70::AID-ADMA70>3.0.CO;2-H](https://doi.org/10.1002/1521-4095(200101)13:1<70::AID-ADMA70>3.0.CO;2-H)
- [8] Fan H. J., Knez M., Scholz R., Hesse D., Nielsch K., Zacharias M., Gösele U.: Influence of surface diffusion on the formation of hollow nanostructures induced by the Kirkendall effect: The basic concept. *Nano Letters*, **7**, 993–997 (2007). DOI: [10.1021/nl070026p](https://doi.org/10.1021/nl070026p)
- [9] Drechsel H., Brechtmann C., Heinrich W., Dreute J., Benton E. V.: Search for anomalous fragments produced in collisions with heavy target nuclei and in  $\Delta Z = 1$  peripheral interactions. *Physical Review Letters*, **54**, 1258–1261 (1985). DOI: [10.1103/PhysRevLett.55.1258](https://doi.org/10.1103/PhysRevLett.55.1258)
- [10] Yin Y., Rioux R. M., Erdonmez C. K., Hughes S., Somorjai G. A., Alvisatos A. P.: Formation of hollow nanocrystals through the nanoscale Kirkendall effect. *Science*, **304**, 711–714 (2004). DOI: [10.1126/science.1096566](https://doi.org/10.1126/science.1096566)
- [11] Wang Y., Cai L., Xia Y.: Monodisperse spherical colloids of Pb and their use as chemical templates to produce hollow particles. *Advanced Materials*, **17**, 473–477 (2005). DOI: [10.1002/adma.200401416](https://doi.org/10.1002/adma.200401416)
- [12] Gao J., Zhang B., Zhang X., Xu B.: Magnetic-dipolar-interaction-induced self-assembly affords wires of hollow nanocrystals of cobalt selenide. *Angewandte Chemie International Edition*, **118**, 1242–1245 (2006). DOI: [10.1002/ange.200503486](https://doi.org/10.1002/ange.200503486)
- [13] Li Q., Penner R. M.: Photoconductive cadmium sulfide hemicylindrical shell nanowire ensembles. *Nano Letters*, **5**, 1720–1725 (2005). DOI: [10.1021/nl050994x](https://doi.org/10.1021/nl050994x)
- [14] Fan H. J., Knez M., Scholz R., Nielsch K., Pippel E., Hesse D., Zacharias M., Gösele U.: Monocrystalline spinel nanotube fabrication based on the Kirkendall effect. *Nature Materials*, **5**, 627–631 (2006). DOI: [10.1038/nmat1673](https://doi.org/10.1038/nmat1673)
- [15] Ng C. H. B., Tan H., Fan W. Y.: Formation of Ag<sub>2</sub>Se nanotubes and dendrite-like structures from UV irradiation of a CSe<sub>2</sub>/Ag colloidal solution. *Langmuir*, **22**, 9712–9717 (2006). DOI: [10.1021/la061253u](https://doi.org/10.1021/la061253u)
- [16] Cao S., Hu B., Liu H.: Fabrication of nano-porous structured polylactide (PLLA) fibers through electrospinning. *Acta Polymerica Sinica*, **10**, 1193–1198 (2010). DOI: [10.3724/SP.J.1105.2010.09391](https://doi.org/10.3724/SP.J.1105.2010.09391)
- [17] Yu Q-Z., Dai Z-W., Lan P.: Fabrication of high conductivity dual multi-porous poly (L-lactic acid)/polypyrrole composite micro/nanofiber film. *Materials Science and Engineering B*, **176**, 913–920 (2011). DOI: [10.1016/j.mseb.2011.05.017](https://doi.org/10.1016/j.mseb.2011.05.017)
- [18] Koombhongse S., Liu W., Reneker D. H.: Flat polymer ribbons and other shapes by electrospinning. *Journal of Polymer Science Part B: Polymer Physics*, **39**, 2598–2606 (2001). DOI: [10.1002/polb.10015](https://doi.org/10.1002/polb.10015)
- [19] Yu Q-Z., Shi M-M., Deng M., Wang M., Chen H-Z.: Morphology and conductivity of polyaniline sub-micron fibers prepared by electrospinning. *Materials Science and Engineering: B*, **150**, 70–76 (2008). DOI: [10.1016/j.mseb.2008.02.008](https://doi.org/10.1016/j.mseb.2008.02.008)
- [20] Xia X., Dong X. J., Wei Q. F., Cai Y. B., Lu K. Y.: Formation mechanism of porous hollow SnO<sub>2</sub> nanofibers prepared by one-step electrospinning. *Express Polymer Letters*, **6**, 169–176 (2012). DOI: [10.3144/expresspolymlett.2012.18](https://doi.org/10.3144/expresspolymlett.2012.18)

# Photovoltaic properties and annealing effects of a low bandgap copolymer containing dithienothiophene and benzothiadiazole units

T. L. Wang<sup>1\*</sup>, Y. T. Shieh<sup>1</sup>, C. H. Yang<sup>1</sup>, T. H. Ho<sup>2</sup>, C. H. Chen<sup>3</sup>

<sup>1</sup>Department of Chemical and Materials Engineering, National University of Kaohsiung, 811 Kaohsiung, Taiwan, Republic of China

<sup>2</sup>Department of Chemical and Materials Engineering, National Kaohsiung University of Applied Sciences, 807 Kaohsiung, Taiwan, Republic of China

<sup>3</sup>Department of Electronic Engineering, Cheng Shiu University, 833 Kaohsiung, Taiwan, Republic of China

Received 13 June 2012; accepted in revised form 29 August 2012

**Abstract.** A conjugated alternating copolymer as the donor material of the active layer in polymer solar cells has been designed and synthesized via Stille coupling reaction. The alternating structure consisted of 3,5-didecanyldithieno[3,2-b:2',3'-d]thiophene (DDTT) donor unit and 5,6-bis(tetradecyloxy)benzo-2,1,3-thiadiazole (BT) acceptor unit. Since both units have been attached pendant chains, the polymer was soluble in common organic solvents. UV-vis spectrum exhibited a broad absorption band in the range of 270–780 nm and a low bandgap of 1.83 eV. The highest occupied molecular orbital (HOMO) and lowest unoccupied molecular orbital (LUMO) energy levels of the polymer were estimated to be –5.10 and –3.27 eV, respectively. Based on the ITO/PEDOT:PSS/PDDTTBT:PCBM/Al device structure, the power conversion efficiency (PCE) under the illumination of AM 1.5 (100 mW/cm<sup>2</sup>) was 0.127%. The effects of annealing temperature (50–150°C) for 30 min on the device performance were studied. It was found that PCE of 0.292% could be acquired under the annealing condition at 50°C for 30 min. The improved device efficiency under the optimal condition was confirmed by the higher light harvest in UV-vis spectra, the enhanced quenching of photoluminescence (PL) emission, and the improved nanoscale morphology by atomic force microscopy (AFM) examination.

**Keywords:** *nanomaterials, polymer solar cells, low bandgap, annealing*

## 1. Introduction

Over the past decades, polymer solar cells (PSCs) based on conjugated polymers have attracted considerable attention because of their potential use for future cheap and renewable energy production [1–3]. In particular, the polymer solar cell has the advantage over all photovoltaic technologies that the possible manufacturing speed is very high and the thermal budget is low because no high temperatures are needed [4]. Efficient polymer-based solar cells utilize donor–electron acceptor (D–A) bulk heterojunction (BHJ) films as active layers [1, 2].

The donor is typically a kind of conjugated polymer, while the acceptor is generally a type of organic or inorganic molecule. The most exploited donor polymers is regioregular poly(3-hexylthiophene) (P3HT), while the acceptor materials are generally the fullerene derivatives such as [6,6]-phenyl C<sub>61</sub> butyric acid methyl ester (PCBM). A bulk heterojunction photovoltaic device combining regioregular P3HT as the electron donor with functionalized fullerenes as the electron acceptor has demonstrated power conversion efficiencies (PCEs) up to 7% [5, 6].

\*Corresponding author, e-mail: [tlwang@nuk.edu.tw](mailto:tlwang@nuk.edu.tw)  
© BME-PT

However, the performance of the photovoltaic cells with these conjugated polymers is considerably limited by their relatively large bandgaps, which result in the mismatch of the absorption spectrum of the active layer and the solar emission, especially in the red and near-infrared ranges. Therefore, the development of the low bandgap donor polymers is of crucial importance for increasing the efficiency. One of the most promising strategies to tailor the energy levels of conjugated polymer is the donor-acceptor route because of the vast possibility in the unit combinations [7–11]. Many D–A type copolymers have been used in PSCs to achieve PCEs above 5% with extensive device engineering efforts [7, 12–14].

For the D–A type copolymers, much research work has been devoted to using the fused thiophene family as the donor due to its stable quinoid form resulting in a low bandgap accompanied by good electrochemical stability [15–17]. Molecules containing fused-ring systems can make the polymer backbone more rigid and coplanar, therefore enhancing effective  $\pi$ -conjugation, lowering bandgap and extending absorption. Introduction of thienothiophene units tends to stabilize the quinoid structure in the polymer chain and thus enhances the planarity along the polymer backbone. The high power conversion efficiency can be attributed to the rigidity and planarity of the polymer backbone, leading to a high hole mobility of the copolymer. In the case of fused-ring systems, dithieno[3,2-b:2',3'-d]thiophene (DTT) is well known as an important building block due to its high mobility [18, 19]. Recently, organic field-effect transistors (OFET) [20, 21] and PSCs [22, 23] containing dithieno[3,2-b:2',3'-d]thiophene (DTT) building block in the D–A type copolymers have been reported.

Recently, 2,1,3-benzothiadiazole (BT) has been utilized to construct some n-type semiconducting polymers showing high electron mobility [24–26]. It has also been used as the acceptor unit in cooperation with varieties of electron-donating (D) units as low bandgap donors in bulk heterojunction polymer solar cells [23, 27–30]. High hole mobility and wide optical absorption band could be achieved for the D–A type BT-containing polymers. Hence, this category of polymer donors has been extensively studied and has shown outstanding photovoltaic performances.

Based on this vision, the copolymer consisting of alternating DTT and BT units, where DTT and BT are adopted as the donor and acceptor segments, should be a promising material for the active layer of solar cells. Recently, this copolymer has been prepared and explored in roll-to-roll coating experiments [31–33]. However, the acquired PCEs of photovoltaic devices based on this polymer are still low. It may be helpful to raise the PCE via the bandgap engineering strategy. Since only alkyloxy side chains were attached on the BT unit in this copolymer, the highest occupied molecular orbital (HOMO) and lowest unoccupied molecular orbital (LUMO) energy levels of the polymer may be modified if pendant chains are attached to both the donor and acceptor units. Herein, we have synthesized a new D–A type copolymer consisting of alternating DTT and BT units, where the DTT and BT unit has pendent alkyl chains and alkyloxy chains, respectively. The optoelectronic properties, PCE and the effect of thermal annealing of the fabricated PSCs were investigated.

## 2. Experimental

### 2.1. Materials

Tetrabromothiophene (Alfa Aesar, USA), undecanal (Alfa Aesar, USA), ethyl mercaptoacetate (Acros, Belgium), n-butyllithium (Acros, Belgium), lithium hydroxide (Alfa Aesar, USA), tin(II) chloride (Alfa Aesar, USA), sodium bichromate (Showa Chemical Co., Japan), potassium carbonate (Showa Chemical Co., Japan), triethylamine (Acros, Belgium), *N*-thionylaniline (TCI, Japan), trimethyltin chloride (Acros, Belgium), bis(triphenylphosphine) palladium(II) dichloride (Alfa Aesar, USA), poly(3,4-ethylenedioxythiophene)-poly(styrenesulfonate) (PEDOT:PSS, Aldrich, USA) and phenyl-C<sub>61</sub>-butyric acid methyl ester (PCBM, FEM Tech., Germany) were used as received. All other reagents were used as received.

### 2.2. Synthesis

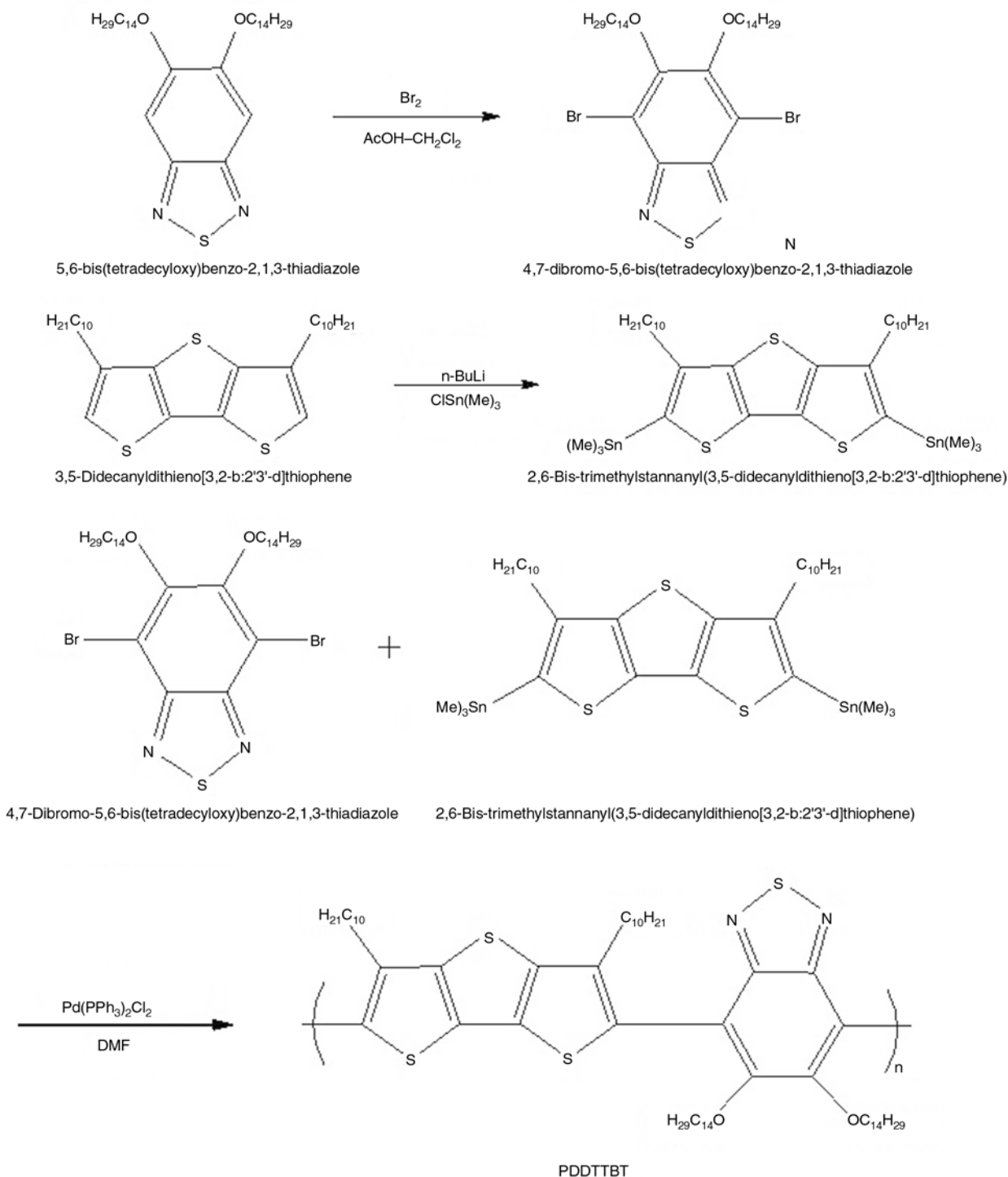
The donor material, 3,5-didecanyldithieno[3,2-b:2',3'-d]thiophene (DDTT), was prepared according to a reported literature method [34]. The acceptor material, 5,6-bis(tetradecyloxy)benzo-2,1,3-thiadiazole (BT) was prepared according to the published procedures [35]. The copolymer poly(3,5-didecanyldithieno[3,2-b:2',3'-d]thiophene-2,6-diyl-



*alt*-5,6-bis(tetradecyloxy)benzo-2,1,3-thiadiazole-4,7-diyl (PDDTTBT) was synthesized via Stille coupling reaction of the donor unit of 2,6-bis-trimethylstannanyl-3,5-didecanyl dithieno[3,2-b:2',3'-d]thiophene with the acceptor unit of 4,7-dibromo-5,6-bis(tetradecyloxy)benzo-2,1,3-thiadiazole.

### 2.2.1. 2,6-Bis-trimethylstannanyl(3,5-didecanyldithieno[3,2-b:2',3'-d]thiophene)

To a solution of 3,5-didecanyldithieno[3,2-b:2',3'-d]thiophene (1.12 mmol) in THF (40 mL) was added dropwise *n*-BuLi (2.5 mmol, 1.6 M in hexane) at  $-78^{\circ}\text{C}$  under argon. The reaction was kept at  $-78^{\circ}\text{C}$  for 2 h. Then trimethylchlorostannane (2.5 mmol)



**Figure 1.** Synthesis of PDDTTBT copolymer

was added. The reaction mixture was allowed to warm to room temperature and react for 10 h, and it was poured into water (100 mL). The crude compound was extracted with dichloromethane three times. The combined organic layers were dried over anhydrous  $\text{MgSO}_4$  and evaporated to dryness. The residue was chromatographically purified on silica gel eluting with *n*-hexane/triethylamine (10:1, v:v) to afford the products as a viscous brown oil, which were used for the following reactions without further purification. The synthetic route is shown in Figure 1. Yield: 41%.  $^1\text{H NMR}$  (500 MHz,  $\text{CDCl}_3$ ,  $\delta$  ppm): 2.62 (t, 4H), 1.83 (m, 4H), 1.25 (m, 28H), 0.88 (t, 6H), 0.27 (s, 18H, Sn- $\text{CH}_3$ ).

### 2.2.2. 4,7-Dibromo-5,6-bis(tetradecyloxy)benzo-2,1,3-thiadiazole

5,6-Bis(tetradecyloxy)benzo-2,1,3-thiadiazole (2.5 mmol) was dissolved in 70 mL of dichloromethane under argon atmosphere. Excess  $\text{Br}_2$  (7.5 mmol) was dissolved in 30 mL of acetic acid and added into the solution. The reaction was stirred in the dark at room temperature for 48 h and then poured into water (100 mL). The organic layer was separated and the aqueous layer was extracted with dichloromethane. The combined organic layer was sequentially washed with de-ionized water, aq.  $\text{NaHCO}_3$  and aq.  $\text{Na}_2\text{SO}_3$  twice. The combined organic layers were dried over anhydrous  $\text{MgSO}_4$  and evaporated to dryness. The crude product was recrystallized from ethanol to give white needle-like crystals. The synthetic route is shown in Scheme 1. Yield: 82%.  $^1\text{H NMR}$  (500 MHz,  $\text{CDCl}_3$ ,  $\delta$  ppm): 4.15 (t, 4H), 1.87 (m, 4H), 1.57 (m, 4H), 1.37–1.26 (m, 40H), 0.88 (t, 6H).

### 2.2.3. Synthesis of D–A type copolymer (PDDTTBT)

In a 100 mL flask, the two monomers (1 mmol of each), 2,6-bis-trimethylstannanyl(3,5-didecanyldithieno[3,2-b:2'3'-d]thiophene) and 4,7-dibromo-5,6-bis(tetradecyloxy)benzo-2,1,3-thiadiazole were dissolved in 40 mL of dry DMF and then flashed by argon for 10 min. Following that, 0.02 mmol of  $\text{Pd}(\text{PPh}_3)_2\text{Cl}_2$  was added, and the reactant was purged by argon for another 20 min. The reaction mixture was then heated at  $120^\circ\text{C}$  for 48 h under the protection of argon. The sticky, deep gray solution was cooled and poured into 100 mL of methanol, where the crude polymer was precipitated and col-

lected as dark brown powder, which was then subjected to Soxhlet extraction with methanol, hexane, and THF. The polymer was recovered from the THF fraction by rotary evaporation. The synthetic route is shown in Figure 1. Yield: 43%.  $^1\text{H NMR}$  (500 MHz,  $\text{CDCl}_3$ ,  $\delta$  ppm): 4.15 (t, 4H), 2.62 (t, 4H), 1.76 (m, 4H), 1.56 (m, 4H), 1.30 (m, 4H), 1.27 (m, 68H), 0.88 (t, 12H). Anal. Calcd for  $(\text{C}_{62}\text{H}_{100}\text{N}_2\text{O}_2\text{S}_4)_n$ : C, 72.03; H, 9.75; N, 2.71. Found: C, 73.42; H, 9.24; N, 3.03. GPC (THF):  $\overline{M}_n = 6800$  g/mol,  $\overline{M}_w = 8200$  g/mol, PDI = 1.21.

### 2.3. Device fabrication and characterization

The device structure of the polymer photovoltaic cells in this study is ITO/PEDOT:PSS/PDDTTBT:PCBM/Al. PDDTTBT acts as the p-type donor polymer and PCBM as the n-type acceptor in the active layer. Before device fabrication, the glass substrates coated with indium tin oxide (ITO) were first cleaned by ultrasonic treatment in acetone, detergent, de-ionized water, methanol and isopropyl alcohol sequentially. The ITO surface was spin coated with ca. 80 nm layer of poly(3,4-ethylene dioxythiophene): poly(styrene) (PEDOT:PSS) in the nitrogen-filled glove-box. The substrate was dried for 10 min at  $150^\circ\text{C}$  and then continued to spin coating the active layer. The PDDTTBT:PCBM blend solutions were prepared with 1:1 weight ratio (10 mg/mL PDDTTBT) in 1,2-dichlorobenzene (DCB) as the active layer. This solution blend was spin-cast onto the PEDOT:PSS layer at 800 rpm for 30 s. The obtained thickness for the blend film of PDDTTBT:PCBM was ca. 110 nm. The devices were completed by evaporation of metal electrodes Al with area of  $6\text{ mm}^2$  defined by masks.

The films of active layers were annealed directly on top of a hot plate in the glove box, and the temperature is monitored by using a thermocouple touching the top of the substrates. After removal from the hotplate, the substrates are immediately put onto a metal plate at the room temperature. Ultraviolet-visible (UV-vis) spectroscopic analysis was conducted on a Perkin–Elmer Lambda 35 UV-vis spectrophotometer. Photoluminescence (PL) spectrum was recorded on a Hitachi F-7000 fluorescence spectrophotometer. After removing Al electrode, the film topography images of active layers were recorded with a Digital Instruments Dimension 3100 atomic force microscope (AFM) in tapping mode under ambient conditions. The  $J$ - $V$  curves were measured

using a Keithley 2400 source meter, under illumination from a solar simulator. The intensity of solar simulator was set with a primary reference cell and a spectral correction factor to give the performance under the AM 1.5 (100 mW/cm<sup>2</sup>) global reference spectrum (IEC 60904-9). External quantum efficiency (EQE) measurements were detected with a QE-3000 (Titan Electro-Optics Co., Ltd.) lock-in amplifier under monochromatic illumination. Calibration of the incident light was performed with a monocrystalline silicon diode.

### 3. Results and discussion

#### 3.1. Synthesis and characterization of the polymer

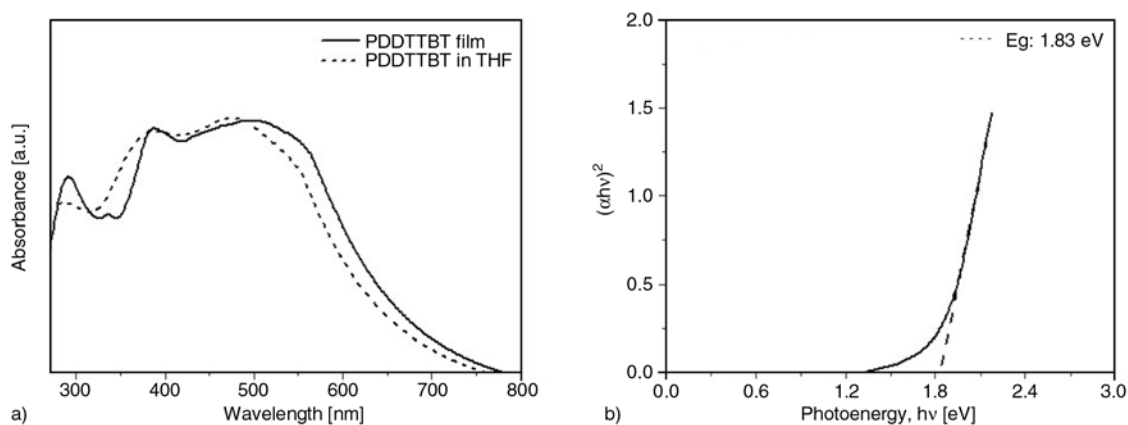
In this study, the D–A type copolymer consists of 3,5-didecanyldithieno[3,2-b:2',3'-d]thiophene (DDTT) and 2,1,3-benzothiadiazole (BT) because 2,1,3-benzothiadiazole (BT) is an electron-accepting heterocycle showing high electron mobility and DDTT is linearly symmetrical and coplanar thienothiophene unit. It is expected that wide sunlight absorption band and high power conversion efficiency could be achieved for the D–A type copolymer using DDTT as the donor and BT as the acceptor.

The synthetic route toward the polymer is outlined in Figure 1. The copolymer PDDTTBT was synthesized via Stille coupling reaction of the donor unit of 2,6-bis-trimethylstannanyl(3,5-didecanyldithieno[3,2-b:2',3'-d]thiophene) with the acceptor unit of 4,7-dibromo-5,6-bis(tetradecyloxy)benzo-2,1,3-thiadiazole. With the attachment of long alkyl and long alkyloxy side chains on the donor and acceptor unit respectively, the bandgap of the copolymer could be fine tuned and the solubility in organic phases increases. The structures of both monomers and

copolymer were confirmed by <sup>1</sup>H NMR and elemental analysis. The polymer is well dissolved in common organic solvents such as chloroform, 1,2-dichlorobenzene, THF, and toluene. Molecular weight of the polymer determined by gel permeation chromatography showed a low  $\bar{M}_n$  value of 6800, which might be due to the steric hindrance of both 3,5-dialkyl and 5,6-dialkyloxy substituent on the polymer backbone. Compared to the copolymer reported in a previous article [33], which has a similar structure without pendent alkyl chains on the donor (dithienothiophene) unit, the PDDTTBT polymer exhibited a lower glass transition temperature ( $T_g$ ) of 72°C due to the attachment of alkyl side chains on the donor unit.

#### 3.2. Optical properties

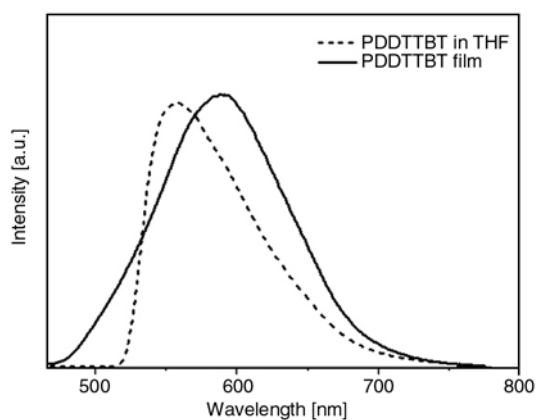
Figure 2a shows the absorption spectra of the PDDTTBT copolymer in dilute THF solution and in thin solid film. The optical absorption threshold at 707 nm from the spectrum of the film corresponds to the bandgap ( $E_g$ ) of the PDDTTBT copolymer. Hence, the estimated optical bandgap is 1.75 eV. To obtain a more accurate optical band gap of PDDTTBT, the fundamental equation  $ahv = B(hv - E_{opt})^n$  developed in Tauc relation [36] was used. The optical bandgap calculated by this equation is 1.83 eV, smaller than that (1.9–2.0 eV) of widely used regioregular poly(3-hexylthiophene) (P3HT), as shown in Figure 2b. In comparison with the polymer which has a similar structure without alkoxy chains on the acceptor (benzothiadiazole) unit [23], the PDDTTBT copolymer exhibits a broader absorption band and lower bandgap. On the other hand, from our previous report [33], the bandgap of the similar copolymer without pendent alkyl side chains



**Figure 2.** (a) UV-vis absorption spectra of PDDTTBT in dilute THF solution and thin film, (b) plot of  $(ahv)^2$  vs.  $hv$  for PDDTTBT film

on the donor (DTT) unit is 1.76 eV (via absorption threshold) or 1.83 eV (via Tauc relation). It is obvious that the bandgaps of both copolymers are almost the same. Therefore, to finetune the bandgap with the attachment of pendant chains on the donor unit seems no significant influence on the value of bandgap in the present case. However, it doesn't mean that the HOMO and LUMO values of both copolymers will be the same, as we will discuss in section 3.3.

As seen from Figure 2a, the UV-vis absorption spectrum of the copolymer in thin solid film exhibited three absorption peaks positioned at about 291, 385 and 505 nm, respectively. The peaks at 291 and 385 nm are probably due to the  $\pi$ - $\pi^*$  transition of the dithienothiophene moiety [37], while the peak in the visible region is assigned to the intramolecular charge transfer (ICT) between the donor and the acceptor [23, 38]. Similarly, the absorption spectrum of PDDTTBT in dilute THF also shows three peaks. The three absorptions in solid state show significant red-shifts compared to those in solution, indicating more efficient  $\pi$ -stacking and stronger intermolecular interactions in the solid state. In particular, the broadened absorption spectrum ranging from 270 to 780 nm indicates a low bandgap polymer has obtained, as evident from the  $E_g$  of PDDTTBT. It is apparent that the ICT interaction between donor and acceptor moieties in D-A copolymers is a practical approach to lower the bandgap and broaden the absorption bands across the entire visible wavelength region of conjugated polymers. Hence, our successful synthesis of a low bandgap D-A type copolymer is further confirmed.



**Figure 3.** Photoluminescence spectra of PDDTTBT in dilute THF solution and thin film with excitation at 400 nm

The photoluminescence (PL) emission spectra of PDDTTBT in dilute THF solution and thin film are shown in Figure 3. Both the fluorescence spectra exhibit the vibronic structure with a maximum at 557 and 589 nm, respectively. As seen from the figure, both spectra show only one emission peak, indicating that an effective energy transfer from the DDTT segments to the BT unit occurs. The red-shift in the spectrum of the PDDTTBT film is probably due to the lowering of bandgap of copolymer by more efficient  $\pi$ -stacking in the solid state.

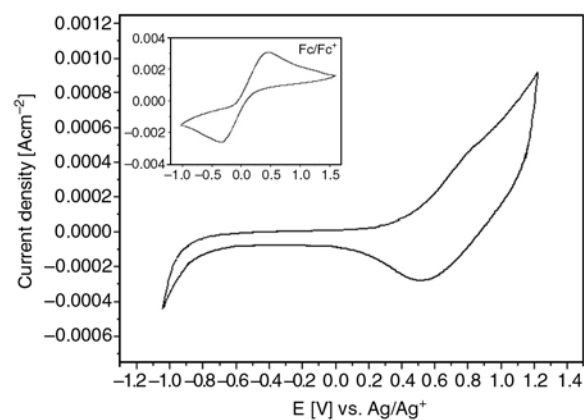
### 3.3. Electrochemical properties

Cyclic voltammetry (CV) is a preliminary characterization technique to determine the redox properties of organic and polymeric materials. The HOMO energy level can be calculated from the onset oxidation potential [ $E_{ox}(\text{onset})$ ] based on the reference energy level of ferrocene (4.8 eV below the vacuum level, which is defined as zero) according to Equation (1). The LUMO level can be obtained from Equation (2) based on the  $E_g$  from Figure 2.  $E_{FC}$  is the potential of the internal standard, the ferrocene/ferrocenium (Fc/Fc<sup>+</sup>) redox couple.

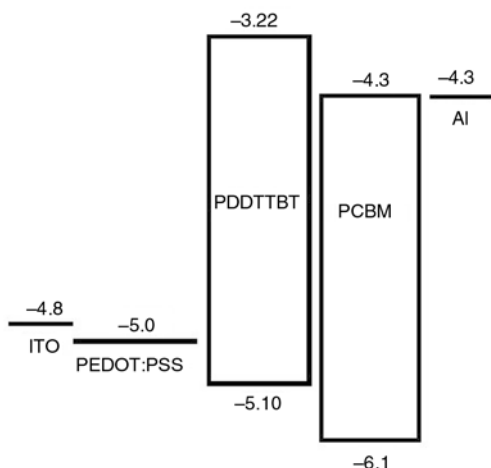
$$\text{HOMO} = - [E_{ox}(\text{onset}) - E_{FC} + 4.8] \text{ eV} \quad (1)$$

$$\text{LUMO} = \text{HOMO} + E_g \quad (2)$$

As seen in Figure 4, the  $E_{ox}(\text{onset})$  for PDDTTBT has been determined as 0.35 V vs. Ag/Ag<sup>+</sup>.  $E_{FC}$  is 0.05 V vs. Ag/Ag<sup>+</sup>. Hence, the HOMO energy for PDDTTBT has been evaluated to be -5.10 eV and the LUMO level determined from Equation (2) is



**Figure 4.** Cyclic voltammograms of PDDTTBT film on an ITO substrate in CH<sub>3</sub>CN/AcOH (V/V = 7/1) containing 0.1 M tetrabutylammonium perchlorate at a scan rate of 50 mV·s<sup>-1</sup>



**Figure 5.** Energy level diagram of the components in the polymer solar cell

–3.27 eV. Since incorporation of electron-donating substituents onto the aromatic unit will raise the HOMO energy, the PDDTTBT polymer thus has a higher HOMO level than that of the similar structure without alkoxy groups on the BT unit [23]. In a similar manner, compared to the similar structure without pendant chains on the DTT unit [33], the HOMO level increases ca. 0.05 eV due to two electron donating alkyl chains were attached onto the fused thiophene ring. Figure 5 shows the schematic diagram representing the potential metrically determined HOMO and LUMO energy of PDDTTBT and PCBM relative to the work function of the electrodes. From the energy level diagram, although the  $\Delta E_{\text{LUMO}}$  between the LUMOs of donor (PDDTTBT) and acceptor (PCBM) is large enough to meet the minimum energy offset (0.3 eV) for efficient charge separation, the increase of HOMO level in donor material may produce a detrimental reduction of  $V_{\text{oc}}$ , as can be seen in the  $J$ - $V$  measurements.

### 3.4. Photovoltaic properties

The bulk heterojunction solar cells based on PDDTTBT in combination of PCBM has been prepared and investigated. The employed device structure was ITO/PEDOT:PSS/PDDTTBT:PCBM/Al. The blend solutions (in DCB) of PDDTTBT:PCBM were prepared with 1:1 weight ratio as the active layer. The photovoltaic performance of the device for the blend film cast at room temperature (RT) was measured under illumination from solar simulator at 100 mW/cm<sup>2</sup> light intensity. The corresponding open-circuit voltage ( $V_{\text{oc}}$ ), short-circuit current ( $J_{\text{sc}}$ ), fill factor (FF), and power conversion efficiency (PCE,  $\eta$ ) are listed in Table 1. The power

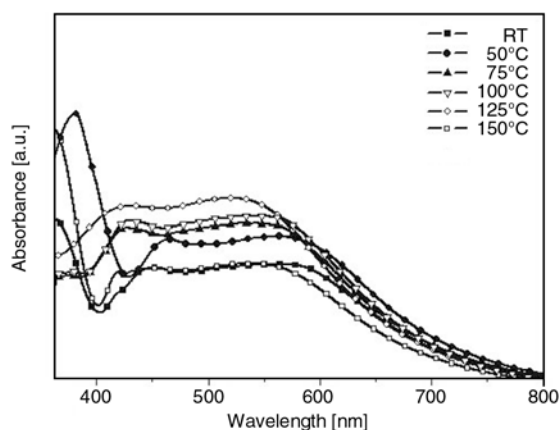
**Table 1.** Photovoltaic characteristics of devices under different annealing temperatures for 30 min

	RT	50°C	75°C	100°C	125°C	150°C
$V_{\text{oc}}$ [V]	0.284	0.451	0.581	0.544	0.433	0.475
$J_{\text{sc}}$ [mA/cm <sup>2</sup> ]	1.512	1.933	1.361	1.123	1.726	1.004
FF [%]	29.510	33.530	32.070	37.310	35.420	32.610
$\eta$ [%]	0.127	0.292	0.254	0.228	0.265	0.155

conversion efficiency of solar cell using the as-prepared blend film as the active layer is 0.127%. This value is only a little higher than that (0.113%) of the similar structure without pendant chains on the DTT unit [33]. As mentioned above, due to the increase of HOMO level in PDDTTBT as compared with that of similar structure [33], a 0.032 V decrease (0.284 V vs. 0.316 V) of  $V_{\text{oc}}$  produced. Therefore, although both  $J_{\text{sc}}$  and FF increased, only a little improvement of PCE was achieved. However, the values of both  $J_{\text{sc}}$  and FF are still low compared to those of high performance PSCs. The low  $J_{\text{sc}}$  may be attributed to the high recombination rate of charge carriers, whereas the low  $V_{\text{oc}}$  resulted from the high HOMO level of PDDTTBT. Regarding the low FF, it is usually caused by shunt resistance, series resistance, and film-forming properties, etc. Consequently, the poor performance of the device may be a result of the non-optimized morphology of the blend film, the poor technique for fabricating the active layer and the device architecture, the nature of the donor material, the fabrication equipments, etc.

### 3.5. Effect of thermal annealing on optical properties

The effect of annealing temperature on the UV-vis absorption spectra for the thin films of PDDTTBT:PCBM (1:1 weight ratio) spun cast on quartz substrates is shown in Figure 6. These films were annealed under nitrogen atmosphere inside the glove box at atmospheric pressure. The annealing time was kept 30 min for all of the annealing temperatures. After annealing at different temperatures, the blend film exhibited distinct intensity changes and shifts of the absorption bands compared with that of untreated PDDTTBT film. For the blend film annealed at 50°C, the spectrum shows a significant increase in intensity for all three absorption bands of PDDTTBT copolymer, especially for the peak at 380 nm. The two bands at lower wavelengths are attributed to the  $\pi$ - $\pi^*$  transition of DDTT segments, whereas the last band is due to ICT interaction as



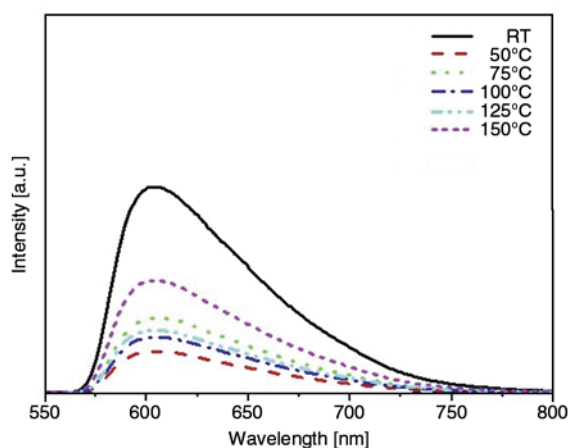
**Figure 6.** UV-vis absorption spectra of PDDTTBT:PCBM blend films after annealing at different temperatures for 30 min

stated above. An increase in the absorption intensity after annealing suggests an increased packing of chains in the PDDTTBT domains, indicating the more ordered structure of PDDTTBT. The redshifts for the three bands imply that the conjugation length in PDDTTBT was enhanced by the heat treatment.

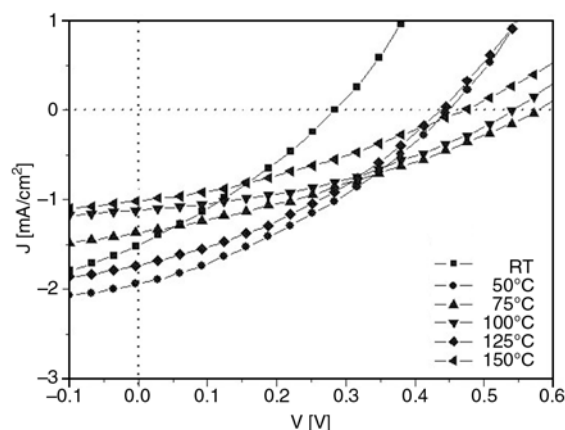
At annealing temperature of 75°C, although the intensities of last two bands increase, the first peak disappears accompanying with a distinctive blue-shift of the entire absorption band. The films heat-treated at 100 and 125°C show similar behaviors. Further increasing the annealing temperature to 150°C, however, results in a dramatic decrease in the intensities of last two bands while the first peak reappears in the vicinity of 362 nm. The irregular changes in intensity and wavelength for the absorption bands with the annealing temperature may be associated with the molecular structure of the D–A type copolymer due to both donor and acceptor segments possessing pendent side chains. When the film annealed at 50°C, the intermolecular packing of both fused-thiophene ring and BT unit could be accommodated by the decrease in the steric hindrance of the pendent side chains because of their easier movements than the rigid polymer backbone. Hence, the total absorption in the entire range is comparatively larger than other annealing temperatures. However, when the annealing temperature was raised to 75°C (above the  $T_g$  of PDDTTBT), the rigid polymer backbone also became mobile accompanying with a development of a new packing state and thus rendering a different absorption pattern. In this case, side chain ordering may decrease while the main chain planarity is enhanced. This may result in

a decrease of intermolecular packing because of the steric hindrance of more mobile side chains and an increase of ICT interaction due to more planar structure of polymer backbone. Therefore, the absorption peak at 380 nm due to the  $\pi$ – $\pi^*$  transition of the dithienothiophene moiety disappears whereas the absorption at 412–580 nm increases. The similar absorption behavior with increasing absorption intensity was observed for the film annealed at 100 and 125°C, indicating that the ICT interaction increased with increasing annealing temperature. For the sample annealing at 150°C, both side chains and main chains of the PDDTTBT molecules could move simultaneously, leading to disordered packing state similar to that of untreated PDDTTBT film. Similar spectrum to that of the untreated PDDTTBT film was thus observed. As a result, the sample annealed at 50 or 125°C could provide optimal optoelectronic properties for PDDTTBT and PCBM blend films, as seen in Table 1.

The PL spectra for blend films annealed at different temperatures are shown in Figure 7. The PL intensity increases with the increase of photogenerated excitons that do not take part in charge separation. Hence, the phenomenon of PL quenching can be attributed to the effective charge transfer in the interfacial region of donor-acceptor junction. Normally, PL quenching increases with the increase of interfacial area between donor and acceptor materials in the active layer. Furthermore, the higher mobility of donor material after thermal annealing may increase the  $\mu_h/\mu_e$  ratio and reduce the mobility mismatch between hole and electron transport and thus enhance the charge separation in the active layer.



**Figure 7.** Photoluminescence spectra of PDDTTBT:PCBM blend films after annealing at different temperatures for 30 min with excitation at 375 nm



**Figure 8.** J-V characteristics of devices under AM 1.5 simulated solar illumination at an intensity of  $100 \text{ mW/cm}^2$  after annealing at different temperatures for 30 min

Therefore, if the charge mobility of the PDDTTBT polymer is improved due to annealing treatment and more ordered packing, the quenching effect will be enhanced. PL quenching provides direct evidence for exciton dissociation, and thus efficient PL quenching is necessary to obtain efficient organic solar cells. As shown in the Figure 6, it seems that the PL intensity decreases with the increase of UV-vis intensity. The PL intensity shows a minimum at thermal annealing of  $50^\circ\text{C}$ . This significant reduction in the PL intensity is attributed to efficient photoinduced charge separation between electron-donating (PDDTTBT) and electron-accepting (PCBM) molecules. This may be attributed to the higher charge carrier mobility or higher interfacial area between D–A molecules compared with those of other annealing temperatures. Hence, the highest power conversion efficiency (0.292%) has been achieved by this blend film as shown in Figure 8 and Table 1.

However, this does not necessarily mean that the stronger the PL quenching, the better the performance of the solar cells, as shown in the curves for the annealing temperature at 75 and  $100^\circ\text{C}$ . Although the PL intensity of the blend film annealed at  $125^\circ\text{C}$  is a little higher in comparison with that of the film annealed at  $100^\circ\text{C}$ , the power conversion efficiency for the film annealed at  $125^\circ\text{C}$  is the second best as

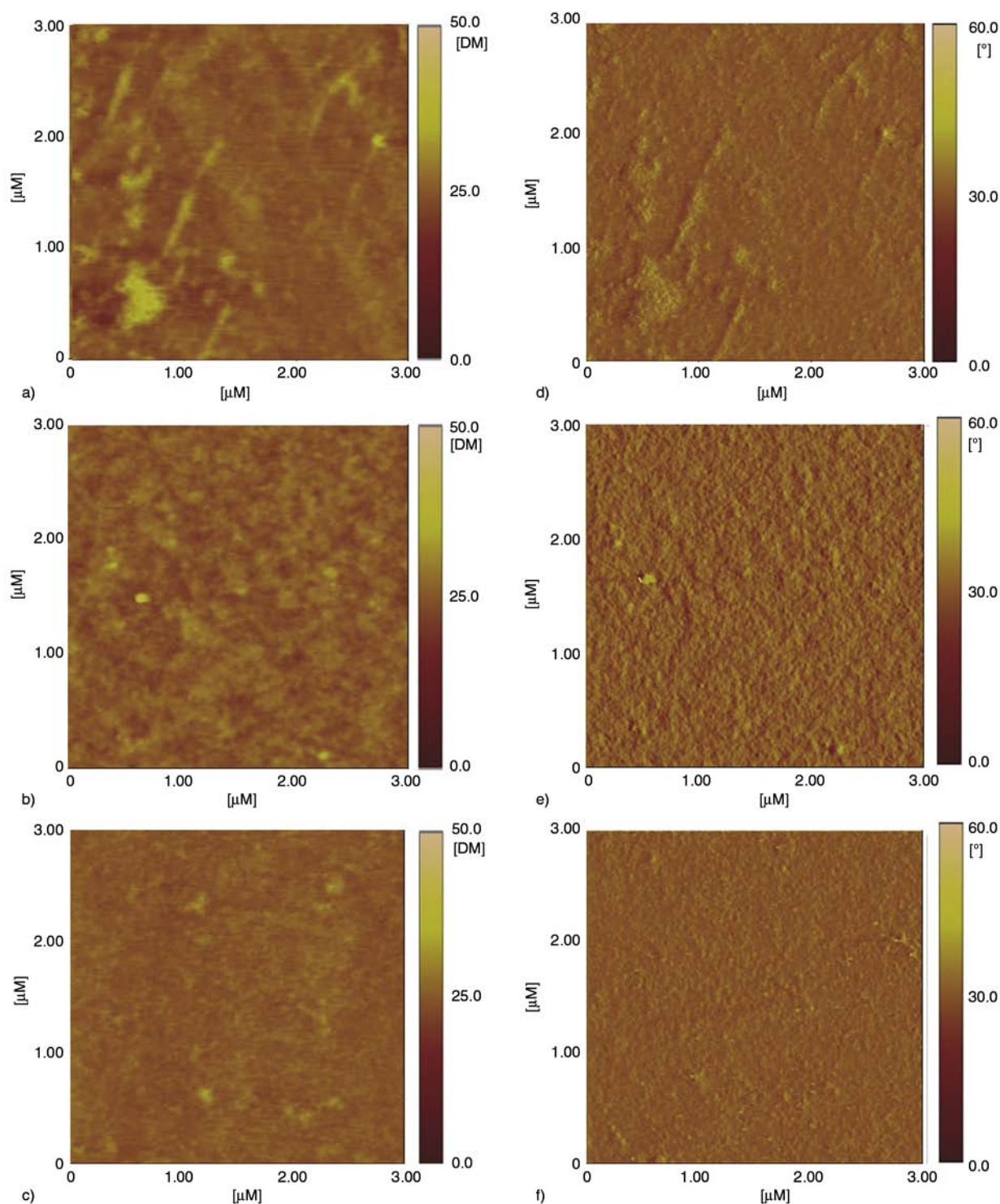
shown in Figure 8 and Table 1. As we stated in a previous study [33], it is probable that (1) the increase of optical absorption in the visible light region, (2) the improved charge carrier mobility in both donor and acceptor phases after thermal annealing, and (3) the increased interfacial area between the donor and acceptor phases, offsets the former effect (PL quenching) and results in an overall improvement in device performance. Moreover, as we will discuss in the following part, it seems that the high value of roughness and higher degree of nanoscale phase separation in the blend film annealed at  $50^\circ\text{C}$  enhance the transport rate of charge carriers to the metal electrode and reduce the charge recombination of the excitons.

### 3.6. Effect of thermal annealing on phase morphology

Since the morphology of the heterojunction plays an important role on the performance of polymer solar cells, we studied the topography of blend films of PDDTTBT:PCBM (1:1, w/w) by AFM. Although the AFM images of film surfaces at different annealing temperatures have been taken, for the sake of simplicity, only three representative images are shown in Figure 9 for comparison. The values of average roughness and root-mean-square roughness for the blend films are shown in Table 2. It is clear that the images for both the as-prepared film and the film annealed at  $150^\circ\text{C}$  look relatively smooth. It is evident that the rougher surface observed in the film annealed at  $50^\circ\text{C}$  increases the contact area between the active layer and the metal electrode. In addition, as shown in Figure 9b and 9e, both PDDTTBT and PCBM domains are uniformly distributed throughout the surface of the film, indicating the nanoscale interpenetrating network has been formed in this blend, which can benefit not only the charge separation but also the charge transport. Hence, the transport rate of charge carriers to the metal electrode is higher and the recombination rate of excitons is reduced. Therefore, the  $J$ - $V$  curve for the film annealed at  $50^\circ\text{C}$  reveals an increase of  $J_{sc}$  to  $1.933 \text{ mA/cm}^2$  which is almost twice of that of the film annealed at  $150^\circ\text{C}$ .

**Table 2.** Surface roughness of PDDTTBT:PCBM blend films obtained from AFM after annealing at different temperatures for 30 min

Annealing temperature	RT	$50^\circ\text{C}$	$75^\circ\text{C}$	$100^\circ\text{C}$	$125^\circ\text{C}$	$150^\circ\text{C}$
Average Roughness [nm]	1.49	1.63	1.57	1.40	1.04	0.92
Root mean square [nm]	2.14	2.75	2.09	1.81	1.39	1.20



**Figure 9.** AFM topography images ( $3\ \mu\text{m} \times 3\ \mu\text{m}$ ) of PDDTTBT:PCBM blend films after annealing at different temperatures for 30 min. 2D height image for the blend film (a) unannealed, (b) annealed at  $50^\circ\text{C}$ , (c) annealed at  $150^\circ\text{C}$ . Phase image for the blend film (d) unannealed, (e) annealed at  $50^\circ\text{C}$ , (f) annealed at  $150^\circ\text{C}$ .

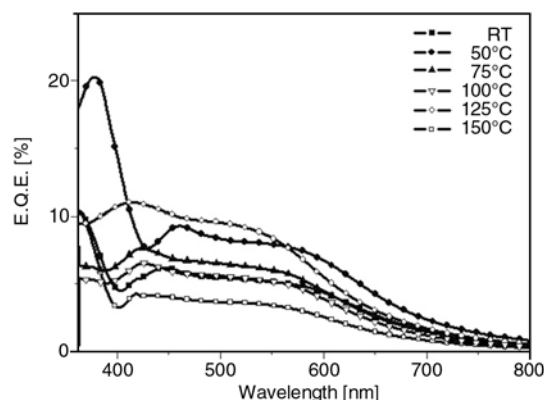
### 3.7. External quantum efficiency and solar cell performance

In order to learn more on the recombination mechanisms in the PDDTTBT/PC<sub>61</sub>BM photoactive layer, EQE measurements with different annealing tem-

peratures were performed on the solar cell devices (Figure 10).

As seen in the figure, the EQE spectra of blend films exhibit similar patterns with the optical data. For the untreated sample, two dominant bands pres-





**Figure 10.** EQE spectra of PDDTTBT:PC61BM blend films after annealing at different temperatures for 30 min

ent at 364 and 446 nm, the obtained EQE is only 10.4 and 6.2%, correspondingly. After thermal treatment for the blend films, the EQE is significantly improved with minor changes in the peak position. Among the EQE spectra taken at different annealing temperatures, the film annealed at 50°C almost demonstrates the highest EQE in the most illuminated regions by possessing the EQE of two dominant bands, at 377 and 460 nm, respectively, reaching ca. 20.2 and 9.3%. Consequently, the highest power conversion efficiency (0.292%) has been achieved by this blend film. However, the EQE values are still small compared to those of high performance PSCs. The low EQE may be attributed to the high recombination rate of charge carriers in the PDDTTBT/PC61BM blend system, which results in the low photocurrent.

#### 4. Conclusions

The D–A type copolymer PDDTTBT based on DDTT and BT units has been synthesized and employed as the donor material in the active layer of BHJ-type polymer solar cells. UV-vis absorption spectra indicated that a low bandgap polymer with a wide absorption band has been obtained. After annealing treatment, an irregular absorption trend in UV-vis spectra was observed due to both donor and acceptor segments possessing pendent side chains. When the blend film was treated at an optimum condition (50°C/30 min), the PV cell performance was dramatically improved and the power conversion efficiency of device reached to 0.292% under white light illumination (100 mW/cm<sup>2</sup>). We attribute the higher efficiency to enhanced 3-D interpenetrating networks in the active layer,

increase of light absorption, and improved carrier mobility.

#### Acknowledgements

We gratefully acknowledge the support of the National Science Council of Republic of China with Grant NSC 99-2221-E-390-001-MY3.

#### References

- [1] Inganäs O., Svensson M., Zhang F., Gadisa A., Persson N. K., Wang X., Andersson M. R.: Low bandgap alternating polyfluorene copolymers in plastic photodiodes and solar cells. *Applied Physics A: Materials Science and Processing*, **79**, 31–35 (2004). DOI: [10.1007/s00339-003-2498-5](https://doi.org/10.1007/s00339-003-2498-5)
- [2] Zhang F., Mammo W., Andersson L. M., Admassie S., Andersson M. R., Inganäs O.: Low-bandgap alternating fluorene copolymer/methanofullerene heterojunctions in efficient near-infrared polymer solar cells. *Advanced Materials*, **18**, 2169–2173 (2006). DOI: [10.1002/adma.200600124](https://doi.org/10.1002/adma.200600124)
- [3] Gadisa A., Mammo W., Andersson L. M., Admassie S., Zhang F., Andersson M. R., Inganäs O.: A new donor–acceptor–donor polyfluorene copolymer with balanced electron and hole mobility. *Advanced Functional Materials*, **17**, 3836–3842 (2007). DOI: [10.1002/adfm.200700441](https://doi.org/10.1002/adfm.200700441)
- [4] Espinosa N., Hösel M., Angmo D., Krebs F. C.: Solar cells with one-day energy payback for the factories of the future. *Energy and Environmental Science*, **5**, 5117–5132 (2012). DOI: [10.1039/C1EE02728J](https://doi.org/10.1039/C1EE02728J)
- [5] Zhao G., He Y., Li Y.: 6.5% efficiency of polymer solar cells based on poly(3-hexylthiophene) and indene-C60 bisadduct by device optimization. *Advanced Materials*, **22**, 4355–4358 (2010). DOI: [10.1002/adma.201001339](https://doi.org/10.1002/adma.201001339)
- [6] Chang C.-Y., Wu C.-E., Chen S.-Y., Cui C., Cheng Y.-J., Hsu C.-S., Wang Y.-L., Li Y.: Enhanced performance and stability of a polymer solar cell by incorporation of vertically aligned, cross-linked fullerene nanorods. *Angewandte Chemie International Edition*, **50**, 9386–9390 (2011). DOI: [10.1002/anie.201103782](https://doi.org/10.1002/anie.201103782)
- [7] Peet J., Kim J. Y., Coates N. E., Ma W. L., Moses D., Heeger A. J., Bazan G. C.: Efficiency enhancement in low-bandgap polymer solar cells by processing with alkane dithiols. *Nature Materials*, **6**, 497–500 (2007). DOI: [10.1038/nmat1928](https://doi.org/10.1038/nmat1928)
- [8] Wang E. G., Wang L., Lan L. F., Luo C., Zhuang W., Peng J., Cao Y.: High-performance polymer heterojunction solar cells of a polysilafluorene derivative. *Applied Physics Letters*, **92**, 033307/1–033307/3 (2008). DOI: [10.1063/1.2836266](https://doi.org/10.1063/1.2836266)

- [9] Zhan X., Tan Z., Domercq B., An Z., Zhang X., Barlow S., Li Y., Zhu D., Kippelen B., Marder S. R.: A high-mobility electron-transport polymer with broad absorption and its use in field-effect transistors and all-polymer solar cells. *Journal of the American Chemical Society*, **129**, 7246–7247 (2007). DOI: [10.1021/ja071760d](https://doi.org/10.1021/ja071760d)
- [10] Zhou E., Yamakawa S., Tajima K., Yang C., Hashimoto K.: Synthesis and photovoltaic properties of diketopyrrolopyrrole-based donor–acceptor copolymers. *Chemistry of Materials*, **21**, 4055–4061 (2009). DOI: [10.1021/cm901487f](https://doi.org/10.1021/cm901487f)
- [11] Li Y.: Molecular design of photovoltaic materials for polymer solar cells: Toward suitable electronic energy levels and broad absorption. *Accounts of Chemical Research*, **45**, 723–733 (2012). DOI: [10.1021/ar2002446](https://doi.org/10.1021/ar2002446)
- [12] Hou J., Chen H.-Y., Zhang S., Li G., Yang Y.: Synthesis, characterization, and photovoltaic properties of a low band gap polymer based on silole-containing polythiophenes and 2,1,3-benzothiadiazole. *Journal of the American Chemical Society*, **130**, 16144–16145 (2008). DOI: [10.1021/ja806687u](https://doi.org/10.1021/ja806687u)
- [13] Liang Y., Wu Y., Feng D., Tsai S.-T., Son H.-J., Li G., Yu L.: Development of new semiconducting polymers for high performance solar cells. *Journal of the American Chemical Society*, **131**, 56–57 (2009). DOI: [10.1021/ja808373p](https://doi.org/10.1021/ja808373p)
- [14] Park S. H., Roy A., Beaupré S., Cho S., Coates N., Moon J. S., Moses D., Leclerc M., Lee K., Heeger A. J.: Bulk heterojunction solar cells with internal quantum efficiency approaching 100%. *Nature Photonics*, **3**, 297–302 (2009). DOI: [10.1038/nphoton.2009.69](https://doi.org/10.1038/nphoton.2009.69)
- [15] Lee K., Sotzing G. A.: Poly(thieno[3,4-*b*]thiophene). A new stable low band gap conducting polymer. *Macromolecules*, **34**, 5746–5747 (2001). DOI: [10.1021/ma0106245](https://doi.org/10.1021/ma0106245)
- [16] Sotzing G. A., Lee K.: Poly(thieno[3,4-*b*]thiophene): A p- and n-dopable polythiophene exhibiting high optical transparency in the semiconducting state. *Macromolecules*, **35**, 7281–7286 (2002). DOI: [10.1021/ma020367j](https://doi.org/10.1021/ma020367j)
- [17] Lee B., Yavuz M. S., Sotzing G. A.: Poly(thieno[3,4-*b*]thiophene)s from three symmetrical thieno[3,4-*b*]thiophene dimers. *Macromolecules*, **39**, 3118–3124 (2006). DOI: [10.1021/ma0526746](https://doi.org/10.1021/ma0526746)
- [18] Sun Y. M., Ma Y. Q., Liu Y. Q., Lin Y. Y., Wang Z. Y., Wang Y., Di C. A., Xiao K., Chen X. M., Qiu W. F., Zhang B., Yu G., Hu W. P., Zhu D. B.: High-performance and stable organic thin-film transistors based on fused thiophenes. *Advanced Functional Materials*, **16**, 426–432 (2006). DOI: [10.1002/adfm.200500547](https://doi.org/10.1002/adfm.200500547)
- [19] Sun Y., Liu Y., Ma Y., Di C., Wang Y., Wu W., Yu G., Hu W., Zhu D.: Organic thin-film transistors with high mobilities and low operating voltages based on 5,5'-bis-biphenyl-dithieno[3,2-*b*:2',3'-*d*]thiophene semiconductor and polymer gate dielectric. *Applied Physics Letters*, **88**, 242113/1–242113/3 (2006). DOI: [10.1063/1.2209213](https://doi.org/10.1063/1.2209213)
- [20] Li J., Qin F., Li C. M., Bao Q., Chan-Park M. B., Zhang W., Qin J., Ong B. S.: High-performance thin-film transistors from solution-processed dithienothiophene polymer semiconductor nanoparticles. *Chemistry of Materials*, **20**, 2057–2059 (2008). DOI: [10.1021/cm703567g](https://doi.org/10.1021/cm703567g)
- [21] Lu K., Di C., Xi H., Liu Y., Yu G., Qiu W., Zhang H., Gao X., Liu Y., Qi T., Du C., Zhu D.: Novel copolymers incorporating dithieno[3,2-*b*:2',3'-*d*]thiophene moieties for air-stable and high performance organic field-effect transistors. *Journal of Materials Chemistry*, **18**, 3426–3432 (2008). DOI: [10.1039/B801603H](https://doi.org/10.1039/B801603H)
- [22] Millefiorini S., Kozma E., Catellani M., Luzzati S.: Dithienothiophene based polymer as electron donor in plastic solar cells. *Thin Solid Films*, **516**, 7205–7208 (2008). DOI: [10.1016/j.tsf.2007.12.077](https://doi.org/10.1016/j.tsf.2007.12.077)
- [23] Zhang S., Guo Y., Fan H., Liu Y., Chen H.-Y., Yang G., Zhan X., Liu Y., Li Y., Yang Y.: Low bandgap  $\pi$ -conjugated copolymers based on fused thiophenes and benzothiadiazole: Synthesis and structure-property relationship study. *Journal of Polymer Science Part A: Polymer Chemistry*, **47**, 5498–5508 (2009). DOI: [10.1002/pola.23601](https://doi.org/10.1002/pola.23601)
- [24] Chen J., Cao Y.: Development of novel conjugated donor polymers for high-efficiency bulk-heterojunction photovoltaic devices. *Accounts of Chemical Research*, **42**, 1709–1718 (2009). DOI: [10.1021/ar900061z](https://doi.org/10.1021/ar900061z)
- [25] Arias A. C., MacKenzie J. D., Stevenson R., Halls J. J. M., Inbasekaran M., Woo E. P., Richards D., Friend R. H.: Photovoltaic performance and morphology of polyfluorene blends: A combined microscopic and photovoltaic investigation. *Macromolecules*, **34**, 6005–6013 (2001). DOI: [10.1021/ma010240e](https://doi.org/10.1021/ma010240e)
- [26] Snaith H. J., Greenham N. C., Friend R. H.: The origin of collected charge and open-circuit voltage in blended polyfluorene photovoltaic devices. *Advanced Materials*, **16**, 1640–1645 (2004). DOI: [10.1002/adma.200305766](https://doi.org/10.1002/adma.200305766)
- [27] Svensson M., Zhang F., Veenstra S. C., Verhees W. J. H., Hummelen J. C., Kroon J. M., Inganäs O., Andersson M. R.: High-performance polymer solar cells of an alternating polyfluorene copolymer and a fullerene derivative. *Advanced Materials*, **15**, 988–991 (2003). DOI: [10.1002/adma.200304150](https://doi.org/10.1002/adma.200304150)

- [28] Boudreault P-L. T., Michaud A., Leclerc M.: A new poly(2,7-dibenzosilole) derivative in polymer solar cells. *Macromolecular Rapid Communications* **28**, 2176–2179 (2007).  
DOI: [10.1002/marc.200700470](https://doi.org/10.1002/marc.200700470)
- [29] Blouin N., Michaud A., Leclerc M.: A low-bandgap poly(2,7-carbazole) derivative for use in high-performance solar cells. *Advanced Materials*, **19**, 2295–2300 (2007).  
DOI: [10.1002/adma.200602496](https://doi.org/10.1002/adma.200602496)
- [30] Moulé A. J., Tsami A., Bünnagel T. W., Forster M., Kronenberg N. M., Scharber M., Koppe M., Morana M., Brabec C. J., Meerholz K., Scherf U.: Two novel cyclopentadithiophene-based alternating copolymers as potential donor components for high-efficiency bulk-heterojunction-type solar cells. *Chemistry of Materials*, **20**, 4045–4050 (2008).  
DOI: [10.1021/cm8006638](https://doi.org/10.1021/cm8006638)
- [31] Bundgaard E., Hagemann O., Manceau M., Jørgensen M., Krebs F. C.: Low band gap polymers for roll-to-roll coated polymer solar cells. *Macromolecules*, **43**, 8115–8120 (2010).  
DOI: [10.1021/ma1015903](https://doi.org/10.1021/ma1015903)
- [32] Bundgaard E., Hagemann O., Jørgensen M., Krebs F. C.: Low band gap polymers for roll-to-roll coated organic photovoltaics – Design, synthesis and characterization. *Green*, **1**, 55–64 (2011).  
DOI: [10.1515/green.2011.005](https://doi.org/10.1515/green.2011.005)
- [33] Wang T-L., Yeh A-C., Yang C-H., Shieh Y-T., Chen W-J., Ho T-H.: Synthesis and photovoltaic properties of a low bandgap donor–acceptor alternating copolymer with benzothiadiazole unit. *Solar Energy Materials and Solar Cells*, **95**, 3295–3302 (2011).  
DOI: [10.1016/j.solmat.2011.07.021](https://doi.org/10.1016/j.solmat.2011.07.021)
- [34] He M., Zhang F.: Synthesis and structure of alkyl-substituted fused thiophenes containing up to seven rings. *The Journal of Organic Chemistry*, **72**, 442–451 (2007).  
DOI: [10.1021/jo061853y](https://doi.org/10.1021/jo061853y)
- [35] Bouffard J., Swager T. M.: Fluorescent conjugated polymers that incorporate substituted 2,1,3-benzooxadiazole and 2,1,3-benzothiadiazole units. *Macromolecules*, **41**, 5559–5562 (2008).  
DOI: [10.1021/ma8010679](https://doi.org/10.1021/ma8010679)
- [36] Tauc J.: *Amorphous and liquid semiconductors*. Plenum Press, New York (1974).
- [37] Cervini R., Holmes A. B., Moratti S. C., Köhler A., Friend R. H.: Synthesis of new conjugated thiophene polymers. *Synthetic Metals*, **76**, 169–171 (1996).  
DOI: [10.1016/0379-6779\(95\)03445-P](https://doi.org/10.1016/0379-6779(95)03445-P)
- [38] Li Y., Xue L., Li H., Li Z., Xu B., Wen S., Tian W.: Energy level and molecular structure engineering of conjugated donor–acceptor copolymers for photovoltaic applications. *Macromolecules*, **42**, 4491–4499 (2009).  
DOI: [10.1021/ma900623p](https://doi.org/10.1021/ma900623p)

# Polyamide from lactams by reactive rotational molding via anionic ring-opening polymerization: Optimization of processing parameters

N. Barhoumi<sup>1</sup>, A. Maazouz<sup>1\*</sup>, M. Jaziri<sup>2</sup>, R. Abdelhedi<sup>2</sup>

<sup>1</sup>Ingénierie des Matériaux Polymères-(IMP/LMM), UMR-CNRS 5223, INSA-Lyon, Université de Lyon, 69621 Lyon, 17 Avenue Jean Capelle, Villeurbanne Cedex, France

<sup>2</sup>Laboratoire d'Electrochimie et Environnement. ENIS- Sfax, 3038 Sfax, Tunisie

Received 17 June 2012; accepted in revised form 1 September 2012

**Abstract.** A reactive rotational molding (RRM) process was developed to obtain a PA6 by activated anionic ring-opening polymerization of epsilon-caprolactam (APA6). Sodium caprolactamate (C10) and caprolactam magnesium bromide (C1) were employed as catalysts, and difunctional hexamethylene-1,6-dicarbamoylcaprolactam (C20) was used as an activator. The kinetics of the anionic polymerization of  $\epsilon$ -caprolactam into polyamide 6 was monitored through dynamic rheology and differential scanning calorimetry measurements. The effect of the processing parameters, such as the polymerization temperature, different catalyst/activator combinations and concentrations, on the kinetics of polymerization is discussed. A temperature of 150°C was demonstrated to be the most appropriate. It was also found that crystallization may occur during PA6 polymerization and that the combination C1/C20 was well suited as it permitted a suitable induction time. Isoviscosity curves were drawn in order to determine the available processing window for RRM. The properties of the obtained APA6 were compared with those of a conventionally rotomolded PA6. Results pointed at lower cycle times and increased tensile properties at weak deformation.

**Keywords:** processing technologies, anionic polymerization,  $\epsilon$ -caprolactam, viscosity, reactive rotational molding

## 1. Introduction

Rotational molding has been regarded as a polymer processing technique with great potential [1]. The obtained products are virtually stress-free and without weld lines. Moreover there is no material waste, and the required molds are relatively inexpensive. Yet, its widespread growth is hindered by long production cycle times as well as by the fact that one can only use dry powders in order to meet material property demands. This is particularly true for polyethylene, which has limited properties. Several high performance resins, such as polyamides and polycarbonates, are also available to rotomolders offering better properties, but at a cost.

One way to overcome issues involved in the rotational molding of powders as well as gain engineering material properties is to utilize liquid resins. Immediate advantages include a reduced cycle time, an excellent reproduction of surface detail and a wider range of material properties. Based on these strong points, the use of liquid resin systems when performing rotational molding would offer numerous manufacturing benefits over the conventional powder process [2].

Additionally, the use of the RRM process renders possible the synthesis of engineering thermoplastics, e.g., polyamide 6 (PA6), with high molecular weights. In the case of PA6, this is done through

\*Corresponding author, e-mail: [Abderrahim.maazouz@insa-lyon.fr](mailto:Abderrahim.maazouz@insa-lyon.fr)  
© BME-PT

anionic polymerization of caprolactam by the aid of chain initiators and catalysts [3].

It is well known that anionic polymerization of  $\epsilon$ -CL (APCL) occurs faster (i.e., over a few minutes) than classical hydrolytic polymerization, which takes about 12–24 h [4]. A fast polymerization process in addition to good mechanical properties of PA6 results in a wide range of applications for this polymer in reaction injection molding [5, 6], rotational molding [1, 7] and centrifugal molding [8–9]. This makes PA6 one of the main engineering materials in use today.

According to different reports [10–17], there are three main parameters that govern the polymerization of APCL: the catalyst (type and concentration), activator (type and concentration), and also the initial polymerization temperature. In almost all published studies, this process has been carried out in an inert atmosphere.

There are a number of problems that are inherent to the processing of reactive monomers and that limit the development and uptake of the process in industry [18]. These problems, which include difficulties in controlling the reaction viscosity and an uneven distribution of material, coupled with a lack of research in this area, have kept the use of reactive monomer systems in the rotational molding industry to a minimum [1]. Thus, one needs to gain fundamental understanding of the RRM of  $\epsilon$ -caprolactam in order to determine a means to control its viscosity during anionic polymerization which in turn would facilitate industrial applications. Although the feasibility of the reaction has been known for a long time, there is still only limited industrial exploitation [19].

The influence of polymerization conditions (i.e., catalyst and activator type and also catalyst/activator combination) on the rate of polymerization is reported in the literature [14, 20, 21]. However, the choice of polymerizations conditions for the RRM process has yet to be described and optimized. As a continuation of previous investigations [1, 2], which report on the possibility of reactive rotomolding of defect-free Nyrin<sup>®</sup> parts, our study presents a complementary approach based on determining the processing parameters required to obtain a polyamide 6 through reactive rotational molding by anionic polymerization of  $\epsilon$ -caprolactam (APA6). The reactive mixture (caprolactam, catalyst and activator) was injected into a mold and the PA6 was formed

*in-situ* by the anionic polymerization of  $\epsilon$ -caprolactam at the set temperature during rotational molding.

In a first step, the article discusses the influence of the concentration and combination of activator and initiator, as well as the effect of the polymerization temperature on the kinetics of polymerization. The aim was to choose a suitable APA6 formulation for RRM processing with shorter cycle times. Subsequently, we attempted to define the optimal conditions of rotational molding by constructing isoviscosity curves and to understand the reactive forming process by monitoring the viscosity. Finally, the process has been described by contrasting it with classical rotational molding, and as a result, the properties of APA6 and PA6 were also compared.

## 2. Experimental

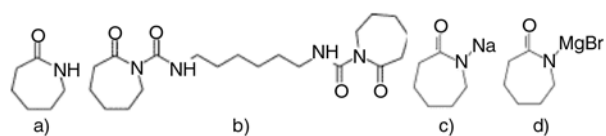
### 2.1. Materials

#### 2.1.1. Monomer, activator and catalysts of anionic polyamide 6

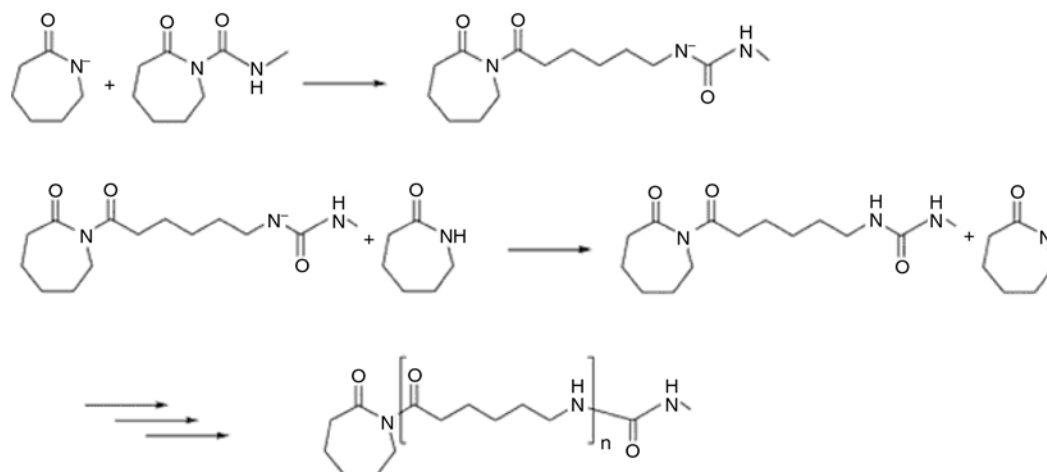
An anionic polymerization grade of the caprolactam monomer (AP-NYLON<sup>®</sup> Caprolactam) was used in this study (Figure 1) as it has a low moisture content (<100 ppm). The monomer also has a low viscosity (4.87 mPa·s at 100°C) and a low melting point ( $T_m = 69^\circ\text{C}$ ).

Brüggolen C20, a difunctional hexamethylene-1,6-dicarbamoylcaprolactam (2 mol/kg concentration in caprolactam) was added as an activator in combination with Brüggolen C10, sodium caprolactamate (1 mol/kg concentration in caprolactam) or Brüggolen C1, caprolactam magnesium bromide (1.4 mol/kg concentration in caprolactam). The melt temperatures of C20, C1 and C10 were 60°C and the substances were used to control the speed and quality of the AP process.

All reactants were supplied by Bruggemann Chemical, Germany, in sealed polyethylene-lined aluminum drums and were used without further processing or purification. Since anionic polymerization of  $\epsilon$ -caprolactam is very sensitive to moisture,



**Figure 1.** Chemical structures of (a)  $\epsilon$ -caprolactam CL, (b) hexamethylene-1,6 dicarbamoylcaprolactam C20, (c) sodium caprolactamate C10, and (d) caprolactam magnesium bromide C1 [14]



**Figure 2.** Anionic polymerization of  $\epsilon$ -caprolactam into polyamide-6, using hexamethylene-1,6-dicarbamoylcaprolactam (C20) as the activator and caprolactam magnesium bromide (C1) as the initiator [14]

all the materials were dried overnight at 40°C under vacuum before use. The chemical structure of each material is presented in Figure 1, and the chemical pathway for the catalyst-activated  $\epsilon$ -caprolactam reaction based on the C1/C20 combination is shown in Figure 2 [14].

### 2.1.2. PA6 (capron) obtained with the classical rotational molding process

The PA6 used in this work is a commercial product referenced as Capron® RXA1482RO HS and supplied by BASF (France). The resin was available in powder form. Its number average molar mass was 34 000 g/mol, and the melting point of this PA6 grade was 224°C.

## 2.2. *In-situ* polymerization of $\epsilon$ -caprolactam

### 2.2.1. Premix preparation

The viscosity of APA6 is a function of the concentration of catalyst and initiator, as well as of temperature and time. Various formulations were investigated. The premix was charged to a reaction vessel and heated in an oil bath at 80°C under a nitrogen atmosphere: the monomer/activator-mixture was thus melted under stirring. In a second vessel, the catalyst was melted with the caprolactam. Subsequently, both mixtures were blended together and immediately characterized by DSC and with a

rheometer in order to monitor *in situ* the anionic polymerization of  $\epsilon$ -caprolactam. The various pre-mixes reported in Table 1 in different mass ratio were denoted CL/CX/CY(% caprolactam/% catalyst/% activator).

### 2.2.2. Polymerization kinetics (chemorheology, DSC)

The polymerization kinetics was monitored through isothermal measurements of the reaction exotherm with a differential scanning calorimeter (DSC Q10, TA Instruments, USA) and an ARES rheometer (Rheometric Scientist, USA) used as a chemical reactor. The temperatures and compositions were varied with the aim of determining the process parameters.

In the case of the rheological analysis, the premix was shaken and quickly introduced with a syringe into the (0.06) mm gap set between the preheated cone and plate geometry at the polymerization temperature. The plate had a diameter of 40 mm. Thus, the exchange surface between the polymerization medium and the area was small in comparison to the volume, thereby limiting the loss of premix by evaporation. The variations in complex viscosity during the polymerization step were then monitored by time sweep oscillatory experiments under a shear stress of 0.05 Pa and an angular frequency of

**Table 1.** Designations and compositions of premixes

Premix	Mass ratio CL [g]	Mass ratio C1 [g]	Mass ratio C10 [g]	Mass ratio C20 [g]
100/3/3(CL/C1/C20)	100	3		3
100/3/3(CL/C10/C20)	100		3	3
100/4/4(CL/C1/C20)	100	4		4

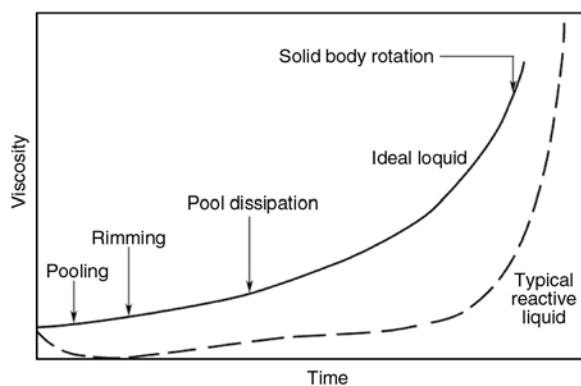
1 rad/s. Nitrogen gas was used to prevent thermal oxidation.

The objective of the isothermal DSC analysis was to measure the reaction of polymerization heat flow versus time at several constant temperatures. The activator and catalyst were added to the molten monomer just above its melting point and this mixture was then quenched in nitrogen liquid to stop the reaction.

### 2.2.3. Reactive rotational molding process of APA6

A Rotoline pilot-scale shuttle-type rotational molding machine with an aluminum cube mold and a volume of  $25 \times 25 \times 10 \text{ cm}^3$  was used to produce the PA6 parts. The Datapaq<sup>®</sup> Tracker Telemetry system was utilized to measure, in real time, the temperatures of the oven, the external wall of the mold, and the internal air/nitrogen during the processing cycle. The reactive premixes were poured in the mold through an air vent, after which the mold's rotation and the thermal cycle were started. The rotation speeds of the two axes were 4 and 5 rpm.

The typical chemorheology of a reactive liquid system is shown in Figure 3 [2]. It includes four main steps, and for each regime a certain viscosity is required. At the start of the process, the viscosity needs to be relatively low so that the rotating pool mixes the ingredients and only deposits a thin film of reactive resin on the mold surface. As the processing time progresses, the viscosity should slowly rise so that the cascading flows distribute a thicker layer evenly over the mold. In the last flow phase, rimming finalizes the even distribution of resin on



**Figure 3.** Typical variation of viscosity with curing time for a reactive liquid compared with an ideal flow behavior [22] (Redrawn from Figure 6.39 of Crawford and Throne with modification)

the mold until gelation occurs, resulting in solid body rotation.

## 2.3. Characterization methods

### 2.3.1. Differential scanning calorimetry (DSC)

Differential scanning calorimetry (DSC Q10, TA Instruments, USA) was performed to investigate the crystallization and melting behaviors of the APA6 samples. Specimens with weights of 5–10 mg were cut for the measurement. Thermograms were recorded in three consecutive runs: (1) a first heating run, from room temperature to 240°C, followed by (2) cooling, from 240 to 25°C and finally (3) a second heating run, from 25 to 240°C. All experiments were performed at a heating/cooling rate of 10°C/min under an argon atmosphere to avoid thermal degradation. The degree of crystallisation,  $\chi_c$ , was calculated considering a melting enthalpy of 190 J/g for a 100% crystalline polyamide 6 [17].

The polymerization was exothermic and the experiments involved measuring the reaction heat flow versus time at several constant temperatures. The activator and catalyst were added to the molten monomer just above its melting point after which the mixture was quenched in liquid nitrogen to stop the reaction. The cold (crystallized) mixture was then sealed in DSC capsules under a dry and oxygen-free atmosphere.

### 2.3.2. Monomer conversion

The degrees of conversion ( $X$ ) of the APA6 samples were determined for various resin formulations at several temperatures. The polymerized samples were ground, weighed ( $m_{\text{tot}}$ ) and refluxed overnight in demineralized water. After drying, the samples were weighed again ( $m_{\text{pol}}$ ). While the caprolactam monomer dissolved easily in water, the polyamide-6 did not and the degree of conversion was consequently determined according to Equation (1) [23]:

$$X = \frac{m_{\text{pol}}}{m_{\text{tot}}} \cdot 100\% \quad (1)$$

### 2.3.3. The viscometric weight-average molecular weight

The molecular weight ( $M_w$ ) of the polyamides was determined by intrinsic viscosity measurements using formic acid as solvent at a concentration of 0.2 g/dL with a suspended-level Ubbelohde viscometer at 25°C. Based on the results from the

intrinsic viscosity measurements ( $\eta$ ),  $M_w$  could be determined according to Equation (2) [5]:

$$M_w = 2.81 \cdot 10^4 \eta^{1.35} \quad (2)$$

### 2.3.4. Mechanical characterization

The tensile specimens were obtained with a tensile Sample Cutting Die from rotomolded parts in press at 80°C.

Tensile tests were carried out using a conventional Instron tensile machine at room temperature according to ASTM D368M test, with a crosshead speed of 10 mm/min. At least five specimens were tested for each material.

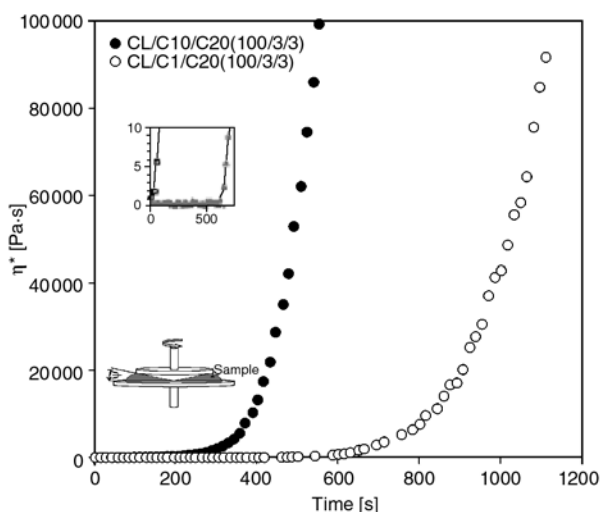
## 3. Results and discussion

### 3.1. Optimizing polymerization conditions for the RRM process

#### 3.1.1. Choice of activator – catalyst combination

The polymerization reaction consists of three steps: (i) anion formation, (ii) complex formation between the catalyst and the activator and (iii) polymerization through the anions during which an anion is regenerated after addition of a monomer [20].

Figure 4 shows the change in complex viscosity during the APCL in the presence of two activator-catalyst combinations (C20–C1 and C20–C10) polymerized at 160°C. The polymerization seemed to get off to a slow start when the C1 catalyst was used, as proven by the viscosity remaining constant at short times since no complex was formed initially [23].



**Figure 4.** In situ polymerization of  $\epsilon$ -caprolactam between the plates of the rheometer at  $T = 160^\circ\text{C}$  for two activator-catalyst combination

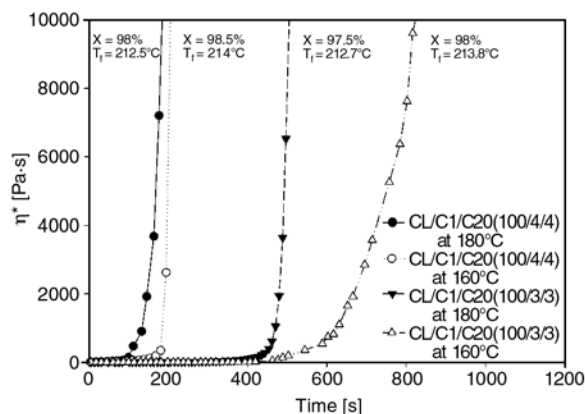
However, after a single monomer addition, the carbamoylcaprolactam group was replaced by an acetylcaprolactam group. Since the latter was able to form a complex with the initiator, the reaction rate increased after a while.

In the case where catalyst C10 was used, there was no induction period for the AAPCL. This behavior was due to the complex formation between the catalyst C10 and the activator C20 [23]. It could thus be concluded that the C20–C10 formulation was unsuitable for the RRM process due to the reaction being immediate and the liquid not having enough time to spread before gelation, causing defects to be generated. As an alternative, the slower reacting formulation, that is C20–C1, could provide the required time window for the RRM process. As can be seen in Figure 4, there was an induction time of 6 minutes before the start of polymerization.

#### 3.1.2. Effect of polymerization temperature and activator-catalyst concentration

Figure 5 shows that the final steady-state value of the complex viscosity did not seem to depend on the temperature, but rather on the time of the polymerization reaction. It can be noted that the induction time decreased with increasing temperature and concentration of C1/C20. Besides the type of activator and initiator used, also the amount of these reactive species and the temperature influenced the reaction [23]. It was shown that the concentration and polymerization temperature increased the polymerization rate.

A higher concentration of the activator increased the amount of initiator points for chain growth [23]. Also, with a higher concentration of catalyst, more



**Figure 5.** Effect of the polymerization temperature and concentration on the viscosity time profile of CL/C1/C20



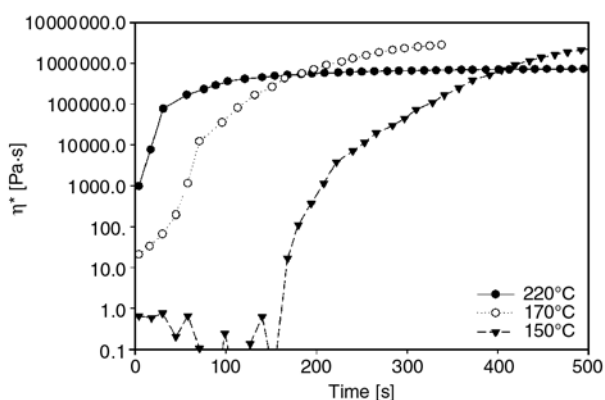
anions were set free and more complexes could be formed. As a consequence, the polymerization rate went up.

#### *In-situ monitoring of polymerization and crystallization by rheology and DSC*

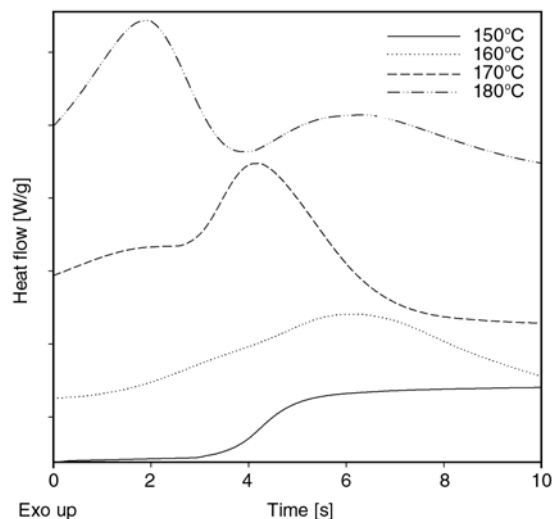
The monitoring of the change in crystallinity of the APA6 material during the reaction is shown in Figures 6 and 7. By combining the curves obtained from isothermal DSC and rheological measurements, it could be concluded that:

At lower temperatures (150–160°C), the crystallization occurred faster and the heat flow pointed at the polymerization and crystallization taking place simultaneously and not being separated in this temperature range. This simultaneous process can affect the crystal morphology and enhance the final properties of the polymer.

At higher temperature (170–180°C), as seen in Figure 7, the crystallization began after the polymerization isotherm was completed. If the polymerization and crystallization were consecutive, i.e., if the molecular weight build-up was completed before the start of crystallization, the crystallization kinetics would not differ from the melt-crystallized PA6 except for a time-shift equal to the time needed for polymerization. Since the polymerization took place below the final polymer melting and crystallization points ( $T_m = 224^\circ\text{C}$ ,  $T_c = 185^\circ\text{C}$ ), the crystallization became initiated during polymerization. In order to obtain optimal polymer properties, it was essential to balance the rate of polymerization and crystallization. The reaction temperature adversely affected both rates: with increasing temperature, the polymerization rate became higher, whereas the crystallization slowed down [23].



**Figure 6.** Viscosity-time profile of CL/C1/C20 (100/4/4) at different temperatures



**Figure 7.** In-situ monitoring by DSC of the crystallization during isothermal polymerization of CL/C1/C20 (100/4/4) at different temperatures

At 220°C, only the PA6 polymerization occurs (the temperature is close to the PA6 melting temperature  $\sim 224^\circ\text{C}$ ). In this case, the viscosity increases during the build-up of the molecular weight.

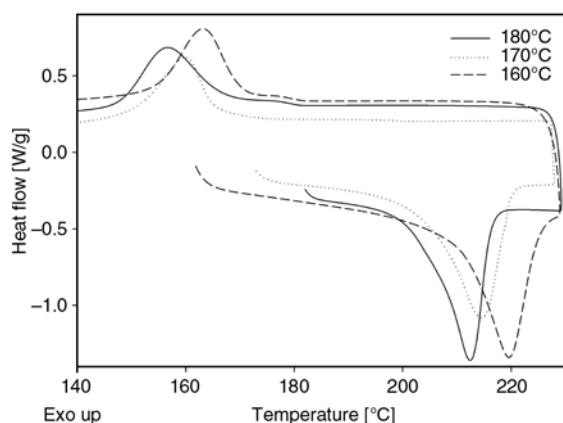
When the reaction temperature was too low, the crystallization was too fast and reactive chain-ends and monomer could get trapped inside the crystals before being able to polymerize. As a result, the final obtained conversions were low. On the other hand, when the reaction temperature was too high, the growth rate of the chains was significant, whereas the formation of crystals became delayed. The higher the molecular weight, the more the polymer chains became entangled. As a consequence, the resistance encountered during crystal formation increased, which reduced the final degree of crystallinity [23].

#### *Influence of polymerization temperature on the polymer melting point*

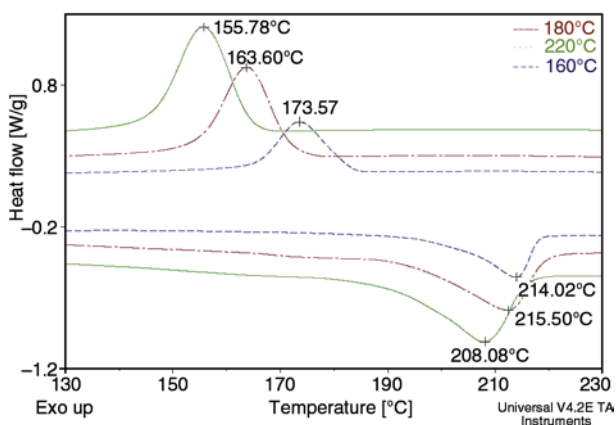
Figures 8 and 9 show typical DSC thermograms of polymer melting and crystallization peaks at several polymerization temperatures. It can be seen that the polymer melting temperature decreased with an increase of the polymerization temperature. At polymerization temperatures below the final melting point, the crystallization occurred during the polymerization and it caused an increase of the maximum melting point. As a result, crystallites formed during polymerization which led to much higher melting temperatures.

When increasing the polymerization temperature from 160 to 180°C, a drop in the polymer melting

point of 2 to 6°C was observed, see Figure 8 and 9. Three possible explanations can be given. First of all, residual caprolactam can reduce the polymer melting point [17]. Ricco et al. have reported melting point depressions between 3.5 and 5.8°C per wt% residual caprolactam [25]. Second, the increasing number of crystal imperfections induced by the formation of branch-points can cause a decrease in melting temperatures, simply because less energy is required in order to break down a crystal [26]. It is reported for APA6 that branching can even cause a transition in the crystal structure [25], which is the third reason for the lower melting points. This is explained as follows. Two types of crystals appear in anionic PA6, i.e., those with the  $\alpha$ -structure ( $T_m = 220^\circ\text{C}$ ) and those with the  $\gamma$ -structure ( $T_m = 214^\circ\text{C}$ ). For anionic PA6, it is reported that due to excessive branching, the  $\gamma$  content can increase [25], hence reducing the melting point.



**Figure 8.** DSC thermograms of heating and cooling of CL/C1/C20 (100/4/4) for various polymerization temperatures after isothermal polymerization in DSC



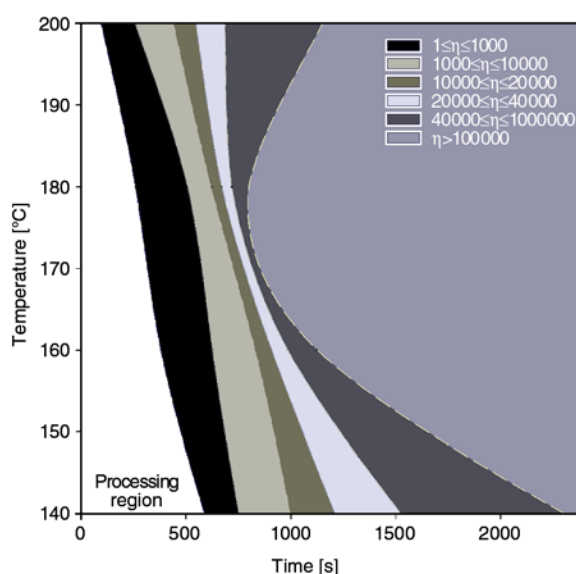
**Figure 9.** DSC thermogram of the cooling and second heating run for CL/C1/C20 (100/4/4) obtained with rheological tests at different temperatures after isothermal polymerization in the rheometer

### 3.2. Processing

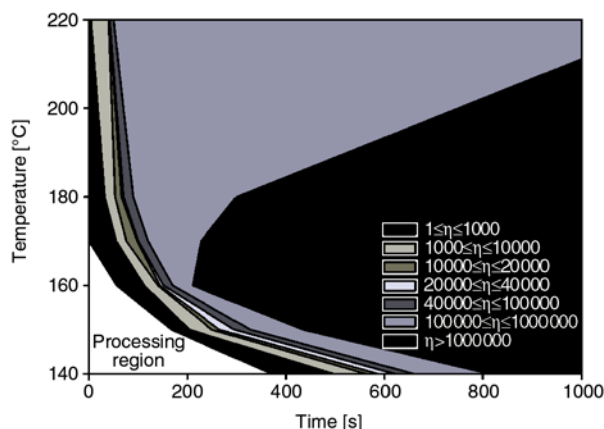
#### 3.2.1. Chemorheology

In the case of reactive rotational molding, the process is controlled by the variation in viscosity during polymerization [2]. Since the viscosity becomes increased as the polymerization progresses, a specific amount of time at a low viscosity is required to spread the liquid in the mold during rotation. It is therefore important to predict this available induction time, as it depends on the reaction kinetics and thus on the temperature.

Figures 10 and 11 present isoviscosity curves versus time and temperature of the two premixed blends CL/C1/C20 (100/3/3 and 100/4/4). The curves, obtained isothermally, range from 1 to  $10^5$  Pa·s. The one at 1 Pa·s renders it possible to determine the



**Figure 10.** The full range of isoviscosities versus time and temperature during polymerization of CL/C1/C20 (100/3/3)



**Figure 11.** The full range of isoviscosities versus time and temperature during polymerization of CL/C1/C20 (100/4/4)

available induction time versus temperature, as reported by Crawford [18]. The ideal viscosity for rotational molding of liquids is between 0.05 and 1 Pa·s. As the viscosity is dependent on temperature and the concentration of catalyst/activator, there was a minimum induction time for an isoviscosity curve at high temperature and concentration. Figure 10 and 11 portray the moldability zones, defining the areas where a successful rotational molding is expected.

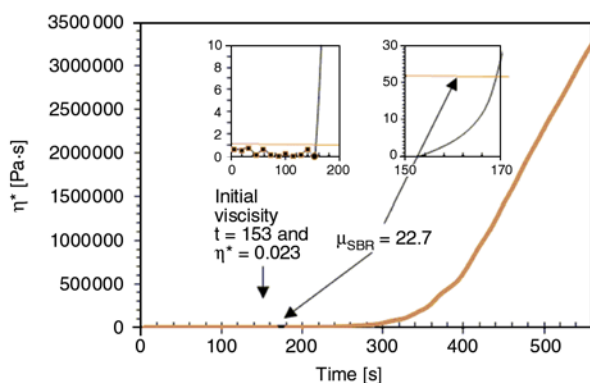
Below the final polymer melting temperature and with short amounts of time, the viscosity increase was caused by the polymerization; at longer periods of time the viscosity increase was also due to the crystallization [19].

The choice of minimum and optimum cycle times requires a minimum temperature representing the cycle that uses the lowest energy in order to obtain the rotomolded APA6 part. Furthermore, it has been shown that a temperature of 150°C offers the highest tensile properties [19, 23, 20]. Therefore, based on the isoviscosity curves of the premix CL/C1/C20 (100/4/4), we can expect the molding operation to be successfully carried out at this temperature with a short cycle time.

### 3.2.2. Criterion for producing defect-free APA6 parts in a biaxially rotating mold

In order to achieve a properly molded part, the material must be in the rubber state before gelation takes place [27]. The material reaction viscosity should increase slowly in the range within which solid body rotation occurs. However, if the initial viscosity is too low, the rate of increase will have no effect on the finished part [18].

Figure 12 shows the viscosity profile of the premix CL/C1/C20 (100/4/4) at 150°C. From this profile,



**Figure 12.** Viscosity-time profile of CL/C1/C20 (100/4/4) at 150°C

the initial and minimum viscosity was determined and, as can be seen, there was sufficient induction time for the spreading.

The rotational speed of the primary ( $W_1$ ) and secondary ( $W_2$ ) axes was respectively 4 and 5 rpm ( $4 \cdot 2\pi/60$  and  $5 \cdot 2\pi/60$ ) rad/s in the rotational molding test. A lowest possible rotational speed should be employed to minimize bubble formation [2]. The material density was assumed to be 1100 kg/m<sup>3</sup>. The wall thickness of the part was 0.002 m and the mold's major ( $R_1$ ) and minor radius ( $R_2$ ): were 0.125 and 0.05 m. The maximum solid-body rotation viscosity for the stated range of conditions was obtained according to Equation (3) as [2]:

$$\mu_{\text{SBR}} = \frac{0.7652\rho d}{R\omega^{1.5}} \quad (3)$$

where  $\mu_{\text{SBR}}$  = viscosity at which solid-body rotation occurs (Equation (4)),  $p$  = fluid density,  $d$  = finished wall part thickness,  $W$  = angular rotation speed ( $W = (W_1^2 + W_2^2)^{1/2}$ ), and  $R$  cylinder radius ( $R = (R_1^2 + R_2^2)^{1/2}$ ).

$$\mu_{\text{SBR}} = \frac{0.7652 \cdot 1100 \cdot 2 \cdot 10^{-3}}{(0.125^2 + 0.05^2)^{1/2} \cdot \left( \left( 5 \cdot \frac{2\pi}{60} \right)^2 + \left( 4 \cdot \frac{2\pi}{60} \right)^2 \right)^{1.5/2}} = 22.7 \text{ Pa}\cdot\text{s} \quad (4)$$

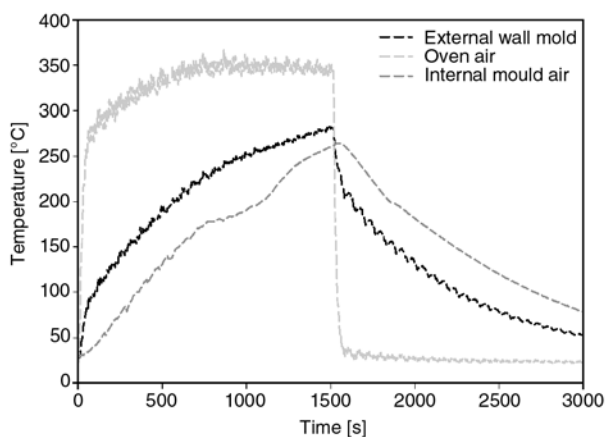
Equation (3) predicts a viscosity of 22.7 Pa·s for solid body rotation, and this result is marked in Figure 12. It can be seen from this that the material was in the rubber state just before the viscosity increased rapidly to gelation.

In summary, based on the rheological and DSC test results, the formulation CL/C1/C20 (100/4/4) at 150°C was selected and was used to fabricate APA6 parts with the RRM process.

### 3.3. Comparison between rotomolding PA6 parts obtained with RM and RRM

#### 3.3.1. Monitoring the process

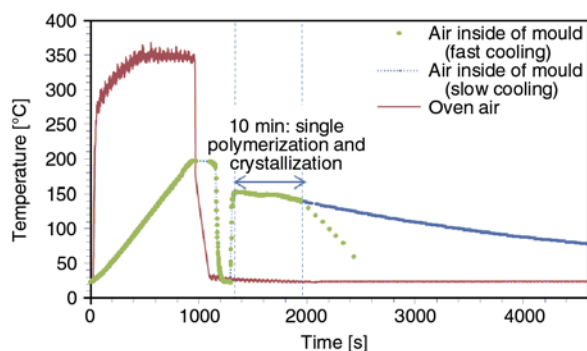
Temperatures profiles for the internal air, external mold and oven were recorded using thermocouples during the heating and cooling cycles of Capron. The processing conditions included: a weight charge of 450 g, an oven temperature of 350°C, a rotational speed of 4 and 5 rpm, and still air cooling. As, can be seen in Figure 13, the internal air temperature rose at a steady rate since it depended on the oven temperature. It exhibited four identifiable stages: induc-



**Figure 13.** Temperature measurement in the oven and the mold during rotational molding of PA6 capron

tion, adherence of powder, melting–sintering of the powder and fusion–densification [28, 29], as proposed by Harkin-Jones and Crawford [2]. The experimental results in Figure 10 suggest a cycle time of 45 minute to obtain a rotomolded PA6 part. The procedure for making a biaxially and reactive rotational molded part was as follows. The mold was placed in the oven until the required mold temperature was achieved. The mold temperature was output onto a computer in real time via a Rotolog temperature measuring system. When the desired temperature was achieved, the mold was removed from the oven and rotated into the correct position for filling. The vent pipe was removed from the mold and the material was poured into the funnel, at which stage the mold was purged with dry nitrogen. The vent pipe was replaced as quickly as possible and the mold was put into rotation for the required cycle time. Finally the cooling cycle (if required) was started.

By combining the viscosity curve of the APA6 material (Figure 12) with the rotational motion of



**Figure 14.** Temperature-time profiles for rotomolded anionic APA6: CL/C1/C20 (100/4/4) at 150°C polymerized out of the mold

the mold, see Figure 14, it was determined that the reactive premix passed through several flow phases. Before the rotation started, the liquid formed a pool at the bottom of the mold. During rotation the liquid was lifted up the mold wall in the direction of the rotation [2, 4]. The thickness of the layer is dependent on the linear velocity of rotation, the liquid viscosity and the liquid density. Based on the exothermic reaction of polymerization, as shown in Figure 12, it should be noted that the heat of melting resulted in the heating of the liquid, reduced the viscosity slightly during molding, before it started to increase again. Eventually, the viscosity of the liquid became sufficiently high for the mold wall to support the entire pool, resulting in solid body rotation. Ideally, solid body rotation should occur just before the viscosity of the plastic starts to increase rapidly as shown in Figure 12 [3].

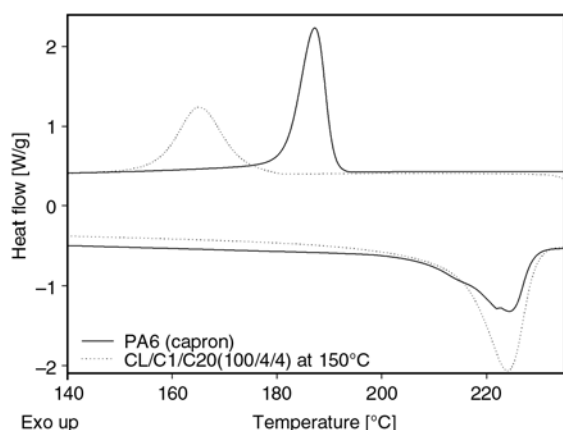
### 3.3.2. Characterization of PA6 obtained with RM and RRM

This section compares the thermal and tensile properties of two polyamides:

- PA6: capron, processed by melt rotational molding (Figure 13).
- APA6: polymerized and rotomolded by reactive processing at a temperature of 150°C (Figure 14). Anionic polymerization at 150°C led to a similar degree of conversion as the melt-processed PA6 (see Table 2). However, in the case of the reactive process, the polymer chains had already attained a high molecular weight. Figure 15 presents typical DSC thermograms obtained for the final samples CL/C1/C20 (100/4/4) prepared at 150°C with RRM and commercial PA6 (Capron) obtained with the

**Table 2.** Material characteristics and processing parameters when comparing classical versus reactive processing

Rotational molding technique of PA6	Classical	Reactive
Temperature	$T \sim 240^\circ\text{C}$	$T = 150^\circ\text{C}$
Cycle time	$t > 40 \text{ min}$	$t = 15\text{--}20 \text{ min}$
Speed ratio (S1/S2)	5/4	5/4
Melting point $T_f$ [ $^\circ\text{C}$ ]	224.3	224
Degree of crystallinity [%]	28	49
Degree of conversion [%]	98.81%	98.93%
Intrinsic viscosity [dL/g]	1.07	7
Molecular weight [g/mol]	30778	182594
<b>Tensile properties</b>		
Young's modulus [MPa]	750	1560
Yield stress [MPa]	62	80
Elongation at break [%]	32	64

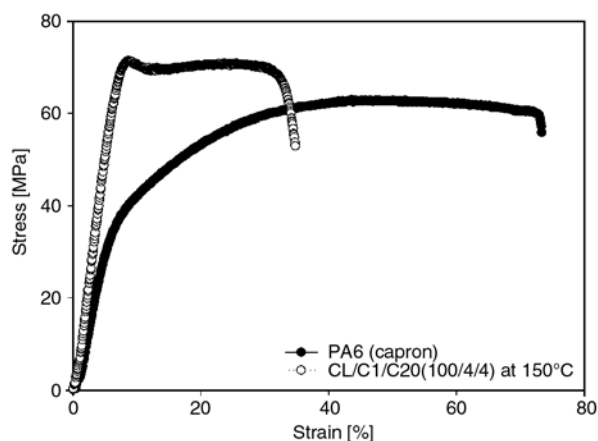


**Figure 15.** DSC traces of the cooling and second heating cycles of a APA6: Capron part obtained with rotational molding

melt process. A comparison of these results indicate that the melting temperature of this sample, i.e., 224°C, is very close to that of PA6, i.e., 224.3°C (see Table 2) [15]. Nevertheless, as can be seen, the heat of melt of APA6 was greater than PA6, indicating a higher degree of crystallinity, is expected to lead to a higher modulus and tensile strength and to a lower elongation [10].

The initial crystallization should take place at approx. 150°C. Since the polymerization occurred below the final polymer melting and crystallization points (i.e.,  $T_m = 224^\circ\text{C}$ ,  $T_c = 187^\circ\text{C}$ ), the crystallization became initiated already during polymerization despite that this temperature was well below the crystallization temperature of PA6 ( $T_c = 187^\circ\text{C}$ ). As a consequence, the crystal nuclei were plentiful and the final size of the spherulites was relatively small. Combining this with the high molecular weight of APA6 [22], one could expect that a single polymer chain was part of many of these small spherulites, which suggests a polymer morphology in which small spherulites were connected by a well-developed network of tie-molecules [23].

Tensile tests were performed on specimens obtained from the rotomolded parts. The typical stress-strain curves of PA6 and APA6 are shown in Figure 16, and a summary of the tensile properties, including Young's modulus ( $E$ ), tensile strength ( $\sigma_{Se}$ ), and elongation at break ( $A_r\%$ ), are listed in Table 2. APA6 polymerized at 150 °C show a pronounced tensile modulus and yield strength when compared with the PA6 elaborated through melting. This was due to the significantly higher degree of crystallinity, cf. Figure 15, Table 2. Furthermore, the corresponding values of elongation at break (Table 2) were



**Figure 16.** Typical stress-strain curves of PA6 Capron and APA6 at a crosshead speed of 10 mm/min

lower. This made APA6 less ductile as compared to the melt-processed capron.

It could therefore be concluded that, as with most semi-crystalline polymers, the mechanical properties of APA6 were predominantly determined by the degree of crystallinity and the level of conversion [14]. Furthermore, such polymerization-induced crystallization might be interesting as a means to decrease internal stresses [20] – a result that supports the studies of K. van Rijswijk *et al.* [14] and Udipi *et al.* [20], in which the highest tensile properties of APA6 at weak deformations were obtained at a mold temperature of 150°C.

#### 4. Conclusions

The kinetics of the APCL were investigated via DSC and rheology. The use of a rheometer as a chemical reactor rendered it possible to monitor the polymerization of  $\epsilon$ -caprolactam.

In order to optimize the processing parameters for a successful rotational molding process, the effect of different activator–initiator concentrations and combinations, as well as of the polymerization temperature, was investigated. It was shown that, while the reaction mechanism was determined by the activator–initiator combination, the concentration and polymerization temperature had a large influence on the reaction rate and the physical properties of the polymer. The catalyst C1 was more suitable than its C10 counterpart as it rendered possible a suitable induction time. The formulation 100/4/4 at temperature of 150°C was thus suggested.

The isoviscosity curves helped us to limit the rotational molding domain. A material with a viscosity profile could thus be formulated and tested. Finally, the APA6 obtained by reactive processing had a

shorter cycle time and superior tensile properties at weak deformation as opposed to melt processed PA6.

## References

- [1] Harkin-Jones E., Crawford R. J.: Mechanical properties of rotationally molded nylon. *Polymer Engineering and Science*, **36**, 615–625 (1996).  
DOI: [10.1002/pen.10449](https://doi.org/10.1002/pen.10449)
- [2] Harkin-Jones E., Crawford R. J.: Rotational molding of liquid plastic systems: An assessment of material moldability. *Advances in Polymer Technology*, **15**, 71–100 (1996).  
DOI: [10.1002/\(SICI\)1098-2329\(199621\)15:1<71::AID-ADV6>3.0.CO;2-H](https://doi.org/10.1002/(SICI)1098-2329(199621)15:1<71::AID-ADV6>3.0.CO;2-H)
- [3] Barhouni N., Lamnawar K., Maazouz A., Jaziri M., Abdelhedi R.: Reactive rotational molding process of PP/PA6 bilayer systems: Experimental investigations. *International Journal of Material Forming*, **1**, 671–674 (2008).  
DOI: [10.1007/s12289-008-0304-9](https://doi.org/10.1007/s12289-008-0304-9)
- [4] Mougou N., Veith C. A., Cohen R. E., Gnanou Y.: Anionic polymerization of lactams in the presence of metal dialkoxylaluminum hydrides: Presentation of a new mechanism. *Macromolecules*, **25**, 2004–2016 (1992).  
DOI: [10.1021/ma00033a026](https://doi.org/10.1021/ma00033a026)
- [5] Brouwer W. D., van Herpt E. C. F. C., Labordus M.: Vacuum injection moulding for large structural applications. *Composites Part A: Applied Science and Manufacturing*, **34**, 551–558 (2003).  
DOI: [10.1016/S1359-835X\(03\)00060-5](https://doi.org/10.1016/S1359-835X(03)00060-5)
- [6] Macosko C. W.: *RIM fundamentals of reaction injection molding*. Hanser, Munich (1989).
- [7] Rusu G., Rusu E.: Nylon 6/SiO<sub>2</sub> nanocomposites synthesized by in situ anionic polymerization. *High Performance Polymers*, **18**, 355–375 (2006).  
DOI: [10.1177/0954008306063392](https://doi.org/10.1177/0954008306063392)
- [8] Rusu G. H., Rusu M., Rusu E., Stoleriu A., Teaca C. A.: Direct centrifugal molding of nylon 6-based products from ε-caprolactam. *Polymer Plastics Technology and Engineering*, **3**, 233–247 (2000).  
DOI: [10.1081/PPT-100100026](https://doi.org/10.1081/PPT-100100026)
- [9] Rusu G., Ueda K., Rusu E., Rusu M.: Polyamides from lactams by centrifugal molding via anionic ring-opening polymerization. *Polymer*, **42**, 5669–5678 (2001).  
DOI: [10.1016/S0032-3861\(01\)00059-3](https://doi.org/10.1016/S0032-3861(01)00059-3)
- [10] Rudolf P., Vladimir K.: *Lactam-based polyamides, Volume I: Polymerization structure*. CRC Press, Boca Raton (1991).
- [11] Goodman I., Kehayoglou A. H.: Anionic copolymers of caprolactam with laurolactam (nylon 6/12 copolymers) II. Crystallisation, glass transitions and tensile properties. *European Polymer Journal*, **19**, 321–325 (1983).  
DOI: [10.1016/0014-3057\(83\)90167-2](https://doi.org/10.1016/0014-3057(83)90167-2)
- [12] Zhang C-L., Feng L., Hu G-H.: Anionic polymerization of lactams: A comparative study on various methods of measuring the conversion of ε-caprolactam to polyamide 6. *Applied Polymer Science*, **101**, 1972–1981 (2006).  
DOI: [10.1002/app.23659](https://doi.org/10.1002/app.23659)
- [13] Nelson W. E.: *Nylon plastics technology*. Newnes-Butterworths, London (1976).
- [14] van Rijswijk K., Bersee H. E. N., Jager W. F., Picken S. J.: Optimisation of anionic polyamide-6 for vacuum infusion of thermoplastic composites: Choice of activator and initiator. *Composites Part A: Applied Science and Manufacturing*, **37**, 949–956 (2006).  
DOI: [10.1016/j.compositesa.2005.01.023](https://doi.org/10.1016/j.compositesa.2005.01.023)
- [15] Khodabakhshi K., Gilbert M., Dickens P., Hague R.: Optimizing conditions for anionic polymerization of caprolactam for inkjetting. *Advances in Polymer Technology*, **29**, 226–236 (2010).  
DOI: [10.1002/adv.20191](https://doi.org/10.1002/adv.20191)
- [16] Ueda K., Nakai M., Hosoda M., Tai K.: Synthesis of high molecular weight nylon 6 by anionic polymerization of ε-caprolactam. Mechanism and kinetics. *Polymer*, **29**, 568–573 (1997).
- [17] van Rijswijk K., Bersee H. E. N., Beukers A., Picken S. J., van Geenen A. A.: Optimisation of anionic polyamide-6 for vacuum infusion of thermoplastic composites: Influence of polymerisation temperature on matrix properties. *Polymer Testing*, **25**, 392–404 (2006).  
DOI: [10.1016/j.polymertesting.2005.11.008](https://doi.org/10.1016/j.polymertesting.2005.11.008)
- [18] Crawford R. J.: *Rotational molding of plastics*. John Wiley & Sons, New York (1996).
- [19] Luisier A., Bourban P-E., Manson J-A. E.: Time-temperature-transformation diagram for reactive processing of polyamide 12. *Journal of Applied Polymer Science*, **81**, 963–972 (2001).  
DOI: [10.1002/app.1518](https://doi.org/10.1002/app.1518)
- [20] Udipi K., Davé R. S., Kruse R. L., Stebbins L. R.: Polyamides from lactams via anionic ring-opening polymerization: 1. Chemistry and some recent findings. *Polymer*, **38**, 927–938 (1997).  
DOI: [10.1016/S0032-3861\(96\)00566-6](https://doi.org/10.1016/S0032-3861(96)00566-6)
- [21] Kim K. J., Hong D. S., Tripathy A. R.: Kinetics of adiabatic anionic copolymerization of ε-caprolactam in the presence of various activators. *Journal of Applied Polymer Science*, **66**, 1195–1207 (1997).  
DOI: [10.1002/\(SICI\)1097-4628\(19971107\)66:6<1195::AID-APP19>3.0.CO;2-0](https://doi.org/10.1002/(SICI)1097-4628(19971107)66:6<1195::AID-APP19>3.0.CO;2-0)
- [22] Crawford R. J., Throne J. L.: *Rotational molding technology*. Plastics Design Library, Norwich (2002).
- [23] van Rijswijk K., Lindstedt S., Vlasveld D. P. N., Bersee H. E. N., Beukers A.: Reactive processing of anionic polyamide-6 for application in fiber composites: A comparative study with melt processed polyamides and nanocomposites. *Polymer Testing*, **25**, 873–887 (2006).  
DOI: [10.1016/j.polymertesting.2006.05.006](https://doi.org/10.1016/j.polymertesting.2006.05.006)

- [24] Hakmé C., Stevenson I., Maazouz A., Cassagnau P., Boiteux G., Seytre G.: In situ monitoring of cyclic butylene terephthalate polymerization by dielectric sensing. *Journal of Non-Crystalline Solids*, **353**, 4362–4365 (2007).  
DOI: [10.1016/j.jnoncrysol.2007.04.051](https://doi.org/10.1016/j.jnoncrysol.2007.04.051)
- [25] Ricco L., Russo S., Orefice G., Riva F.: Anionic poly ( $\epsilon$ -caprolactam): Relationships among conditions of synthesis, chain regularity, reticular order, and polymorphism. *Macromolecules*, **32**, 7726–7731 (1999).  
DOI: [10.1021/ma9909004](https://doi.org/10.1021/ma9909004)
- [26] Young R. J., Lovell P. A.: *Introduction to polymers*. Chapman and Hall, London (1991).
- [27] Throne J. L., Gianchandani J.: Reactive rotational molding. *Polymer Engineering and Science*, **20**, 899–919 (1980).  
DOI: [10.1002/pen.760201309](https://doi.org/10.1002/pen.760201309)
- [28] Bellehumeur C. T., Kontopoulou M., Vlachopoulos J.: The role of viscoelasticity in polymer sintering. *Rheologica Acta*, **37**, 270–278 (1998).  
DOI: [10.1007/s003970050114](https://doi.org/10.1007/s003970050114)
- [29] Liu S.-J.: Sintering rheology of semi-crystalline polymers. *International Polymer Processing*, **13**, 88–90 (1998).

# Microencapsulation of self-healing agents containing a fluorescent dye

H. H. Noh, J. K. Lee\*

Department of Polymer Science and Engineering, Kumoh National Institute of Technology, #1 Yangho-Dong, Gumi-City, Gyungbuk 730-701, Korea

Received 11 June 2012; accepted in revised form 3 September 2012

**Abstract.** Two different self-healing agent candidates, *endo*-dicyclopentadiene (*endo*-DCPD) and 5-ethylidene-2-norbornene (ENB), containing a fluorescent dye surrounded by a melamine–urea–formaldehyde (MUF) shell were microencapsulated by *in-situ* polymerization and the resulting microcapsules were characterized in this work. The microcapsules showed a narrow size distribution with a spherical shape and rough outer and smooth inner surfaces for both healing agent systems. Shell thicknesses of the microcapsules were  $\sim 880 \pm 80$  nm for *endo*-DCPD and  $\sim 620 \pm 60$  nm for ENB. The incorporation of a fluorescent dye as tracer into self-healing agents did not disturb the formation of microcapsules. The release of self-healing liquid into the induced crack from ruptured microcapsules in an epoxy coating layer was observed using a fluorescence microscopy. The use of a fluorescent dye is very effective in the observation of a damage site.

**Keywords:** coatings, self-healing, microencapsulation, fluorescent dye

## 1. Introduction

A lot of research on self-healing technology is underway for microcapsule-based coating systems over the last decade [1–6]. In this technique, microcapsules rupture upon damage inducing cracks in the coating layer, releasing their encapsulated liquid healing agent into the crack planes. The organic and inorganic self-healing materials, surrounded by urea-formaldehyde (UF) thermosetting shell were microencapsulated, and the microcapsules were embedded into different polymer coating materials, showing protective ability on steel plate (e.g., effective inhibition from metal corrosion and rusting) [1, 2]. A norbornene-based ring opening metathesis polymerization (ROMP) healing agent, *endo*-dicyclopentadiene (*endo*-DCPD), as self healing agent was also microencapsulated with UF shell [7–12]. UF capsules filled with *endo*-DCPD were devel-

oped in nano-size, which is important in fabricating thin coating applications [3].

Recently, self-healing agents, 5-ethylidene-2-norbornene (ENB) and ENB with crosslinkers, showing a faster ROMP rate at lower catalyst loadings, were microencapsulated with a ternary melamine–urea–formaldehyde (MUF) shell in this laboratory [11, 12]. The fabrication process is relatively very simple with no external control of pH, and produced a narrow size distribution of capsules with no debris. These microcapsules also had a rough outer surface and exhibited significantly higher thermal stability and less core material permeability when compared to UF capsules. Small changes in the core material during encapsulation process (e.g., going from one core material to a closely related core material), the manufacturing procedure (e.g., order of input), the ratio of the reactants and additives (e.g., typically the ratio between the main compo-

\*Corresponding author, e-mail: [jklee@kumoh.ac.kr](mailto:jklee@kumoh.ac.kr)  
© BME-PT



nents of shell forming reagents), and the reaction conditions (e.g., reacting temperature and time) often lead to significant changes in the formation of acceptable microcapsules.

One of the key aspects for achieving a successful microcapsule-based self-healing system lies with production of adequate microcapsules to be embedded. Thus, microcapsules must be carefully engineered in order to possess requisite strength during handling and processing, long shelf life during storage, and excellent adhesion with the cured polymer matrix [13]. It is also critical that the liquid healing agent within microcapsules is effectively delivered into the crack planes after damage in order to provide efficient recovery of properties. Therefore, it is beneficial to track the release of healing agent through invisible cracks from incorporated microcapsules for the development of self-healing. The addition of tracers such as X-ray dye [14] and UV fluorescent material [15] for hollow fiber reinforced composites and red dye [1] for microcapsule containing coatings into the self-healing agents have been reported for visual observations of damages.

In this study, microcapsules were synthesized for two different self-healing agents, *endo*-DCPD and ENB, containing a fluorescent dye surrounded by MUF shell. A particle size analyzer (PSA), a thermogravimetric analyzer (TGA) and a scanning electron microscope (SEM) were used to investigate particle size/size distribution and thermal resistance of the microcapsules and to observe morphology of the capsules, respectively. The MUF microcapsules containing a fluorescent dye were dispersed in an epoxy coating layer and a fluorescence microscope (FM) was used to track the transport of liquid healing agent through cracks after inducing the damage on the epoxy coating.

## 2. Experimental

### 2.1. Preparation of microcapsules and coatings

Two healing agent candidates, *endo*-DCPD (with 95% *endo*-isomer, Acros Chemical Co., Belgium) and ENB (Sigma–Aldrich, USA) as core material, were microencapsulated by *in-situ* polymerization of melamine (M) (Sigma–Aldrich, USA), urea (U) (Sigma–Aldrich, USA) and formaldehyde solution, 37 wt% in H<sub>2</sub>O (F) (Sigma–Aldrich, USA) to produce the MUF polymer shell in an aqueous solution. Sodium lauryl sulfate (SLS, Junsei, Japan)

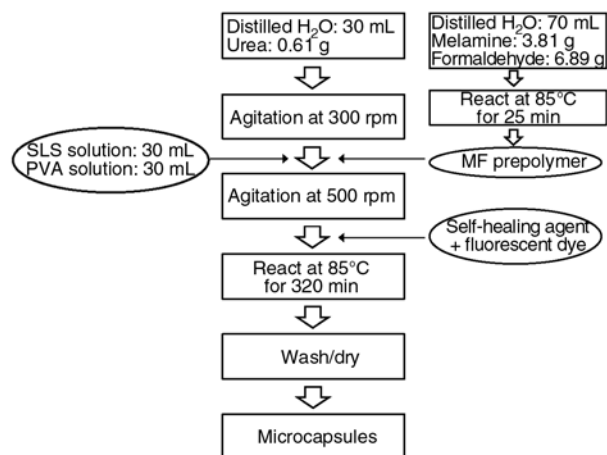
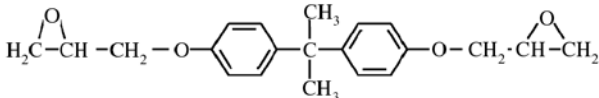
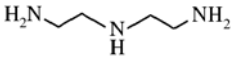

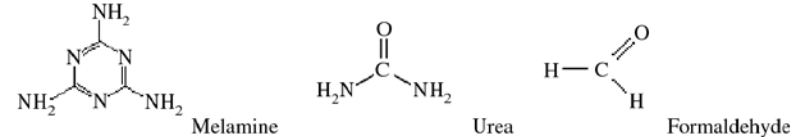
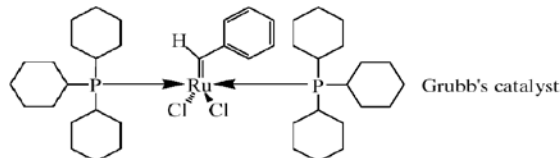


Figure 1. Microencapsulation process

was used as emulsifier, and poly(vinyl alcohol) (PVA, degree of polymerization = 500, degree of hydrolysis = 99.0 mol%, Junsei, Japan) as stabilizer. Figure 1 shows the microencapsulation process in this work. A fluorescent dye (derivative of 4,4'-diamino-2,2'-stilbenedisulfonic acid, Hwasung Chemical Co., Ltd., Korea) of 0.05 g/L was dissolved in self-healing agents at room temperature for 10 min before encapsulation. Also, SLS (0.5 wt%) and PVA (6.3 wt%) aqueous solutions were prepared by heating at 70°C for 20 min and 2 h, respectively. MF prepolymer solution was obtained from a mixture of 3.81 g melamine and 6.89 g 37 wt% formaldehyde aqueous solution with 70 mL distilled water by heating at 70°C for 25 min until it becomes clear. Urea (0.61 g) was dissolved in 30 mL distilled water at RT in a 250 mL reaction beaker. Subsequently, the MF solution, 30 mL SLS solution, and 30 mL PVA solution were added into the reaction beaker, after raising the agitating speed to 300 rpm. Prior to slowly adding 30 mL of core healing agent (*endo*-DCPD or ENB + fluorescent dye) into the beaker, the agitation speed was increased to 500 rpm, leading to the formation of small droplets of the core materials. This agitation step was allowed to continue for 10 min at RT to generate the stabilized emulsion, before the temperature was raised to the nominal reaction temperature of 85°C for 40 min and maintained for 320 min under continuous agitation. The microcapsule slurry formed after the isothermal reaction was decanted on filter paper (Advantec no. 2, Toyo Roshi Kaisha Ltd., Japan). The microcapsules were separated into individual capsules easily by hand-shaking after rinsing and drying. The microcapsules produced were mechanically dispersed into diglycidyl ether of bisphenol-A

**Table 1.** Chemicals used for microencapsulation and epoxy coatings

Thermosetting system (matrix)	Matrix resin	 DGEBA
	Curing agent	 DETA
Microcapsule	Healing agent	 DCPD   ENB   Fluorescent agent
	Shell	 Melamine   Urea   Formaldehyde
Catalyst	 Grubbs' catalyst	

(DGEBA, equivalent weight = 188 g·eq<sup>-1</sup>, Kukdo Chem., Korea) epoxy coatings cured with diethylenetriamine (DETA, equivalent weight = 190 g·eq<sup>-1</sup>, Kukdo Chem., Korea) at room temperature for 24 hours. Table 1 has chemicals used for microencapsulation and epoxy coatings.

## 2.2. Characterization of microcapsules

The thermal stability of the microcapsules was examined with a thermogravimetric analyzer (TGA, Auto-TGA Q500, TA Instruments, USA) upon heating from room temperature (RT) to 500°C for ENB- and 600°C for *endo*-DCPD-microcapsules at a scanning rate of 10°C/min in a nitrogen atmosphere. The size and size distribution of the microcapsules were obtained with a particle size analyzer (PSA, Mastersizer 2000, Malvern Instrument, UK). The capsule surface and shell wall thickness were analyzed using a scanning electronic microscope (SEM, JSM-6380, Jeol, Japan) after the microcapsules were spread on an adhesive tape, punctured using a razor blade, and heated on a hotplate at 150°C for 12 hours to ensure that the core material completely evaporated.

## 2.3. Damage observations

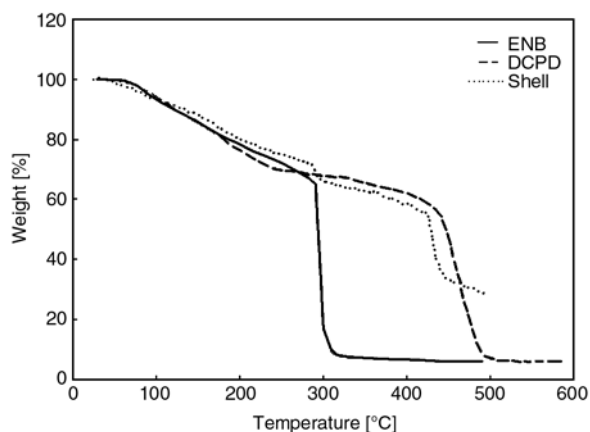
DGEBA epoxy resin was mixed with 5 wt% of Grubbs catalyst using a mechanical stirrer for 10 min at 500 rpm, followed by adding DETA curing agent in an equivalent weight and mixing for additional 10 min. 5 wt% of microcapsules was added to the

epoxy solution and mixed at a slower stirring speed of 150 rpm for 10 min. Air bubbles were removed under vacuum for 10 min. The mixed epoxy resin was then poured into a mold (50 mm × 5.3 mm × 0.2 mm) made by polyurethane, and then cured at RT for 24 h and at 50°C for 4 h. A fluorescent microscope (Axiovert 40 CFL, Zeiss, Germany) was employed to observe microcapsules before damage and the transport of healing agent through cracks after damage to the cured coating layer given by hand. The excitation wavelengths used for the observation in this work were  $\lambda = 350, 480, \text{ and } 546 \text{ nm}$ .

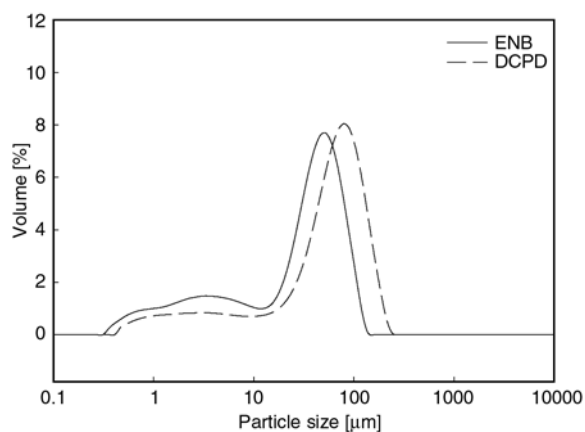
## 3. Results and discussion

### 3.1. Thermogravimetric analysis

Figure 2 shows the weight loss curves of *endo*-DCPD- and ENB-microcapsules containing a fluorescent dye and the MUF capsule shell without the core material. As shown in the figure, there are gradual and similar decreases down to ~70% in weight for both *endo*-DCPD- and ENB-microcapsules up to ~300°C above which there are sudden weight drops for ENB-microcapsules as reported in the previous work [11]. For *endo*-DCPD-microcapsules, the sudden drop occurred at ~430°C, much higher than that of ENB-microcapsules. The dramatic weight loss in a particular temperature of the microcapsules is due to a sudden release of the healing agent. As the temperature increases, the microcapsules become weaker and burst beyond the critical level at a certain temperature by increasing



**Figure 2.** TGA thermogram of *endo*-DCPD- and ENB-microcapsules



**Figure 3.** Particle size analysis of *endo*-DCPD- and ENB-microcapsules

the internal pressure of the microcapsules and the collapse of the weakened shells [11]. Notice the sudden loss of MUF shell mass at  $\sim 420^{\circ}\text{C}$ , indicating thermal degradation, which would lead to a dramatic decrease in mechanical strength of the shell. The gradual weight loss below the temperature at which the sudden weight loss takes place may be attributed to the diffusion and evaporation of self-healing agent through walls of microcapsules. The thicker capsule shell thickness of *endo*-DCPD-microcapsules leads to the dramatic weight loss temperature higher than ENB-microcapsules, as will be shown in the SEM image.

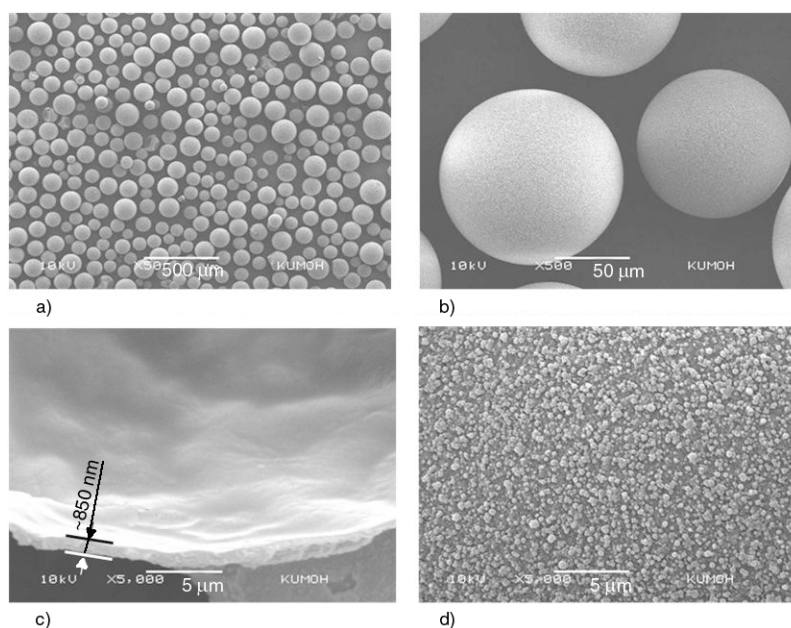
### 3.2. Particle size analysis

Figure 3 shows the distribution of the microcapsules using a particle size analyzer. Average diameters

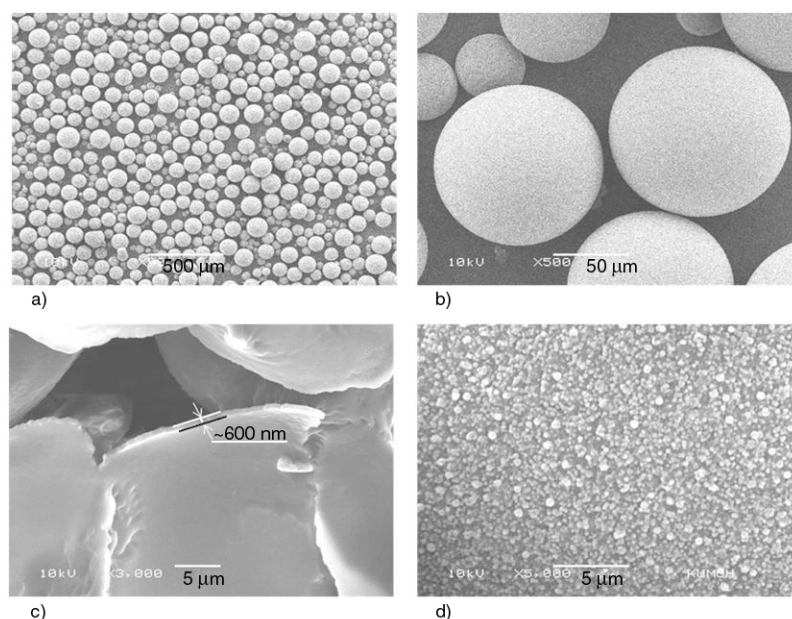
of *endo*-DCPD- and ENB-microcapsules are found to be  $\sim 80$  and  $\sim 52$   $\mu\text{m}$ , respectively. A relatively higher viscosity of *endo*-DCPD than that of ENB produces larger self-healing agent droplets, leading to larger *endo*-DCPD-microcapsules than ENB-microcapsules in average diameter. The particle size can readily be adjusted by rpm of propeller during dispersion of healing agents in water. The shoulder in the range of  $1\sim 10$   $\mu\text{m}$  in this figure may be due to the particles formed by self-coagulation of the wall materials.

### 3.3. SEM observations

Scanning electron microscope images for microcapsules filled with *endo*-DCPD and ENB were respectively shown in Figures 4 and 5. As noticed from the images in both figures, a perfect sphere



**Figure 4.** Scanning electron microscopic pictures of *endo*-DCPD-microcapsules at rpm = 500 showing the shape of the microcapsules (a and b), and fractured microcapsules showing inner (c) and outer surface (d)



**Figure 5.** Scanning electron microscopic pictures of ENB-microcapsules at rpm = 500 showing the shape of the microcapsules (a and b), and fractured microcapsules showing inner (c) and outer surface (d)

with similar inner and outer surfaces was produced. There is no debris for both self-healing agents. Looking at the surface is somewhat rough external surface and smooth inner wall. The rough outer surface of microcapsules is thought to contribute to improving the adhesion between the host matrix and capsules by increasing contact area with the matrix material. The thicknesses of the shells were found to be  $\sim 880 \pm 80$  and  $\sim 620 \pm 60$  nm from SEM images of *endo*-DCPD- and ENB-microcapsules, respectively.

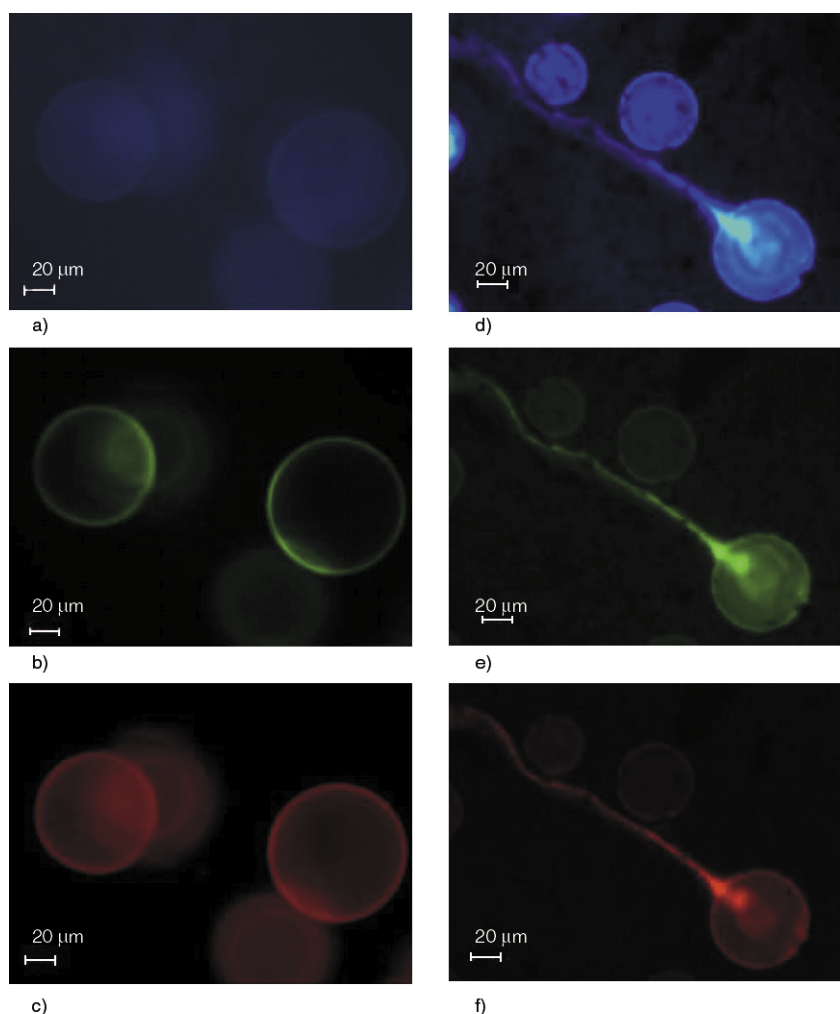
### 3.4. Fluorescence microscope observations

In this study, the morphology of microcapsules and the release of the self-healing agent from microcapsules were observed after inducing cracks on an epoxy coating layer dispersed with 5 wt% of *endo*-DCPD-microcapsules by means of a fluorescence microscope. Figure 6 contains fluorescent microscope images (a), (b), and (c) before damaging and (d), (e), and (f) after damaging taken at different excitation wavelengths of 350, 480, and 546 nm, respectively. The vivid images could be viewed for all excitation wavelengths in different emission colors; blue at 350 nm, green at 480 nm, and red at 546 nm. Note that the image without a fluorescent dye showed completely black in color. The images showed a spherical shape of microcapsules as observed by SEM. It is interesting to notice that the capsule shell is very bright, indicating the incorporation of fluorescent dye into the shell material. Note that the dye

was mixed with self-healing agent, followed by dispersion in water and then in-situ polymerization of shell materials reaction at higher temperature. This is presumably due to the migration of dye to shell forming material during the initial stage of reaction. The images (d), (e), and (f) in Figure 6 for cracked coating layer embedded with 5 wt% of Grubbs catalyst and 5 wt% of microcapsules show a bright line starting from microcapsules. This is considered to be the trace of transport of self-healing agent between crack planes released from a microcapsule. The brightest fluorescence was observed in the vicinity of the microcapsules where the release of self-healing agent starts to the cracks because the larger amount healing agent is spread to the exit of crack. Also, it is shown that the propagating crack runs around one of small microcapsule at left-top in the image. The black spots shown in the images (d), (e), and (f) are believed to come from the Grubbs catalyst in the matrix. In this work, the addition of a fluorescent dye to self-healing agent enables to observe the track of the self-healing agent release into cracks from microcapsules at three different UV wavelengths. This means that the addition of fluorescent dye to self-healing agent may be useful in studying the details of cracks which are crucial in a microcapsule-based self-healing methodology.

### 4. Conclusions

In this study, microcapsules containing self-healing agents, *endo*-DCPD and ENB, and a fluorescent



**Figure 6.** Fluorescent microscope images for a coating layer dispersed with *endo*-DCPD microcapsules containing a fluorescent dye (before damage, left) and a fluorescent dye in the presence of Grubbs catalyst (after damage, right) at different excited wavelengths; (a) and (d) at  $\lambda = 350$  nm, (b) and (e)  $\lambda = 480$  nm, (c) and (f)  $\lambda = 546$  nm

dye surrounded by the MUF shell were successfully synthesized and analyzed to develop a self-healing coating system. Thermogravimetric analysis showed that *endo*-DCPD-microcapsules have a significantly higher thermal stability than ENB-microcapsules. From scanning electron microscope observations, both *endo*-DCPD- and ENB-microcapsules have similar morphologies in shape and inner/outer surfaces but different shell thicknesses. The use of a fluorescent dye gave rise to the clear visual images of microcapsules and cracks filled the self-healing agent from ruptured microcapsules after damage at different excited wavelengths.

### Acknowledgements

This research was supported by Basic Science Research Program through the National Research Foundation of Korea (NRF) funded by the Ministry of Education, Science and Technology (2011-0009510).

### References

- [1] Kumar A., Stephenson L. D., Murray J. N.: Self-healing coatings for steel. *Progress in Organic Coatings*, **55**, 244–253 (2006). DOI: [10.1016/j.porgcoat.2005.11.010](https://doi.org/10.1016/j.porgcoat.2005.11.010)
- [2] Sauviant-Moynot V., Gonzales S., Kittel J.: Self-healing coatings: An alternative route for anticorrosion protection. *Progress in Organic Coatings*, **63**, 307–315 (2008). DOI: [10.1016/j.porgcoat.2008.03.004](https://doi.org/10.1016/j.porgcoat.2008.03.004)
- [3] Blaiszik B. J., Sottos N. R., White S. R.: Nanocapsules for self-healing materials. *Composites Science and Technology*, **68**, 978–986 (2008). DOI: [10.1016/j.compscitech.2007.07.021](https://doi.org/10.1016/j.compscitech.2007.07.021)
- [4] Cho S. H., White S. R., Braun P. V.: Self-healing polymer coatings. *Advanced Materials*, **21**, 645–649 (2009). DOI: [10.1002/adma.200802008](https://doi.org/10.1002/adma.200802008)
- [5] García S. J., Fischer H. R., van der Zwaag S.: A critical appraisal of the potential of self healing polymeric coatings. *Progress in Organic Coatings*, **72**, 211–221 (2011). DOI: [10.1016/j.porgcoat.2011.06.016](https://doi.org/10.1016/j.porgcoat.2011.06.016)

- [6] Samadzadeh M., Hatami Boura S., Peikari M., Kasirihha S. M., Ashrafi A.: A review on self-healing coatings based on micro/nanocapsules. *Progress in Organic Coatings*, **68**, 159–164 (2010). DOI: [10.1016/j.porgcoat.2010.01.006](https://doi.org/10.1016/j.porgcoat.2010.01.006)
- [7] Brown E. N., Kessler M. R., Sottos N. R., White S. R.: In situ poly(urea-formaldehyde) microencapsulation of dicyclopentadiene. *Journal of Microencapsulation*, **20**, 719–730 (2003). DOI: [10.1080/0265204031000154160](https://doi.org/10.1080/0265204031000154160)
- [8] Li H., Wang R., Hu H., Liu W.: Surface modification of self-healing poly(urea-formaldehyde) microcapsules using silane-coupling agent. *Applied Surface Science*, **255**, 1894–1900 (2008). DOI: [10.1016/j.apsusc.2008.06.170](https://doi.org/10.1016/j.apsusc.2008.06.170)
- [9] Wang R., Li H., Hu H., He X., Liu W.: Preparation and characterization of self-healing microcapsules with poly(urea-formaldehyde) grafted epoxy functional group shell. *Journal of Applied Polymer Science*, **113**, 1501–1506 (2009). DOI: [10.1002/app.30001](https://doi.org/10.1002/app.30001)
- [10] Yuan L., Liang G-Z., Xie J-Q., He S-B.: Synthesis and characterization of microencapsulated dicyclopentadiene with melamine-formaldehyde resins. *Colloid and Polymer Science*, **285**, 781–791 (2007). DOI: [10.1007/s00396-006-1621-5](https://doi.org/10.1007/s00396-006-1621-5)
- [11] Liu X., Sheng X., Lee J. K., Kessler M. R.: Synthesis and characterization of melamine-urea-formaldehyde microcapsules containing ENB-based self-healing agents. *Macromolecular Materials and Engineering*, **294**, 389–395 (2009). DOI: [10.1002/mame.200900015](https://doi.org/10.1002/mame.200900015)
- [12] Liu X., Lee J. K., Kessler M. R.: Microencapsulation of self-healing agents with melamine-urea-formaldehyde by the shirasu porous glass (SPG) emulsification technique. *Macromolecular Research*, **19**, 1056–1061 (2011). DOI: [10.1007/s13233-011-1009-3](https://doi.org/10.1007/s13233-011-1009-3)
- [13] Mauldin T. C., Kessler M. R.: Self-healing polymers and composites. *International Materials Reviews*, **55**, 317–346 (2010). DOI: [10.1179/095066010X12646898728408](https://doi.org/10.1179/095066010X12646898728408)
- [14] Bleay S. M., Loader C. B., Hawyes V. J., Humberstone L., Curtis P. T.: A smart repair system for polymer matrix composites. *Composites Part A: Applied Science and Manufacturing*, **32**, 1767–1776 (2001). DOI: [10.1016/S1359-835X\(01\)00020-3](https://doi.org/10.1016/S1359-835X(01)00020-3)
- [15] Pang J. W. C., Bond I. P.: A hollow fibre reinforced polymer composite encompassing self-healing and enhanced damage visibility. *Composites Science and Technology*, **65**, 1791–1799 (2005). DOI: [10.1016/j.compscitech.2005.03.008](https://doi.org/10.1016/j.compscitech.2005.03.008)

# A versatile characterization of poly(*N*-isopropylacrylamide-co-*N,N'*-methylene-bis-acrylamide) hydrogels for composition, mechanical strength, and rheology

A. Chetty<sup>1</sup>, J. Kovács<sup>2</sup>, Zs. Sulyok<sup>2</sup>, Á. Mészáros<sup>3</sup>, J. Fekete<sup>3</sup>, A. Domján<sup>4</sup>, A. Szilágyi<sup>2</sup>, V. Vargha<sup>2\*</sup>

<sup>1</sup>CSIR Materials Science and Manufacturing, Polymers and Composites, PO Box 395, 0001 Pretoria, South Africa

<sup>2</sup>Budapest University of Technology and Economics, Department of Physical Chemistry and Materials Science, Műegyetem rkp. 3. H/1, H-1111 Budapest, Hungary

<sup>3</sup>Budapest University of Technology and Economics, Department of Inorganic and Analytical Chemistry, Műegyetem rkp. 3. Ch/A, H-1111 Budapest, Hungary

<sup>4</sup>NMR Spectroscopy Laboratory, Institute of Organic Chemistry, Research Centre for Natural Sciences, Hungarian Academy of Sciences, Pusztaszeri út 59–67, H-1025 Budapest, Hungary

Received 26 June 2012; accepted in revised form 6 September 2012

**Abstract.** Poly(*N*-isopropylacrylamide-co-*N,N'*-methylene-bisacrylamide) (P(NIPAAm-co-MBA)) hydrogels were prepared in water using redox initiator. The copolymer composition at high conversion (>95%) was determined indirectly by HPLC (high performance liquid chromatography) analysis of the leaching water and directly by solid state <sup>13</sup>C CP MAS NMR (cross polarization magic angle spinning nuclear magnetic resonance) spectroscopy of the dried gels, and was found to be close to that of the feed. The effect of cross-linker (MBA) content in the copolymer was investigated in the concentration range of 1.1–9.1 mol% (R:90–10; R = mol NIPAAm/mol MBA) on the rheological behaviour and mechanical strength of the hydrogels. Both storage and loss modulus decreased with decreasing cross-linker content as revealed by dynamic rheometry. Gels R70 and R90 with very low cross-linker content (1.2–1.5 mol% MBA) have a very loose network structure, which is significantly different from those with higher cross-linker content manifesting in higher difference in storage modulus. The temperature dependence of the damping factor served the most accurate determination of the volume phase transition temperature, which was not affected by the cross-link density in the investigated range of MBA concentration. Gel R10 with highest cross-linker content (9.1 mol% MBA) behaves anomalously due to heterogeneity and the hindered conformation of the side chains of PNIPAAm.

**Keywords:** polymer gels, PNIPAAm, rheology, mechanical properties, copolymer composition

## 1. Introduction

Poly(*N*-isopropylacrylamide) (PNIPAAm) based hydrogels belong to the family of ‘intelligent’ materials, since they are able to undergo a volume phase transition at 32–34°C on the application of an external stimulus, namely change in temperature. By increasing the temperature the molecules of the polymer gel change their conformation from coil to

globule resulting in a change in their hydrophilic-hydrophobic character. Many applications of these smart hydrogels are being investigated such as thermo-responsive membranes [1], efficient and reversible immobilization of biomacromolecules [2–5], *in vitro* cell cultivation [6], separation of lignin [7] or phenols from aqueous mixtures [8–10] and drug and gene delivery [11]. Some special uses such

\*Corresponding author, e-mail: [vvargha@mail.bme.hu](mailto:vvargha@mail.bme.hu)  
© BME-PT

as biosensors [12], molecular imprinting [13], fluid microchips [14], as well as numerous biomedical applications are also being studied [3–5].

Since PNIPAAm homopolymer is water-soluble, for making hydrogels it must be cross-linked and for this purpose *N,N'*-methylene-bisacrylamide (MBA) is mostly used. The molar ratio of PNIPAAm and the cross-linker MBA in the feed composition is often expressed as R. The real ratio of the cross-linker in the copolymer however is hardly referred to in the literature. Further on cross-linking is purposed to improve the mechanical and elastic properties of the hydrogel. Dynamic rheometry provides important characterization with respect to linear viscoelasticity, strength, relaxational and phase transition of the material. In addition to the conventional methods, such as measuring the swelling ratio, turbidity measurements, calorimetry etc., dynamic rheometry also offers an alternative technique to accurately determine the volume phase transition of the gels. Petit and co-workers grafted PNIPAAm onto polyacrylamide backbone and investigated the thermoassociating properties of the graft copolymer by dynamic rheometry. Upon heating, PNIPAAm grafts dehydrate and self-aggregate into hydrophobic microdomains which promote the formation of a physical network above 36°C [15]. Senff and Richtering [16] investigated the effect of MBA cross-linker content on the rheological properties of PNIPAAm microgels. Zeng *et al.* [17] investigated the rheological behaviour of PNIPAAm homopolymer solutions in water during phase separation and proved the formation of physical network.

In this study P(NIPAAm) was cross-linked with MBA in the range of 1.10–9.10 mol% (R90–10). The copolymer composition at high conversion was determined directly by analyzing the resulted dry gels with solid state magic angle spinning (MAS) <sup>13</sup>C NMR spectroscopy and indirectly by analyzing the leaching water after polymerization via high

performance liquid chromatography. The effect of MBA cross-linker on the mechanical strength, rheological behavior, and volume phase transition of P(NIPAAm-co-MBA) hydrogels was investigated.

## 2. Experimental

### 2.1. Materials

*N*-isopropylacrylamide (NIPAAm) (Acros Organics, Belgium, stabilized with 500 ppm *p*-methoxyphenol), *N,N'*-methylene-bis-acrylamide (MBA), ammoniumpersulfate (APS) and *N,N,N',N'*-tetramethylethanediamine (TEMED) were supplied by Sigma-Aldrich, Germany and used as received. Chromatographic grade acetonitrile was obtained from Merck (Merck, Darmstadt, Germany). The high purity water was produced by Millipore system (Millipore, Billerica, USA).

### 2.2. Preparation of the gels

P(NIPAAm-co-MBA) hydrogels were prepared by redox free radical polymerization in water according to the method described by other authors [18, 19]. Briefly, to 5 ml aqueous solution of NIPAAm (1.0 M stock solution), the required quantity of MBA aqueous solution (0.1 M stock solution) was added resulting in an R value varying from 10 to 90 as indicated in Table 1. The quantity of APS and TEMED was 2 wt% respectively based on NIPAAm weight. The polymerization was performed in an ice-bath for 30 minutes, and left to stand for 72 hours at 25°C. After polymerization gels were washed in copious amount of deionized water at 25°C to remove the homopolymer and any unreacted components and all amount of the leaching water was collected. Gel purity was confirmed by testing the leaching water for residual monomers using UV-VIS spectroscopy (190–250 nm), and for PNIPAAm homopolymer by heating the leaching water to 50°C (above the phase transition temperature). No opacity of leaching water was experienced referring

**Table 1.** Feed and copolymer composition of P(NIPAAm-co-MBA) hydrogels determined by HPLC and by solid state <sup>13</sup>C CP MAS spectroscopy (R = mol NIPAAm/mol MBA)

Feed	R	10	30	50	70	90
	NIPAAm mole%	90.91	96.77	98.04	98.59	98.90
Copolymer by HPLC from leaching water	R	9.33	27.65	45.30	63.94	81.65
	NIPAAm mole%	90.32	96.51	97.84	98.46	98.79
Copolymer by HPLC from Soxhlet extract	R	9.81	29.77	49.51	70.43	86.72
	NIPAAm mole%	90.75	96.75	98.02	98.60	98.86
Copolymer by <sup>13</sup> C CP MAS NMR	R	9.65	22.15	42.48	49.51	83.03
	NIPAAm mole%	90.61	95.68	97.70	98.02	98.81



to the lack of PNIPAAm. Another series of the gels was purified after polymerization by Soxhlet extraction with water. The collected leaching water and the Soxhlet extracts were analyzed for NIPAAm and MBA content with high performance liquid chromatography (HPLC). This served as an indirect method for determining the real copolymer composition of the gels. The gels purified by leaching with water were dried at 50°C in vacuum until constant weight and directly tested for composition by <sup>13</sup>C solid state NMR spectroscopy.

## 2.3. Methods of characterization

### 2.3.1. High performance liquid chromatography

An integrated Hewlett Packard 1090 high performance liquid chromatograph (HPLC) was used with a UV detector (HP, Santa Alto, USA), at a detection wavelength of 220 nm. The column was BDS Hyper-sil C18 (100×4.6 mm, particle size 3 μm) purchased from Thermo Electron Corporation (Thermo Fisher Scientific Inc., Waltham, USA). The mobile phase used for chromatographic separation of NIPAAm and MBA was 5 v/v% of acetonitrile in high purity water. The collected leaching water was diluted with the mobile phase of the same volume. An isocratic elution technique was applied with a flow rate of 0.5 ml/min and an injected volume of 5 μl. Three parallel measurements were performed for each sample. A calibration graph was prepared using serial dilutions of 10, 30, 50, 70 and 100 μg/mL.

### 2.3.2. Solid state <sup>13</sup>C-NMR spectroscopy

The solid state magic angle spinning (MAS) <sup>13</sup>C spectra of the samples were recorded on a Varian NMR System (Varian Inc., Palo Alto, CA, U.S.A.) operating at <sup>1</sup>H frequency of 600 MHz with a Chemagnetics 3.2 mm narrow bore triple resonance T3 probe in double resonance mode. The <sup>13</sup>C spectra were measured with the cross polarization (CP) technique under the Hartmann-Hahn conditions [20] and a rotor spinning rate of 10 kHz. The proton  $\pi/2$  pulse was 3 μs and ramped cross polarization was used. The contact time was 3 ms and SPINAL-64 proton decoupling with a power of 83 kHz was applied [21] during the acquisition. The dry network samples were manually grained and kept in a vacuum chamber at 50°C for one day before measurements. The presence of residual solvent was checked by one pulse proton spectra and all the

samples were found to be free of remaining solvent molecules. The measuring temperature was 25°C and adamantane was used as the external chemical shift reference.

### 2.3.3. Dynamic rheometry

For rheological measurements an Anton Paar UDS 200 rheometer (Anton Paar GmbH, Graz, Austria) was used with a plate-plate arrangement. The distance of the plates was 0.5 mm. The dry gel samples were applied to the plate, deionised water was added, and equilibrium swelling was attained. Excess water was wiped with a tissue paper and after the sample thickness was adjusted, excess water was again added to the plate to avoid the loss of water from the sample during the measurements. Three parallel measurements were taken, on individual samples. For each of the samples, small deformation linearity was checked in the deformation range of 0.01–100 % strain amplitude at 10 Hz angular frequency at 25°C. Temperature sweeps were taken with the same arrangement between 25–60°C at 3°C·min<sup>-1</sup> heating rate, 10 Hz angular frequency and 1% strain amplitude. Frequency sweeps were carried out at 25°C in the range of 0.1–600 Hz angular frequency and 1% strain amplitude. After the temperature sweeps a frequency sweep was taken at 60°C with the same arrangement.

### 2.3.4. Stress-strain measurements

Uniaxial compression modulus of the gels was measured by a single column mechanical tester using Instron 5543 equipment (Pulse Technology, Sonoma, CA, U.S.A.) with a load cell of 5 N. Cylindrical gels were prepared, and the measurements were performed after the gels achieved their swelling equilibrium in water at ambient temperature. The height and the diameter of the cylindrical test specimen were measured under water without load. Three samples of each kind of gels were measured. The elastic modulus, *E*, was determined from the slope of linear dependence described by Equation (1) [22]:

$$\sigma = \frac{F}{A_0} = E(\lambda - \lambda^{-2}) \quad (1)$$

where  $\sigma$  is the applied stress, *F* is the value of measured force, *A* is the cross section of the undeformed swollen cylindrical gel, and  $\lambda$  is the relative deformation of the measured specimen.

### 3. Results and discussion

#### 3.1. Copolymer composition

P(NIPAAm-co-MBA) copolymers with different monomer ratios (i.e. R varying from 90–10 corresponding to 90.9–98.9 mol% NIPAAm respectively) were synthesized by free radical polymerization in water solution with APS/TEMED as redox initiator system. In order to determine the yield of the polymerization reaction, the purified gels were weighed after drying. The yield was >95% in each case. All the gels appeared transparent and clear, except Gel R10, which was opaque. The copolymer composition of the gels was determined indirectly using HPLC analysis of the collected leaching water, as well as of the Soxhlet extracts, and directly by solid state NMR analysis of the dry gels.

##### 3.1.1. Results of high-performance liquid chromatography

The retention times for MBA and NIPAAm were  $5.54 \pm 0.01$  and  $9.02 \pm 0.01$  minutes respectively for the applied chromatographic system. The other compounds used in the polymerization reaction (i.e. APS and TEMED) were not detected at the operating wavelength (220 nm). The detection limits for NIPAAm and MBA were calculated from the signal to noise ratio 3 to 1 and were found to be 160 and 332 ng/mL respectively. The selectivity of separation was proven by injection of blank solution and no signals were detected at the retention times of the solutes of interest.

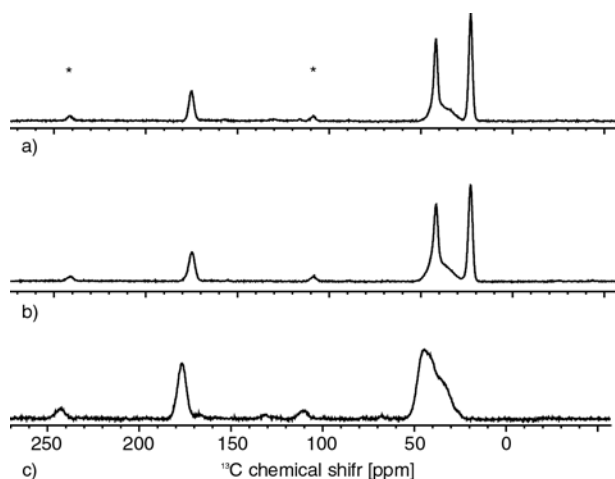
NIPAAm monomer content (mol% and the corresponding 'R' values) in the feed and in the copolymer detected by HPLC analysis of the leaching water as well as of the Soxhlet extracts are given in Table 1. On heating the leaching water to 50°C, i.e. above the temperature of volume phase transition, no precipitation of the homopolymer PNIPAAm could be detected visually. For both series at high conversion the composition of the resulting copolymer is close to that of the monomer feed. This also means that the R values (the molar ratio of NIPAAm to MBA) in the feed closely approximates the composition of the formed polymer gels as found by HPLC analysis.

It should be noted that in the 2<sup>nd</sup> series of experiments Soxhlet extraction was used to purify the gels despite the temperature of purification being higher than the phase transition temperature. Gupta *et al.*

[23] have also used Soxhlet extraction for removing ungrafted PNIPAAm homopolymer from grafted cellulose. It was expected that impurities become entrapped at higher cross-link ratio in the gel during Soxhlet purification, due to the high cross-link density, and collapsed structure of the gels during extraction. To test the presence of residual homopolymer trapped in the gels, gels were reversibly swelled (at room temperature) and shrunk in the leaching water following Soxhlet extraction. Surprisingly, neither homopolymer nor monomers could be detected by HPLC following the cooling-heating cycle. This perhaps could be attributed to the presence of some porosity in the network structure (even in the higher cross-link range, and with the temperature being above the LCST of PNIPAAm) which enabled the precipitated polymer to be released. However, due to the non-solubility of the homopolymer above the phase transition temperature, we do not recommend Soxhlet extraction for purification of PNIPAAm gels.

##### 3.1.2. Results of NMR spectroscopy

Nuclear magnetic resonance spectroscopy is a unique and direct method to determine the composition of polymeric materials. From signal intensities of the different groups the composition can be determined with high accuracy. Unfortunately, for the P(NIPAAm-co-MBA) gels, the monomer and the cross-linker units display similar chemical structures. By analysis of the <sup>1</sup>H and <sup>13</sup>C solution state NMR spectra of the monomers, only the proton resonances of the CH<sub>2</sub> group of the MBA (4.6 ppm) was distinguishable from the signals of the main chain CH<sub>2</sub> groups. However, the proton spectra of the highly swollen polymer gels displayed broad lines and the resonances of the CH<sub>2</sub> group of MBA overlapped with that of the CH group of NIPAAm, and the former peak could not be deconvoluted. From the <sup>13</sup>C-NMR spectra the ratio of the carbonyl and methyl signal intensities enables the calculation of the composition. Due to inhomogeneities of the sample in the NMR tube, however, the <sup>13</sup>C signals were very broad (spectra not shown). To get a good carbon spectra in the liquid state several days are needed. By using the cross polarization technique in the solid state, the measuring time was dramatically shortened (3 h). The application of cross polarization technique combined with magic angle spinning of



**Figure 1.**  $^{13}\text{C}$  CP MAS spectra of (a) PNIPAAm, (b) P(NIPAAm-co-MBA) gel with 90.9 mole% NIPAAm ( $R = 10$ ), and (c) poly( $N,N'$ -methylene-bis-acrylamide) (PMBA). The asterisks denote the spinning sidebands of the carbonyl signal ( $\nu_R = 10$  kHz).

the rotors and proper decoupling method resulted in excellent carbon spectra with good resolution as shown in Figure 1.

The signal intensity in the cross polarization  $^{13}\text{C}$  spectra depends on the cross polarization dynamics. The measuring parameters were chosen to get optimum signals for both the carbonyl and the methyl groups. At these polymeric networks the proton environment of the carbonyl groups is very similar. The measuring temperature was far below the glass transition temperature, so the mobility of the chains was very low and approximately the same in all investigated samples. With these approximations and using the ratio of the carbonyl and methyl signal intensities with cross polarization  $^{13}\text{C}$  spectra, the composition of the P(NIPAAm-co-MBA) gels could be calculated with an accuracy of 2%.

Table 1 contains the copolymer composition determined by solid state magic angle spinning (MAS)  $^{13}\text{C}$ -NMR. With respect to an accuracy of 2% of solid state  $^{13}\text{C}$  CP MAS-spectroscopy, these results support the findings of HPLC analysis, namely that at high conversion the composition of the copolymer gels are close to the feed composition. The  $R$  values are very sensitive to the molar ratio of the co-monomers, therefore the deviations from the  $R$  values of the feed are higher than the those of the molar concentrations. For simplicity during further evaluations we will refer to the  $R$  values of the feed composition, such as  $R$  10, 30, 50, 70 and 90.

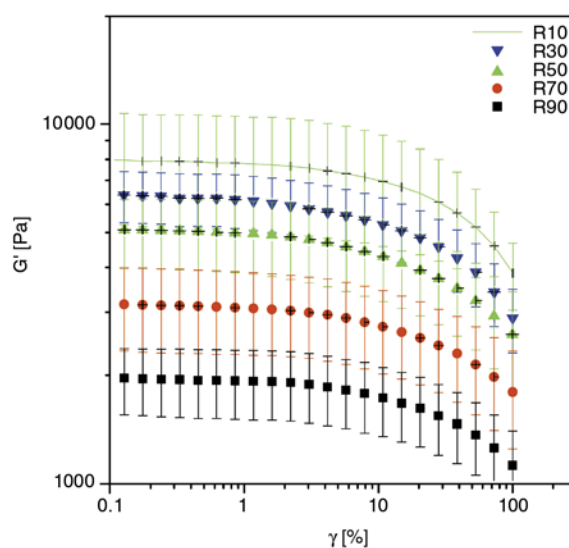
In addition to determining the composition of the synthesized gels, the efficiency of the purification method could be verified by solid and liquid state NMR spectroscopy. On the proton spectra no signals belonging to solvent or other small molecules (such as MBA or TEMED) were detected. Additionally, in the  $^{13}\text{C}$  chemical shift range of C–C double bonds (110–135 ppm) no signals were identified, indicating the absence of any residual monomer. It can be stated that the impurity content of the gels was less than 1–2% which is within the sensitivity range of the applied methods.

## 3.2. Dynamic rheometry

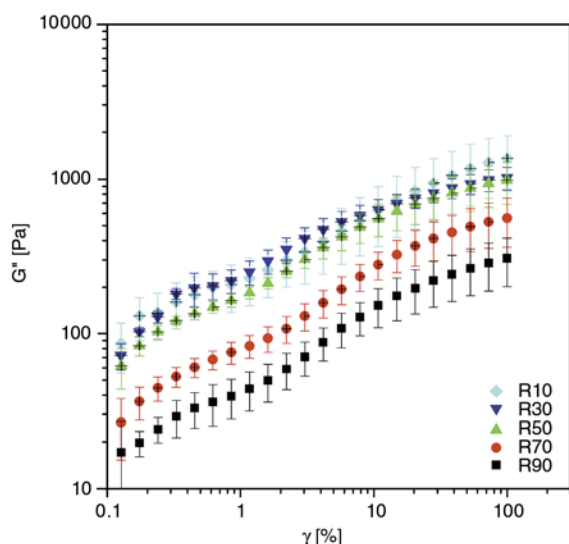
### 3.2.1. Strain-amplitude sweep of the gels of different cross-link density at constant frequency and temperature

The stability of the structure of viscoelastic materials is measured with increasing strain. This means the measurement at constant angular frequency ( $\omega = 10$  Hz) and temperature ( $25^\circ\text{C}$ ) with increasing controlled strain amplitude ( $\gamma$ ). This measurement refers to the strength of the gels. Its aim is the determination of the threshold limit of linear viscoelasticity (LVE), in order to select the strain for further measurements. The change of storage ( $G'$ ) and loss modulus ( $G''$ ) of the gels with strain-amplitude is given in Figures 2 and 3 respectively.

With the decrease of cross-linker (MBA) content (i.e. with increasing  $R$ ) the storage modulus decreased. This is comprehensible, since the lower the concen-



**Figure 2.** Change of storage modulus ( $G'$ ) with strain amplitude ( $\gamma$ ) for P(NIPAAm-co-MBA) hydrogels with different cross-linker content ( $\omega = 10$  Hz,  $T = 25^\circ\text{C}$ ,  $n = 3$ )



**Figure 3.** Change of loss modulus with strain amplitude for P(NIPAAm-co-MBA) hydrogels with different cross-linker content ( $\omega = 10$  Hz,  $T = 25^\circ\text{C}$ ,  $n = 3$ )

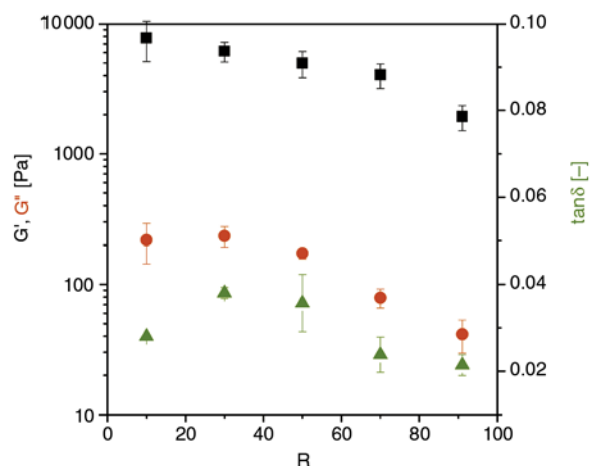
tration of the network points, the easier the deformation of the gel. For gels R 10–50, however, the difference in storage modulus is significantly lower in the whole deformation range, than for the gels with lower cross-linker content (for gels R70 and 90). This may be attributed to the very loose network structure of these gels.

For all the gels the storage modulus remained constant with an increase in strain amplitude up until a threshold limit of the linear viscoelastic range, beyond which a sudden drop in storage modulus was observed for each gel (see Figure 2). As expected, the threshold limit of linear viscoelasticity (LVE) also decreases with decreasing cross-linker content (Table 2). For further measurements the strain amplitude  $\gamma = 1\%$  was selected since all of the gels were still stable at this deformation.

In contrast to the change of storage modulus, the loss modulus continuously increases with increas-

**Table 2.** Threshold limit of linear viscoelastic range of P(NIPAAm-co-MBA) hydrogels with different cross-linker content

Gel	Strain [%]	Storage modulus [Pa]	
		Average	St. dev.
R10	7.85	7143	2467
R30	5.73	5570	1022
R50	2.21	4863	1160
R70	1.89	3036	777
R90	1.61	1917	417



**Figure 4.** The change of storage modulus, loss modulus and damping factor with decreasing cross-linker content at  $\gamma = 1\%$  strain amplitude ( $\omega = 10$  Hz,  $T = 25^\circ\text{C}$ ,  $n = 3$ )

ing deformation. As for the storage modulus, the loss modulus was also dependent on the cross-link density, and in the whole range of deformation with decreasing cross-linker content (i.e. with increasing R) the loss modulus decreased. Hydrogels R10, R30 and R50 have practically identical loss modulus within the range of standard deviation, while hydrogels with less cross-linker content – R70 and R90 – have significantly lower loss modulus and their difference is also much higher. This fact also supports the assumption that the cross-link structure of gels R70 and R90 significantly differs from those with higher cross-linker content. Figure 4 shows the change of storage modulus, loss modulus and damping factor ( $\tan \delta = \text{loss modulus/storage modulus}$ ) with varying cross-linker content selected at  $\gamma = 1\%$  strain amplitude ( $\omega = 10$  Hz at  $25^\circ\text{C}$ ). With decreasing cross-linker content, i.e. with the increase of R, the moduli decrease. Above R70 the decrease in modulus is more pronounced. This is especially interesting, since in respect to the molar concentration gel R70 only slightly differs from R90 but the change is even more expressive than for gels with R10, 30 and 50 where there is much higher difference in the molar concentration of cross-linker. The loss factor ( $\tan \delta$ ) decreases with decreasing cross-linker content, which may be attributed to the decreasing interaction between the polymer molecules. Gel R10 behaves anomalously, which may be caused by gel heterogeneity.

### 3.2.2. Temperature dependence of modulus with constant frequency and strain-amplitude

The change in storage modulus, loss modulus and in  $\tan\delta$  of all of the gels as a function of temperature is given in Figure 5. These measurements were carried out with controlled strain of 1%, and a frequency of 1 Hz.

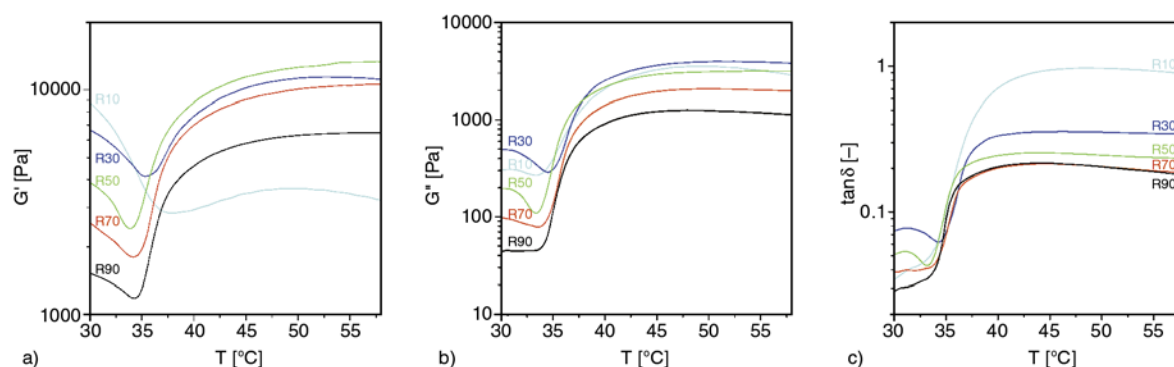
As expected, below the temperature of volume phase transition the values of storage modulus are successively higher for the gels with higher cross-linker content. Up to the temperature of volume phase transition the storage modulus decreases with increasing temperature for all the gels. This may be understood by higher mobility and higher water uptake of the molecules with increasing temperature. The volume phase transition involves a dramatic increase in storage modulus for all of the gels (except R10) until equilibrium is reached. For gels R30–90 the volume phase transition involves a conformational change of the molecules from coil to globule, water is expelled and the more compact structure results in a dramatically higher storage modulus. The behaviour of Gel R10 is anomalous. This could be attributed to the higher MBA content in the R10 gel compared to the others. Due to the highest cross-linker concentration, the heat evolved during polymerization is higher, than for the gels with lower cross-linker content, resulting in local increase of the temperature above that of the phase

transition leading to inhomogeneity. This is also supported by the opaque appearance of gel R10. Similarly to all the gels the volume phase transition of gel R10 starts at the same temperature (33°C), but it extends within a higher temperature range and the storage modulus does not increase after the phase transition. The reason for this may be the hindrance of conformation due to the high cross-link density. From the abrupt change of storage moduli the temperature of volume phase transition is in the range of 33–37°C, although this is not the most adequate parameter for its determination.

At the temperature of volume phase transition the loss moduli dramatically increase. Their onset temperature is almost identical for all the gels. With respect to the change of loss modulus with temperature Gel R10 also shows anomalous behaviour.

The most accurate method for determining the temperature of volume phase transition is monitoring the change of damping factor with temperature. Gels R70 and 90 are similar and have the lowest damping factor below and above phase transition. These are actually the best performing gels. The temperature of volume phase transition of the hydrogels determined from the change of rheological parameters with temperature is given in Table 3.

The cross-link density in the investigated range of MBA concentration (1.2–9.7 mol% in the copolymer) did not affect the temperature of volume phase



**Figure 5.** Change in storage modulus (a), loss modulus (b) and damping factor ( $\tan\delta$ ) (c) with temperature for hydrogels with different cross-linker content ( $\gamma = 1\%$ ,  $\omega = 1$  Hz)

**Table 3.** Onset temperature of volume phase transition of P(NIPAAm-co-MBA) hydrogels with different cross-linker content from dynamic rheometry

Gel	From storage modulus		From loss modulus		From damping factor	
	Average	St. dev.	Average	St. dev.	Average	St. dev.
R10	33.1	0.7	32.3	0.1	32.5	0.5
R30	34.4	0.2	33.2	0.2	33.3	0.2
R50	33.2	0.3	33.0	0.2	33.0	0.1
R70	33.0	0.2	33.3	0.2	33.2	0.1
R90	33.8	0.5	33.3	0.6	33.0	0.1

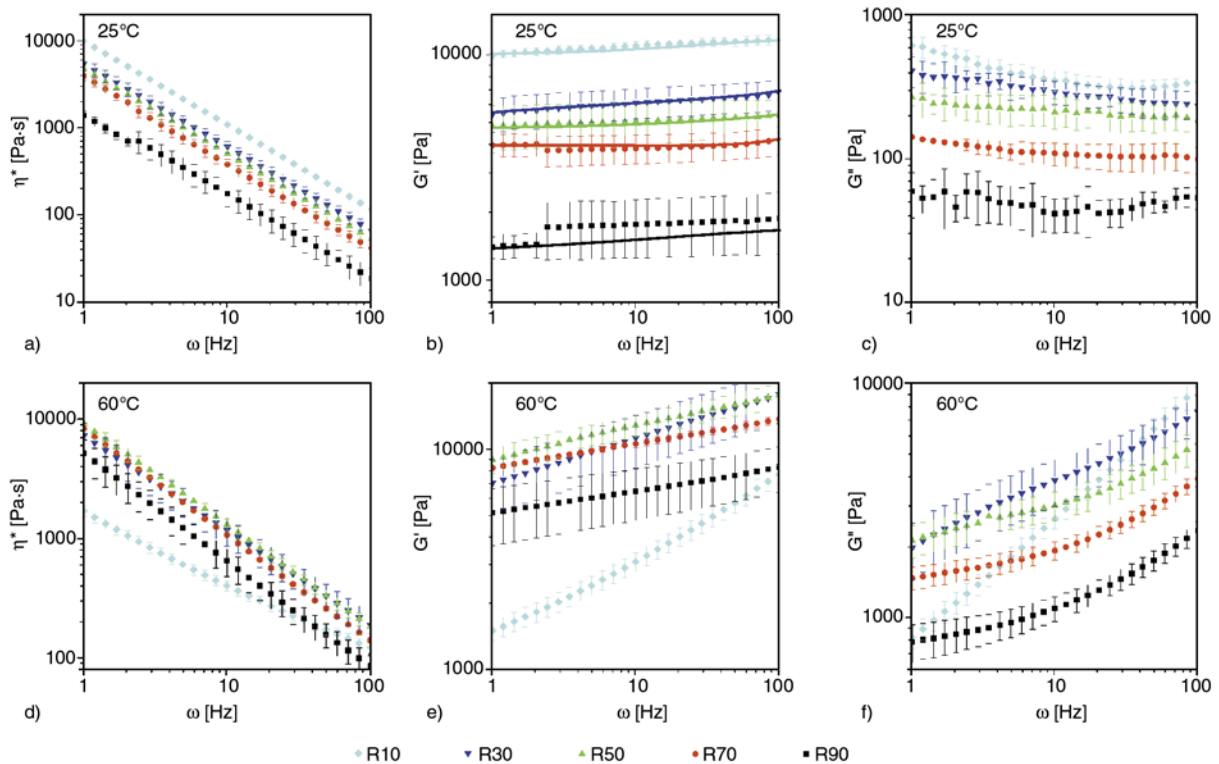
transition, although 9.7 mol% MBA resulted in a broader temperature range of transition of Gel R10.

### 3.2.3. Frequency-sweep measurements at constant strain-amplitude below and above the temperature of volume phase transition

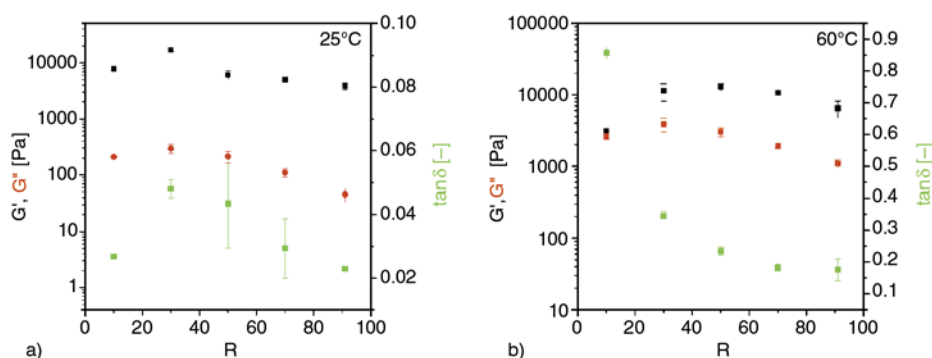
For presetting the strain with constant amplitude ( $\gamma = 1\%$ ), oscillatory measurements were carried out with increasing frequency (strain frequency sweep). These tests were conducted to verify the stability of the structures of viscoelastic materials below and above the phase transition temperature. The change of complex viscosity, storage modulus and loss modulus with angular frequency below and above the volume phase transition for the different hydrogels is represented in Figure 6.

The linear decrease of the complex viscosity with an increase in frequency is an indication of the cross-linked structure of the gels. The complex viscosity decreases with decreasing cross-linker content (with increasing R). Above the phase transition Gel R10 behaves anomalously just as in case of the temperature sweep. The reason may be heterogeneity and the differing gel structure due to the increased

cross-link density. The mobility of the side chains of PNIPAAm is mostly hindered. Practically there is no change in the storage modulus with frequency below the phase transition, which refers to a stable, cross-linked structure. Above the phase transition the hydrophobic gels behave like polymers, meaning that the modulus slightly increases with increasing frequency for each gel, except for Gel R10, where a steep increase in storage modulus was observed. This may be due to a peculiar change in the structure of Gel R10 above phase transition temperature. Figure 7 represents the change of storage modulus, loss modulus and damping factor with cross-linker content from frequency sweep measurements at  $\omega = 10$  Hz at 25 and 60°C. Below the volume phase transition the values of storage modulus are about two orders of magnitude higher than the values of the loss modulus, while above the phase transition temperature the difference between them is much lower. It follows that above the phase transition the loss modulus is impacted to a greater extent than the storage modulus. With decreasing cross-linker content both the storage and the loss modulus decrease.



**Figure 6.** The change of complex viscosity( $\eta^*$ ) (a, d), storage modulus ( $G'$ ) (b, e) and loss modulus ( $G''$ ) (c, f) at 25°C (a–c) and 60°C (d–f) for the gels with different cross-linker content ( $\gamma = 1\%$ )



**Figure 7.** The change of storage modulus, loss modulus and damping factor ( $\tan \delta$ ) with decreasing cross-linker content at 25 (a) and at 60°C (b) from frequency sweep measurements at 10 Hz angular frequency ( $\gamma = 1\%$ )

### 3.3. Mechanical behaviour

Rheological characterization was completed with mechanical tests. Compressive elastic modulus of the gels was calculated and summarised in Table 4. Elastic modulus of the P(NIPAAm-co-MBA) hydrogels increased as the cross-linking density increased. Equilibrium swelling degree of hydrogels decreased as a function of cross-linking density. It presented a larger network density in the gels which caused an increased rigidity. Modulus of Gel R10 was anomalous, structure inhomogeneity appeared in a small modulus. In that case the modulus was not in correlation with the cross-linking density.

### 4. Conclusions

The composition of P(NIPAAm-co-MBA) copolymer hydrogels with varying cross-linker content in the range of 1.1–9.1 mol% MBA was determined. At high conversion ( $>95\%$ ) the composition of the copolymers was close to the feed composition as determined by HPLC analysis of the leaching water and Soxhlet extracts following polymerization. This was also confirmed by solid state  $^{13}\text{C}$  CP MAS NMR spectroscopy of the formed gels. Due to the less accuracy of solid state NMR the R values calculated from the copolymer composition have higher deviations from those of the feed, since they are very sensitive to the molar concentration of the monomers.

At constant angular frequency with increasing controlled strain amplitude dynamic rheometry revealed that with the decrease of cross-linker (MBA) content (i.e. with increasing R) the storage modulus decreases. The threshold limit of linear viscoelasticity (LVE) also decreases with decreasing cross-linker content. The difference in both the storage and the loss moduli of hydrogels with the lowest

**Table 4.** Elastic modulus of P(NIPAAm-co-MBA) hydrogels with different cross-linker content

R	Elastic modulus [kPa]	
	Average	St. dev.
10	2.2	0.2
30	7.6	0.8
50	6.3	0.4
70	5.2	0.0
90	4.4	0.3

cross-linker content (Gel R70 and R90) during strain amplitude sweep is much higher than those between the gels with higher cross-linker content. This significant difference may be attributed to the loose network structure of these gels (R70 and R90). By selecting the data from the strain amplitude sweep at  $\gamma = 1\%$  and showing the change of storage modulus, loss modulus and damping factor with cross-linker content of the hydrogels, both storage and loss modulus decrease with decreasing cross-linker content. For hydrogels R90 and R70 the decrease in moduli is especially impressive. The damping factor ( $\tan \delta$ ) decreases with decreasing cross-linker content, which may be attributed to the decreasing interaction between the polymer molecules.

The temperature dependence of the damping factor served the most accurate determination of the volume phase transition temperature of the hydrogels. The cross-link density in the investigated range of MBA concentration (1.2–9.7 mol% in the copolymer) did not affect the temperature of volume phase transition, although 9.7 mol% MBA resulted in a broader temperature range of transition of Gel R10 due to its anomalous behavior during the temperature sweep.

The frequency dependence of the complex viscosity, and storage modulus below and above the volume phase transition temperature support the stable

cross-linked structure of the hydrogels. Both complex viscosity, storage and loss modulus decrease with decreasing cross-linker content (increasing R). Gel R10 with the highest cross-linker content (9.7 mol% MBA in the copolymer) behaves anomalously due to heterogeneity and the hindered conformation of the side chains of PNIPAAm. Below the volume phase transition temperature the values of storage modulus are about two orders of magnitude higher than the values of the loss modulus, while above the phase transition temperature the difference between them is much lower. It may be concluded that above the phase transition temperature the loss modulus is impacted to a greater extent than the storage modulus.

Elastic modulus of the P(NIPAAm-co-MBA) hydrogels increased as the cross-link density increased. Modulus of Gel R10 was anomalously low due to structure inhomogeneity.

### Acknowledgements

Authors thank the Hungarian Scientific Research Fund OTKA K75182, the Hungarian Science and Technology Foundation ZA-9/2006, the Hungarian project GVOP-3.2.1.-2004-04-0210/3.0, the National Science Foundation (South Africa), and the CSIR (South Africa), for financial support.

### References

- [1] Li P-F., Ju X-J., Chu L-Y., Xie R.: Thermo-responsive membranes with cross-linked poly(*N*-isopropyl-acrylamide) hydrogels inside porous substrates. *Chemical Engineering and Technology*, **29**, 1333–1339 (2006). DOI: [10.1002/ceat.200600174](https://doi.org/10.1002/ceat.200600174)
- [2] Fänger C., Wack H., Ulbricht M.: Macroporous poly(*N*-isopropylacrylamide) hydrogels with adjustable size ‘cut-off’ for the efficient and reversible immobilization of biomacromolecules. *Macromolecular Bioscience*, **6**, 393–402 (2006). DOI: [10.1002/mabi.200600027](https://doi.org/10.1002/mabi.200600027)
- [3] Lu Z-R., Kopečková P., Kopeček J.: Antigen responsive hydrogels based on polymerizable antibody fab’ fragment. *Macromolecular Bioscience*, **3**, 296–300 (2003). DOI: [10.1002/mabi.200390039](https://doi.org/10.1002/mabi.200390039)
- [4] Zhang X. X., Li J., Gao J., Sun L., Chang W. B.: Determination of morphine by capillary electrophoresis immunoassay in thermally reversible hydrogel-modified buffer and laser-induced fluorescence detection. *Journal of Chromatography A*, **895**, 1–7 (2000).
- [5] Zhang X-X., Li J., Gao J., Sun L., Chang W-B.: Determination of doping methyltestosterone by capillary electrophoresis immunological analysis with thermally reversible hydrogel and laser-induced fluorescence. *Electrophoresis*, **20**, 1998–2002 (1999). DOI: [10.1002/\(SICI\)1522-2683\(19990701\)20:10<1998::AID-ELPS1998>3.0.CO;2-C](https://doi.org/10.1002/(SICI)1522-2683(19990701)20:10<1998::AID-ELPS1998>3.0.CO;2-C)
- [6] Haraguchi K., Takehisa T., Ebato M.: Control of cell cultivation and cell sheet detachment on the surface of polymer/clay nanocomposite hydrogels. *Biomacromolecules*, **7**, 3267–3275 (2006). DOI: [10.1021/bm060549b](https://doi.org/10.1021/bm060549b)
- [7] Cai W., Anderson E. C., Gupta R. B.: Separation of lignin from aqueous mixtures by ionic and nonionic temperature-sensitive hydrogels. *Industrial and Engineering Chemistry Research*, **40**, 2283–2288 (2001). DOI: [10.1021/ie0009435](https://doi.org/10.1021/ie0009435)
- [8] Kosik K., Wilk E., Geissler E., László K.: Distribution of phenols in thermoresponsive hydrogels. *Macromolecules*, **40**, 2141–2147 (2007). DOI: [10.1021/ma0624806](https://doi.org/10.1021/ma0624806)
- [9] László K., Kosik K., Rochas C., Geissler E.: Phase transition in poly(*N*-isopropylacrylamide) hydrogels induced by phenols. *Macromolecules*, **36**, 7771–7776 (2003). DOI: [10.1021/ma034531u](https://doi.org/10.1021/ma034531u)
- [10] Kosik K., Wilk E., Geissler E., László K.: Interaction of phenols with thermo-responsive hydrogels. *Colloids and Surfaces A: Physicochemical and Engineering Aspects*, **319**, 159–164 (2008). DOI: [10.1016/j.colsurfa.2007.07.022](https://doi.org/10.1016/j.colsurfa.2007.07.022)
- [11] Hoare T. R., Kohane D. S.: Hydrogels in drug delivery: Progress and challenges. *Polymer*, **49**, 1993–2007 (2008). DOI: [10.1016/j.polymer.2008.01.027](https://doi.org/10.1016/j.polymer.2008.01.027)
- [12] Chang D. P., Dolbow J. E., Zauscher S.: Switchable friction of stimulus-responsive hydrogels. *Langmuir*, **23**, 250–257 (2007). DOI: [10.1021/la0617006](https://doi.org/10.1021/la0617006)
- [13] Yamashita K., Nishimura T., Ohashi K., Ohkouchi H., Nango M.: Two-step imprinting procedure of interpenetrating polymer network-type stimuli-responsive hydrogel-adsorbents. *Polymer Journal*, **35**, 545–550 (2003). DOI: [10.1295/polymj.35.545](https://doi.org/10.1295/polymj.35.545)
- [14] Sugiura S., Szilágyi A., Sumaru K., Hattori K., Takagi T., Filipesei G., Zrínyi M., Kanamori T.: On-demand microfluidic control by micropatterned light irradiation of a photoresponsive hydrogel sheet. *Lab on a Chip*, **9**, 196–198 (2009). DOI: [10.1039/B810717C](https://doi.org/10.1039/B810717C)
- [15] Petit L., Karakasyan C., Pantoustier N., Hourdet D.: Synthesis of graft polyacrylamide with responsive self-assembling properties in aqueous media. *Polymer*, **48**, 7098–7112 (2007). DOI: [10.1016/j.polymer.2007.09.040](https://doi.org/10.1016/j.polymer.2007.09.040)



- [16] Senff H., Richtering W.: Influence of cross-link density on rheological properties of temperature-sensitive microgel suspensions. *Colloid and Polymer Science*, **278**, 830–840 (2000).  
DOI: [10.1007/s003960000329](https://doi.org/10.1007/s003960000329)
- [17] Zeng F., Zheng X., Tong Z.: Network formation in poly(*N*-isopropyl acrylamide)/water solutions during phase separation. *Polymer*, **39**, 1249–1251 (1998).  
DOI: [10.1016/S0032-3861\(97\)00471-0](https://doi.org/10.1016/S0032-3861(97)00471-0)
- [18] László K., Kosik K., Geissler E.: High-sensitivity isothermal and scanning microcalorimetry in PNIPAA hydrogels around the volume phase transition. *Macromolecules*, **37**, 10067–10072 (2004).  
DOI: [10.1021/ma048363x](https://doi.org/10.1021/ma048363x)
- [19] Zhang X., Zhuo R., Yang Y.: Using mixed solvent to synthesize temperature sensitive poly(*N*-isopropylacrylamide) gel with rapid dynamics properties. *Biomaterials*, **23**, 1313–1318 (2002).  
DOI: [10.1016/S0142-9612\(01\)00249-6](https://doi.org/10.1016/S0142-9612(01)00249-6)
- [20] Hartmann S. R., Hahn E. L.: Nuclear double resonance in the rotating frame. *Physical Review*, **128**, 2042–2053 (1962).  
DOI: [10.1103/PhysRev.128.2042](https://doi.org/10.1103/PhysRev.128.2042)
- [21] Fung B. M., Khitrin A. K., Ermolaev K. J.: An improved broadband decoupling sequence for liquid crystals and solids. *Journal of Magnetic Resonance*, **142**, 97–101 (2000).  
DOI: [10.1006/jmre.1999.1896](https://doi.org/10.1006/jmre.1999.1896)
- [22] Muniz E. C., Geuskens G.: Compressive elastic modulus of polyacrylamide hydrogels and semi-IPNs with poly(*N*-isopropylacrylamide). *Macromolecules*, **34**, 4480–4484 (2001).  
DOI: [10.1021/ma001192l](https://doi.org/10.1021/ma001192l)
- [23] Gupta K. C., Khandekar K.: Temperature-responsive cellulose by ceric(IV) ion-initiated graft copolymerization of *N*-isopropylacrylamide. *Biomacromolecules*, **4**, 758–765 (2003).  
DOI: [10.1021/bm020135s](https://doi.org/10.1021/bm020135s)